2016

Geometrically-Complex Magnetic Field Distributions Enabled By Bulk, Laser-Micromachined Permanent Magnets At The Submillimeter Scale

Brock Alan Peterson
University of Pennsylvania, brockpeterson@seas.upenn.edu

Geometrically-Complex Magnetic Field Distributions Enabled By Bulk, Laser-Micromachined Permanent Magnets At The Submillimeter Scale

Abstract
High-energy-product permanent magnets (PM) are utilized in many industrial, research, consumer, and commercial applications. Indeed, there are many potential applications that can utilize sub-mm PM to create miniaturized versions of motors, generators, energy harvesters, undulators, sensors, actuators, and other microelectromechanical systems (MEMS) devices. Magnets in MEMS are both important and useful because they can provide a strong force at a distance within a compact package; however, there exists a gap in magnet technologies today where magnets have little to no presence between bottom-up microfabricated PM and top-down machined bulk PM. Thus, there is a need for a form of PM that can be 100–500□□m thick with lateral dimensions of the same order to fill this gap and provide the advantageous magnetic properties of bulk PM at this scale. This dissertation presents the development of laser micromachining as a fabrication technology that enables the microfabrication of PM to generate geometrically complex magnetic fields at the sub-mm scale. Generating geometrically complex magnetic fields at the sub-mm scale opens up new possibilities in medical technology, energy generation, and many other applications. Models simulating magnetic properties and the effects of laser machining are presented and compared to measurements. The fabrication technology discussed here allows sub-mm, geometrically complex magnetic fields to be achieved while maintaining the characteristics of bulk PM. The utility of this advance in fabrication technology is demonstrated through multiple research vehicles, including undulators for radiation generation and multipole energy harvesters operable at low frequency. Such vehicles represent a small sample of the potential applications for this work.

Degree Type
Dissertation

Degree Name
Doctor of Philosophy (PhD)

Graduate Group
Electrical & Systems Engineering

First Advisor
Mark G. Allen

Keywords
Laser Micromachining, Magnetic Field, Micromagnet, Permanent Magnet, Submillimeter, Undulator

Subject Categories
Electrical and Electronics | Electromagnetics and Photonics | Elementary Particles and Fields and String Theory

GEOMETRICALLY-COMPLEX MAGNETIC FIELD DISTRIBUTIONS ENABLED BY BULK, LASER-MICROMACHINED PERMANENT MAGNETS AT THE SUBMILLIMETER SCALE

Brock Alan Peterson

A DISSERTATION

in

Electrical and Systems Engineering

Presented to the Faculties of the University of Pennsylvania

in

Partial Fulfillment of the Requirements for the

Degree of Doctor of Philosophy

2016

Supervisor of Dissertation

_____

Dr. Mark G.	Allen	Alfred Fitler Moore Professor Scientific Director of the Singh Center for Nanotechnology

Graduate Group Chairperson

_____

Dr. Alejandro	Ribeiro	Rosenbluth Associate Professor

Dissertation Committee

Dr. Nader	Engheta	H. Nedwill Ramsey Professor, Department of Electrical and Systems Engineering
Dr. David	Issadore	Assistant Professor of Bioengineering and Electrical and Systems Engineering
Dr. Kevin	Turner	Professor, Department of Mechanical Engineering and Applied Mechanics

GEOMETRICALLY-COMPLEX MAGNETIC FIELD DISTRIBUTIONS ENABLED BY BULK, LASER-MICROMACHINED PERMANENT MAGNETS AT THE SUBMILLIMETER SCALE

Dedication

To Allison Peterson for her love, support, and encouragement and sharing in the wonderful moments as part of beginning and raising a family as a graduate student.

ACKNOWLEDGMENT

I would first like to thank my advisor and mentor, Dr. Mark Allen, for his extensive support and guidance while at Georgia Tech and Penn and for trusting me with purchasing the micromachining lasers at Penn. I would also like to thank my dissertation committee for the ideas generated and guidance in finishing my graduate work at Penn. Additionally, I would also like to thank Richard Shafer and Florian Herrault for the knowledge disseminated during our time at Georgia Tech.

I would like to acknowledge the efforts of our collaborators at University of Florida as part of the Interdisciplinary Microsystems Group: David Arnold, Alexandra Garraud, Ololade David "Lola" Oniku, and William "Chip" Patterson. They provided many hours of conference calls, magnetic field images, and joint testing at our collaborators. Thanks also goes to our collaborators at University of Michigan – Ann Arbor, Center for Ultrafast Optical Science (Dr. Alec Thomas and his team); University of California - Los Angeles, Particle Beam Physics Laboratory (Dr. James Rosenzweig, Ivan Gadjev, and their team); Stanford Linear Accelerator Center (Mark Hogan, Christine Clark, and others); Los Alamos National Labs (Michael Di Rosa, Scott Evans, and Yong Ho Kim); and Nora Dempsey and Damien Le Roy of Institut Néel of Grenoble, France.

I would like to thank Yuan Li and Melissa Tsang for their friendship, insight, perspective, and advice these past five years. Their friendship has lifted me and my family up in numerous ways. It is my hope that my influence on them can be nearly as significant.

I would like to thank the rest of the MSMA Group members at both GT and Penn, Purnima Sharma of GT and John Russell of Penn. I would also like to acknowledge the assistance of Noah Clay and many other Singh and SEAS personnel, including (but not limited to) Matt Brukman, Jamie Ford, Eric Johnston, David Jones, Kyle Keenan, Ira Winston and Leandra Davis. Their help in training on and teaching how to best use tools as well as maintenance,

acquirement, and installation of the micromachining lasers and other tools were instrumental to my work.

The IPG Photonics – Microsystems Division team was instrumental in my efforts to understand laser machining, namely Jeff Sercel, Joshua Stearns, Rouzbeh Sarrafi, Marco Mendes, and others. Additionally, Resonetics provided the Nd:YLF laser detailed in this dissertation that was used at GT and Glenn Ogura and his team provided valuable insights during our investigations to purchase new laser micromachining systems.

I would like to also thank the ESE staff and faculty who have been part of my time at Penn, specifically Irene Tan and Lilian Wu for their help in the transition from GT and throughout.

I would like to thank the MRI staff at Penn, Stephen Pickup and Weixia Liu, and Georgia Tech, Johannes Leisen and his team. Their MRI facilities were essential for my magnet studies.

I would like to thank Neal Bangerter, my research advisor during my undergraduate research at BYU, for the many hours of advice, mentoring, and friendship; the Biomedical Imaging Research team at BYU (Danny Park, Brady Quist, Steven Allen, Hilary Price, and Hyrum Griffin) for their friendship and collaboration; and the IMMERSE summer research program and faculty involved. This program provided my introduction to microelectronics research, a path I have followed to this day.

Lastly, I would like to express appreciation to my parents (all five of them) and grandparents for the help and love provided in my life and especially to my wife, Allison, and our children, without whom I would not be where I am today. I love them with all my heart and would not be complete with them. I would also like to express gratitude to my Heavenly Father for the guidance and comfort provided to my family and I over the years.

ABSTRACT

GEOMETRICALLY-COMPLEX MAGNETIC FIELD DISTRIBUTIONS ENABLED BY BULK, LASER-MICROMACHINED PERMANENT MAGNETS AT THE SUBMILLIMETER SCALE

Brock Alan Peterson

Dr. Mark G. Allen

High-energy-product permanent magnets (PM) are utilized in many industrial, research, consumer, and commercial applications. Indeed, there are many potential applications that can utilize sub-mm PM to create miniaturized versions of motors, generators, energy harvesters, undulators, sensors, actuators, and other microelectromechanical systems (MEMS) devices. Magnets in MEMS are both important and useful because they can provide a strong force at a distance within a compact package; however, there exists a gap in magnet technologies today where magnets have little to no presence between bottom-up microfabricated PM and top-down machined bulk PM. Thus, there is a need for a form of PM that can be 100–500 μm thick with lateral dimensions of the same order to fill this gap and provide the advantageous magnetic properties of bulk PM at this scale. This dissertation presents the development of laser micromachining as a fabrication technology that enables the microfabrication of PM to generate geometrically complex magnetic fields at the sub-mm scale. Generating geometrically complex magnetic fields at the sub-mm scale opens up new possibilities in medical technology, energy generation, and many other applications. Models simulating magnetic properties and the effects of laser machining are presented and compared to measurements. The fabrication technology discussed here allows sub-mm, geometrically complex magnetic fields to be achieved while maintaining the characteristics of bulk PM. The utility of this advance in fabrication technology is demonstrated through multiple research vehicles, including undulators for radiation generation and multipole energy

harvesters operable at low frequency. Such vehicles represent a small sample of the potential applications for this work.

TABLE OF CONTENTS

LIST OF TABLES

LIST OF ILLUSTRATIONS

LIST OF NOMENCLATURE

Electromagnetic Properties [SI Units]

ϕ – Magnetic Flux [Wb or Vs]

$\vec{B}$ – Magnetic Flux Density [T]

$\vec{E}$ – Electric Field [V/m]

$\vec{H}$ – Magnetic Field [A/m]

$\vec{M}$ – Magnetization [A/m]

$\vec{m}$ – Magnetic moment [Am^2]

μ_0 – Vacuum Magnetic Permeability [H/m]

μ_r – Relative Magnetic Permeability

$\mu_0\vec{M}$ – Magnetization [T]

B_r, M_r – Magnetic Remanence [T, A/m]

M_s – Magnetic Saturation [A/m]

H_c – Coercivity [A/m]

H_{ci} – Intrinsic Coercivity [A/m]

T_{max} – Maximum use temperature for a magnet [˚C]

T_{Curie} – Temperature at which magnet loses magnetization [˚C]

T_{melt} – Melting Temperature [˚C]

Laser Properties

λ – Wavelength [m]

E_{pulse} – Pulse Energy [J]

P_{avg} – Average Power [W]

P_{peak} – Peak Power [W]

I – Intensity [W/m^2]

E_{ph} – Photon Energy [J, or eV]

h – Plank Constant [Js]

Undulator Related Parameters

λ_u – Undulator/Wiggler Period [m]

λ_{rad} – Undulator Output Radiation Wavelength [m]

γ – Lorentz Factor

K – Undulator Parameter

E_e – Electron Energy [J, or eV]

E_0 – Electron Rest Energy [J, or eV]

m – Electron Rest Mass [kg]

$\vec{v}$ – Electron Velocity [m/s]

c – Speed of Light [m/s]

CHAPTER 1 INTRODUCTION

1.1 Scope and Significance of the Problem

Spatially complex magnetic systems where lateral spatial frequencies are on the order of tens to hundreds of microns and thicknesses are on the order of hundreds of microns are essential for the fabrication of magnetic MEMS. Permanent magnets (PM) give a high stroke length, provide contactless forces, can be arranged so as to produce various magnetic patterns, and benefit from the ability of a magnet to be shrunk and maintain magnetic fields at the same relative distance from the magnet [1]. Large magnets are already used in many large-scale devices that could be redesigned to exist on the submillimeter scale. However, it is currently challenging to fabricate high quality magnets on such scales through traditional means, whether considering traditional top-down machining approaches or microfabrication-based bottom-up approaches. Traditional top-down machining approaches often lack the precision or tooling to machine to lateral submillimeter dimensions and the delicacy required in handling some magnetic materials, or the economics of reducing the volume of a magnet make it impractical.

Of particular import in magnetic microsystems, generally, is maintaining a strong magnetic field a significant/useable distance from the surface of the magnet. Bottom-up microfabricated magnets are normally too thin to provide sufficient magnetic fields at reasonable distances of tens to hundreds of microns from their surface, due to inferior magnetic properties [2] or as a result of the magnetic field decreasing substantially with distance from the magnet surface [3]. This decrease in field with distance can be

illustrated by the analytical expression for the magnetic field along the axis of a disc magnet, as in Figure 1.1,

$$\vec{B}(z) = \frac{B_r}{2}\left(\frac{z}{\sqrt{z^2+R^2}} - \frac{z-L}{\sqrt{(z-L)^2+R^2}}\right), \quad (1.1)$$

where z is distance from the surface, R is the radius, L is the length or thickness, and B_r is the remanence of the material [3]. For inferior materials, B_r can be small, and for thin films, L is small.

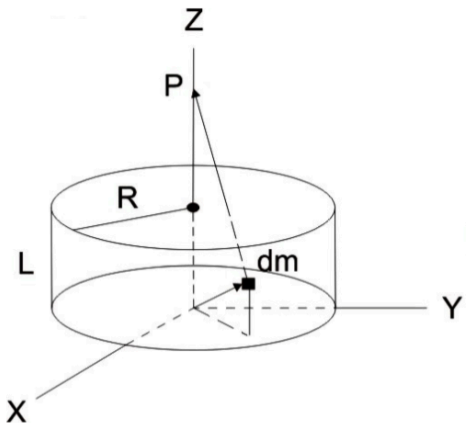

Figure 1.1 Schematic of a disc magnet

This dissertation asserts that 1) high energy product magnets are a challenge to fabricate between 50 μm and 300 μm in thickness 2) while maintaining feature sizes of similar submillimeter dimensions and that 3) spatially complex magnetic field profiles are important in order to implement magnetic systems on the submillimeter scale. This dissertation hypothesizes that submillimeter-scale, geometrically-complex magnetic fields can be enabled by laser micromachining bulk-produced permanent magnets. The background and mechanisms involved with the laser machining of these magnets are presented. The process and limits of this fabrication technology are detailed. The

fabrication process includes laser machining and post-processing the magnet substrates, magnetizing as appropriate, and assembling into a pre-designed magnetic pattern. Models and magnetic measurements characterize the effectiveness of the fabrication technology. Lastly, applications demonstrating some of the capabilities of laser-machining-enabled, submillimeter-scale magnets and directions for possible future research are detailed.

1.1.1 The Challenges of Fabricating Micromagnets

Magnetic materials have been partially understood for at least two millennia and have been in regular use, mainly as a compass needle, for nearly one millennium. Magnetism itself became better understood with the experiments of William Gilbert in the 1600s, but the physics behind and connections between magnetic and electric fields remained unexplored until the early nineteenth century. Prior to the 20th century, permanent magnets had limited uses, mostly in compasses and experimental physical attractions. Over the next century, new magnetic materials were discovered (i.e., beyond lodestone/magnetite and iron), and new applications were developed. Magnetic material properties, such as energy product, coercivity, remanence, and Curie temperature, have also greatly improved as a result of these developments and discoveries [4] [5] [6].

Bulk magnets are included in many large-scale devices due to the fact they do not require energy to maintain their fields, they can be used to hold objects many times their volume, they exhibit a contactless force, and they can function over a large range of temperatures [7]. Today, magnets or magnetic fields are incorporated in many devices, such as electron undulators and wigglers [8], electron path bending magnets [9], PM motors and generators [10] [11], Magnetic Resonance Imaging [12], door locks and

latches [13], fridge magnets, alignment magnets [14], magnetic computer RAM, computer hard disks [15], vehicles [5], and sensors and actuators [16]. Naturally, with this kind of versatility, magnets in MEMS and other small-scale devices have been sought after more and more in recent years [2] [4] [5] [17] [18] [19].

In order to understand if shrinking magnet dimensions is indeed desirable, it is instructive to examine how magnetic fields and interactions change as the sources of this field are reduced in size. If a magnet is reduced by a scale factor k, where L' = L/k, R'=R/k, and the measurement distance z' = z/k and use equation 1.1:

$$\vec{B}'(z', L', R') = \vec{B}'\left(z' = \frac{z}{k}, L' = \frac{L}{k}, R' = \frac{R}{k}\right) = \frac{B_r}{2}\left(\frac{\frac{z}{k}}{\sqrt{\left(\frac{z}{k}\right)^2+\left(\frac{R}{k}\right)^2}} - \frac{\frac{z}{k}-\frac{L}{k}}{\sqrt{\left(\frac{z}{k}-\frac{L}{k}\right)^2+\left(\frac{R}{k}\right)^2}}\right) =,$$

$$\frac{B_r}{2}\left(\frac{1/k}{1/k}\frac{z}{\sqrt{z^2+R^2}} - \frac{1/k}{1/k}\frac{z-L}{\sqrt{(z-L)^2+R^2}}\right) = \frac{B_r}{2}\left(\frac{z}{\sqrt{z^2+R^2}} - \frac{z-L}{\sqrt{(z-L)^2+R^2}}\right),$$

$$\vec{B}'(z', L', R') = \vec{B}(z, L, R), \tag{1.2}$$

the magnetic field remains the same [3], as in Figure 1.2, assuming $B_r = 1\ [T]$ for simplicity. Note how $\vec{B}'(z') = \vec{B}(z)$, where k = 2 and z' = z/2 (i.e. distance from magnet surface z = 2 mm, z' = 1 mm, R = 3 mm, R' = 1.5 mm, L = 1.5 mm, and L' = 0.75 mm; $\vec{B}(z)$ is the blue solid line and $\vec{B}'(z')$ is the green dashed line).

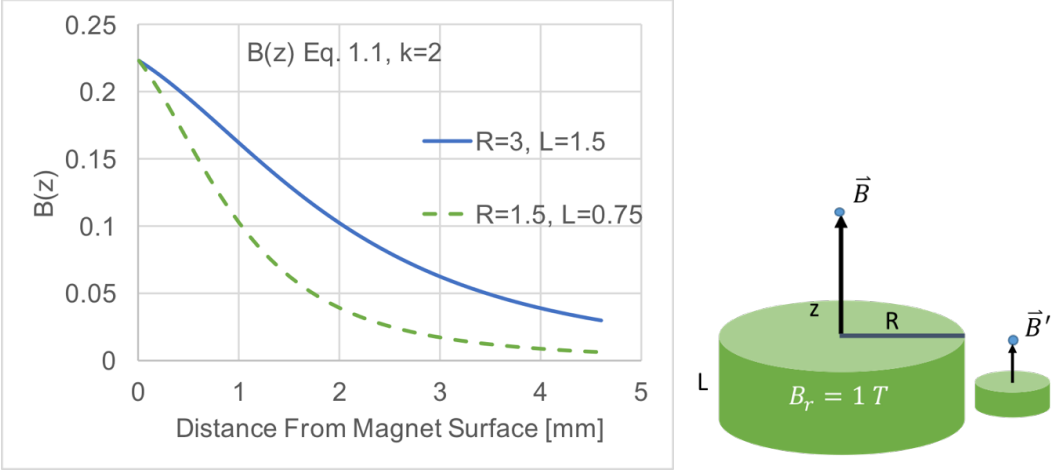

Figure 1.2 (left) Chart showing results of eq. 1.1 and scale factor k=2 and (right) a schematic representing the dimensions that scale

Similarly, Figure 1.3a shows the same magnetic flux density, again assuming $B_r = 1\ [T]$, but at a given distance from the surface as a function of the ratio of radius to length, R/L, and the ratio of length to measurement height, L/z. The bottom two lines of the chart show two examples where the measurement height is equal to the height of the magnet, 1 mm and 2 mm. Note how they follow the same curve. The other three curves represent when the measurement height, z, is less than the thickness/length of the magnet, L. The maximum flux density attainable at a constant height increases with increasing L/z. Figure 1.3b shows another example at a smaller scale using the measurement height of 100 μm with various magnet thicknesses. Note how low the magnetic flux density is at a measurement height of 100 μm from the surface for magnets only on the order of tens of microns in thickness. This chart reveals something else important for magnet assemblies: specific feature sizes for a given thickness will help maximize the magnetic

flux density available at a given height and the design should follow that rule when possible.

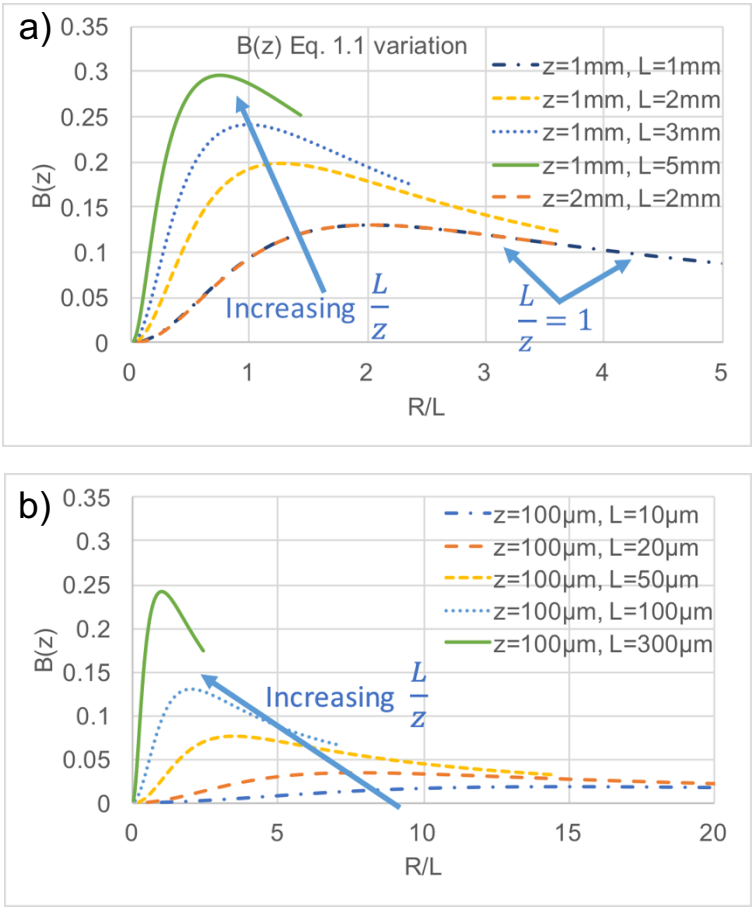

Figure 1.3 Chart showing results of eq. 1.1 showing B(z) as a function of the ratio radius to length and as the ratio length over measurement distance increases for a) mm-scale magnets and b) magnets tens to hundreds of microns thick

Another representation of this equation takes a cylinder magnet where the measurement height from the disk is equal to half its radius and both are scaled equally for a given cylinder/disk length and remanence of 1 Tesla, as in Figure 1.4. Different curves represent five cylinder lengths. Moving vertically on this chart shows how increasing the

length of the cylinder can increase the magnetic field for a given measurement height and radius. In order to maintain a flux density over 0.1 Tesla for this geometry at a height of 100 μm, the disk must have a length of at least 20 μm. This demonstrates the need for relatively thick magnets on the order of the measurement height.

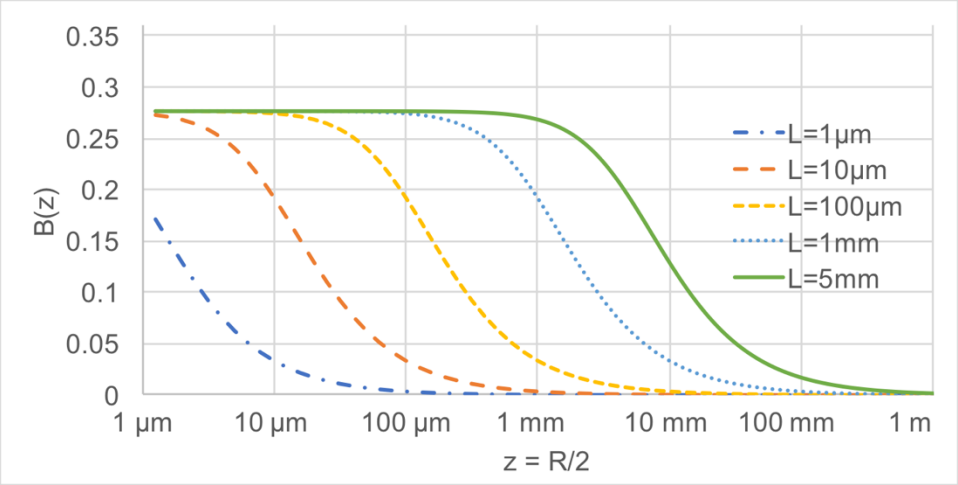

Figure 1.4 Chart showing results of eq. 1.1 showing B(z) as a function of measurement height (the radius is maintained at twice the measurement height) and magnet length

Similar analytical expressions exist for other azimuthally symmetric shapes such as a cone or sphere. More relevant to this dissertation are the equations for the flux density along the center axis of a ring and a rectangular prism. The same rules for scaling of dimensions hold true for these other shapes as well. The equation for a ring is simply the flux density of a cylinder/disk the size of the outer radius, subtracting the flux density of a cylinder/disk the size of the inner radius:

$$\vec{B}(z) = \frac{B_r}{2}\left[\left(\frac{z}{\sqrt{z^2+R_1^2}} - \frac{z-L}{\sqrt{(z-L)^2+R_1^2}}\right) - \left(\frac{z}{\sqrt{z^2+R_2^2}} - \frac{z-L}{\sqrt{(z-L)^2+R_2^2}}\right)\right], \quad (1.3)$$

where R_1 is the outer radius, R_2 is the inner radius, L is the length, and z is the measurement height. The equation for a slightly less azimuthally symmetric rectangular prism (or block) is slightly more complicated as:

$$\vec{B}(z) = \frac{B_r}{\pi}\left[\tan^{-1}\left(\frac{ab}{(z-c)\sqrt{a^2+b^2+(z-c)^2}}\right) - \tan^{-1}\left(\frac{ab}{(z+c)\sqrt{a^2+b^2+(z+c)^2}}\right)\right], \quad (1.4)$$

where a is half the length in the x direction, b is half the width in the y-direction, c is half the height in the z-direction, and z is the measurement height [3]. Figures representing each are shown in Figure 1.5.

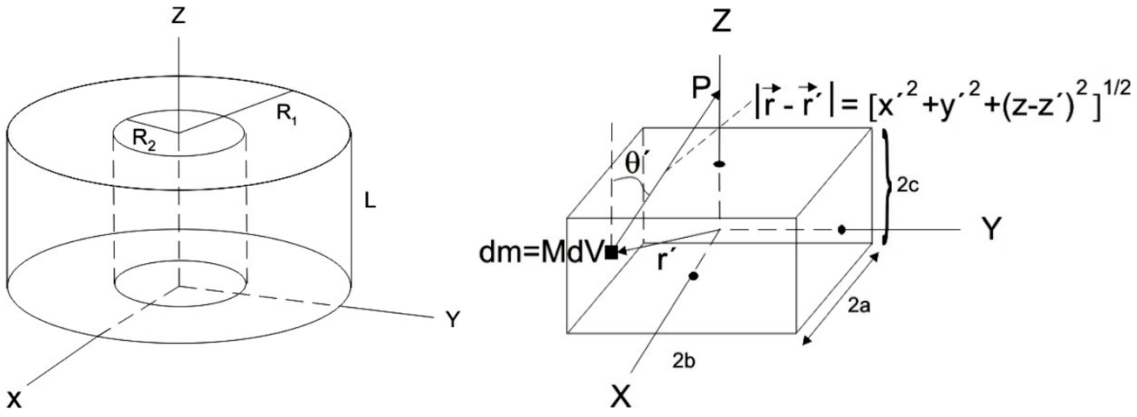

Figure 1.5 Schematics for equations a) 1.3 and b) 1.4 of the magnetic flux density produced by a ring- and rectangular-shaped magnet, respectively.

Interestingly, for the same scale factor k, the field gradients are multiplied by k and, by extension, the magnetic forces between magnetic materials are also multiplied by k [7]. A similar analysis showing how current-generated magnetic forces scale is described by Trimmer [20], and is expanded upon by Cugat, et. al for interactions with additional sources of magnetic field and the results are shown in Table 1.1 [7]. The right side of

Table 1.1 shows the same table when accounting for increased allowable current densities for small scale pulsed currents. Note how interactions between two magnets (when one is a hard-magnetic PM and the other is either a soft-magnetic iron or hard-magnetic PM) are favorable, and interactions between a magnet and a current (e.g. coils) at least maintain their ability to interact, and possibly benefit from the reduction in size based on the type of current utilized. The primary conclusion here is that PM are key to creating efficient magnetic micro-actuators and systems, although it is also interesting that the interaction between PM and an inductive coil are not as favorable.

Table 1.1 The effect of scale reduction 1/k on basic magnetic interactions between magnetic elements for (left) constant current and (right) pulsed; multiplication by k indicates increased magnetic interaction

Reduction Factor 1/k	Magnet	Current	Iron	Induction
Magnet	*k	-	*k	/k
Current	-	/k	/k	$/k^2$

Reduction Factor 1/k	Magnet	Current	Iron	Induction
Magnet	*k	$*k_i$	*k	/k*freq
Current	$*k_i$	$*k_{i1} *k_{i2} /k$	$*k_i/k$	$*k_i/k^2$*freq

Although magnetic systems can benefit greatly from a reduction in scale [1] [20], top-down fabricated magnets currently tend to either be too brittle for traditional machining, or too thick and too large in lateral dimensions to be used in MEMS of any size (See Appendix A for a compilation of magnet sizes as specified by some current manufacturers). These more traditional mechanical machining methods struggle to reach appropriate thickness and lateral submillimeter sizes in order to fit magnets within a package or a MEMS system. Bottom-up fabricated micromagnets, on the other hand, tend to be tens of microns thick at most [2] [4] [21] [22] [23], produce fields that are either

not as strong as corresponding bulk magnets or limited to short distances (i.e., on the order of microns) from the magnet surface (as seen in eq. 1.1 for a thin disc), and are challenging to fully magnetize in more than one direction to obtain geometrically-complex magnetic fields [22] [24]. The ability to magnetize in more than one direction is necessary for use in objects such as motors and generators, undulators, and other devices that utilize a spatially oscillating or otherwise varying magnetic field pattern. However, when interaction lengths (the distance from magnet to whatever is interacting with the magnet) are less than 10 μm, these thin films can be an attractive option.

The fabrication technology presented in the following chapters helps bridge the dimension and property gaps between bulk-fabricated magnets and microfabricated films while producing strong magnetic fields at the tens of micron to sub-millimeter distances from the surface of the magnet. Figure 1.6 shows the size-thickness gap that can be filled by laser micromachining magnets. The shapes in the figure here are only semi-quantitative, but represent numbers obtained from industry sources for bulk magnets and papers describing thin films (see Appendix A) [2]. As noted previously, thin film magnets are limited in their thickness, but theoretically can be manufactured up to the scale of a wafer in feature size, and should be used when interaction lengths are very small. On the other end, bulk produced magnets cannot be purchased below one to three hundred microns in thickness, depending on the material used, and feature sizes are one millimeter and larger, but that is very dependent on the thickness of the sample, hence the slopes of the parallelograms in the figure.

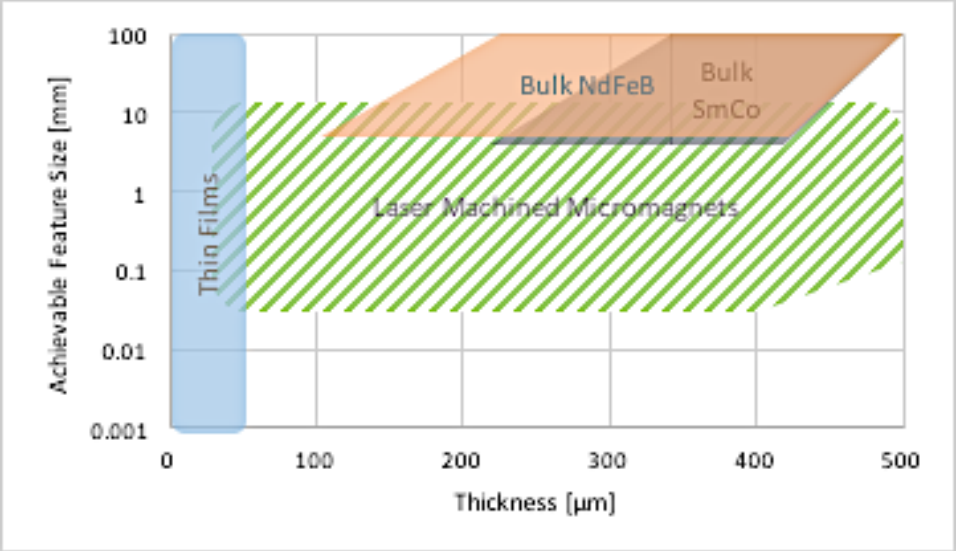

Figure 1.6 Thickness/feature size tradeoffs for different magnet fabrication technologies

Laser micromachining allows for magnetic devices with feature sizes on the order of tens of microns up to millimeters at thicknesses equal to or thinner than that provided by bulk magnet manufacturers. Thinner magnets are possible since the magnets can be trimmed down in height from the bulk purchased magnet height. In Figure 1.6 and in accordance with eq. 1.1, thickness correlates to the interaction length of a magnetic system (the distance between elements in the system). As shown, in order to utilize a magnet efficiently, a device interacting with the magnet (whether another magnet, an electromagnet, or an inductive coil) should be within one or two thicknesses. This fabrication technology allows for the characteristics of bulk-produced magnetic materials to be utilized over the entire shaded region in the figure, from feature sizes of tens of microns to ten millimeters and from thicknesses of tens of microns to at least one millimeter.

1.1.2 Magnetic Fields and Magnetic Material Properties

This section discusses some of the key properties used to describe magnetic materials. Figure 1.7 identifies how each property manifests in a typical B-H curve [2]. An M-H curve or loop is obtained for a specific material by measuring the magnetization, $\vec{M}$, of the sample while that sample is in an applied magnetic field, $\vec{H}$. That applied field then sweeps from positive to negative and back to positive. The applied field should be high enough to fully saturate the magnetic material. As the applied magnetic field sweeps from positive applied field to negative applied field, the magnetic flux density and magnetization should range from positive saturation to negative saturation, where the M-H curve becomes horizontal, drawing out a hysteresis loop as in Figure 1.4. A B-H loop is then obtained using the relationship between $\vec{B}$, $\vec{M}$, and $\vec{H}$

$$\vec{B} = \mu_0(\vec{M} + \vec{H}), \tag{1.5}$$

where $\vec{B}$ is the magnetic flux density, $\vec{M}$ is the magnetization of the sample, $\vec{H}$ is the applied field, and μ_0 is the vacuum permeabililty.

Remanence, M_r or B_r, is the amount of magnetization the magnet retains when an applied magnetic field is removed. This characteristic defines the field strength available at a given distance from the magnet. Coercivity, H_c, is the resistance of a material to being demagnetized by an applied or external field and defines the amount of applied field required to make the magnet appear as if it has no magnetization. The product of coercivity and remanence forms the energy product of a magnetic material, the maximum of which is known as $(BH)_{max}$, and is equal to the maximum area under the B-H curve in the second quadrant. The maximum energy product is generally the primary

figure of merit for magnets, but remanence and coercivity can be just as important, depending on the application [2]. Magnetic materials also exhibit a saturation magnetization, which is the maximum field a magnetic material can maintain in an applied field; an intrinsic coercivity, H_{ci}, which is the applied field required to fully demagnetize the magnetic material; and a relative permeability, which is the slope of the B-H curve or the rate at which the magnetic flux density changes as the applied field transitions from a negative to positive field. The latter metric is usually more important for soft or non-permanent magnetic materials. In addition, T_{max} is the maximum temperature at which, after returning the magnet to room temperature, the magnet regains all magnetization, and the Curie temperature defines at what temperature the magnetic material becomes fully demagnetized; Curie temperature is of particular importance to the studies presented in Chapter 2, which address the laser micromachining of magnets. Connected to this are the material properties defining the reversible temperature coefficients of remanence and coercivity that define how remanence and coercivity decrease with temperature [25].

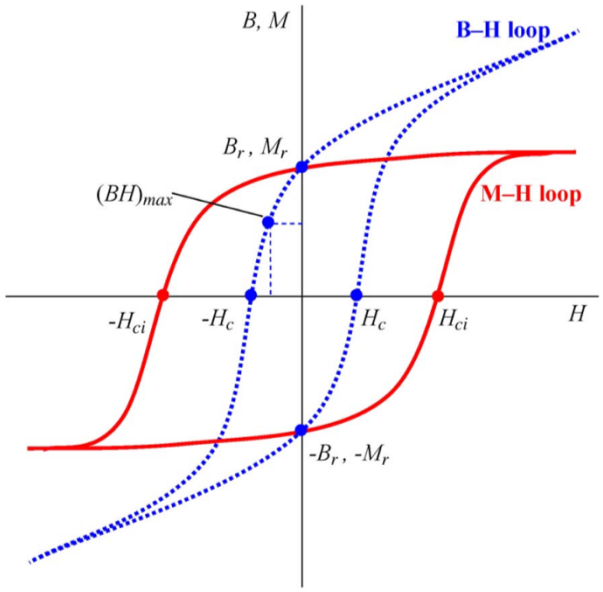

Figure 1.7 B-H and M-H Loop showing relevant magnetic parameters

Each of these properties is related to the magnetic domains of a material, an example of which is shown in Figure 1.8. Magnetic domains act as a collection of miniature magnets within a material. As the magnetic moments of each domain begin to align, the magnetization of the magnet increases until the domains completely align near saturation, as shown in Figure 1.8b. After a magnet is removed from an applied field where it was saturated (i.e., all domains aligned in the same direction), the directions of the domains settle such that not all domains remain pointing in the same direction. This is the state of remanence. The resistance of a domain to being demagnetized is a material-specific property, but is related to the domains trying to maintain the direction of their moment through domain wall pinning and other mechanisms [26].

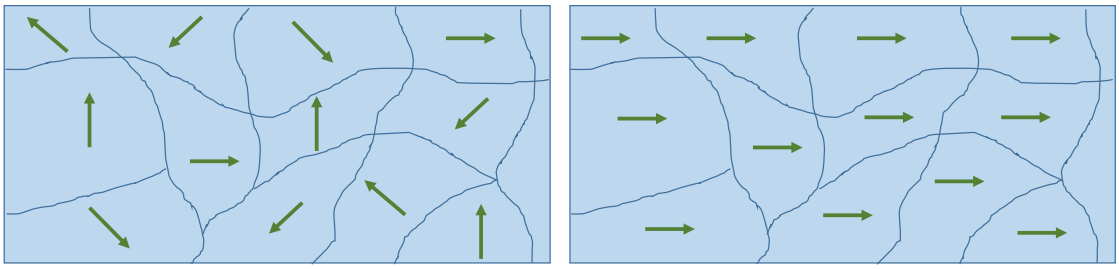

Figure 1.8 a) Randomly-oriented and b) aligned magnetic domains

1.1.3 Magnetic Field Superposition

In addition to the ability to machine individual magnets at the microscale, the fabrication and integration of magnets with different magnetizations to, ultimately, achieve a targeted magnetic field pattern establishes the framework for exploring new applications in magnetic systems. Fortunately, for the sake of simplicity, magnetic fields follow the principle of superposition. That is, the magnetic fields produced in a given volume of space are equivalent to the summation of the magnetic fields produced by the constituent magnets within the volume of space, as long as saturation of a magnet/magnetic material within that volume is not reached [27] [28]. This can be mathematically expressed as:

$$\vec{B}_{total} = \vec{B}_1 + \vec{B}_2 + \vec{B}_3 + \cdots + \vec{B}_n. \tag{1.6}$$

Figure 1.9 illustrates the principle of magnetic field superposition. Figure 1.10 expands upon this concept by showing the schematic of a larger set of magnets (Figure 1.10a) and the graphical representation of the corresponding magnetic field in the individual (Figure 1.10b) and superimposed form (Figure 1.10c). The research discussed in Chapters 2, 3, and 4 of this dissertation build heavily upon the superposition principle.

Any models presented in this dissertation, such as that in Figure 1.10, were simulated in COMSOL Multiphysics using the electromagnetics and/or thermal modeling packages.

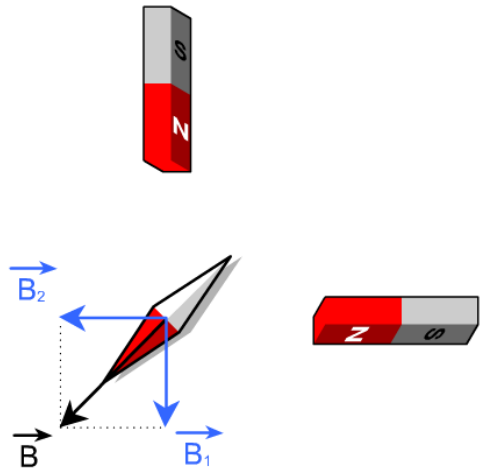

https://www.edumedia-sciences.com/en/media/2-superposition-of-2-magnetic-fields

Figure 1.9 Diagram demonstrating magnetic field superposition

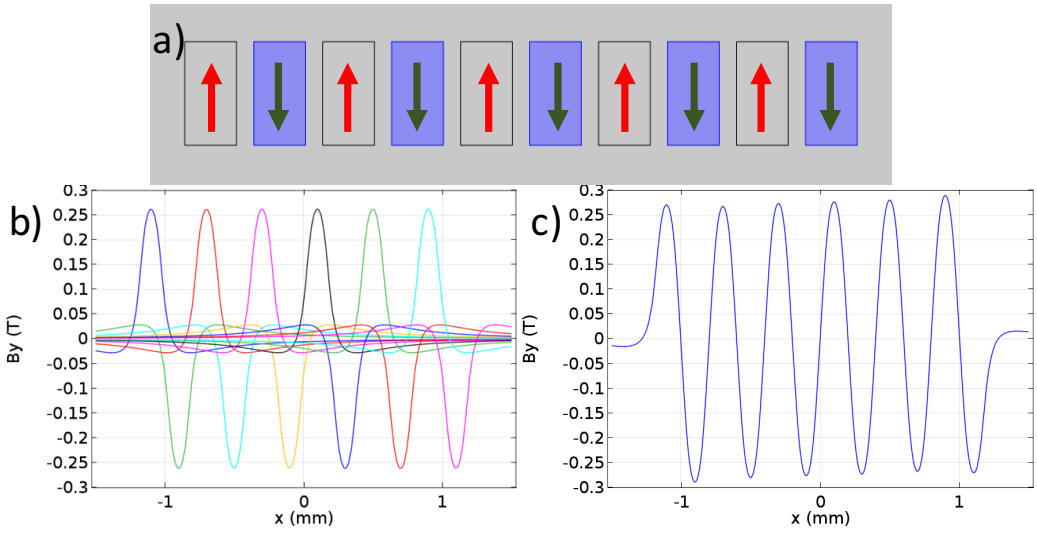

Figure 1.10 a) Cross-section-view schematic of a 200-μm-thick magnet array and resulting magnetic field pattern at 100 μm height above the magnets for b) the individual magnets and c) as a combined set

1.2 Micromagnet Fabrication Techniques

Traditionally, magnets are made to size using compressive molds and sintering [29], bonding magnetic particles within a polymer [30], or physically machining to size with an end mill or by electronic discharge machining (EDM) [31]. The high temperatures required for sintering would not be permissible in a MEMS fabrication process, unless sintering was done as the first step. The brittle nature of these materials prevents an end mill from machining the magnets to the submillimeter scale, and EDM can work for some materials but is slow and requires a conductive substrate. Additionally, bonded magnets can be physically cut or punched out of a larger piece of the material with relative ease [30], but have inferior magnetic properties when compared to sintered magnets. These fabrication techniques are limited because they cannot reliably achieve millimeter-scale dimensions. Indeed, until recently, methods to fabricate very small magnets had been limited to techniques such as screen printing of a magnetic composite polymer [21] and fracturing of a hardened sheet of polymer magnets [32], each with their own disadvantages.

Magnets at the micron-scale (micromagnets) must exhibit requisite characteristics in order to be used in MEMS and other micro-scale devices. Some of the requirements include maintaining a high magnetic field at a distance, possessing a high resistance to demagnetization (e.g. when placed near RF sources or in a plasma etch tool), resistance to heat of on the order of 400 ˚C (for MEMS processing), small physical size, and compatibility with device integration. Two options that are generally available for creating magnetic fields at or near these dimensions are electromagnets and thin film permanent magnets. Table 1.2 details the characteristics of some thin film magnetic materials

beside some bulk magnet properties [2] [7] [21]. The materials used in laser machining in this dissertation are described in section 2.1.2, with some additional information in Appendix C.

Table 1.2 Permanent magnet properties, including thin film magnets.

Material	Category	Manuf. Method	H_{ci} [kA/m]	Br [T]	BH_{max} [kJ/m3]	Curie Temp [˚C]	T_{max} [˚C]	Reversible Temp.Coeff. Remanence [%/˚C]	Corrosion Resistance
MO $6(FE_2O_3)$	Ferrite	Powder	200-380	0.2-0.4	8-30	460	200-300	-0.2	Excellent
Al-Ni-Co	Metal Alloy	Cast, Powder	40-170	0.7-1.3	11-72	830	450-550	-0.02	Very Good
Sm_2Co_{17}	Rare Earth	Powder	560-2100	1.0-1.2	130-200	800	300-350	-0.03	Moderate
$Nd_2Fe_{14}B$	Rare Earth	Powder	880-3300	1.0-1.4	190-400	310	125-150	-0.1	Poor
CoPt	Thin Film	Electro-deposited	330	1.0	69	Thickness: 8 μm; on (110) Si substrate			
FePt	Thin Film	Pulsed Laser	19-25	1.4	12-105	Thickness: 5-20 μm, small area			
CoNiMnP	Thin Film	Electro-deposited	70-100	0.2-0.3	14	Thickness: 10-45 μm			
$SrFe_{12}O_{19}$	Bonded Thin Film	Polyimide Carrier	320	0.16-0.28	5-12	Thickness: 10-20 μm, spin-cast			
SmCo	Thin Film	Sputter	1035	0.8	140	Thickness: 5 μm; 400˚C Deposition w/ 750˚C Anneal			
NdFeB	Thin Film	Sputter	1280	1.4	400	Thickness: 5 μm; 500˚C Deposition w/ 750˚C Anneal			
NdFeB	Thin Film	Pulsed Laser	1000	0.55	77	Thickness: 120 μm; 650˚C Anneal, small area			

As an example of some bulk produced magnets, Appendix A lists several product specifications from industry stating some of the dimensions of the products they offer. In particular, Pacific PAC Technologies lists minimum thicknesses of 100 and 200 μm for a 10 x 5 mm NdFeB magnet sheet and a 500 μm diameter NdFeB disc, respectively, and 300 and 250 μm for a 10 x 5 mm SmCo magnet sheet and a 3 mm diameter SmCo disc, respectively. Another company, K&J Magnetics, lists a minimum thickness of 1/32” or approximately 800 μm. Correlated Magnetics Technologies creates highly customizable magnets by way of a proprietary magnetizing method where they take existing magnets

1 mm and thicker (of various lateral sizes) and magnetize them to create the equivalent of printed magnetic pixels. They are able to achieve magnetic field variations on the order of at least hundreds of microns, but are not fully magnetizing the materials. One industry source additionally claimed the costs of these magnets become too high if using magnets of a thickness less than or equal to 1 mm because of the material that has to be removed to achieve such thicknesses (See Appendix A). Indeed, the largest costs with rare-earth magnets are the material and machining.

1.2.1 Electromagnets

Electromagnets are a form of magnet that is used for various applications due to the magnetic field of electromagnets that can vary based on the applied current, the reversal of field direction by reversing the current flow, and the fact they can have dimensions as large as several meters or as small as hundreds of microns, provided that sufficient current is supplied [33]. Additionally, the highest magnetic field producing magnets in the world can only operate as electromagnets, utilizing superconducting materials to carry the high currents necessary to maintain that field. The Biot-Savart Law describes the field around a wire in vacuum as:

$$d\vec{B} = \frac{\mu_0 I d\vec{L} \times \hat{r}}{4\pi r^2}, \tag{1.7}$$

where μ_0 is the vacuum magnetic permeability, I is the current traveling through the wire, $d\vec{L}$ is the infinitesimal length along the wire, and r and $\hat{r}$ are the distance and direction, respectively, to the point at which $d\vec{B}$ is measured. Another application of the Biot-Savart Law leads to the magnetic field along the axis of a loop of current (eq. 1.8) and the magnetic field along the axis in the center of a solenoid (eq. 1.9):

$$\vec{B} = \frac{\mu_0 n I R^2}{2(R^2+x^2)^{3/2}}, \tag{1.8}$$

$$\vec{B} = \mu_0 n I, \tag{1.9}$$

where μ_0 is the vacuum permeability, I is the current traveling through the wire, n is the number of windings in the coil or solenoid, R is the coil radius, and x is the distance away from the coil center. From these equations, it is evident that the current can be increased to increase the magnetic field. This process has limits, but with superconducting wires, the magnetic fields can become quite high.

Given these characteristics, the operation of electromagnets is fairly simple, safe (the high fields and electrical currents can be removed in an emergency to prevent harm to individuals and objects), and stable over long periods of time. The fields can be as high as 30-45 T for current state of the art superconducting magnet architectures [34], whereas individual permanent magnets, as seen previously, are limited to approximately 1-1.5 T. With the help of magnetic field superposition with permanent magnets, higher fields can be obtained, but will not reach as high as that of superconducting magnets.

As with permanent magnets, research has been conducted to reduce the overall size of electromagnets to the microscale to harness their favorable characteristics in microdevices. Examples of these include a microundulator (Figure 1.11a) [35], a bi-stable switch (Figure 1.11b) [19], and a microgenerator stator (Figure 1.11c) [17]. These electromagnetic structures are essentially limited by the complexity of fabrication at the micro-scales or the current densities that the microwires can carry. For example, comparing a microelectromagnet to Figure 1.1 and 1.4 describing the magnetic field

produced by a micromagnet, for a loop of current 200 μm in diameter with a single wire, at 100 μm away from the coil, it would require nearly 45 amperes in the coil to reach the same magnetic field as that produced by a permanent magnet of the same radius and 100 μm thickness. Even with short pulses that can enable higher current densities, and utilizing a higher number of turns, these current values are difficult to achieve [1].

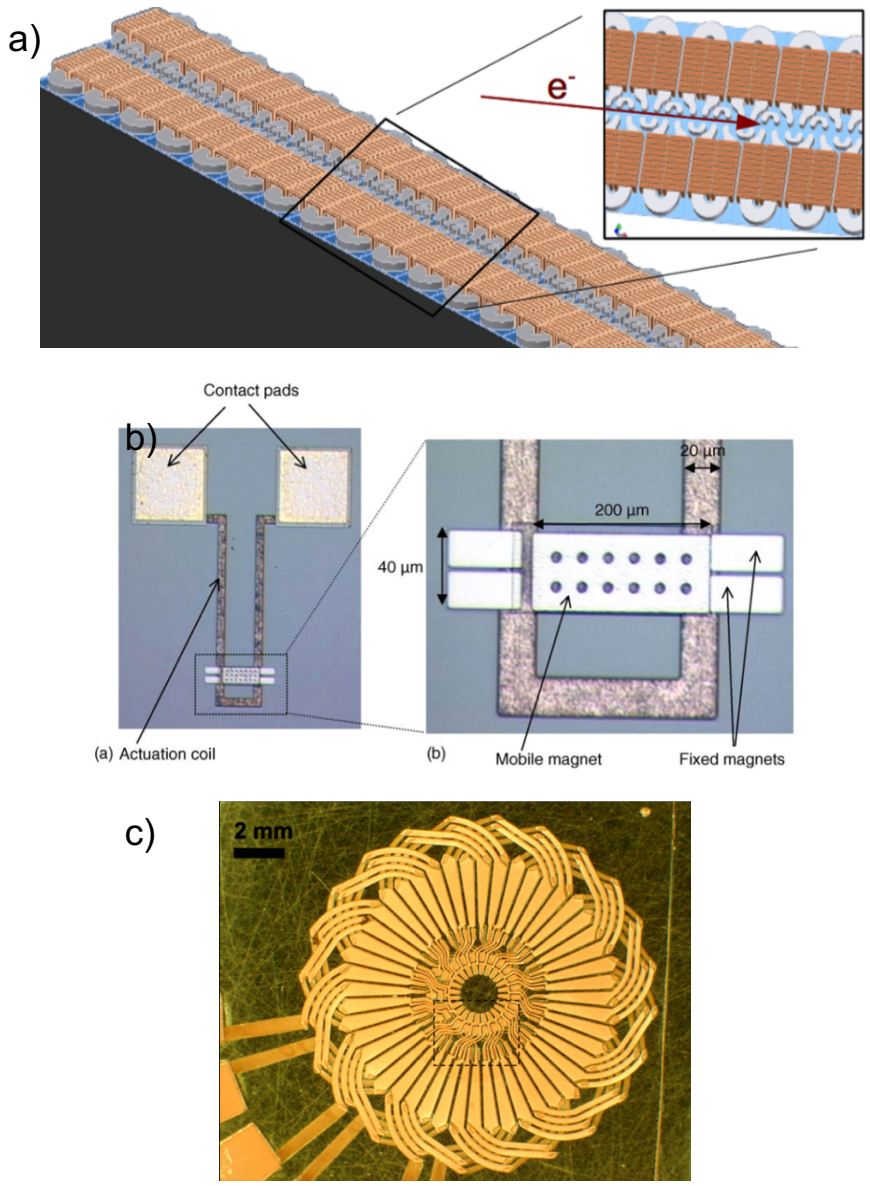

Figure 1.11 a) Model of a microundulator comprising many arrayed electromagnets, and b) photographs of a bi-stable switch and c) the stator of a microgenerator

1.2.2 Thin Film Deposited Permanent Magnets

The processing of permanent magnets at the microscale has almost entirely consisted of a bottom-up fabrication approach, beginning with material deposition onto a substrate.

As can be seen in Table 1.2, some micromagnet fabrication methods include electrodeposition [23] [24] [36], sputtering [36], and pulsed laser deposition [37]. Examples of microfabricated magnetic devices are shown in Figure 1.12, which include an array of NdFeB micromagnets [4] and a multipole magnetized film of 15–μm–thick CoPt (top) and 5–μm–thick NdFeB (bottom) [8]; some of the magnetic properties of these devices were also shown in Table 1.2. The bottom image of Figure 1.8 shows the magnetic field as an image using Magneto-Optical Imaging Film (MOIF). Non-traditional fabrication includes powder-based fabrication techniques, such as screen-printing [21], spin-casting, dry-packing, and magnetic composite electroplating [2]. As the grain size of bulk magnets are on the order of 5–10 μm, care must be taken when creating magnets of similar dimensions from these powders [2] [36].

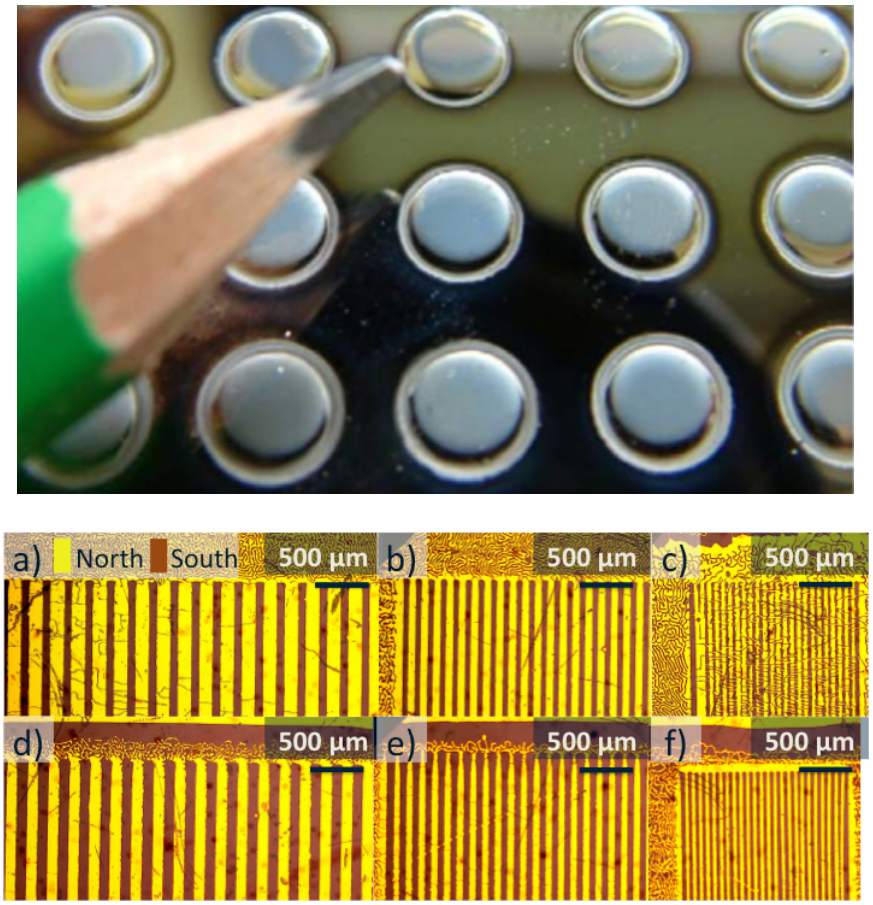

Figure 1.12 Photographs showing thin film magnets as a) an array of NdFeB micromagnets and b) a multipole magnetized film of (top) 15–µm–thick CoPt and (bottom) 5–µm–thick NdFeB using MOIF imaging

These microfabricated permanent magnet films are promising but lacking in several key aspects. First, these magnets will only be able to be fully magnetized in a single direction, otherwise they will be partially magnetized in one direction followed by a reverse magnetization with a specially designed magnetic yoke to guide the field as in Figure 1.12b [8]. Either method leaves a tradeoff: either there is no variation in the magnetic field direction across the sample, or the magnet has an alternating but

partially-magnetized field. Additionally, due to the thickness of these magnets as in Figure 1.12 and the additional characteristic of periodicity as in Figure 1.12b, the magnetic field of these magnets will be minimal at a distance from their surface equal to their thickness, which is already very thin, similar to what was shown for a disc magnet in eq. 1.1. For a periodic array of magnets facing north-south-north-south-north… the equation describing how the magnetic field varies with distance from the surface of one of the magnets is as follows [38]:

$$B = -B_r \cos\left(\frac{2\pi s}{\lambda_u}\right) \frac{\sin\left(\frac{\varepsilon\pi}{M}\right)}{\frac{\pi}{M}} e^{-2\pi g/\lambda_u} \left(1 - e^{-2\pi h/\lambda_u}\right), \tag{1.10}$$

where s is the distance along the array, λ_u is the periodicity of the array, ε is the fill factor where 1 means there is no gap between magnets, M is the number of magnets per period rotating magnetization directions through 360˚ (2 magnets - 0˚/180˚/0˚ - N/S/N, 4 magnets - 0˚/90˚/180˚/270˚/0˚ - N/Left/S/Right/N, etc.), h is the thickness or height of the magnets, and g is the gap from the magnet surface to the point of measurement. Note how this equation decreases even faster than eq. 1.1, exponentially rather than as an inverse square root. This type of alternating field structure as in Figure 1.10a and Figure 1.12b, also called a linear Halbach array [39], will be discussed further in Chapters 3 and 4.

According to the criteria already established, an interaction length (distance between magnet and additional object) would ideally be less than approximately three magnet thicknesses. As an example, for an arrangement of magnets of radius 3 mm and height 1.5 mm with one magnet directly above the other, the force between them decreases by approximately an order of magnitude after just two thicknesses [40]. As such, for

interaction lengths of tens to hundreds of microns, magnets of similar submillimeter thicknesses should be used.

Laser machining these magnets provides a solution with the best qualities of bulk machining techniques such as EDM, and precision fabrication that would allow for submillimeter magnets to be realized. Further assembly of these magnets provides the ability to have a complex magnetic field structure at this same scale using magnets fully magnetized in differing directions. This assembly of PM to create alternating fields will be further discussed in Chapter 3.

1.3 Laser Cutting and Machining

Although lasers were first conceived and demonstrated as recently as the late 1950s and early 1960s, laser machining developed as a fabrication technology c.1965 and its applications expanded in the 1970s with the invention of the carbon dioxide (CO_2) laser [41]. Various lasers have since been invented, including gas lasers such as excimer lasers based on halogen gases, copper gas lasers, pumped neodymium crystal lasers, and fully solid state lasers, as a result of the telecom industry. Lasers can be utilized for a versatile set of applications, such as for distance measurement, targeting reticles, serving as a pump laser in a larger laser system, free space and fiber-based communication, computer vision or LIDAR, along with the laser machining and cutting discussed previously. The material in this section is based on two canonical books: Fundamentals of Laser Micromachining, by Ronald Schaeffer [42] and Chapter 2 of Laser Precision Microfabrication by Matthew Brown and Craig Arnold [43].

Lasers operate by the principle of stimulated emission, which is also where the name comes from: Light Amplification by Stimulated Emission of Radiation. Lasers have several generic common parts, as shown in Figure 1.13. First, the laser cavity that holds the gain medium (gas, liquid, or solid) is stimulated, or pumped. In most cases, this is done electrically by applying a specific voltage or current, as in a gas laser or laser diode, or optically by a seed laser or flash lamp. Upon being stimulated to an excited energy state (E3), the atoms fall quickly into a nearly stable state (E2), as shown in Figure 1.14a, without radiating optical energy. This is the necessary population inversion required to achieve lasing, when most of the atoms are in this excited but somewhat stable energy state. As the atoms drop in energy from E2 to E1, photons are released of the same energy as the difference between E2 and E1:

$$E_{laser} = E_2 - E_1, \tag{1.11}$$

and therefore a specific wavelength:

$$\lambda_{laser} = \frac{hc}{E_{laser}}, \tag{1.12}$$

where c is the speed of light and h is Plank's constant.

Additionally, as some of the atoms release photons, these photons then cause the other atoms to release photons and drop in energy, creating a cascade of photons. The mirrors at either end of the gain medium reflect the light to increase this effect and increase the optical gain. One of these mirrors is fully reflective. The output mirror is then less reflective such that it allows some of the laser light to escape. At the end of the photon cascade, the lasing action stops until pumped and the process starts again.

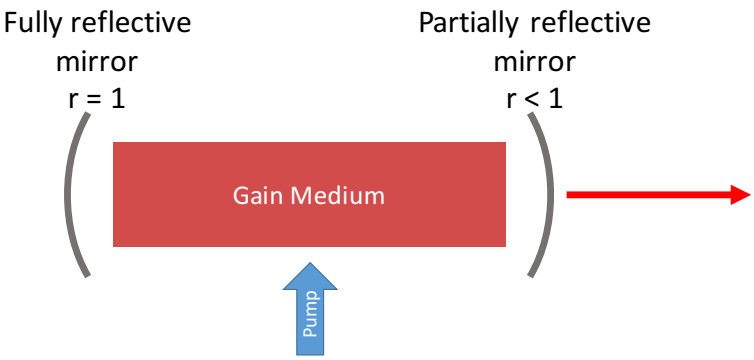

Figure 1.13 Schematic of laser source and gain medium where stimulated emission occurs

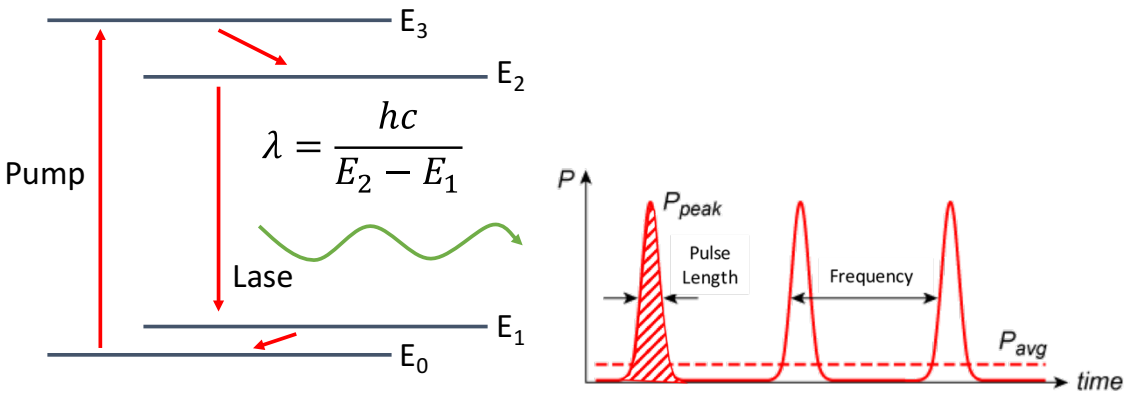

Figure 1.14 a) Population inversion based on a four-level system and b) a chart showing power as a function of time for a series of laser pulses, filled area signifies pulse energy

Each rise and fall in optically released energy is a laser pulse, as shown in Figure 1.14b. Pulse lengths can range anywhere from milliseconds to several femtoseconds, depending on the laser. The rest of this dissertation will focus here on pulsed lasers, but continuous wave lasers operate under similar principles. As can be seen in Figure 1.15, lasers of many different wavelengths have been discovered or engineered. The availability of various wavelengths is important for the purposes of machining as each material responds differently to different wavelengths of light. For example, the 10 μm

CO2 laser works very well for cutting wood and plastics, the 1 μm Nd-doped crystal lasers work well for cutting metals, and the sub 250 nm excimer lasers are good at machining transparent materials such as glass and polymers. This is mainly due to the photon absorption characteristics of each material at the laser wavelength of interest; if a material absorbs the light instead of reflecting or transmitting it, the light energy can result in cutting or ablation, as described in the next sections. The UV and near UV wavelengths (<375 nm) also reach energy levels consistent with the breaking of chemical bonds and vaporize materials in that manner. Another important parameter of lasers is their pulse energy, shown as the shaded region in Figure 1.14b, which can vary greatly from laser to laser. The ratio of energy to pulse length is known as the peak power, shown as the peak of a pulse in Figure 1.14b. For either high pulse energies or ultra-short pulse lengths, peak powers can reach upwards of megawatts. Peak power intensity is then peak power per unit area [42]. This is another extremely important parameter for efficient and clean ablative machining as described in section 1.3.3.

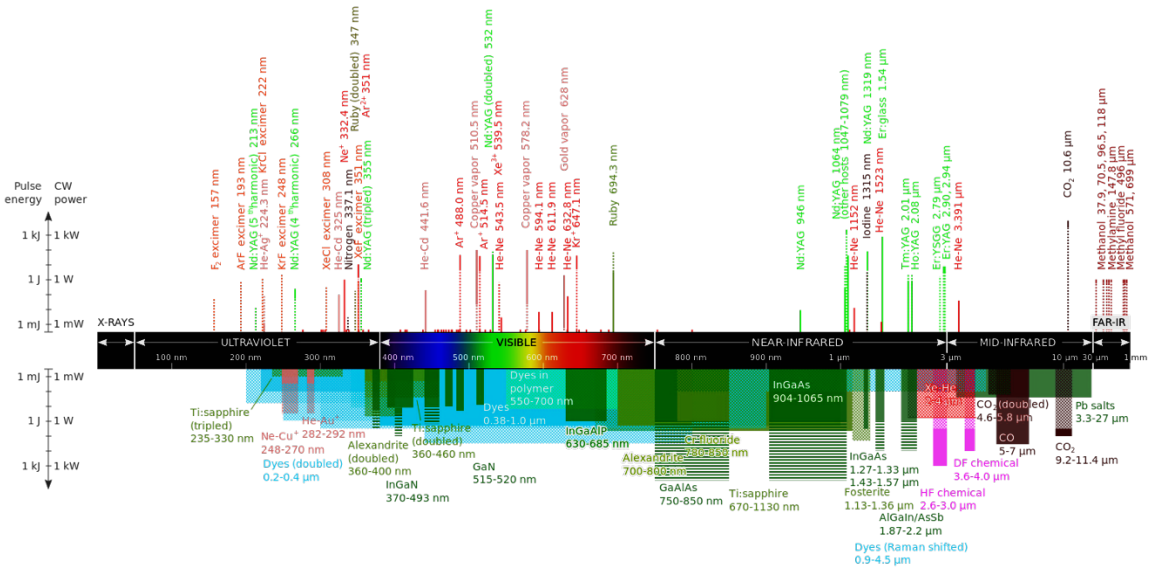

https://upload.wikimedia.org/wikipedia/commons/thumb/4/48/Commercial_laser_lines.svg/1550px-Commercial_laser_lines.svg.png

Figure 1.15 A schematic illustrating the spectrum of laser wavelengths, designated by laser type and power.

Once the laser is emitted from the laser cavity and gain medium, the laser pulse is delivered to the material being machined. This is normally done with various mirrors or an optical fiber. This beam delivery system may also contain any number of beam shaping or focusing optics to increase uniformity or alter the location of the focus of the laser. In masked lasers, a metal mask is also placed in the beam path to provide a desired beam shape, an example of which is shown in Figure 1.16c. The processes behind material removal are discussed in the following sections.

While lasers can feature a broad range of wavelengths, pulse lengths, and pulse energies (examples shown in Figure 1.15), the appropriate laser characteristics for machining and cutting are specific to the material being machined and the desired geometry. Lasers can machine materials in various ways. Lasers are capable of providing sufficient thermal output to heat, melt, and weld similar or dissimilar materials.

Lasers can also cut a material with a single pass by melting and purging that melted material. This is utilized in processes for metals, plastics and polymers, wood, and ceramics. This photothermal machining is discussed in section 1.3.3. In addition, another type of laser can machine to only a small depth of material directly under the laser spot and, in this manner, precisely ablate that section of material by the equivalent of a micro-explosion. Ablation, described in section 1.3.4, is the principal method implemented in the micromachining industry to delicately and precisely machine various materials at the micron scale.

1.3.1 Laser Machining Process

The procedure for laser machining any material is a fairly standard process. Given a material type and thickness, a laser must be chosen. Various laser types and parameters can be selected to optimize the machining for the particular application. After a laser is chosen, the material is prepared, if necessary, by adhering to a substrate and/or treating the surface, then placing the material in the laser system.

The first time a material is processed in any laser, laser parameters must be chosen or found that will machine the material with the desired characteristics. Some of these characteristics include low kerf width (kerf width being the lateral difference between the top and bottom of the cut, as in Figure 1.16a), speed of machining, clean surface, through cut/holes versus blind channel/holes (blind refers to machining to depth and not cutting through the material, as in Figure 1.16b), hole shape and size (for a masked laser such as an excimer laser, as in Figure 1.16c), a heat affected zone (described in section 1.3.5), etc. A photograph showing an example parametric array can be seen in Figure 1.17, and shows multiple holes as a function of laser pulse energy and number of

shots. Note how the holes from the low energy and low number of shots section appear clean whereas the high pulse energy has larger holes with what appears to be a lip around the hole. From this image, optimal parameters can be chosen [44]. Laser parameters can include laser power or energy, pulse length (if variable for the chosen laser), repetition rate (number of pulses per second), mark speed (the speed of the stage as the laser is on), jump speed (the speed of the stage when the laser is off), assist gas (oxygen, nitrogen, clean dry air, helium, etc.), etc.

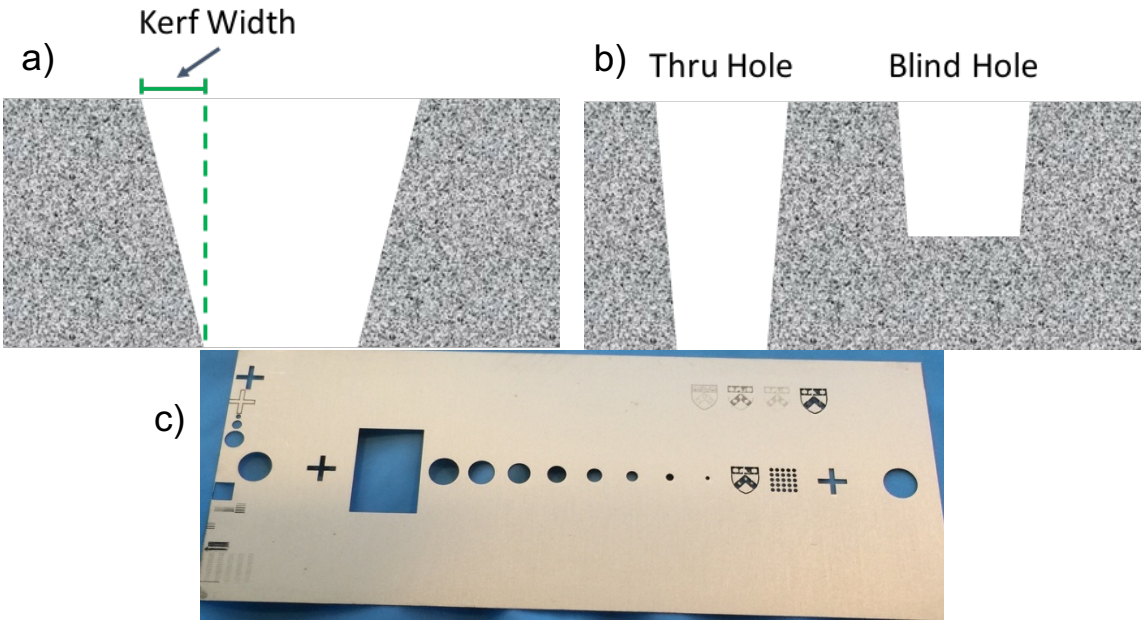

Figure 1.16 Schematics of laser machined materials showing a) kerf width and b) hole types, and c) a photograph of a mask with various shapes and sizes

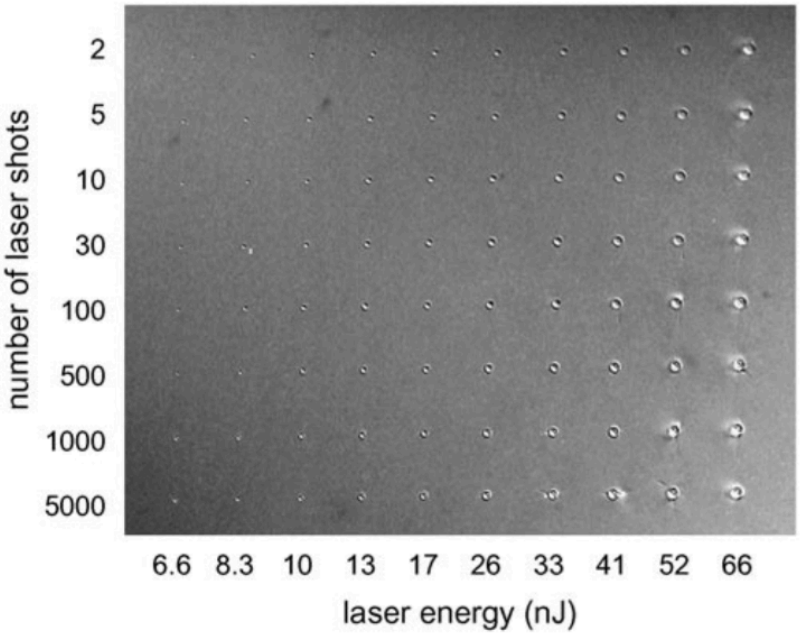

Figure 1.17 Photographs of a machining parametric array

Once the appropriate laser characteristics are found (laser power/energy, repetition rate, mark speed, etc.), a machining program is designed. This is first done by, and most commonly, choosing a CAD file that contains lines, arcs, and points, but can also include selecting a picture, for the laser software to convert into stage moves and laser firing. In some laser software, the user can manually program specific stage moves and firing of the laser with finer control. The material is then placed in the laser. The part is aligned to the laser and stages, and the laser is focused onto the part (most commonly by raising and lowering the stage the material is resting on). At this point, the laser machining program, or macro, can be executed. Additionally, a cleaning process may need to take place after machining to clean up any laser debris (i.e. physical rubbing/polishing, chemical bath, electropolishing, plasma, etc.).

1.3.2 Thermalization Time

The absorption coefficient of a material defines how much light is absorbed as a function of depth in a material, and is related to the dielectric properties and conductivity of a material. The method by which that light interacts with the material depends on the material and wavelength of the laser, but generally the photons will interact with available electronic or vibrational states of the material. In non-metals, the photons can cause resonant excitations (i.e. valence to conduction band or between sub-bands within a particular band) [45]. As such, for laser photon energies smaller than either type of bandgap, absorption will not occur; exceptions to this would be material defects/impurities that might couple to the laser or multiphoton absorption. Similarly, phonons (material/crystal lattice vibrational states) can also be excited. In metals, photon absorption normally occurs with free electrons and those excited electrons then transfer energy to lattice phonons through collision; other excitation methods also include other electron and phonon mechanisms, along with diffuse electron scattering and surface plasmons and polaritons [46].

The time required to transfer energy from the excited electron states to the phonons and create heat in the surrounding material is called the thermalization time. For most metals, thermalization time is in the several to hundreds of picoseconds range, while non-metals have a much larger variation and up to several microsecond thermalization times [45] [47]; polymers and dielectrics are normally on the slower end of this scale. For materials with longer thermalization times, ablation can proceed even with nanosecond laser pulses if a short (e.g., UV) wavelength is used [42] [43].

1.3.3 Photothermal Laser Machining

Lasers where the excitation rate is low in comparison to the thermalization time (i.e. use a low peak power, defined as the ratio of pulse energy to pulse length), typically operate by thermal, or photothermal/pyrolytic, mechanisms. In this case, the laser pulse is sufficiently long so that the laser excited electrons have time to transfer their energy into the surrounding material. As such, all laser energy can be assumed to transfer directly into heat in the material.

Photothermal laser machining systems can feature continuous wave lasers or pulsed lasers with pulse lengths as small as tens of nanoseconds, as long as the material thermalization time is shorter than the pulse length. Here, the laser impinges on and melts the material. A plasma forms directly above the molten material and the molten material directly heated by the laser then melts the solid material underneath. In many cases, an assist gas is used to direct the melt through the solid and to clear the area of debris. Figure 1.18 shows the different aspects of photothermal laser machining. As the laser continues, the melt falls completely through the material and the laser moves along the cut path defined in the program. The resulting edges of the laser cut path can be covered in laser remelt, oxides or nitrides, and exhibit other surface and material defects. The composition of the laser cut edge depends on many factors, including the type of assist gas, laser power/peak power, and thickness. Generally, thicker materials require reduced cut velocity and/or increased laser power in order to efficiently cut the material.

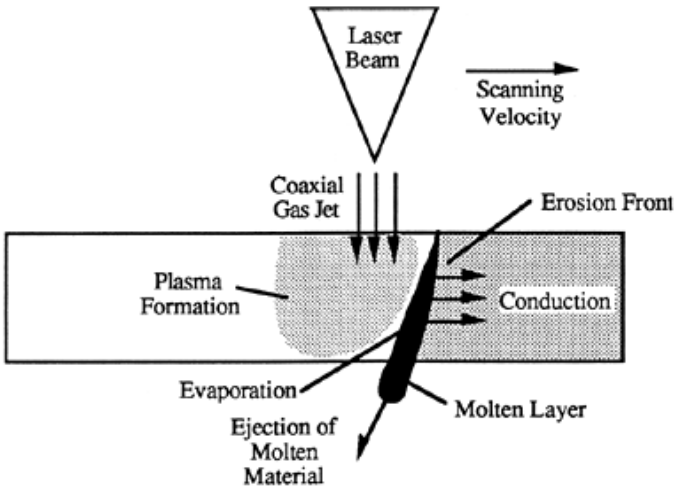

Figure 1.18 Schematic illustrating the process of thermal laser machining.

1.3.4 Ablative Laser Machining

Another form of laser machining involves more vertical removal of material and relies less on the downward purging of melted material; specifically, ablation-based laser machining. Such machining can be photochemical in nature, such as in the laser machining of many polymers using ultraviolet wavelengths. However, ultrafast lasers where the excitation rate is the same as or smaller than the thermalization time of the material can also induce an ablative reaction. Even though photochemical mechanisms can dominate the machining process, it is still possible to transfer heat to the surrounding material. As such, most ablative machining is a blend of these mechanisms, photothermal and photochemical.

The principal mechanism of ablation is the direct absorption of laser energy by the material such that a threshold fluence is achieved. Fluence is defined as the energy per unit area of a given laser pulse. The threshold fluence depends on material absorption at

the laser wavelength, pulse energy, pulse length, additional material properties and sample defects. For example, if a material is non-absorptive at the laser wavelength or even reflective, the threshold fluence will likely not be achieved. As the pulse length of the laser decreases from tens of nanoseconds to below one nanosecond, such as in the picosecond and femtosecond range, the pulse energy deposits more rapidly into the material, establishing higher ablation rates and higher peak powers. These ultra-short pulse lasers can even enable materials normally transparent to a wavelength to become absorptive due to non-linear machining effects at these low pulse lengths (sub 1 ns) [44]. However, even when a continuous wave laser is used, ablation is still possible when sufficient laser energy is deposited. Typical laser fluence thresholds are between 1-10 J/cm^2 for metals, 0.5-2 J/cm^2 for inorganic insulators, and 0.1-1 J/cm^2 for organic materials [48].

As the laser impinges on the material, instead of transferring the heat to the bulk material as with melting in the photothermal machining case, the material vaporizes, as depicted in Figure 1.19 [49]. Above the ablation threshold, the volume of material removed per pulse typically increases logarithmically with fluence in accordance with the Beer-Lambert Law [43], which says that, for a constant attenuation, α, the intensity decreases exponentially with depth, z:

$$I(z) = I_0 e^{-\alpha z}. \tag{1.13}$$

Decreasing the pulse length can also reduce the ablation threshold for a given material. As can be seen in the schematic of Figure 1.19a with the longer nanosecond pulse lengths, there are a number of effects that must be taken into account. As material is still

being melted and ejected at these pulse lengths, but not entirely vaporized, the surface will contain a certain amount of remelt debris and the sides of the channel being machined will have recast material on the side wall. Additionally, there is a heat affected zone and microcracks that are propagated by the shockwave the laser pulse creates with the heating and cooling of the material. As the pulse length becomes shorter, that shockwave is diminished. Lastly, and this is particularly important for micromachining of non-homogenous material or pre-processed material, structures immediately adjacent to the laser cut will show defects related to these shockwaves and debris. Care must be taken in laser parameter selection to limit these problems. However, if not using an ultra-short-pulse laser, these problems will most likely be present in some fashion.

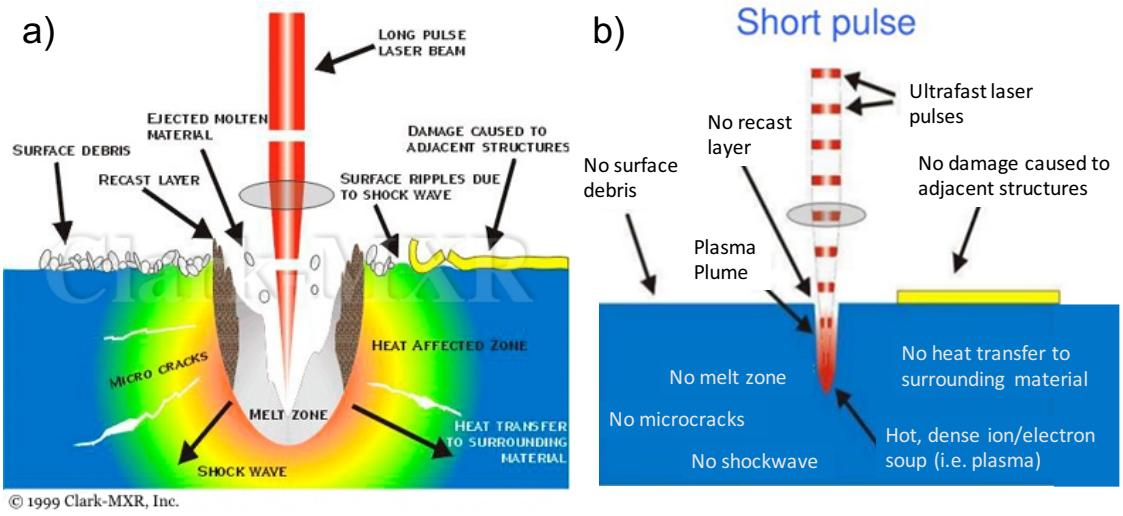

Figure 1.19 Schematic detailing what happens within the material upon being irradiated by pulsed lasers of varying pulse lengths. a) Long pulse machining; b) short pulse machining

At relatively low fluences, the photothermal mechanisms of evaporation and sublimation are more prevalent. Composite materials may exhibit dissimilar ablation rates among the composite constituents, resulting in changes to the chemical composition of a material [50]. If heating is sufficiently rapid, such that the material reaches the thermodynamic critical temperature with higher fluences, the nucleation of vapor bubbles and explosive boiling can occur and remove solid and liquid fragments [51]. However, as the excitation time, or pulse length becomes shorter than the thermalization time of the material, photochemical processes take over. Examples of some of these mechanisms include direct ionization and the formation of dense plasmas. These can lead to athermal phase transformations, direct bond-breaking, and explosive disintegration of the lattice (Coulomb explosion) [52]. The use of high fluence, short pulse lengths, and/or short wavelengths can, ultimately, reduce the heat affected zone of the laser micromachined material.

1.3.5 Heat Affected Zone

As can be seen in the schematics of Figure 1.19, a portion of the laser machined material immediately adjacent to the laser cut can be damaged due to its close proximity to the melted or superheated material. The size of this region, or the heat affected zone (HAZ), will vary by material and laser settings, such as laser type, pulse energy, pulse length, and material thermalization time. In some cases, such as in laser cutting or welding of uniform metals, the HAZ depends not only on laser parameters, but can also depend on how the material was manufactured (e.g., extrusion, casting, rolling, etc.). In addition, the HAZ can be large due to the rapid thermalization time of metals, or any material where the thermalization time is larger than the laser pulse length. In other

cases, such as with inhomogeneous materials or material composites, the laser can completely damage the material if suboptimal laser settings or laser type are used. On the other hand, if appropriate laser choices are made, the HAZ can be virtually non-existent, such as with polymers and proteins on a short wavelength UV laser.

By extension, the importance of addressing HAZ increases in micromachining, as the dimensions of the sample can be of the same order as the laser focus spot size and HAZ itself. The next sections will elaborate on the analysis of HAZ on magnetic materials due to laser micromachining.

1.3.6 Thermal Effects on Magnetic Properties

Above absolute zero, remanence always decreases slightly as temperature increases. As the temperature of the magnet approaches the Curie temperature, the thermal agitation within the material causes all the domains to return to a more random state (recall section 1.1.2 and Figure 1.8); this behavior begins gradually, but becomes rapid as the temperature approaches the Curie temperature. Figure 1.20a shows how the remanence can decrease with temperature up to a maximum use temperature, T_{max}, where the remanence begins to decrease permanently (i.e., until placed in a new magnetizing field). If the temperature never exceeds T_{max}, the remanence should recoil to its ideal state when the temperature returns to room temperature. If the temperature surpasses T_{max}, the magnetic material begins to be demagnetized until complete demagnetization at the Curie temperature; this demagnetization is reversible. Figure 1.20b shows the general effects of these temperature changes on the B-H and M-H demagnetization curves [2]. Note how both the remanence (y-intercept) and coercivity (x-intercept) are decreasing with temperature in Figure 1.20b. These decreases are

reflected in the material parameter Reversible Temperature Coefficient of Remanence and similarly for coercivity, expressed as a percentage per degree Celsius. This parameter for remanence is listed in Table 1.2 as an example. In addition, temperatures above the Curie temperature are capable of affecting the magnetic grains in various ways, such that the affected grains irreversibly lose magnetization.

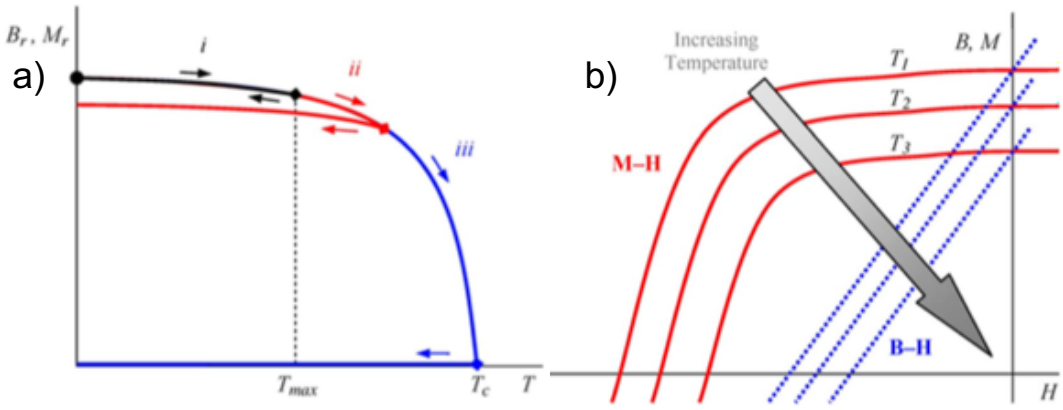

Figure 1.20 Representative plots as a function of temperature for a) remanence and b) the second quadrant of the B-H and M-H curves

This dissertation will focus solely on hard ferromagnetic materials, or permanent magnets (PM). While many different PM materials exist, this dissertation examines two materials in particular: neodymium-2-iron-14-boron ($Nd_2Fe_{14}B$, or generally NdFeB), grade N48, and samarium-2-cobalt-17 (Sm_2Co_{17}, or generally SmCo), grade SmCo 30/25. This is due to their high energy product, general availability, and high remanence and coercivity. As one of the research goals was to create sub-millimeter scale magnets, these properties were most pertinent. SmCo is also chemically resistant, which facilitates the fabrication process and integration with MEMS; heat resistant, with a high Curie temperature and low reversible temperature coefficients of remanence and coercivity;

and is resistant to oxidation. These characteristics render SmCo more desirable in spite of its lower remanence and energy product compared to NdFeB, but multiple comparisons are still made. Figure 1.21 shows the 2nd quadrant of the M-H curves (or demagnetization curves) for five bulk magnetic materials.

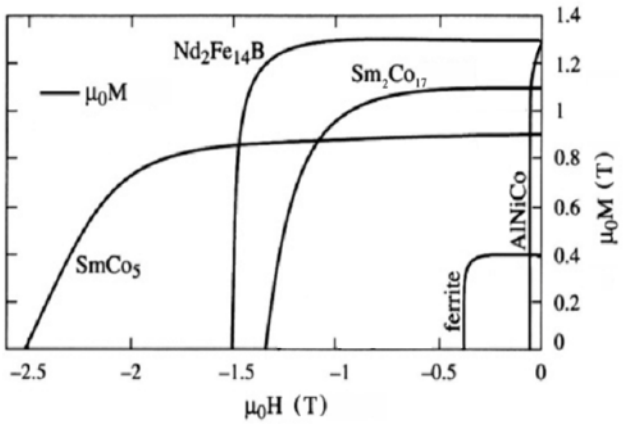

Figure 1.21 Five M-H demagnetization curves for bulk magnetic materials

1.4 Proposed Fabrication Technology Summary

This dissertation provides a foundation and explanation of laser micromachining, and specifically that of magnets, intended to allow the reader to replicate the micromachining of magnets, enabling future devices with spatially varying magnetic fields on the submillimeter scale. The process involves selecting the desired magnetic material from bulk magnetic material options, selecting the best laser for the desired outcome, and physically machining the magnets to size. Post machining processing includes cleaning the magnets, magnetizing in the desired direction, and integrating into a larger magnetic system.

1.5 Dissertation Structure

This dissertation investigates the feasibility of designing and fabricating devices with geometrically complex magnetic fields at the submillimeter scale, as enabled by laser micromachining. The present chapter introduced the field of laser machining, magnets and magnetic materials, and how micromagnets can be used in devices at the submillimeter scale along with a discussion of the challenges in creating submillimeter scale magnetic field structures. Chapter 2 details how the laser micromachining of magnetic materials can affect the magnetic fields that micromagnets can produce. This is done through two separate experiments: laser machining of magnetic materials followed by 1) a vibrating sample magnetometer measurement or 2) a magnetic force microscope scan. Chapter 3 presents the design, fabrication, and characterization of an undulating array of micromagnets and explores several of its applications. Chapter 4 details additional types of magnetic field distributions and their corresponding applications, demonstrating the versatility of this fabrication technology. Lastly, Chapter 5 presents conclusions and future work in the laser micromachining of sub-mm PM and geometrically complex magnetic field distributions. Modeling of the appropriate magnetic fields is presented throughout for comparison and confirmation.

CHAPTER 2 LASER MICROMACHINING OF MAGNETS

Laser micromachining has become more relevant to manufacturers in the last decade or so as devices have continued to shrink and systems have become more complex. Many companies now exist that strictly laser micromachine various materials for external customers, creating stents, angioplasty balloons, lifting LEDs off a sapphire substrate, cutting RFID cards, etc. [53] [54]. With the history of laser micromachining and micromagnets in the MicroSensors and MicroActuators research group [17] [55] [56] [57] [58] [59], fabrication of submillimeter scale magnetic microstructures by laser micromachining was an attractive proposal. Obviously, the issue of extreme heat deposition into a heat sensitive material would need to be addressed.

It is expected that laser machining will enable magnets to be machined down to widths of 50 μm, given the materials in use and the reasonable ability to handle and machine individual magnets, although holes machined out of a larger piece should be able to be machined down to 25 μm in diameter. This laser machining is a naturally extreme environment in the immediate vicinity of the laser pulses, due to the high temperatures, high temperature gradients, and the effects these temperatures can have on diffusivity, oxidation, etc. As such, it is expected that some minimal zone near the edge of the magnets will be permanently damaged. Given that, this chapter investigates the extent to which these magnets are damaged and possible mechanisms of this damage.

2.1 Laser Machining of Magnets

The first thing to demonstrate was if a micromachining laser could machine a magnet similar to, or better than, fabrication technologies such as end milling or electrical discharge machining (EDM). Laser micromachining a material, much less a metal, with a

thickness greater than 100 μm tends to be a challenge. The purchased magnets were 500–μm–thick NdFeB and SmCo and 300–μm–thick SmCo. Nevertheless, as per section 1.3.1, appropriate laser parameters were discovered with which one could fabricate, in a repeatable fashion, individual pieces of magnetic material.

2.1.1 Lasers Used for Experiments

The lasers used in the first phase of testing were a Resonetics flash lamp pumped Nd:YLF crystal laser (Nd:YLF) operating at 1047 nm with a 180 ns pulse length, 4 mJ pulse energy, 22 kW peak power, and a 4 W average power; and a Coherent Talisker Ultra (Coherent) operating at 355 nm with a 10–15 ps pulse length, ~25 μJ pulse energy, 1.66 MW peak power, and 5 W average power. Section 2.2 details the work done using these lasers and Figure 2.1 shows an example of some magnets machined with this Nd:YLF laser and Figure 2.2a shows an image of the Nd:YLF laser system.

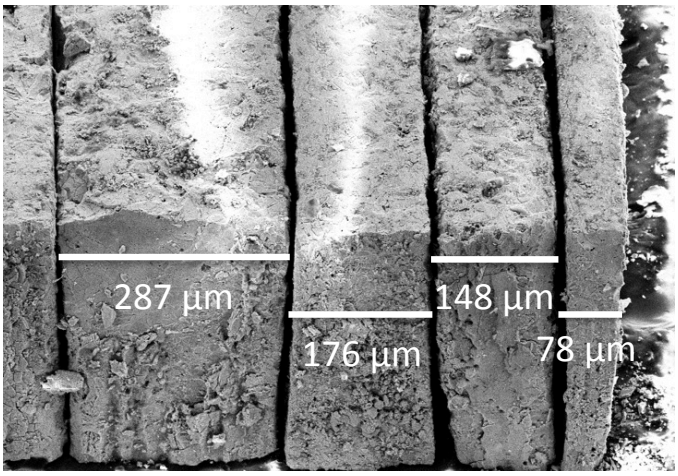

Figure 2.1 Scanning electron micrograph showing rectangular magnet pieces of various widths, all are 300 μm thick.

The second phase of testing was performed using two laser systems provided by IPG Photonics. The first system is an IX255 that contains an ArF excimer laser (Excimer) at 193 nm with up to 10 mJ energy output per pulse and a 10 ns pulse length, giving 1 MW peak power with 10 W average power, with a variable beam spot masked from 1 μm up to 300 μm and a pulse frequency of 1 kHz. The second system, an IX280ML, contains two fiber-based lasers. One laser (model: GLPR-100-1-10) is a green laser (Green) operating at 532 nm with a short pulse length of 1.3 ns (at the upper limit of what is defined as ultra-short pulse lasers), a pulse energy of 85 μJ, a Gaussian spot size with radius 10 μm, a peak power of 65 kW and average power of 8.5 W, and a pulse frequency of up to 300 kHz. The other (model: YLR-150/1500-QCW) is a fiber-delivered quasi-continuous-wave (QCW) infrared (IR) laser operating at 1070 nm that can utilize a varying pulse length from 0.1–50 ms. It has a pulse energy up to 15 J, a peak power of up to 1500 W and an average power of 150 W, and a Gaussian spot size of radius 20–30 μm. Each of these lasers enables a slightly different form of laser machining and provides a good cross-section of material cutting capabilities. Images of the IPG Photonics laser systems are shown in Figure 2.2 b and c, respectively. All three IPG photonics provided lasers are capable of cutting micromagnets. As such, a comparison will be made as to how the different laser types affect the magnetic materials (NdFeB and SmCo) in different ways. Section 2.3 describes the work completed using these three lasers. The parameters for these lasers are included in Table 2.1 for comparison.

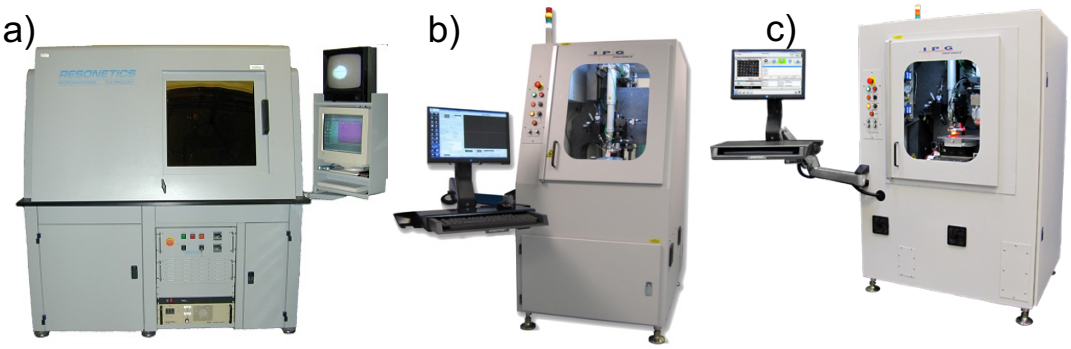

Figure 2.2 Photographs of laser systems used: a) Nd:YLF, b) ArF Excimer, and c) dual fiber laser (containing Green and QCW lasers)

Table 2.1 Laser specifications for lasers used during this dissertation

Parameter	*Resonetics Nd:YLF*	*Coherent Talisker Ultra*	*IPG IX255 ArF Excimer*	*IPG IX280ML Green Fiber*	*IPG IX280ML QCW IR Fiber*
Wavelength, nm	1047	355	193	532	1070
Spot Radius, µm	20	20	1-300 masked	10	20
Pulse Energy	4 mJ	25 µJ	10 mJ	85 µJ	15 J
Pulse Length	180 ns	15 ps	10 ns	1.3 ns	100 µs–50 ms
Repetition Rate	1 kHz	200 kHz	Up to 1 kHz	20-300 kHz	20 Hz–5 kHz
Peak Power	22 kW	1.66 MW	1 MW	65 kW	1500 W
Fluence [J/cm^2]	320	8	100 hi fluence 11 low fluence	27	1200000
Peak Power Intensity [GW/cm^2]	1.75	530	10 hi 1.1 low	20.7	0.12
Average Power	4 W	5 W	10 W	8.5 W	150 W
Label	Nd:YLF	Coherent	Excimer	Green	QCW

In referring to Figure 1.20 of laser ablation and 1.15b of pulse shape and repetition, each laser parameter affects the machining of a particular material in a different way. The specific photon wavelength (and associated frequency and energy) determines the types of bonds the photons are capable of breaking and each material absorbs, reflects, and transmits the specific wavelengths differently. An extension of this is the pulse energy,

the integrated optical power of the pulse over pulse length, again the shaded region of Figure 1.14b, or the number of photons at a specific wavelength/energy added together and multiplied by the energy of the photons. A higher pulse energy generally means the laser can remove more material per pulse and can machine deeper into a material over multiple passes. However, pulse energy works in conjunction with the spot size to give a laser fluence, as mentioned previously in section 1.3.4. A laser with the same pulse energy and a smaller spot size will have a higher fluence. Additionally, each material has a fluence threshold that must be reached, otherwise no ablative material removal will take place. The rate at which the optical energy increases is governed by the pulse length. As long as the pulse length is shorter than the thermalization time, heating effects are diminished. In other words, the transfer of energy from photons to electrons to phonons is decreased. For metals, this time is in the tens of picoseconds; for polymers, it is in the microseconds range; and for other materials, the thermalization time is somewhere between the two. Finally, the pulse length and fluence together form peak power intensity, which defines how much power is deposited in a given area over a single pulse. A high peak power intensity usually results in relatively small heating effects and clean laser machining. Not all machining parameters can be optimized at the same time, but every effort should be made to achieve clean machining, at an appreciable rate of removal, with as small a HAZ as possible.

2.1.2 Magnetic Materials Used

The magnetic materials used in this dissertation were chosen for their accessibility and the fact they had been used for previous machining attempts within the MicroSensors and MicroActuators lab as described at the beginning of this chapter. The magnetic

properties are listed in Table 2.2 and additional mechanical properties are listed in Appendix C. As part of trying to understand how temperature changes affect these specific materials, each was run through a battery of thermal magnetic testing. The magnetic properties were measured at various temperatures, showing how remanence and coercivity degrade with temperature, both reversibly and irreversibly.

Table 2.2 Properties for permanent magnets used in this dissertation

Material	Category	Manuf. Method	H_{ci} [kA/m]	Br [T]	BH_{max} [kJ/m3]	Curie Temp [˚C]	T_{max} [˚C]	Reversible Temp.Coeff. Remanence [%/˚C]	Corrosion Resistance
Sm_2Co_{17} 30/25	Rare Earth	Powder	2000	1.1	240	800	300	-0.03	Moderate
$Nd_2Fe_{14}B$ N48	Rare Earth	Powder	1000	1.4	358	310	100	-0.12	Poor
$Nd_2Fe_{14}B$ N52	Rare Earth	Powder	1000	1.45	406	310	100	-0.12	Poor

Bulk magnet temperature effects were measured by Dr. Alexandra Garraud of University of Florida, and provide a basis for magnetic property degradation due to laser machining. The experiment involved measuring the magnetic properties of the magnets as the temperature was cycled between increasingly higher temperatures and room temperature. Figure 2.3 shows how the magnetic properties degrade with temperature, up to 1000 K. Figure 2.3.a1 shows demagnetization curves as a function of temperature for 300–µm–thick Sm_2Co_{17}. Figure 2.3.a2 shows the normalized remanence, saturation magnetizations, as well as coercivity as a function of temperature for Sm_2Co_{17}. Figure 2.3.a3 shows how cycling the temperature affects the remanence magnetization. Note how the remanence after cycling back to room temperature only significantly decreases when the temperature exceeds 550 K or 275 C. After 550 K, the magnetization never fully returns to the original value until remagnetization by an applied field. Figures 2.3.b1,

b2, and b3 refer to 500–μm–thick NdFeB of the N48 variety, where N48 refers to a maximum energy product of 48 Mega-Gauss Oersted (MGOe). Note how the remanence begins to decrease almost immediately above room temperature. The difference here between SmCo and NdFeB is consistent with the fact that SmCo has a much higher T_{max} than NdFeB.

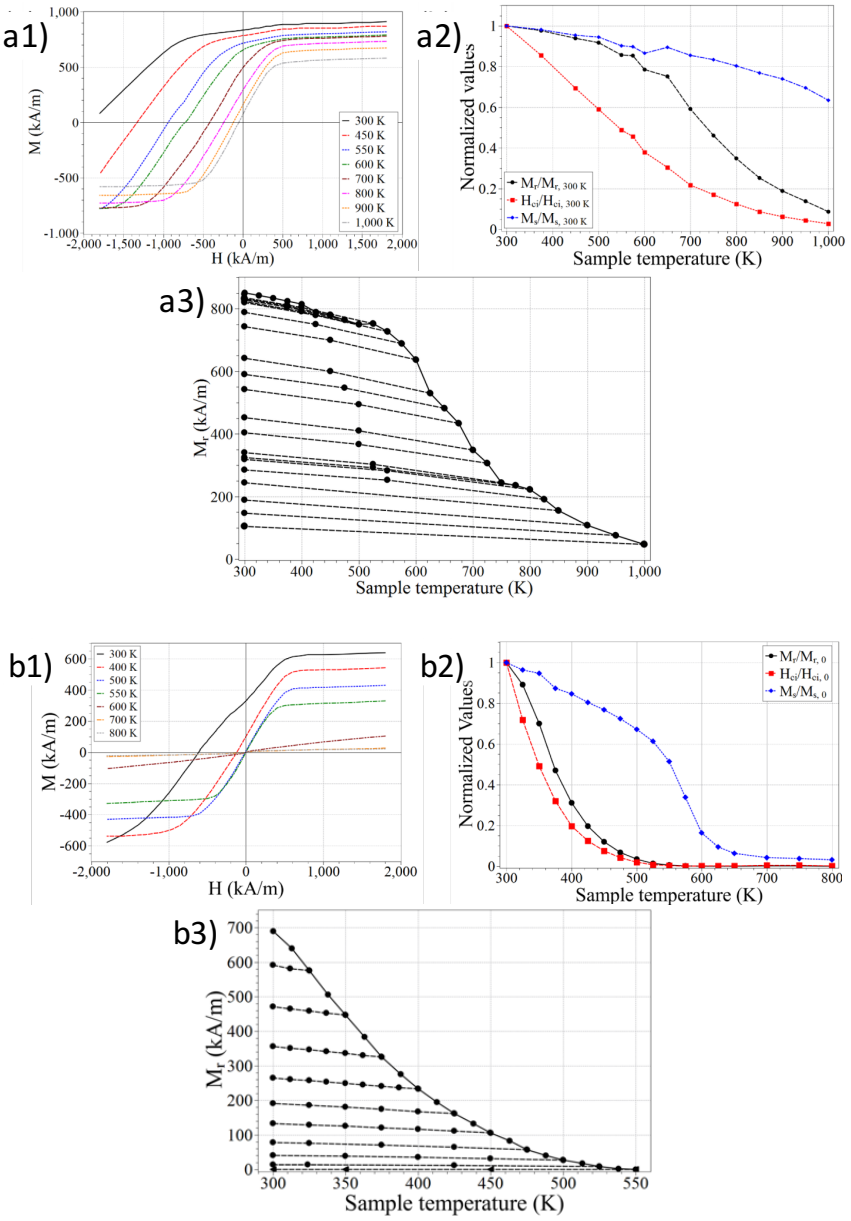

Figure 2.3 Various charts showing the effects of temperature on the magnetic material properties of (a) SmCo and (b) NdFeB. The charts show (1) demagnetization curves at varying temperatures; (2) normalized remanence, coercivity and saturation as a function of temperature; and (3) remanence with temperature cycling (solid – increasing temp, dashed – decreasing temp)

2.2 Vibrating Sample Magnetometer Measurement of Magnet Heat Affected Zone

The goal of this work was to understand the limits of laser micromachining magnets while still maintaining an appreciable magnetic field to create magnets with widths in the tens of microns from a 300– or 500–μm–thick substrate. This work is mostly described by Peterson, et. al in IEEE Transactions on Magnetics [60].

2.2.1 Model Representing HAZ as Measured by VSM

A model for how the heat-affected zone alters the magnetic properties was devised, such that the HAZ could be measured in a vibrating sample magnetometer (VSM) and compared to expectations.

The model comprised a rectangular area with damaged sections on both sides of the changing width, as shown in Figure 2.4a. The size of the damaged section was held constant and the damage or loss of magnetization was assumed to be complete within the damaged section. As the width decreases until twice the size of the damaged section, the fraction of overall magnet with magnetic field would ideally decrease linearly to zero. The physical volume of one rectangular magnet is

$$V_0 = L * W * T, \tag{2.1}$$

where L, W, and T are the length, width, and thickness, respectively, and the effective magnetic volume, excluding the HAZ, is

$$V' = (L - 2d) * (W - 2d) * T = T(LW - 2Ld - 2Wd + 4d^2), \tag{2.2}$$

where d is the depth to which the magnet is damaged. Neglecting terms in d^2

$$V' = V_0 - 2dLT - 2dWT. \tag{2.3}$$

In order to obtain the percent of the volume that has useful magnetic material, the ratio of these two quantities, effective magnetic volume and physical volume, is calculated, which gives

$$\frac{V\prime}{V_0} = -2d \cdot \left(\frac{1}{W}\right) - \left(1 - \frac{2d}{L}\right). \tag{2.4}$$

Lastly, assuming L >> d for this model and subsequent experiment, the second term can be neglected and the percent useful volume equation simplifies to

$$\frac{V\prime}{V_0} = -2d \cdot \frac{1}{W}. \tag{2.5}$$

Plotting eq. 2.5 as a function of inverse width gives a straight line with a negative slope that is twice the size of the damaged/heat-affected zone, as in Figure 2.4b. In the case of magnetic measurement, where the magnetization is first obtained, dividing the measured magnetization by the bulk remanence, or the magnetization of the ideal sample of equal physical volume, gives percent useful volume. This is due to the fact that the damaged volume of material is assumed to be completely demagnetized.

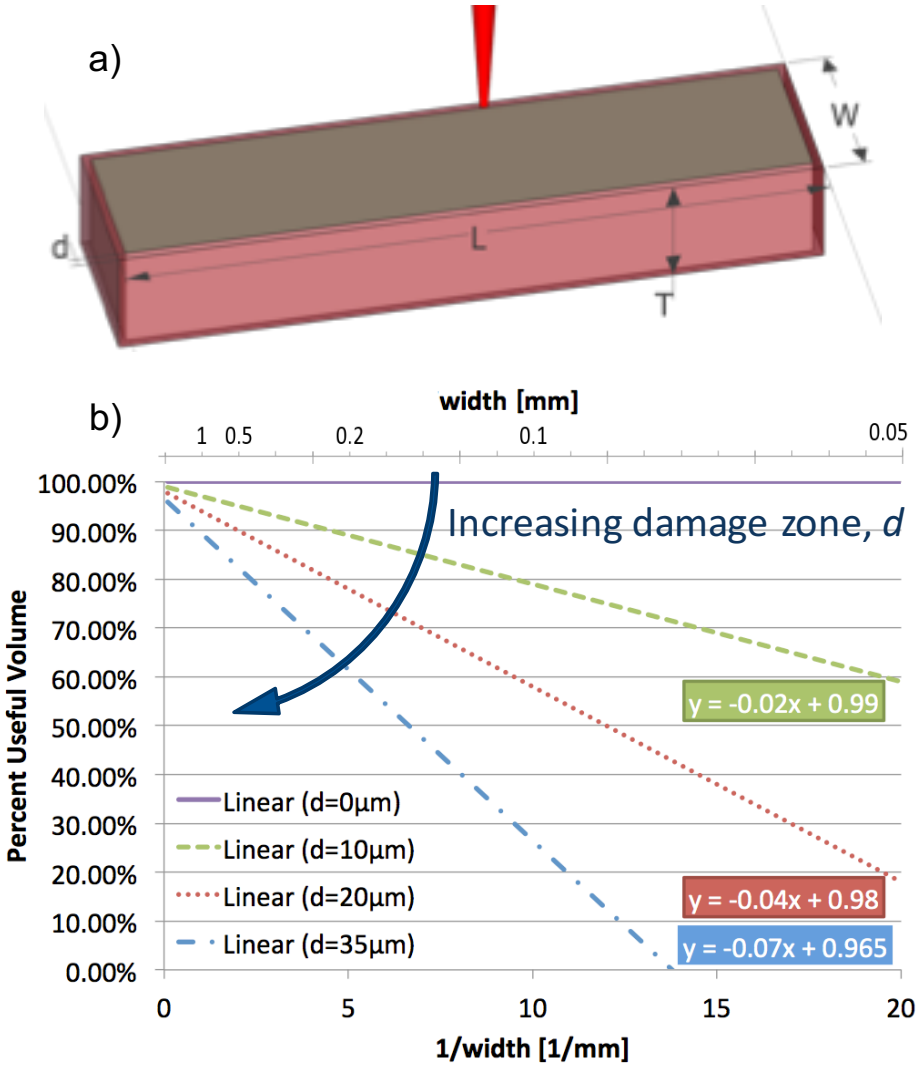

Figure 2.4 a) Schematic of laser machined magnet sample from model and b) ideal results of analytical model

2.2.2 Fabrication and Measurement

In order to facilitate magnet micromachining, an array of laser machining parameters was traversed, similar to Figure 1.17, attempting to find the most suitable laser and stage movement settings (detailed in Appendix B). The Nd:YLF laser has a fixed pulse

frequency, so the only variables to adjust were the pulse energy, stage speed, and number of passes. The parameters that gave the cleanest magnet cut were then selected. Figure 2.5 shows a parametric array with the results of the Nd:YLF laser machining SmCo. Notice how the top line in the center column is more consistently cut (dark line) and has much less protruding laser melt. This would be the best set of laser parameters from this parametric array. Additional parametric arrays could be performed, using this selected line as a basis, varying additional parameters. When laser machining the magnets, it was desirable to have a relatively small kerf width, be machined all the way through, and have relatively little black remelt on the magnet surface, with a relatively short overall machining time. A small kerf width was necessary for this testing because an accurate measurement of length and width would be needed for calculating the volume of each sample. For more complex magnets, a low kerf width means additional magnets can be placed in closer proximity to each subsequent magnet. Additionally, the magnets needed to be fully released in this case since each individual magnet would go through magnetic measurement via the VSM. However, for more complex magnetic field patterns, a through-cut is not necessarily the most desirable outcome, and additional parameters would need to be found for micromachining to depth into a magnet. Laser parameters and code used for each laser and each material being processed can be found in Appendix B.

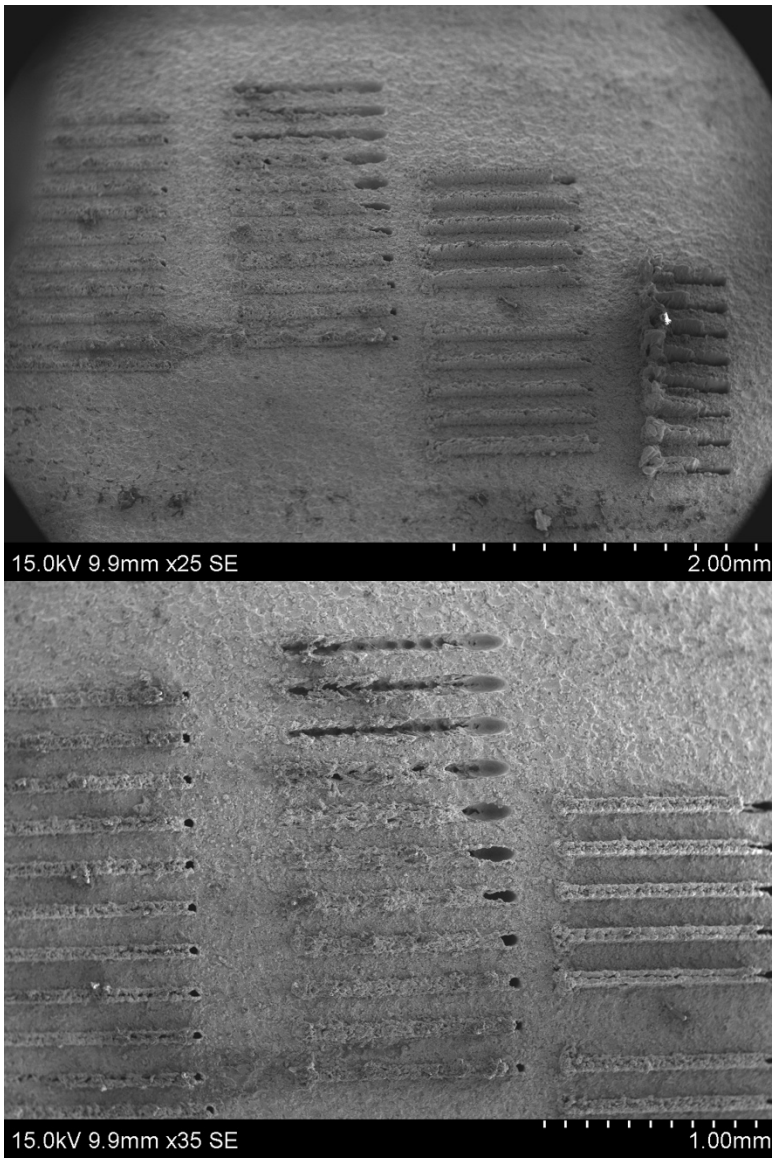

Figure 2.5 SEM images showing a parametric array of laser machined lines in SmCo as machined on the Nd:YLF laser

Given the sizes of the materials being machined (no larger than 5 – 10 mm), the magnets needed to be adhered to a carrier substrate. This is preferably glass, Kapton, dicing tape, a silicon wafer, or something similar that will not weld to the laser machined part, and can be adhered by tape, glue, or something similarly easy to remove. For most

of the machining in this dissertation, the magnets were adhered on top of glass (either with double-sided tape or water soluble glue), whether they were magnetized before or after machining. However, in the case of this Nd:YLF and the QCW laser described in section 2.1, the magnets were suspended using a custom-made frame that allowed the magnet melt and air assist to fall freely through the magnet and proceed to the fume/dust extractor.

Rectangular prisms, with a constant length of 2 mm and thickness of either 300 or 500 μm, were fabricated to test this model. The widths of these magnets ranged from 500 μm down to 40 μm, similar to what was shown in Figure 2.1. Multiple pieces of each size were laser machined and the length, width, thickness, and mass of each piece was measured on a measuring microscope (with a minimum resolution of approximately one micron) and a microbalance, respectively. The magnets were either left as is, cleaned with a 15% citric acid solution at 80C followed by a dip in an ultrasonic bath, or cleaned with a cloth to remove the laser remelt. Figure 2.6 shows the effect of this cleaning process. Note the significant amount of laser melt debris on the sample with no cleaning and the relatively smooth surface of the cleaned piece.

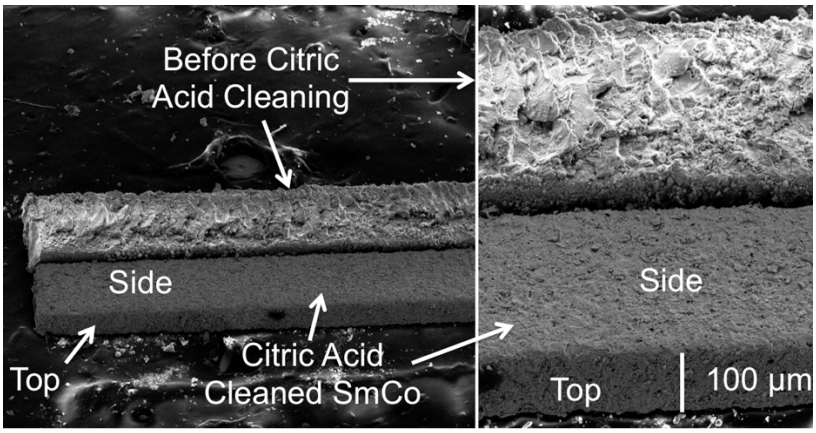

Figure 2.6 SEM of citric acid cleaned slice next to a laser-machined slice without cleaning

The magnets were then magnetized. General good practice for sufficiently magnetizing a magnet is that the applied/magnetizing field should be at least three times the coercivity. The NdFeB, due to its lower coercivity, was magnetized in a pulse magnetizer (Oersted Technologies, Magnetizer 340B, 3.5 T applied field). The SmCo would not be sufficiently magnetized at 3.5 T, so a high field strength superconducting magnet (Bruker DSX 300 Small Bore Animal MRI, B_0 = 7 T) was used instead.

Once the magnets were cut, cleaned, and magnetized, the remanence of each piece was then measured in a vibrating sample magnetometer (VSM - Lake Shore Cryotronics, 7304 Series VSM System, $H_{applied,max}$ = 1120 kA/m = 14 kOe; or ADE EV9 VSM, $H_{applied,max}$ =2000 kA/m = 25 kOe). Each individual magnet was measured by attaching to a VSM sample holder, inserting the sample holder, aligning the magnet on the VSM axes, and measuring the remanence. For several samples of each material, an incomplete B-H loop was obtained; the loop is incomplete because the VSM applied field is not strong enough to saturate and reverse the magnetization of the magnet. Figure 2.7

shows a sample of this raw VSM B-H output for six samples. Note how the remanence decreases with decreased width of the magnet samples. As there were various samples for each desired width, this allowed for each size to have several data points for each material.

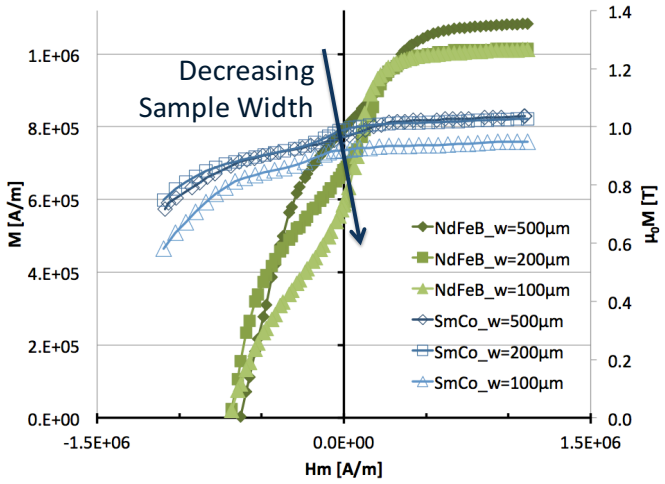

Figure 2.7 Chart showing raw VSM demagnetization curves for SmCo and NdFeB at widths of 500 μm, 200 μm, and 100 μm

2.2.3 Analysis of Results

As the analytical model predicted, when the width of a magnet sample decreases, its normalized magnetization, compared to bulk remanence, decreases linearly with respect to inverse width. This is more pronounced for the NdFeB samples than it is for the SmCo samples because the NdFeB appears to have a larger HAZ, measured at approximately 13 μm (see Figure 2.8), even when machined by a picosecond laser. The SmCo still has a HAZ as well, with a measured HAZ of approximately 8 μm for the samples that were not cleaned, (the NdFeB were not cleaned either). These results make sense once one considers that NdFeB has a much lower Curie temperature than SmCo (310˚C and

850˚C, respectively) and a correspondingly higher magnitude reversible temperature coefficient of remanence (-0.12%/˚C and -0.03%/˚C, respectively) and coercivity (-0.62%/˚C and -0.2%/˚C, respectively). It is unlikely that material parameters such as thermal conductivity and heat capacity play as much of a role here as the parameters are quite similar between NdFeB and SmCo (see Appendix C). It is interesting to note from Figure 2.8b that utilizing a cleaning method with SmCo can effectively remove the damaged material. Also, at dimensions below 100 μm, physical cleaning methods (sanding/polishing) are to be avoided as these magnets are brittle and difficult to handle. In the case where a magnet is to be machined in place, this is especially true. As such, chemical cleaning methods appear to be the best option available.

Additionally, as can be seen in Figure 2.9, there is additional useful information to be gathered from this representation of the same data, which is a comparison of the same magnet samples, but plotting remanence instead of percent useful volume, which is normalized to the bulk remanence. Importantly, despite the depth of the HAZ in the material, a transition occurs at around 300 μm widths such that at larger widths the NdFeB magnet pieces have higher magnetization, but at lower widths the SmCo fares better. Indeed, if using a magnet system with magnets larger than 300 μm as the minimum feature size, NdFeB will provide for a higher field value at a set measurement distance. Due to the results of this study, and the other benefits mentioned previously, such as chemical resistance and the lack of a need to coat the material to prevent oxidation, SmCo became the laser machined magnet of choice.

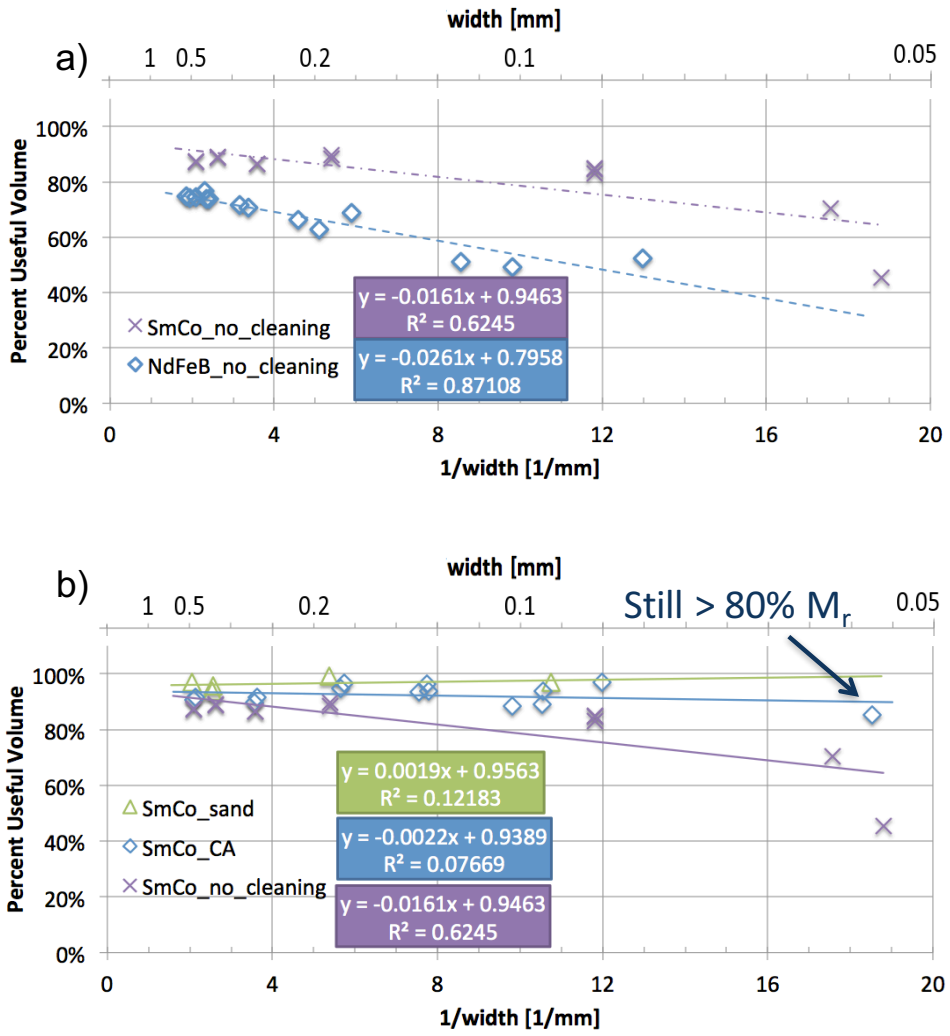

Figure 2.8 Charts showing percent useful volume as a function of inverse width for a) machined NdFeB and SmCo without cleaning and b) SmCo both without cleaning and cleaning with citric acid or a cloth. Implied damage zones are half the slope of these lines as per equation (2.5)

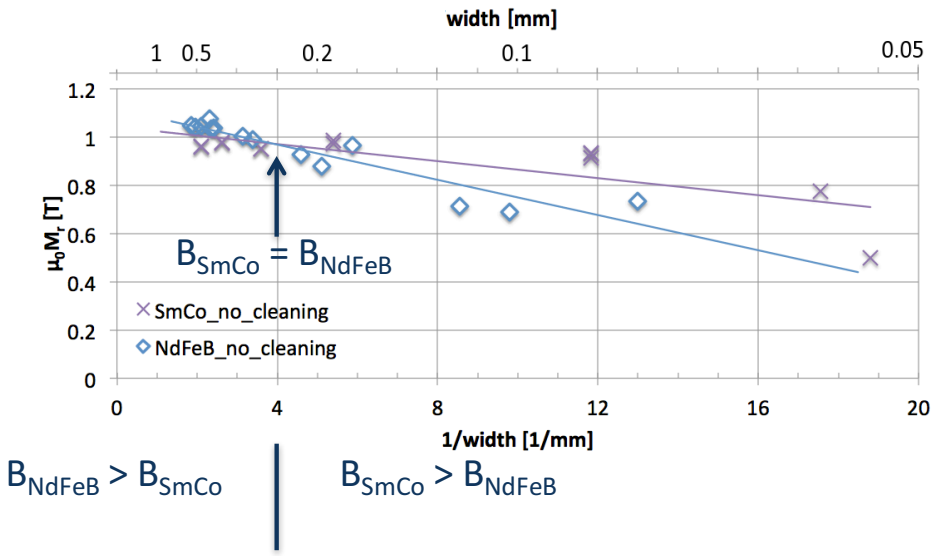

Figure 2.9 Chart showing magnetization in SmCo and NdFeB pieces, instead of percent available magnetic material, as a function of inverse width

2.3 Thermal Model of Laser Deposited Heat

As mentioned in section 1.3.6, laser machining will affect the magnetic materials, and from the previous section it was shown that the depth to which a material is irreversibly magnetized can be partially ascertained. Continued investigation is warranted to help ascertain the different effects laser machining is having on these materials, an example of which is shown in Figure 2.10a. When laser machining a magnet that is already magnetized, any section of material that rises in temperature to more than T_{max}, as mentioned previously, will be at least partially demagnetized. Above the Curie temperature, likely approaching and exceeding the melting temperature, there are additional effects that prevent the magnets from being remagnetized; the section of material becomes irreversibly demagnetized. This will happen to a magnet whether or

not the magnet is magnetized prior to laser machining and is what was partially measured in the previous section.

In order to better understand the effects of the laser machining of magnetic materials and the temperature distributions within the material, a thermal model was created using COMSOL Multiphysics. The model contains magnet and air, with a small section defined as the laser heat input. Due to the complexity of ablation and material removal in modeling, only the heat deposited into the material was accounted for. There are example models of laser heating and melting in the public domain [61] [62], but they also do not include true ablation, but utilize a change in emissivity or something similar. A schematic of the model is shown in Figure 2.10b. The model is two-dimensional and axisymmetric, about r=0, due to the fact the laser spot is also circular. The bottom half is magnet (gray) and the top is air (blue). The small section in the middle is the laser heated zone (red) that is approximately the same size as the region the laser would heat, 1 μm thick with a 10 μm radius.

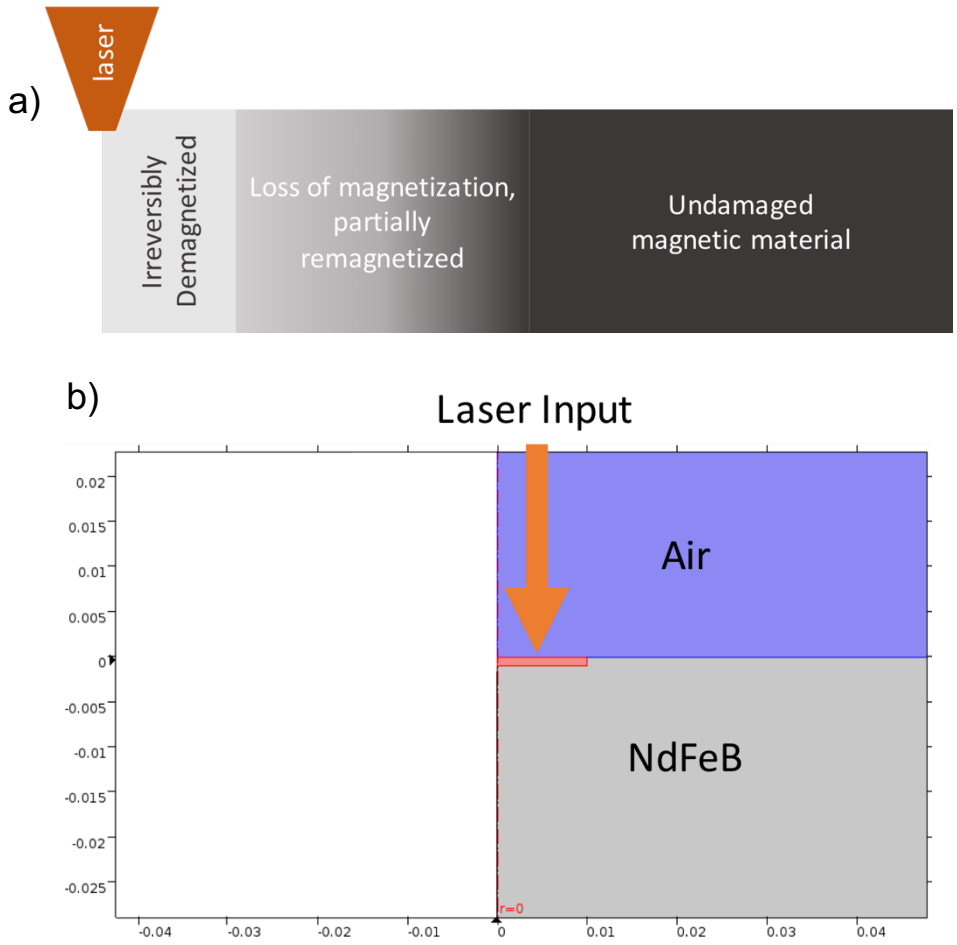

Figure 2.10 a) Conceptual drawing of laser-induced damage to magnets and b) schematic representation of the thermal model showing NdFeB (gray), air (blue), and small laser heated region (red)

The heat input resembles a series of laser pulses similar to the green laser described previously, except that the laser spot does not move, as is normally done with laser machining, to reduce model complexity. The peak power of 65 kW was applied over 1 ns with a spacing of 10 μs between each of five pulses (100 kHz repetition rate). Figure 2.11 shows the temperature profiles of the model for each pulse immediately prior to the

subsequent laser pulse (10 μs); the axes dimensions are in millimeters. With the laser spot moving linearly at a speed of 125 mm/s (up to at least 2.5 m/s) for magnet machining and a repetition rate of 100 kHz, there is a 1.25 μm spacing between laser pulses, or approximately 16 laser pulses over the 20 μm diameter of the Gaussian laser spot. Each successive laser pulse increasingly affects a stationary position until immediately adjacent to it, then the effects decrease again as the distance to the laser spot increases. Due to this fact, the five stationary laser pulses with a constant peak energy should be an adequate representation of the temperature profile from a moving laser spot. Note how after five pulses the material reaches 1600 K (1300 ˚C) at approximately 15 μm from the laser spot, the same order distance as the HAZ in laser machined magnets. Additional similar modeling was completed for the Excimer and QCW lasers. The excimer laser model used a 10 ns, 1 MW laser pulse over a larger area that corresponded to the larger beam spot of the excimer laser. The QCW model used a 100 μs, 300 W pulse and the full thickness was selected as the excitation area as the QCW laser melts through the entire substrate in a single pulse. Interestingly, the melting temperature is also on the order of the measured HAZ for these two lasers as well.

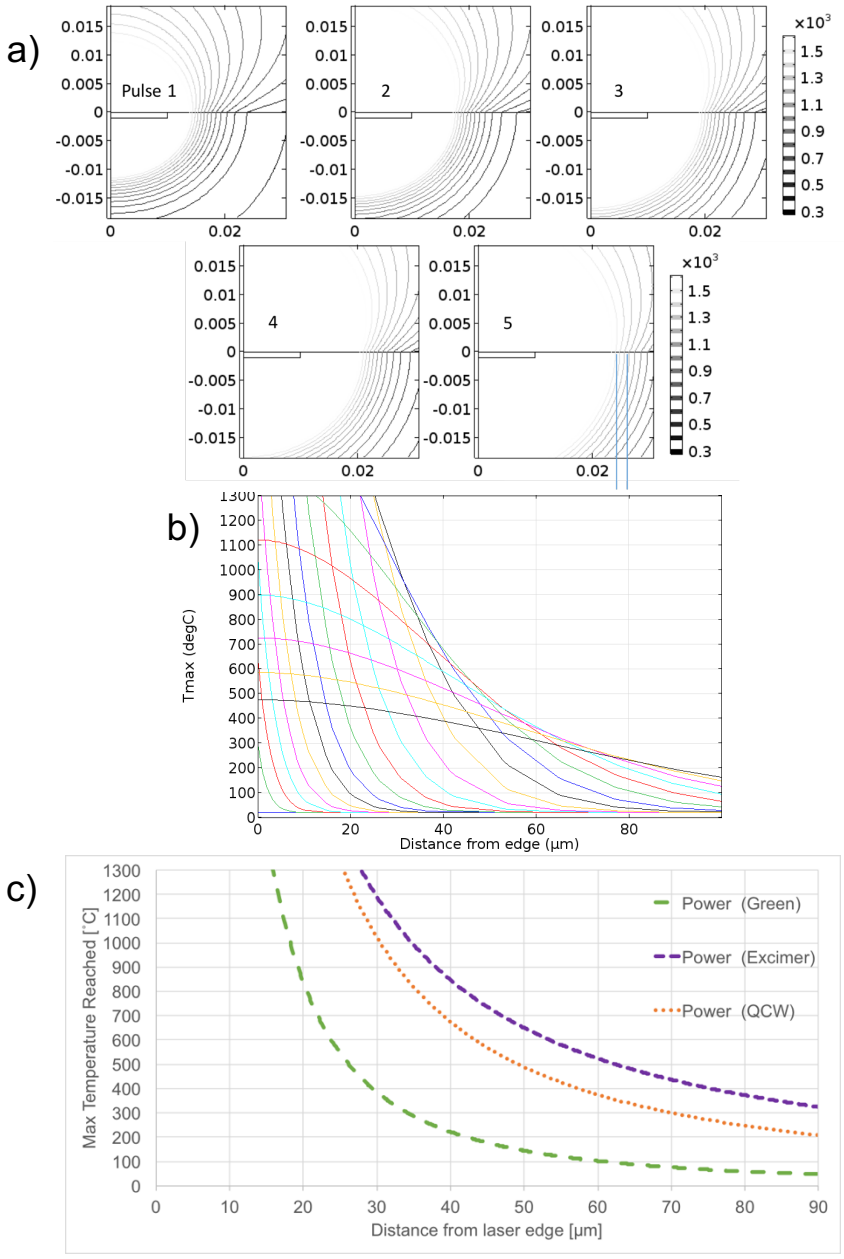

Figure 2.11 Temperature profiles showing the effect of laser heat input over a) five consecutive laser pulses on the green laser with the temperature bar on the right in Kelvin, b) maximum temperature reached after a laser pulse on the QCW laser as a function of distance from the laser edge, and c) a comparison of the model for the green, excimer, and QCW lasers

The melting temperatures of NdFeB, Fe, Nd, and SmCo are 1180-1300 ˚C, 1538 ˚C, 1021 ˚C, and 1340 ˚C, respectively. The NdFeB phase diagram in Appendix C shows that between 1180 ˚C and 1300 ˚C the material is part liquid and part crystalline. Due to this, the temperature profile only shows contours of constant temperature between room temperature and NdFeB melting temperature in Kelvin, at steps of 100 K. Note how after five laser pulses, the zone that includes melting temperatures reaches at least 15 μm into the material. As mentioned previously, most thermal characteristics of the SmCo and NdFeB magnets are relatively similar. Therefore, only NdFeB was modeled thermally because of those similarities and because its HAZ appears larger than SmCo. The biggest differences between NdFeB and SmCo are the Curie temperature, the grain structure, the fact NdFeB is a ternary compound, and the fact that NdFeB has the part liquid, part crystalline phase over a wide temperature range while SmCo does not. NdFeB magnets are additionally well-known for their susceptibility to oxidation. The results of this modeling and some of these factors provided a basis for attempting to ascertain what is causing the NdFeB to irreversibly lose its magnetization away from the laser machined surface.

In addition, the process of additive machining, done with metals, ceramic, plastic, and glass by lasers, utilizes a process called Selective Laser Sintering or Machining (SLS/SLM) or Direct Metal Laser Sintering (DMLS) [63]. This additive machining heats beads of a material (titanium, steel, etc.) to a specific temperature to achieve full melting, partial melting, or liquid-phase sintering. For solid state sintering, the material is heated to between half and full melting temperature, achieving a diffusion of material between the grains. This could be similar to what is happening in the case of NdFeB near the

laser machined edge due to the fact the grain boundaries already often contain a slightly different composition (Nd-rich or Fe-rich) from the crystalline grains. As an additional possibility, partial melt sintering melts only the outside of the grains, leaving the bulk of the grains unaffected. Lastly, any significant amount of melting would also have a detrimental effect on the precisely pressed and sintered NdFeB grains.

Each of these processes essentially alters the grain structure of the magnet material, either by reorienting the grains or increasing grain size, or a similar mechanism. In this case, it is likely that the physical NdFeB platelet-shaped grains are being altered from the precisely processed state via one of these mechanisms or oxidation is occurring and inhibiting magnetization. NdFeB and SmCo magnets are made similarly by first forming the magnetic material into a powder by melt spinning or jet milling to a fine grain size (in an inert environment – 3-7 μm grain sizes) and pressing the powder in a mold at elevated temperatures. Creating a preferred magnetization in the magnet is either done by pressing in a magnetic field or utilizing a technique called dye-upsetting. The magnets are then sintered (high temperature under pressure), machined to a more precise size, and plated for protection, if necessary, prior to magnetization [64] [65]. If the orientation or size of these particles changes slightly, magnetization will be lost or reduced in that region [36] [66] [67]. Due to these various possibilities further experiments were performed and measurements taken to ascertain further detail within the HAZ: e.g. how much material is reversibly damaged (above the Curie temperature) in contrast to irreversibly damaged (as in the case of the NdFeB).

2.4 Magnetic Edge Vs Physical Edge

The goal of the work in this section was to assess how different lasers can affect NdFeB and SmCo, determine the extent of HAZ, and to see what the difference is between laser machining a premagnetized magnet versus magnetizing a magnet after laser machining. Figure 2.12 details the difference between the magnetic edge (green line) and the physical edge (orange line), as well as the effect of partially damaged material after laser machining. If there is no irreversibly damaged material, the orange and green lines would coincide with one another. The methods and results are described in the sections that follow. This work is previously unpublished.

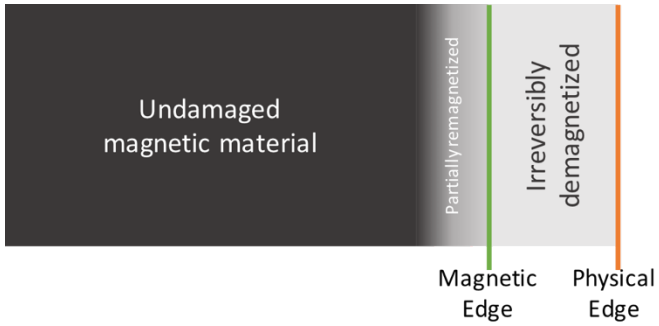

Figure 2.12 a) Conceptual drawing highlighting the (orange line) physical and (green line) magnetic edge whether the magnet is only partially or is fully remagnetized after laser machining

Magnetic Force Microscopy (MFM) was used in an attempt to ascertain a more detailed understanding of the magnet HAZ than that previously described in section 2.2. It was presumed that MFM would allow for a more direct measurement at the edge of a magnet than is possible with a volumetric measurement. In order for this to be the case, an understanding of the fundamentals was required to identify how an MFM tip would

respond to the magnetic fields produced by the magnet. The MFM tips used were coated in materials (CoNi or Ni) that were easily saturated by the magnetic fields produced so close to the surface of these magnets. As such, they were essentially soft ferromagnetic, and the force they would detect is a result of magnetic field gradient,

$$\vec{F} = \nabla(\vec{m} \cdot \vec{B}). \tag{2.6}$$

The magnetic moment is a specification given by the MFM tip manufacturer and the B field, and its gradient, can be readily modeled directly above the surface of a magnet edge.

Figure 2.13 shows how the force on an MFM tip coated with a magnetic layer should appear as a result of an MFM scan. The curves represent magnets of widths 50 μm, 70 μm, 90 μm, and 110 μm. The set of curves represent the force on a 15-μm-wide magnetic tip at a distance 10 μm above the surface of the magnet. The running average is meant to imitate the effects of having magnetic material on the entire cantilever, the way most MFM probes are manufactured, and not just the end of the tip.

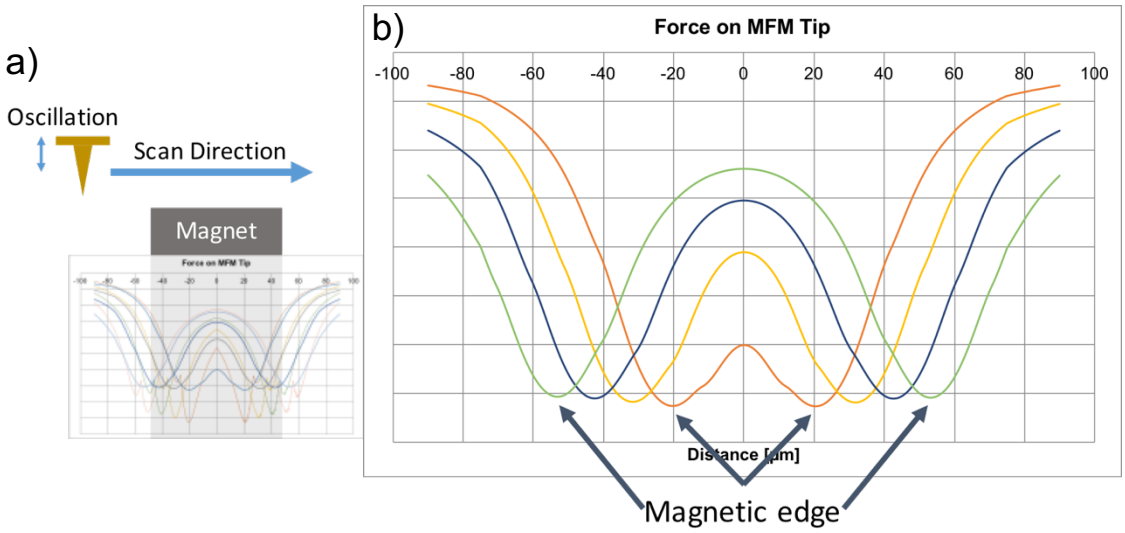

Figure 2.13 a) Schematic of an MFM tip traveling over the surface of a magnet and b) chart showing relative force on an MFM tip, using a COMSOL Multiphysics model, 10 μm above the magnet surface for magnet widths 50 μm, 70 μm, 90 μm, and 110 μm

A number of problems arose in the process of using MFM for measuring the fields from a bulk magnet near its edge. To explain, this is not a typical application for MFM. Normally MFM is used to measure small magnetic forces [68], to see magnetic grains in partially magnetized magnets, or to view the magnetic bits on the surface of a hard disk [69]. In this case, the effects of laser machining at the edge of a fully magnetized or partially locally demagnetized bulk magnet need to be measured. Normally, the magnetic forces would not encompass the entire MFM tip, but due to the size of the magnets in these experiments, the effects of the tip at the close separation distance of 10 μm, as shown in Figure 2.13, must be accounted for.

One of the first problems to arise in scanning the MFM probe over the edge of the magnets, was that the tip was moving from entirely over the magnet to partially over the

magnet, while the base of the MFM cantilever is always over the magnet as in Figure 2.14a. Since the magnetic forces are associated with the field gradients, and the strongest gradients of a magnet are at the edge, and because the MFM tip generally has magnetic material over the entire surface, there will be an offset in at least half of the data whether the magnet is on the left or right in Figure 2.14a. This offset problem was only mitigated upon rotation of the magnets such that the cantilever and tip were affected by the gradients at the same time as in Figure 2.14b.

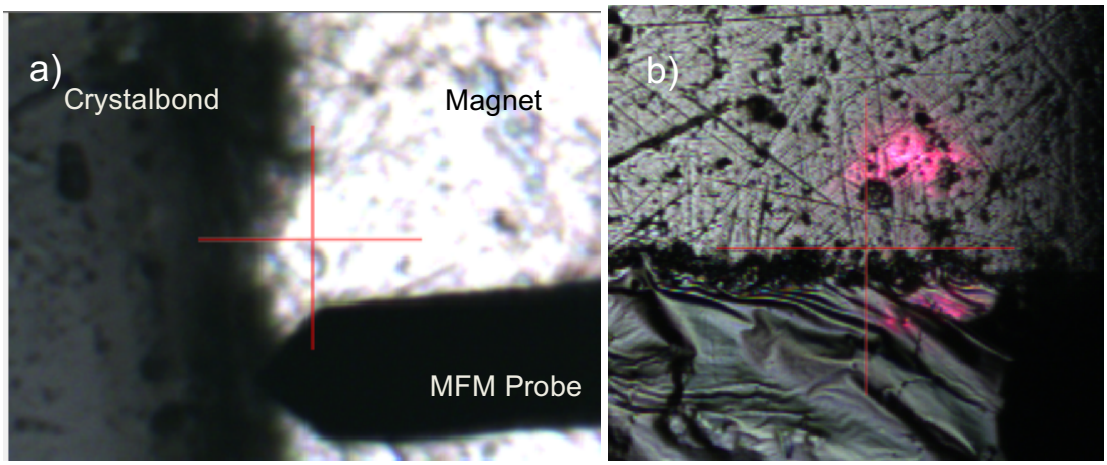

Figure 2.14 Microscope images of MFM cantilever and sample underneath with the cantilever a) perpendicular to the magnet edge and b) parallel to the magnet edge

Another problem that became apparent was the averaging of the magnetic field across the width of the MFM probe. Two methods were devised to reduce the averaging effects of the magnetic material of the cantilever. Both had the intent of creating a tip with minimal magnetic material, by either removing the magnetic material from the probe or sputtering magnetic material onto a small section of the probe. Both attempts were only partially successful. Indeed, only one company (Asylum Research,

https://afmprobes.asylumresearch.com/probes/sc-35-m.html) was eventually found that even has access to a tip similar to this, and they hold none in stock. For removing the CoNi magnetic coating from the tip, photoresist was used to cover the end of the MFM tip. Unfortunately, when the photoresist dries it wicks along the tip and does not fully cover the tip. So, when the CoNi was etched in Ferric Chloride, the tip material was also etched, destroying the magnetic characteristic of the MFM probe.

For the sputtering method, both the photoresist and a laser-etched polyimide sheet were used as a mask. Attempting to align the micron scale tip to a 20–μm–diameter hole etched by a laser in a 1-inch polyimide sheet proved to be challenging. An example of this alignment is shown in Figure 2.15a. Note how the probe tip created the swirly scratches in the polyimide during the alignment process. This method mostly provided a masked sputter of Ni as can be seen in Figure 2.15b, but was not small enough to mitigate the problem mentioned. Note how the cantilever has a curved brighter section that curls around the tip; this is the sputtered nickel. Additionally, note the string-like features on the cantilever; these are formed from the scratched polyimide that was subsequently coated in nickel with the rest of the probe tip. The second mask type relied on the same photoresist as mentioned previously, but instead used the wicking of the photoresist as a feature of a liftoff process. Nickel was again sputtered onto the photoresist-covered probe and the photoresist was used to lift off the unwanted nickel. This was the most successful method, but still did not provide a sufficient reduction in the averaging effect as seen in the model shown in Figure 2.13. Figure 2.16 shows the SEM image of the probe tip with Ni on the tip and partially lifted off by the photoresist (Ni is near the top of the tip in the image).

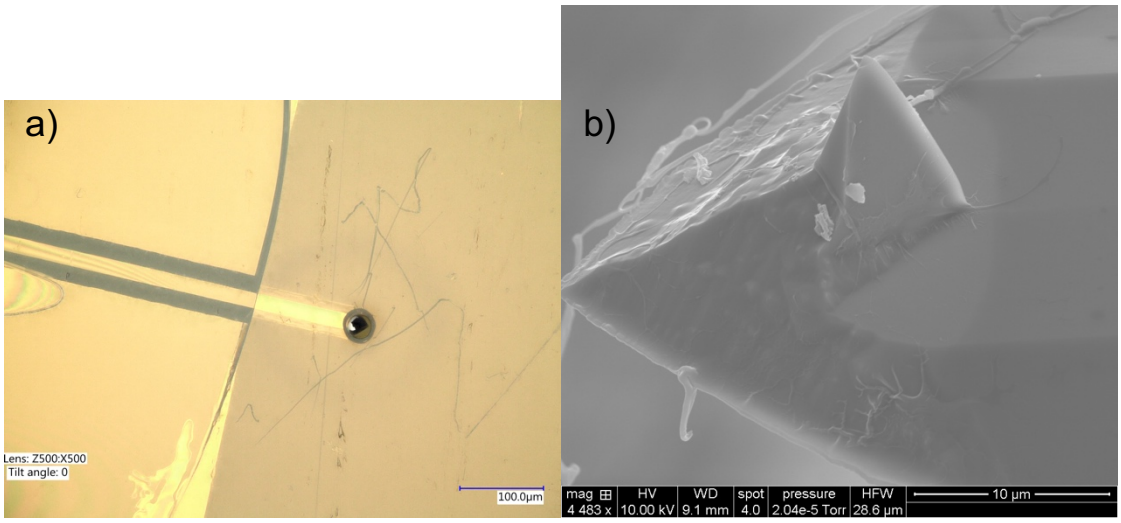

Figure 2.15 a) Photograph of masked AFM probe and b) SEM image of resulting masked sputter of Ni

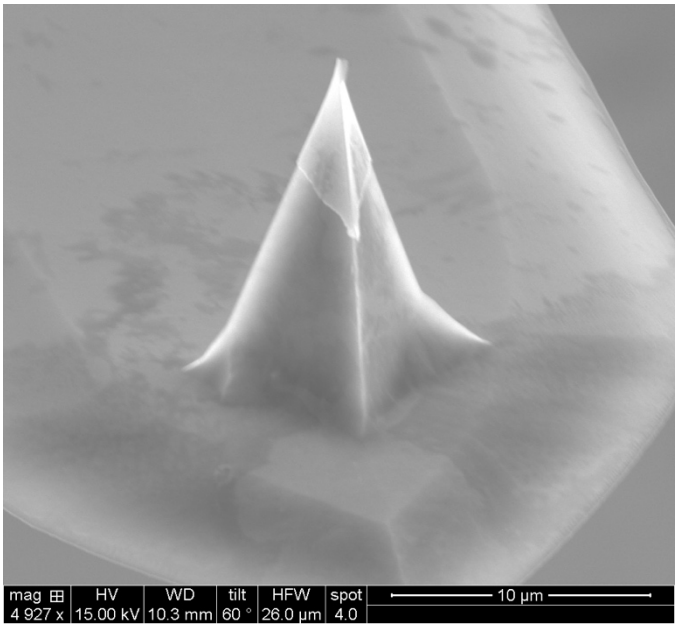

Figure 2.16 SEM image of Ni coated tip fabricated by liftoff

Although these tips did function as desired, with a smaller section of magnetic material, the sputtered Ni MFM probes did not adequately reduce the averaging effect shown in the MFM images. For the measurements conducted as part of the experiment detailed in the rest of this section, conventional MFM probes were utilized.

2.4.1 Magnetic Force Microscopy Procedure

The procedure for preparing a magnet to scan the laser machined edge with the MFM is comprised of the following steps; MFM introductory information comes mostly from Chapter 3: Magnetic Force Microscopy: Basic Principles and Applications by Ferri, F.A., et. al in the book “Atomic Force Microscopy - Imaging, Measuring and Manipulating Surfaces at the Atomic Scale” [68]. First, a magnet is laser machined and cleaned. Next, a glass slide is heated to 80˚C and Crystalbond (http://www.2spi.com/) is placed on the glass slide, whereupon it softens or flows. The magnets are then placed flat in the Crystalbond (magnetization direction normal to the glass surface) and the slide is allowed to cool; the Crystalbond holds the magnets in place and is used specifically for polishing. Next, the glass slide is placed in a rock thin-section slide polishing tool, and the magnets and Crystalbond are then polished down using progressively smaller grain sandpaper (200, 400, and 1000 grit) and polishing papers (3 μm and 1 μm) until the magnets are shiny and the Crystalbond is smooth, as in Figure 2.17a. The resulting magnets are 200 μm thick as defined by the polishing tool. In addition to holding the magnets in place, the polished Crystalbond allows for a somewhat continuous and smooth physical surface for the MFM as the cantilever moves over the edge of the sample or as it approaches the sample with each pass. The slide, if it contains NdFeB magnets especially, can then be coated in 100 nm Ni using a Kurt J. Lesker PVD75

Sputterer to prevent normal oxidation, as shown in Figure 2.17b where the nickel has cracked over time; the straight line of the semicircle is a laser machined edge of the circular NdFeB magnet. The magnets that are to be magnetized post laser machining are magnetized at this time. Again, a high field strength superconducting magnet is preferred for this process. The resulting magnets can then be scanned in the MFM and analyzed.

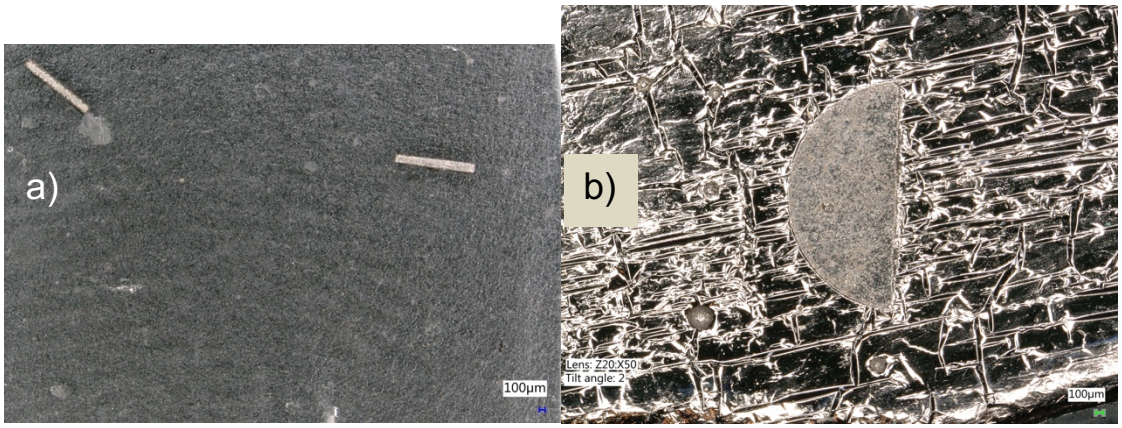

Figure 2.17 Photograph of glass slide with polished magnets embedded in Crystalbond a) without and b) with a nickel coating for protection

The procedure for acquiring Atomic Force Microscopy (AFM) images, with MFM as the end objective, begins by inserting the MFM tip in the tip holder and attaching the tip holder to the piezoelectric drive mount. The laser that measures the deflection of the AFM tips must then be aligned to the center of the camera sensor. The alignment here is critical as this is where all measurement takes place; if the tip moves in any way, this alignment must be repeated. The probe is then excited in air as a free cantilever over a range of frequencies to try to find the operating frequency of the probe (varies probe to probe as this resonance depends on cantilever dimensions and materials) and sets the

appropriate amplitude of vibration at the determined frequency. The probe must also be calibrated in contact mode under a varying force. This calibrates the variation of voltage on the laser camera sensor to the amount of cantilever deflection. For MFM the software is then switched back to a lift-interleave mode to measure both physical and magnetic profiles of the material.

Magnetic Force Microscopy images are acquired in two steps. First, a normal AFM image is obtained in tapping mode and used as a reference for the MFM. Second, the tip is raised by one to two hundred nanometers, and a second pass is made. This time, instead of measuring physical height and phase characteristics, the piezoelectric tip holder adjusts the tip height to match the physical offset from the previous scan line and the magnetic forces are measured. Figure 2.18 shows a schematic of this process, where tapping mode is the physical measurement and lift mode is the magnetic measurement. The lift mode height used for most MFM images used in this dissertation was 175 nm. This pattern is repeated until an entire image forms, no larger than 90 μm on a side, in the case of the Bruker Icon AFM used here, an example of which is shown in Figure 2.19 (many of the raw MFM images are listed in Appendix E). Additional images, offset away from the magnet edge by 60 μm, were scanned and combined to reach larger distances from the physical edge, as necessary. The output MFM file can give eight channels of data, but the most important channels for this study are the AFM height sensor, AFM amplitude error, MFM amplitude, and MFM tapping mode deflection. These images are then processed to obtain the distance information necessary to understand how far from the physical edge the magnetic edge is located.

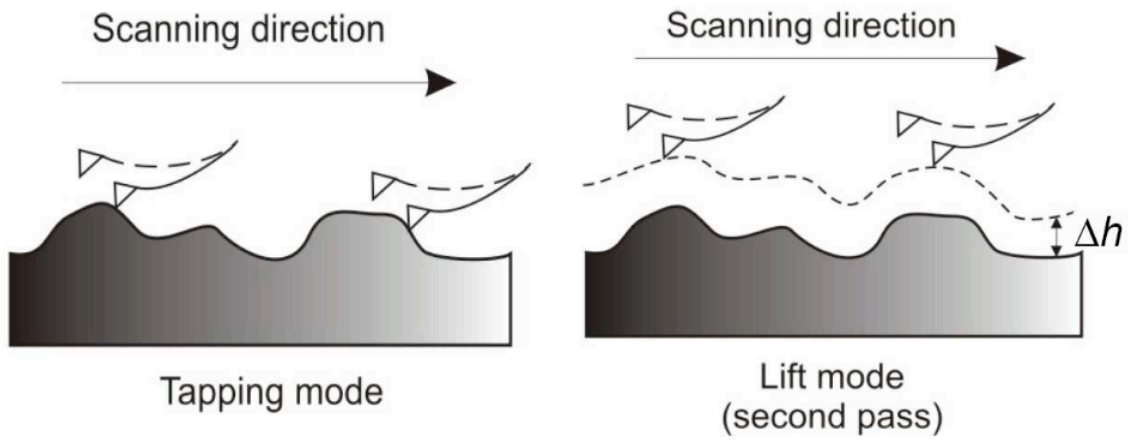

Figure 2.18 Schematic of MFM process

A significant amount of information can be gathered from the set of output images in Figure 2.19. From the Amplitude image on the top left and the cross section of that same image as a profile on the top right (the white lines across the top left image represent the profiles in the top right), it is possible to see how the force on the MFM tip is greatest at the magnetic edge of this magnet as was shown from the comparison model from Figure 2.13. The Amplitude image is a representation of the amplitude of the vertically oscillating tip. As the tip is under the influence of greater force near the edge of a magnet, the tip oscillates with a lower amplitude (as compared to the free amplitude during calibration). The lower right profile is called a Tapping Mode Deflection in the lift mode (magnetic) and is taken along the same profile lines as in the top images. Tapping-mode deflection (TMDef) represents the position around which the tip is oscillating. Both the MFM Amplitude and TMDef can be measures used here to calculate the magnetic edge of the material, using the minimum value in the profile. The physical edge is found in Amplitude Error images, similar to that in the bottom left, by locating where the material roughness changes from a characteristically magnet roughness to

Crystalbond roughness. The difference in microns is the magnetic to physical edge separation.

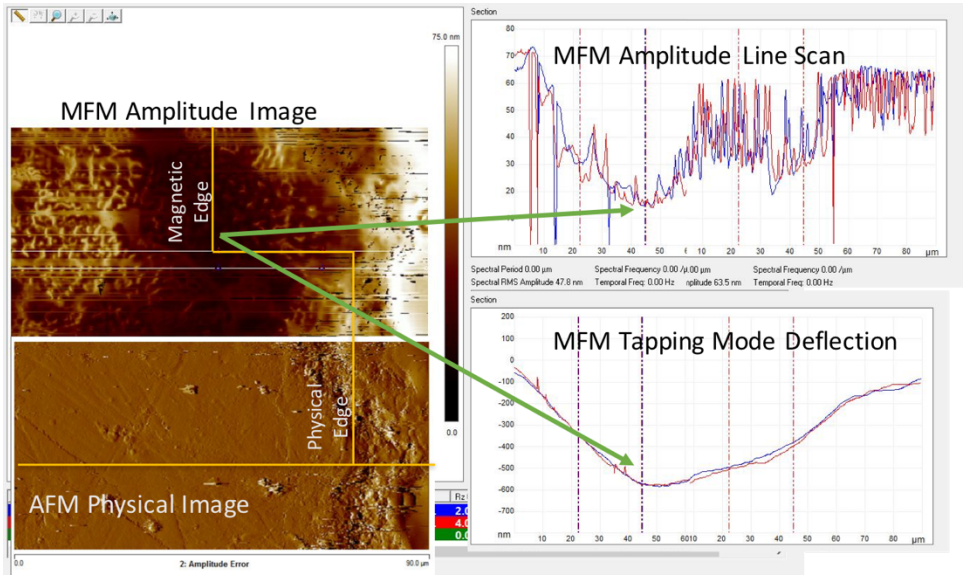

Figure 2.19 MFM Image showing (top left, top right, and bottom right) magnetic edge and (bottom left) physical edge

2.4.2 MFM Results and Discussion

From the MFM images, gathered from both magnets magnetized then machined and those magnetized post-machining, both qualitative and quantitative information regarding the physical edge and what is defined here as the magnetic edge, or minimum MFM amplitude and tapping mode deflection, can be obtained. Figure 2.20 shows the TMDef profiles for both magnetic materials (NdFeB and SmCo), laser machined by three different lasers (Y – IR/QCW/YLR, E – Excimer, G - Green), where the magnets were either machined while magnetized (NdFeB and SmCo) or magnetized post-machining (NdFeBM and SmCoM). As can be seen in Table 2.3, the average distance between the

physical edge and the magnetic edge is recorded. Of note is the lack of magnetic properties for the NdFeB magnet laser machined on the green laser. The quality recorded in this table indicates the magnetic strength of the magnet. For this qualitative measurement, a soft ferromagnetic material was placed next to the magnet to categorize the force on the material produced by the magnet. In general, as expected, the magnet strength increased after remagnetization. Indeed, whenever possible, the magnets should be magnetized after the machining takes place.

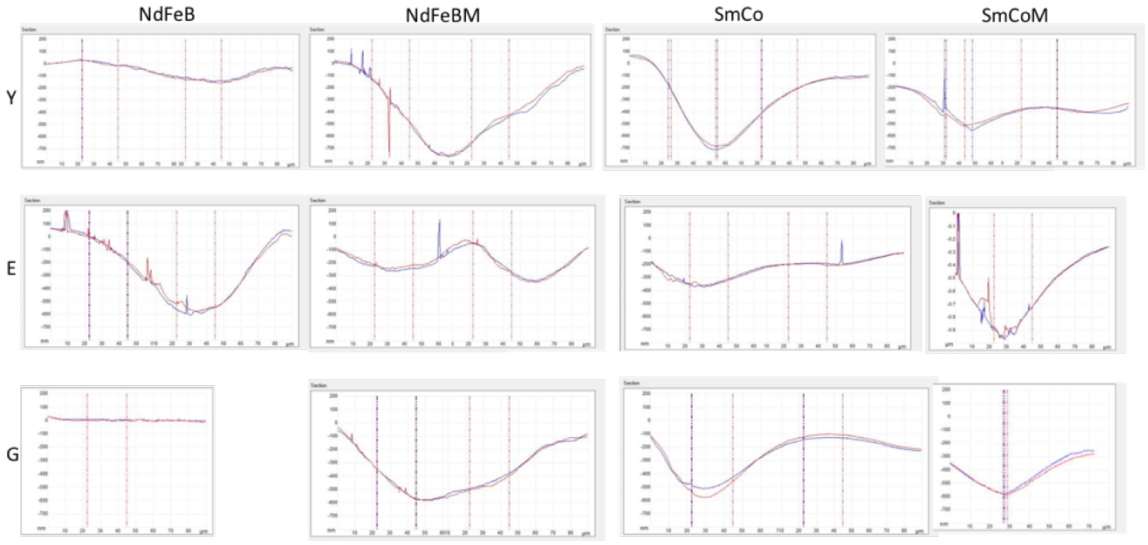

Figure 2.20 The TMDef profile for the magnets separated by laser type, magnet material, and magnetized prior to or post-machining

Table 2.3 The separation distance in μm between physical and magnetic edges of the magnets and the relative strength of the magnets separated by laser type, magnet material, and whether remagnetized post-machining

	DISTANCE BETWEEN MAGNETIC EDGE AND PHYSICAL EDGE			
Laser	NdFeB	NdFeB Remag	SmCo	SmCo Remag
QCW	50 μm	30 μm	25 μm	16 μm
Excimer	60 μm	30 μm	Negligible (~0-2 μm)	Negligible
Green	N/A	30-40 μm	7 μm	Negligible
	STRENGTH OF MAGNETIC FORCE ON NEARBY SOFT FERROMAGNETIC MATERIAL			
QCW	Weak near laser edge	Medium	Strong	Medium
Excimer	Medium near laser edge	Strong	Medium	Strong
Green	None	Weak near laser edge	Strong	Strong

There are several things to note from the numbers in this table. First, the distance between physical and magnetic edges is always reduced upon magnetizing after laser machining, no matter the laser or material. This was expected but a good confirmation of expectations. Second, the magnetized NdFeB column has almost the same separation distance of 30 μm for all three lasers. This likely indicates that the material nearest the laser machined edge is damaged or modified in some fashion so as to render the thin volume of material magnetically inert. Appendix C contains the phase diagrams for both magnetic materials and it is possible that either the NdFeB material is oxidizing with the high heat (it is a high-concentration iron material and iron readily oxidizes), or a new phase of material is created such that the physical grain boundary properties are different (thicker, changed composition, etc.) from the original sintered magnet. The exact mechanism of this damaged material is not yet known and requires further investigation. Third, the green laser entirely demagnetizes the NdFeB, but after magnetization the NdFeB returns to the same state as those magnets machined by the

other lasers and magnetized. Fourth, the shapes of the deflection curves seem fairly consistent for the SmCo pieces, and for the magnetized SmCo pieces, but the magnetized pieces seem to have a sharper minimum. This could indicate a sharper magnetic edge, or less gradual transition from magnetically poor material to functional material. The NdFeB curves vary significantly and have either a wide minimum or multiple minima. Lastly, there appears to be close to no separation between the physical and magnetic edge for the post-magnetized SmCo when using either the excimer or the green laser, while the QCW laser leaves a 16 μm separation distance, which is consistent with the results in section 2.2.3 from VSM measurements.

It can be inferred that if a premagnetized NdFeB magnet is to be machined, the excimer laser seems to be the best laser choice. If, however, the NdFeB is going to be magnetized post-machining, either laser seems adequate. In any case, with the NdFeB magnets, the significant HAZ must be taken into account during the designing stages. Section 2.6 details how a design such as this could be adjusted to account for the magnetic to physical edge separation.

For SmCo, the excimer laser appears to be the best choice when laser machining a premagnetized magnet (i.e. when pre-embedded in a system), although the green laser seems adequate as well with a small HAZ. When laser machining a magnet that is to be magnetized post-machining (the ideal case), both the excimer and green lasers are a good choice with negligible HAZ, although the green laser is faster for the lasers studied in this dissertation. Even the QCW laser machines SmCo to an adequate degree, and is better than any laser included in these studies machining NdFeB, when comparing the HAZ.

Figure 2.21 shows a graphical representation of the data in Table 2.3. The edge difference numbers are plotted as a function of laser peak power in Watts or peak power intensity in W/mm^2, which is the peak power divided by the size of the laser spot. Interestingly, as the peak power increases, the edge difference decreases for SmCo (for both premagnetized and magnetized post-machining). The same is true for peak power intensity as well. Also interesting is that as peak power intensity increases, the premagnetized NdFeB edge difference increases. The green laser NdFeB point is missing from the charts because no magnetic properties could be detected.

Figure 2.21c repeats Figure 2.11c from the laser model highlighting some of the numbers from Figure 2.21b. Interestingly, the melting temperature is reached 25-30 μm away from the laser edge for the QCW and Excimer lasers, and the Curie temperature is reached about 55-60 μm and 75-80 μm for the QCW and Excimer lasers, respectively. This correlates fairly well with the data points in Figure 2.21b for the NdFeB that is magnetized prior to and after machining. The green laser and SmCo do not appear to correlate quite as well, indicating another mechanism (i.e. not melting) could be present.

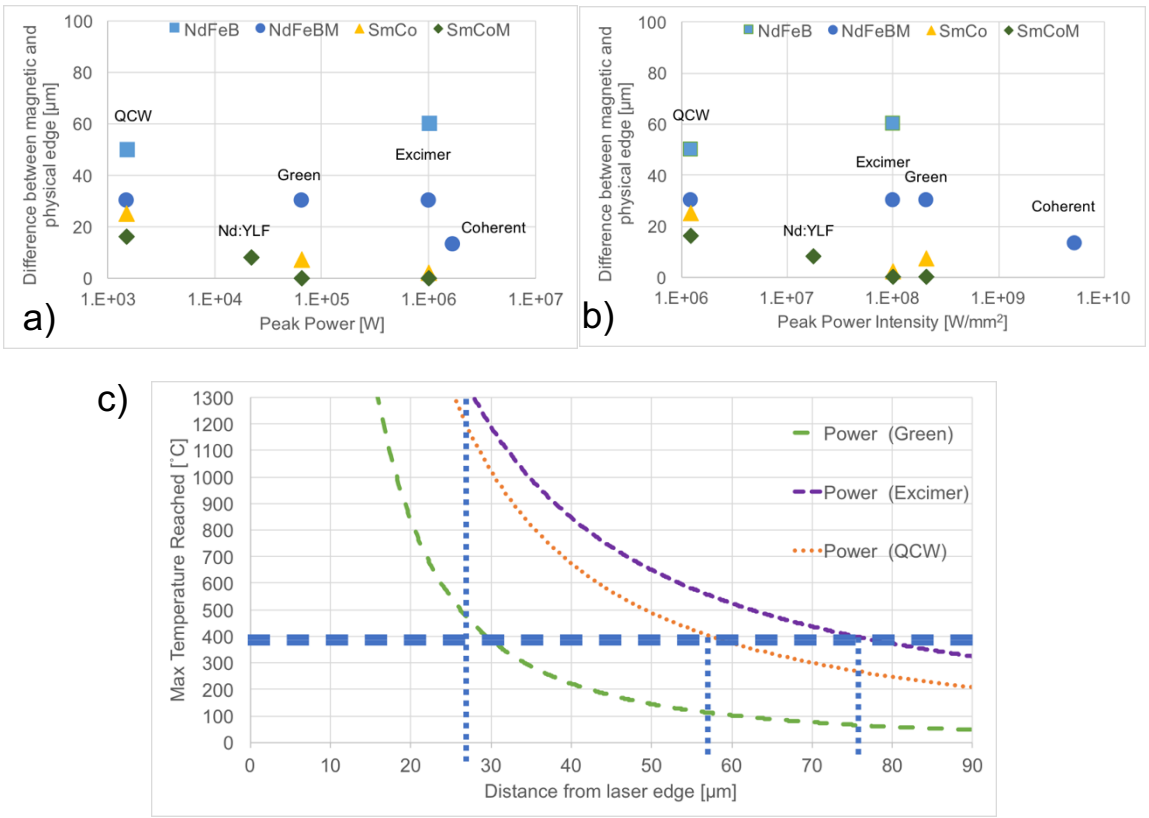

Figure 2.21 Charts showing the difference between magnetic and physical edges when laser machining after and prior to magnetization as a function of laser a) peak power and b) peak power intensity with laser type listed; c) Figure 2.11c is copied here with horizontal dashed line representing the Curie temperature of NdFeB, and the vertical dashed lines indicating the physical location where Curie or melting temperature is reached for the excimer and QCW lasers, according to the thermal model of section 2.3

The results of this MFM study confirm the initial impression that SmCo magnetic materials are a better magnetic choice than NdFeB when laser machining submillimeter scale magnets; again, this is likely due to the Curie temperatures of the respective

magnetic materials. Additionally, the study confirms that laser machining is an adequate magnet fabrication technology that allows for submillimeter scale magnets.

2.5 Additional Measurement of NdFeB Magnet Edge

Energy-dispersive X-ray spectroscopy (EDS) was also used on these magnet samples to try to determine the cause of the irreversible loss in magnetization in the HAZ. Two of the possibilities, as mentioned in section 2.3, include oxidation and grain composition or structure changes. There is a significant amount of information in the scientific literature on NdFeB grain composition [70], grain structure [66] [70], heat oxidation effects [71], and even rapid quenching of NdFeB magnets [67]. Figure 2.22 shows an example EDS image and line scan for a typical NdFeB magnet after oxidation in an oven [71]. Note how there is a visible step in the oxygen (e) and iron (c) content images, and especially in the line scan chart (b). The magnet here was placed in an oven at 410 ˚C for 3 days. This set of images clearly shows oxidation in the SEM backscatter image (darker material), and in the line scan (step height difference for iron and oxygen) and iron and oxygen content maps (brighter for oxygen map and darker for iron map). The same imaging technique was used on the laser machined NdFeB. SmCo was not included in this study because of the minimal HAZ created with the green and excimer lasers. Further study of SmCo is warranted to determine the cause of the HAZ in IR laser machined SmCo, but NdFeB was used here because the HAZ was fairly consistent no matter the laser used.

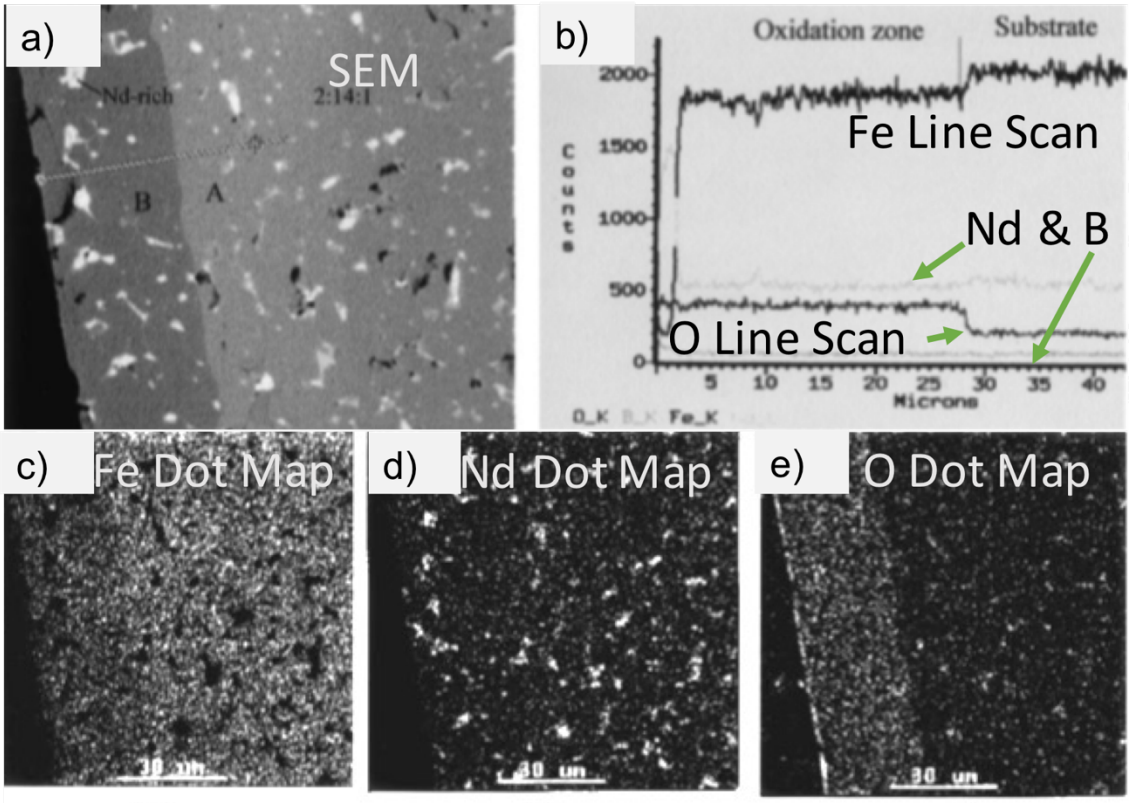

Figure 2.22 a) Scanning electron micrograph of a polished, oxidized NdFeB magnet baked at 410 ˚C for 3 days and EDS b) line scan and maps of c) iron, d) neodymium, and e) oxygen content for the same image

Different samples of NdFeB were imaged in the SEM and EDS was utilized to measure composition content of the sample and the results are shown in Figures 2.23, 2.25, and 2.26. In these figures, a) is the SEM image (an edge with crystal bond is shown in each and the brighter spots within the material are Nd-rich regions), b) is the Fe content image, c) is the oxygen content image, d) is the Nd content image, and e) is either a line scan or a Ni content image. Figure 2.23 is a set of images of a laser machined NdFeB ring. The ring was dipped in an ultrasonic bath, but otherwise untouched. Note how the

oxygen content, in either the EDS image or line scan, stays low over the entire surface of the magnet. Neodymium rich regions, marked in the figure, are normal as part of the fabrication process of NdFeB magnets as was shown in the previous figure.

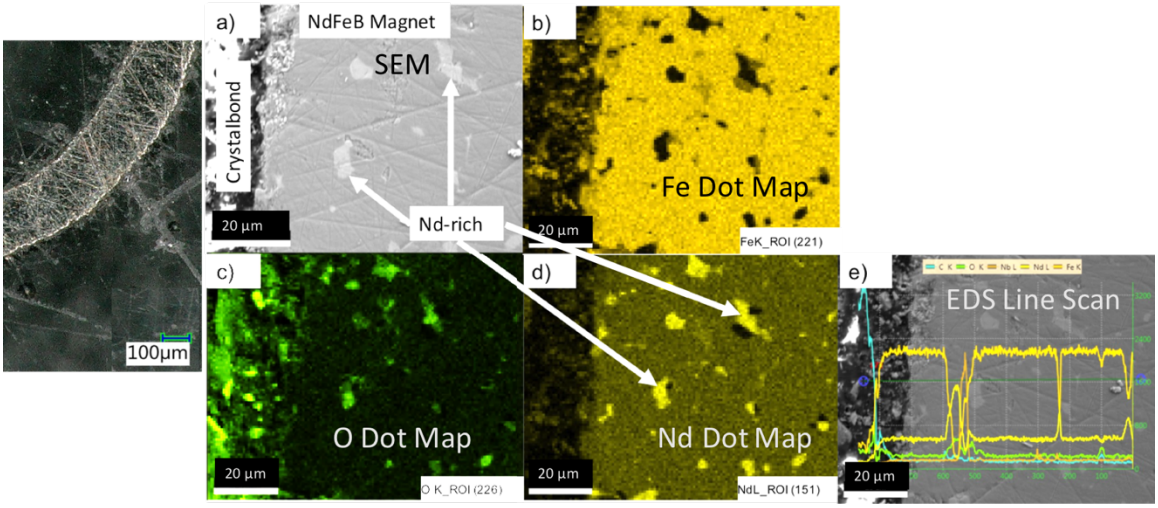

Figure 2.23 a) Scanning electron micrograph of a polished, laser machined NdFeB ring and EDS composition content images of b) Fe, c) O, and d) Nd with a e) line scan of the same

Due to the lack of a high oxygen content within the region of irreversible magnetization (25-30 µm for laser machined surface), additional theories were investigated. The authors that investigated the rapid quenching of heated magnets found that the magnetic properties of the magnet diminished as a function of heated temperature, as shown in Figure 2.24, due to microcracking within the material [67]. A fit line is drawn over the figure from this paper to illustrate how the trend might continue if the temperature were increased to laser machining temperatures. One particularly important aspect of this paper notes how after an anneal step at 650 ˚C for one hour, the magnetic properties of the material return to the previous state of full magnetization.

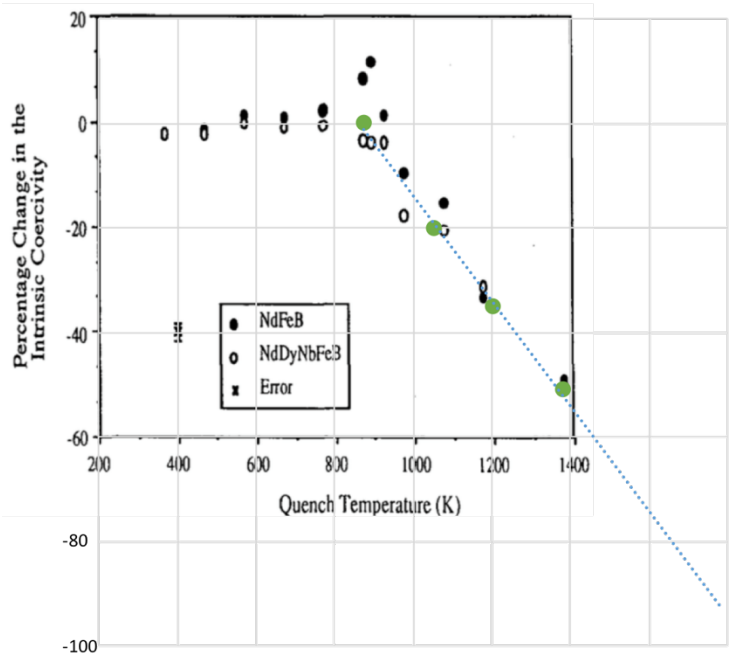

Figure 2.24 Chart showing the effect of quenching a magnet from a specific temperature with an extrapolation fit line to laser machining temperatures

An experiment was performed to determine whether annealing could restore magnetic functionality to laser machined micromagnets. The laser machined magnets were coated in a 1–μm–thick Ni coating and placed in an oven with a bulk, as-purchased NdFeB magnet at 650 ˚C for one hour, followed by a magnetization step. The bulk magnet was used to confirm that the magnetic properties were not being destroyed. Figure 2.25 is a set of images of the bulk, as-purchased, NdFeB disc that was placed in the oven. Again note how the oxygen content, shown in 2.25c stays low across the magnet material, due to the 10–μm–thick Ni-Cu-Ni coating shown in 2.25e. Figure 2.26 is a set of images of a laser machined NdFeB ring that was placed in the oven at 650 ˚C for one hour, again followed by a magnetization step. Note how there is a noticeable increase in the oxygen

content near the laser machined edge of the magnet, and a crack is clearly visible (similarly oxidized). Additionally, almost all magnetic properties of this ring were destroyed. While this shows that the nickel coating was likely insufficient to prevent oxidation, and the anneal step in this case failed, the most relevant result for this dissertation is the confirmation that laser machining is not oxidizing the NdFeB since the oven clearly oxidizes the samples over a significant portion of material.

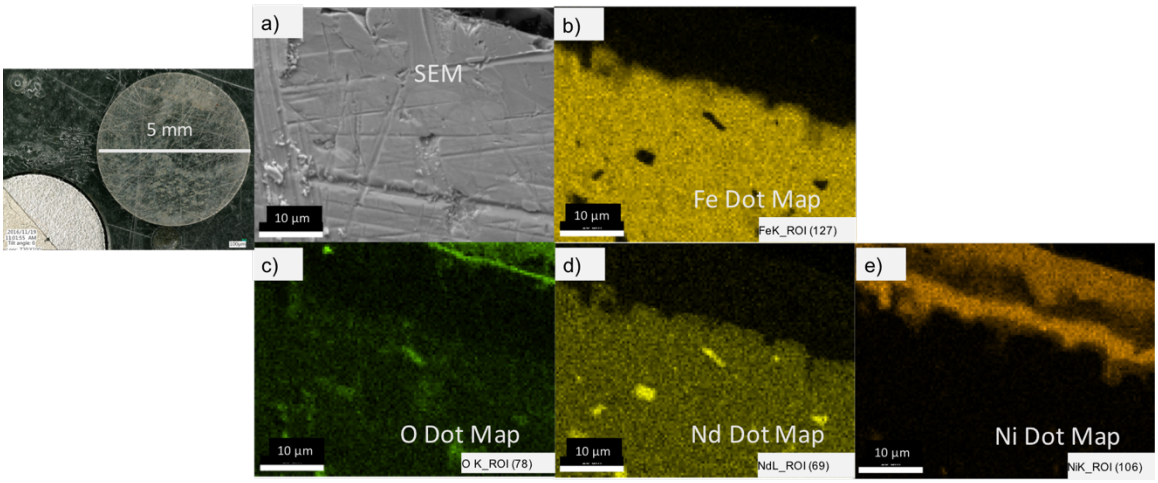

Figure 2.25 a) Scanning electron micrograph of a polished, bulk, as-purchased NdFeB disc (left) and EDS composition content images of b) Fe, c) O, d) Nd and e) Ni of the same

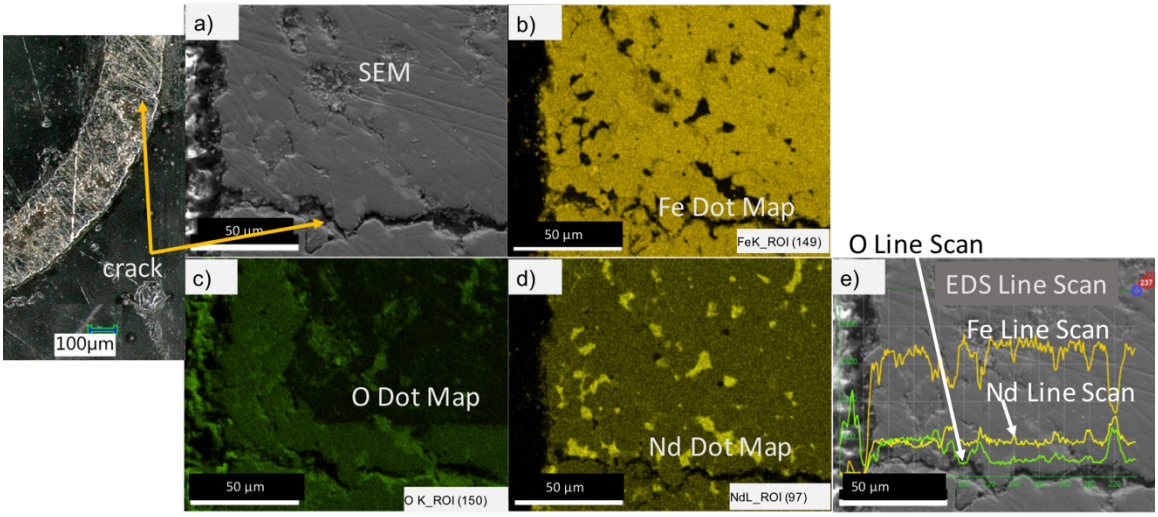

Figure 2.26 a) Scanning electron micrograph of a polished, laser machined NdFeB ring (left) that was placed in an oven at 650 ˚C and EDS composition content images of b) Fe, c) O, and d) Nd with a e) line scan of the same

The source of the irreversible loss in magnetization is still not known and warrants further study, along with the SmCo loss in magnetization, but could be associated, at this point, with a change in the grain structure. The likely options are microcracks near the laser machined surface due to the severe temperature gradients and partial melting due to the high temperatures involved with laser machining.

2.6 Laser Micromachining Process Adjusted for HAZ

In order to attempt adjusting the design for the size of the HAZ, ring magnets were laser machined of a physically desired size and the corresponding magnetically desired size. The designed magnetic dimension for this investigation was a 125 µm wide ring with a center radius of 1 mm. A laser machined ring is shown in Figure 2.27; the NdFeB thickness is 500 µm. NdFeB was used here due to the significant HAZ resulting from

laser machining, but the same can be done for SmCo depending on the laser used. The ring magnet in this image is sitting on polyimide tape and both were covered in 1 μm of sputtered nickel for protection purposes, resulting in the highly reflective surface.

Figure 2.27 Photograph of nickel coated NdFeB ring magnet of width 125 μm with a ring radius of 1 mm

With a HAZ of 25 μm – 30 μm, the physical width of the ring needs to be increased by 50 μm – 60 μm to allow for the magnetic size to be the desired width. For the example of the desired dimension mentioned, with a 125 μm wide magnetic ring, a 185 μm wide ring must be physically machined and magnetized. This will result in approximately 125 μm of usable magnetic ring. MFM scan images across the width of the HAZ adjusted magnetic ring are shown in Figure 2.28. The MFM amplitude scan showing physical edge is on top, with the TMDef image directly below it. At the bottom are TMDef line scans from multiple scan images, joined together to see the full ring width. The magnetic

width, defined in this dissertation as the width between TMDef minima, is approximately 125 μm and the HAZ is highlighted with dimensional measurements.

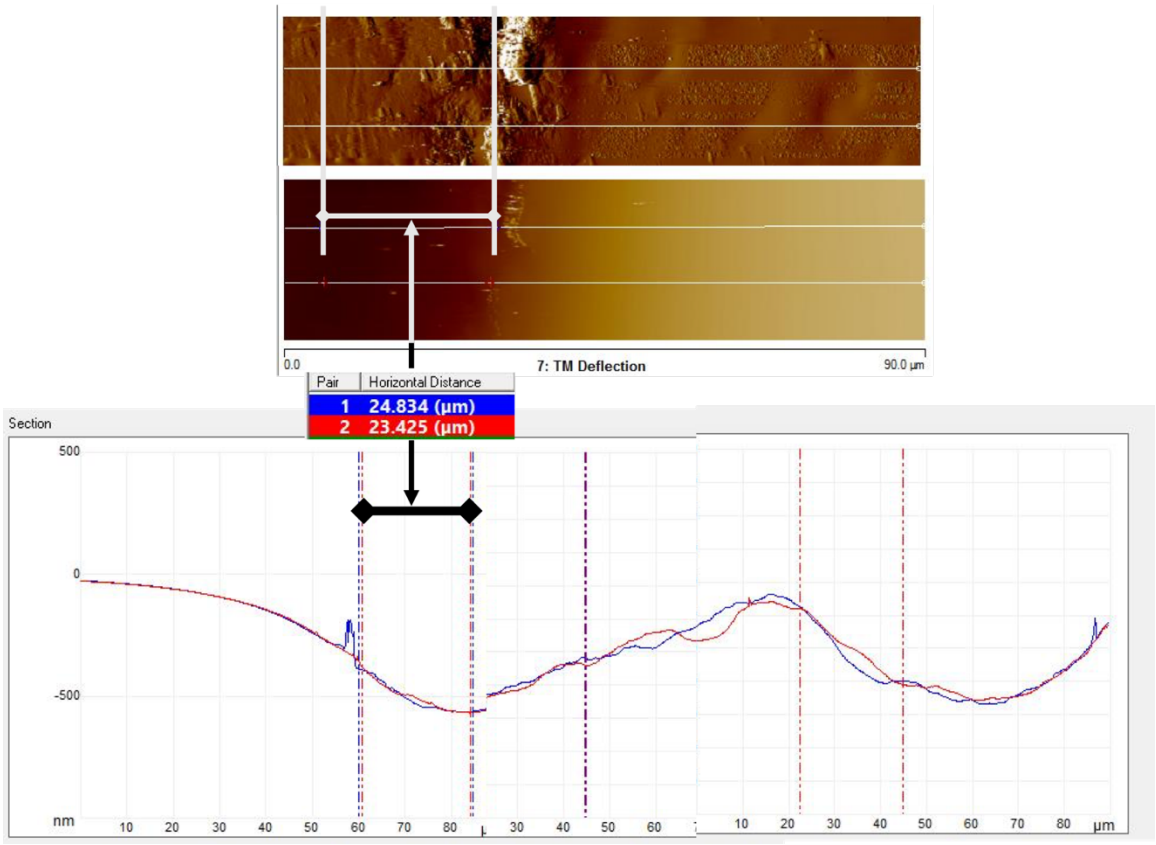

Figure 2.28 MFM Scans showing (top) physical edge, (middle) TMDef for magnetic edge, and (bottom) joined TMDef line scans showing the full magnetic width of the ring as the distance between the minima

This chapter has demonstrated that laser micromachining of magnetic materials is possible and can produce magnets with dimensions on the submillimeter scale. The heat affected zone associated with laser machining can be measured and the dimensions incorporated into magnetic system design. Thermal and magnetic modeling further

enable additional understanding of the effects of the loss of this magnetic material. The nature of the irreversible damage near the laser edge of these magnetic materials is still not known and requires further investigation. However, possibilities for this irreversible damage include microcracking, grain size modifications, and grain chemical composition changes.

CHAPTER 3 PERMANENT MAGNET MICROUNDULATORS

This portion of dissertation research was funded by the United States Department of Defense, DARPA Advanced X-Ray integrated Sources (AXiS) Program under Grant N66001-11-1-4198 and includes information from publications at PowerMEMS 2012 [72] and in Physics Procédia [8], along with additional unpublished material. The goal of this grant was to create a high brightness x-ray source that could fit on a table. In this work, the feasibility of using spatially alternating magnetic field distributions on the submillimeter scale for x-ray generation from electron beams was explored.

3.1 Undulator Background

Electromagnetic (EM) radiation can be generated by accelerating a charged particle or a magnetic dipole. This is feasible whether an electron is in the conductor of an antenna or in vacuum. The force that acts on an electron is called the Lorentz Force and is given by the equation:

$$\vec{F} = q\left(\vec{E} + \vec{v} \times \vec{B}\right), \tag{3.1}$$

where q is the charge of the particle, $\vec{E}$ is the electric field, $\vec{v}$ is the velocity of the charged particle, and $\vec{B}$ is the magnetic field through which the charged particle is passing. Note how a stationary charged particle can only be accelerated by an electric field, whereas a moving particle can additionally be accelerated by a magnetic field if the magnetic field is perpendicular to its direction of travel. For non-radiative use, cathode ray tube televisions or computer monitors and electron beam evaporators utilize this same magnetic force. The background material presented here on synchrotron radiation, insertion devices, and undulators comes from “The Science and Technology of

Undulators and Wigglers” by J. Clarke [38], “Soft X-Rays and Extreme Ultraviolet Radiation: Principles and Applications” by D. Attwood [73], “Wiggler and Undulator Magnets - A Review” by G. Brown, et. al [74], and course notes for a class at University of California - Berkeley titled “Synchrotron Radiation for Materials Science Applications” [75]. Additionally, this work was completed in collaboration with Dr. David Arnold and Dr. Alexandra Garraud of University of Florida and their team.

In the case of an antenna, an oscillating voltage or electric field is what drives electron motion. However, if electrons are moving freely, likely in a vacuum or some other relatively long mean-free-path medium, and pass through a transversely oriented magnetic field, the electrons will move perpendicular to the magnetic field and the direction of travel due to the magnetic portion of the Lorentz force equation (3.1). This is the underlying premise of radiative electron motion within a magnetic field. Figure 3.1 shows an example of such movement within a bending magnet and the resulting EM radiation profile.

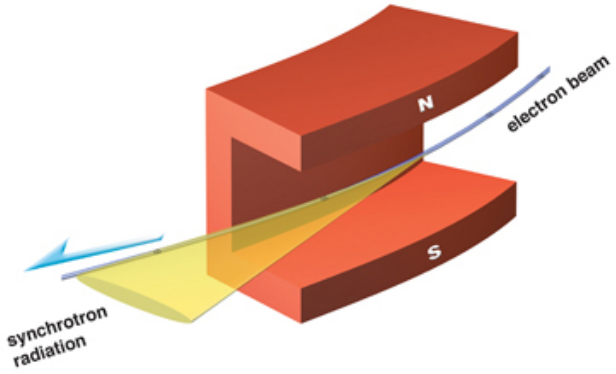

http://www.nsrrc.org.tw/english/img/about/c-lightsource-3-l.jpg

Figure 3.1 Schematic showing a bending magnet that also highlights the path of an electron beam within the bending magnet and the EM radiation profile emitted

A horizontally stationary, vertically oscillating charge, such as that in an antenna, will emit omnidirectional radiation in a doughnut pattern, as shown in Figure 3.2. This pattern remains true for a moving charge if viewing from the frame of reference of the charged particle. Now, if that charge happens to be moving at relativistic velocities, and the stationary/laboratory frame of reference is used, the radiation is Doppler shifted, the output EM radiation frequency downstream from the electrons is up-converted (wavelength is down-converted) to a new value, and the output radiation is focused in the direction of electron travel. Figure 3.2 also shows how this EM radiation changes from being omnidirectional in the case of a horizontally stationary, vertically oscillating dipole to the highly directional case of a horizontally relativistic electron that continues to oscillate vertically. Note how the EM radiation is focused in front of the electron along its travel path. Realistically, the EM radiation is still omnidirectional (this can be verified by analyzing in the relativistic frame), but due to the relativistic velocity of the electron, to an observer at rest, the radiation frequencies change such that the relevant, bright, and coherent radiation is only in front. Additionally, along the orbit/oscillation plane, the output radiation is linearly polarized, as in dipole radiation [76]. Slightly off axis, the light becomes slightly elliptically polarized. This synchrotron radiation is the method by which hard and soft X-Rays, and deep UV, focused light sources are generated in particle storage rings and linear accelerators.

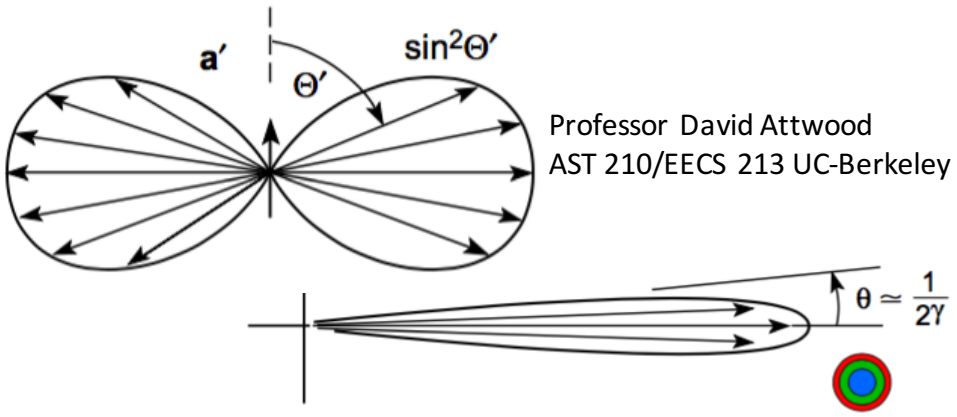

Figure 3.2 Schematic of EM radiation from stationary dipole vs. relativistic

The process of synchrotron radiation begins with an electron source that releases electrons in bunches into the vacuum of the beam line. The electron bunches are normally a Gaussian shape (physically in x, y, and z) and are accelerated to maximum beam energy (different for each facility) frequently using radio frequency excited electrodes located along the beam line. It is important to remember that the Gaussian shape of the electron beam acts similar to a laser beam envelope; it can be focused and defocused, but it will remain Gaussian. So, while a beam spot/bunch size may be specified, the wings of the Gaussian will extend beyond that bunch size.

Bending magnets are essentially a single magnet pole that bends the path of a relativistic electron bunch and generates EM radiation in this manner for high energy particle physics and associated experiments. Figure 3.3 shows a schematic indicating the magnetic arrangement of a bending magnet and the radiation pattern emitted from an electron as it passes through. If, instead, the electron is allowed to oscillate repeatedly within the field of multiple magnets arranged with sequentially alternating

poles (e.g. North-South-North-⋯), instead of bending around a single magnet pole, the result is wiggler or undulator radiation.

The only physical difference between an undulator and a wiggler is the period length of the magnetic field, and consequently the amount of deflection experienced by a relativistic electron. The undulator parameter, K, roughly defines what qualifies as either a wiggler or an undulator:

$$K \equiv \frac{eB_0\lambda_u}{2\pi mc} \cong 0.9337\, B_0[T]\, \lambda_u[cm], \tag{3.2}$$

where B_0 is the undulator sinusoidal magnetic field amplitude, e is the charge of an electron, m is the mass of an electron, c is the speed of light, and λ_u is the periodicity of the magnet array. When the magnetic field is sinusoidal:

$$K = \gamma\delta, \tag{3.3}$$

where 2δ is the angular excursion of the electron beam as it passes through the undulator/wiggler, and γ is the relativistic Lorentz factor

$$\gamma = \frac{1}{\sqrt{1-\frac{v^2}{c^2}}} = \frac{E_e}{E_0}. \tag{3.4}$$

where v is the electron velocity, E is the energy of the electron and E_0 is the rest energy of an electron. When $K < 1$, the device is an undulator, as 2δ is small.

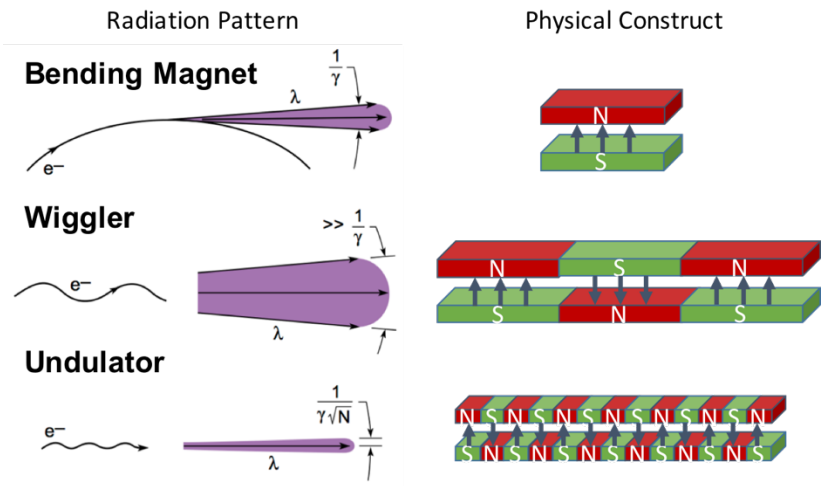

Figure 3.3 Schematic showing the electron path, radiation pattern, and physical magnet construct for the corresponding bending magnet, wiggler, and undulator

For a large number of periods, the alternating magnet array (undulator) spectrum is then given by:

$$\lambda_{rad} \cong \frac{\lambda_u}{2n\gamma^2}\left(1 + \frac{K^2}{2} + \gamma^2\theta^2\right) \quad n = 1,2,3,4 \ldots, \tag{3.5}$$

where n is the harmonic number, and the angle of observation

$$\theta = \frac{1}{\gamma\sqrt{N}}, \tag{3.6}$$

where N is the number of periods. Harmonics are generated as K increases due to the pulses of light observed as synchrotron radiation, as in the top of Figure 3.4b. A sinusoidal function contains a single (the first) harmonic, or one peak in frequency as in the lower half of Figure 3.4a. In order to generate a light pulse, instead of a sinusoid, multiple frequencies must be used that together form a pulse; each is associated with a

different harmonic number, n, as in eq. 3.2. For $K \ll 1$, only the fundamental frequency peak is of any importance. However, for $K = 1$, the power in the fundamental is maximized and additional harmonics begin to be significant. This is demonstrated for two K factors in Figure 3.4 where the electric field generated by the electrons is plotted as a function of time and the photon flux/intensity is plotted as a function of frequency [38]. Note how for $K \ll 1$ a single harmonic dominates the spectrum, but for $K > 1$, multiple harmonics are clearly visible. The electric field is only measurable at specific times due to the fact that the radiation cone flashes past the point of observation, for $K > 1$, at each oscillation (observable range is marked in Figure 3.4b with horizontal dotted lines). However, for the $K \ll 1$ case, in Figure 3.4a, the radiation cone is always present at the observation point and only a single harmonic is produced. For $K \gg 1$, the wavelength bandwidth of the fundamental becomes wider and additional harmonics are added until many closely spaced harmonics join to form the wiggler bandwidth profile shown in Figure 3.5 [38], where the wiggler radiation spectrum resembles that of a bending magnet.

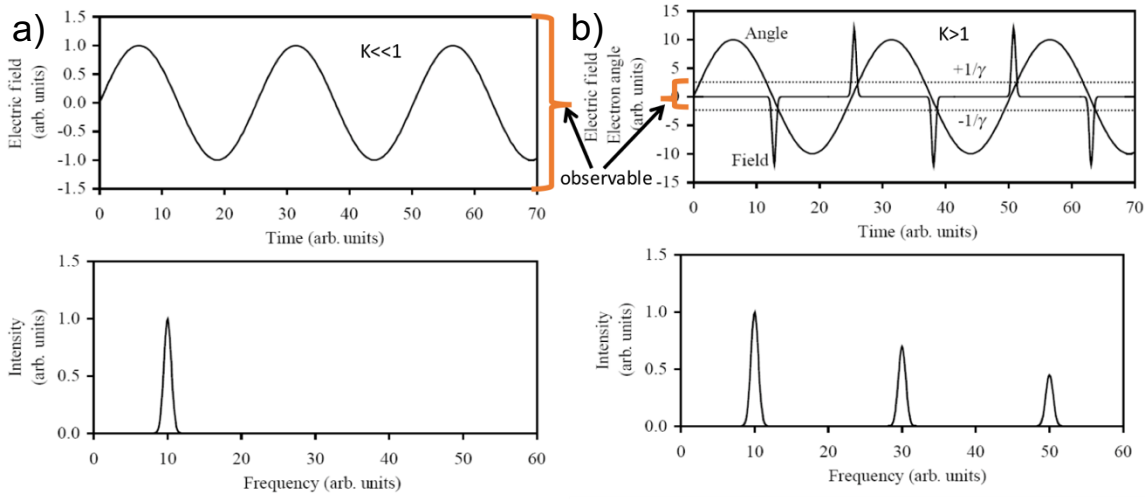

Figure 3.4 Charts showing angle of electron deflection and corresponding electric field, and the resulting photon intensity for a) an undulator with K<<1 and b) a wiggler with K>1

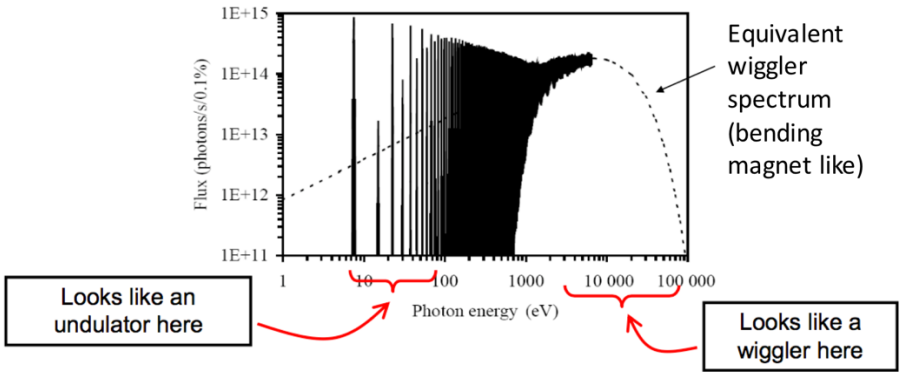

Figure 3.5 Chart showing an example wiggler photon flux as a function of energy

Bending magnets, wigglers, and undulators are classified as “insertion devices” placed in an electron beam path to generate a wide variety of EM radiation, normally in the deep UV, soft x-ray, and hard x-ray wavelengths. A plot showing example brightness levels as a function of output wavelengths is shown in Figure 3.6. Brightness is defined

as the number of photons per second in a specified small area within a small bandwidth and is dependent on beam parameters such as beam spot size and divergence. Note how the brightness for the undulator is multiple orders of magnitude higher than the bending magnet or wiggler. This is in large part due to the small deflection of the electron beam as it passes through the undulator and the focused EM radiation the electrons emit.

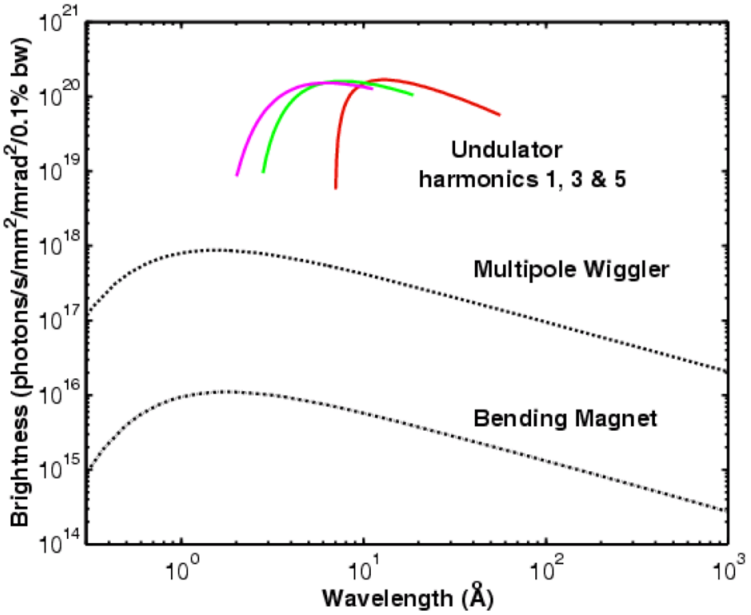

http://pd.chem.ucl.ac.uk/pdnn/inst2/insert.htm

Figure 3.6 Plot showing brightness as a function of wavelength, being emitted by bending magnets, wigglers, or undulators

Figure 3.7 shows an (a) example of a state of the art undulator with a periodicity of 7 cm and (b) how an undulator functions. Note that traditional undulators have periodicities on the order of at least several centimeters and tend to be meters long overall. Figure 3.8 shows the current state of the art for magnetic undulator sizes, input electron energy

sources, and output wavelengths and the space where this research was intended to fill. Note how there is an output hard x-ray (10-100 keV) range where the current state of the art cannot achieve. The undulator presented here is designed to achieve higher output radiation wavelengths using lower input electron energy accelerators.

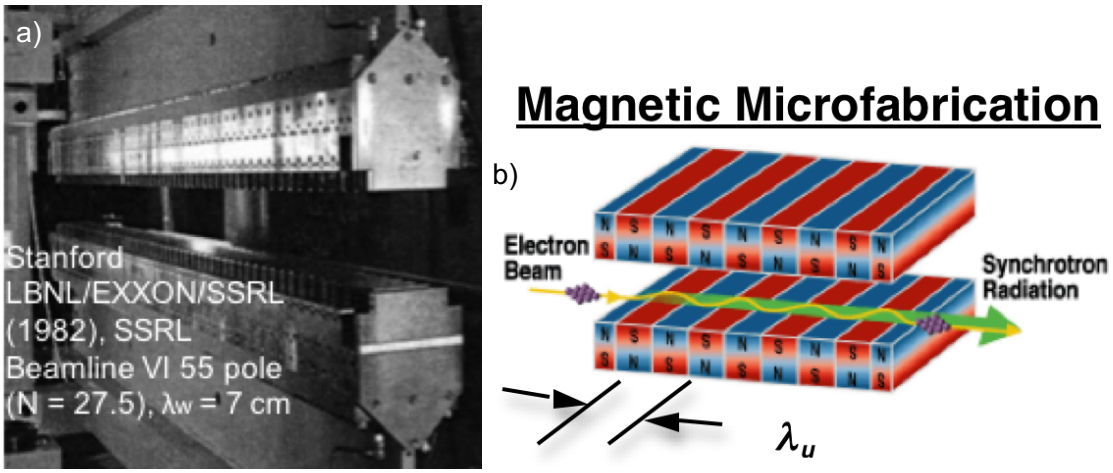

Figure 3.7 a) Photograph of a Stanford undulator with a 7 cm period and b) a schematic showing the function of an undulator

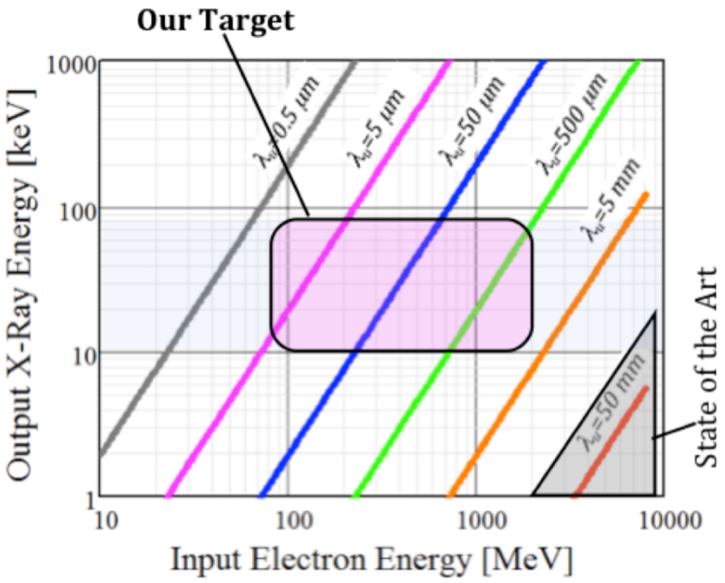

Figure 3.8 White-space chart showing the state of the art undulators in the bottom right corner and where the undulators funded by this grant would fit

The goal of this project was to create an undulator with a magnetic periodicity on the submillimeter scale. The undulator parameter in the case of a 400–μm–period undulator is:

$$K \cong 0.9337\, B_0[T]\, \lambda_u[cm] = 0.9337 \cdot 0.2[T] \cdot 0.04[cm] = 0.0074, \tag{3.7}$$

and the associated output radiation on axis would become

$$\lambda_{rad} \cong \frac{\lambda_u}{2\gamma^2}\left(1 + \frac{K^2}{2} + \gamma^2\theta^2\right) \cong \frac{\lambda_u}{2\gamma^2}, \tag{3.8}$$

where λ_{rad} would only depend on undulator period, λ_u, and input electron energy, γ. This essentially makes the output radiation a function of undulator period and the relativistic speed of the electron.

One additional form of radiation, similar to the oscillating electron described previously, is Bremsstrahlung radiation, sometimes called braking radiation. This is when an accelerated particle (an electron in this case) passes an atomic nucleus, is steered around the nucleus, and slows down as a result of the interaction, as shown in Figure 3.9. When passing through a material, there are many of these interactions that result in a broad range of accelerations (based on proximity to the nucleus), and thereby wavelengths emitted. This is an important effect to discuss for microundulators as the Gaussian electron bunch size is on the order of the gap between the magnet arrays. As such, the wings of the electron bunch (the electrons outside the defined Gaussian bunch size) could interact with the materials that make up the microundulator. Figure 3.10 shows a representative example of Bremsstrahlung radiation over different wavelength ranges.

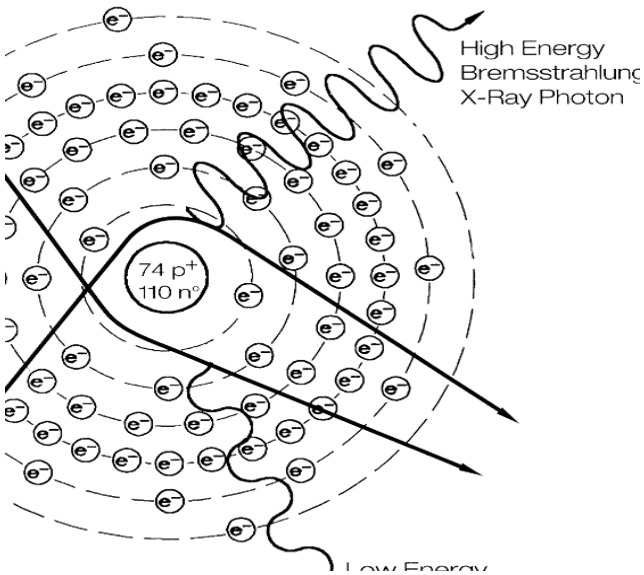

http://cmap.ucfilespace.uc.edu:8085/rid=1K1KWL86L-J2CKH7-457/1K1KQ5LSTIJ8VRQ6IC2Iimage

Figure 3.9 Schematic representation of Bremsstrahlung radiation show high and low energy photons emitted

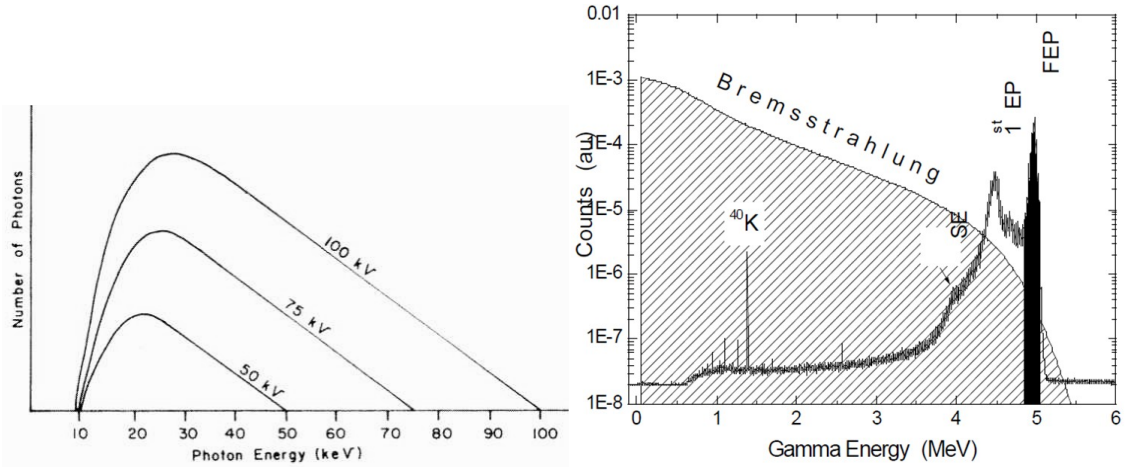

http://www.sprawls.org/ppmi2/XRAYPRO/, http://www.tunl.duke.edu/groups/nnsa/nrf.html

Figure 3.10 Charts representing Bremsstrahlung radiation from different energy input electrons

3.2 Modeling of Spatially Alternating Magnetic Field Structures

Many magnetic systems benefit from an alternating magnetic field pattern in practice, and this continues into the realm of MEMS. A PM array with high energy density and high magnetic flux density near the surface of the array is required. In order to find the best arrangement of magnets for creating a spatially sinusoidal magnetic field pattern (all fields here are temporally static, spatially varying), COMSOL Multiphysics was used to simulate various magnet arrangements and parameters.

3.2.1 Undulator Magnetic Field and Parametric Variation

The starting place for this research utilized a book section titled “Permanent Magnet-Based Design of Insertion Devices” in The Science and Technology of Undulators and Wigglers by J. Clarke [38]. Insertion devices are bending magnets, wigglers, undulators, quadrupoles, and similar devices inserted into a beam line for various reasons. Equation 1.10 comes from this book and defines analytically the magnetic field along the axis of an undulator (the center line between two arrays of magnets as in Figure 3.1). It is repeated here for convenience,

$$B = -B_r \cos\left(\frac{2\pi s}{\lambda_u}\right) \frac{\sin\left(\frac{\varepsilon\pi}{M}\right)}{\frac{\pi}{M}} e^{-2\pi g/\lambda_u} \left(1 - e^{-2\pi h/\lambda_u}\right), \tag{1.10}$$

where B_r is the remanence of the magnets used in the array, λ_u is the periodicity of the array, ε is the fill factor, M is the number of magnets per period, g is the gap between the magnets, h is the thickness/height of the magnets, and s is the horizontal position along the array. Equation 1.10 shows that a number of parameters can be varied without severely decreasing the sinusoidal amplitude of the magnetic field. Some initial design parameters were first chosen that might be achievable by a micromagnet fabrication

technology. Figure 3.11a shows a schematic of two stacked magnet arrays forming an undulator with the relevant physical parameters labeled between the magnets and the arrows inside the magnets representing the magnetization direction of individual magnets. Figure 3.11b shows a plot of undulator magnetic flux density along the center axis of the undulator. The fixed parameters include magnet thickness, h, of 200 μm; undulator gap or distance between magnet arrays, g, of 200 μm; undulator period, λ_u, of 400 μm; fill factor, ε, of 0.75 or 75%; and 2 magnets per period, M.

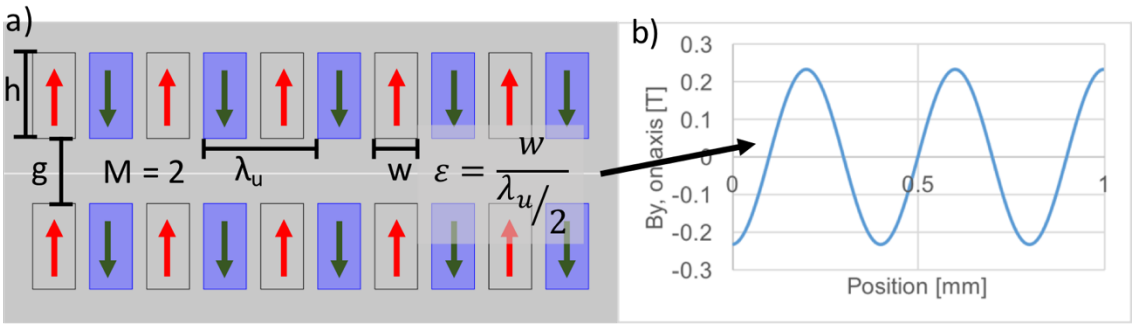

Figure 3.11 a) Schematic showing an undulator magnet array with labeled magnetization directions and physical dimensions and b) corresponding magnetic flux density along the axis of the undulator (shown as a white line in (a))

Figure 3.12 shows how the parameters from equation 1.10 can be manipulated to fit specifications of micromachining while maintaining close to ideal magnetic field amplitude. Figure 3.12a shows how the vertical magnetic flux density, B_y, varies as a function of gap. Figure 3.12b shows how B_y varies as a function of fill factor, as there is always going to be a space of some size between individual magnets. Figure 3.12c shows how B_y varies as a function of magnet thickness, again important due to the

polishing or trimming of the magnet thickness. Figure 3.12d shows how B_y varies as a function of undulator period, where undulator period is on the same order as the magnet thickness. Figure 3.12e shows how B_y varies as a function of the number of magnets per period rotating through 360˚, as was discussed in section 1.2.2 with eq. 1.10 and will be elaborated on more in this section. Note how the undulator period in Figure 3.12d can greatly influence the amplitude of field when choosing values between 0.2 mm and 1 mm for a gap and magnet thickness of 0.2 mm. For fill factor and magnet thickness it is convenient that not much change occurs above 75% fill factor or as long as the magnet thickness is greater than half the gap. Each of these plots is interconnected with the others, but each gives some variability such that fabrication constraints can be eased.

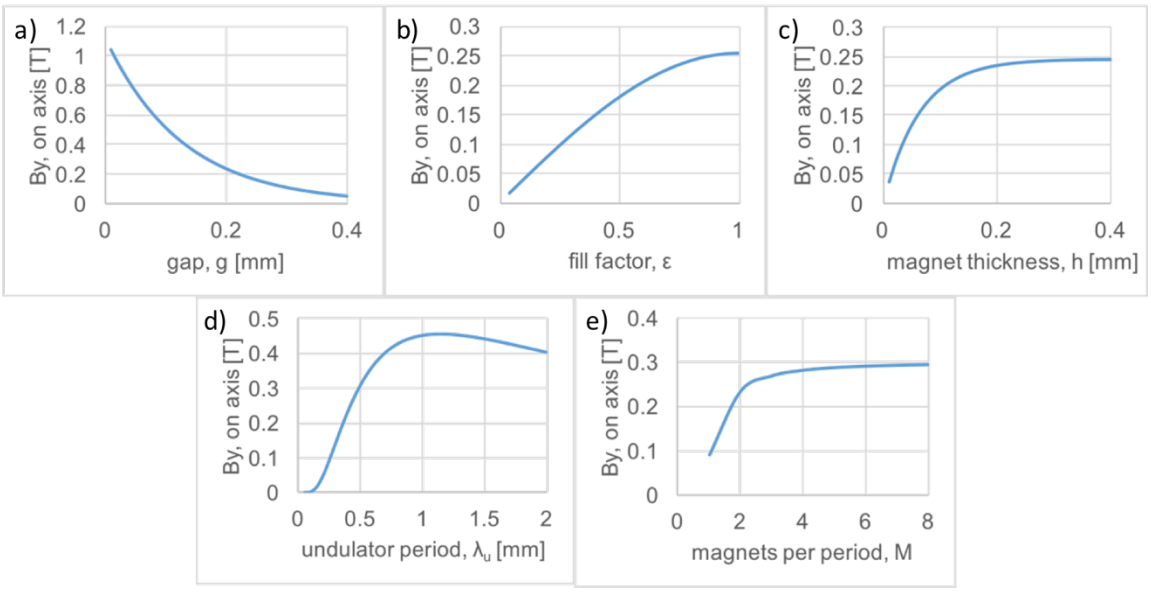

Figure 3.12 Charts showing the magnetic flux density sinusoidal amplitude as a function of a) gap, b) fill factor, c) magnet thickness, d) undulator period, and e) number of magnets per period, given other fixed parameters

3.2.2 Simulations Off-Axis and With Alternative Undulator Architectures

A series of COMSOL Multiphysics models were created that confirm the results of this analytical equation but additionally provided additional insight off center axis. Additionally, some models included several changes in the magnet structure. Figure 3.13 shows the magnetic flux density profile on axis and tens of microns off axis (parallel to x, offset in z+ in Figure 3.13a) for flux densities pointing in the z- and x-direction. The gap is 200 μm, the magnet thickness is 200 μm, and the period is 400 μm. Note the strong z-component sinusoidal field even while offset from the axis. Additionally, the x-component on axis is zero, whereas the off-axis component rises significantly when off axis by at least 20 μm. This indicates that maintaining the electron bunch passing through the undulator close to the center axis is important.

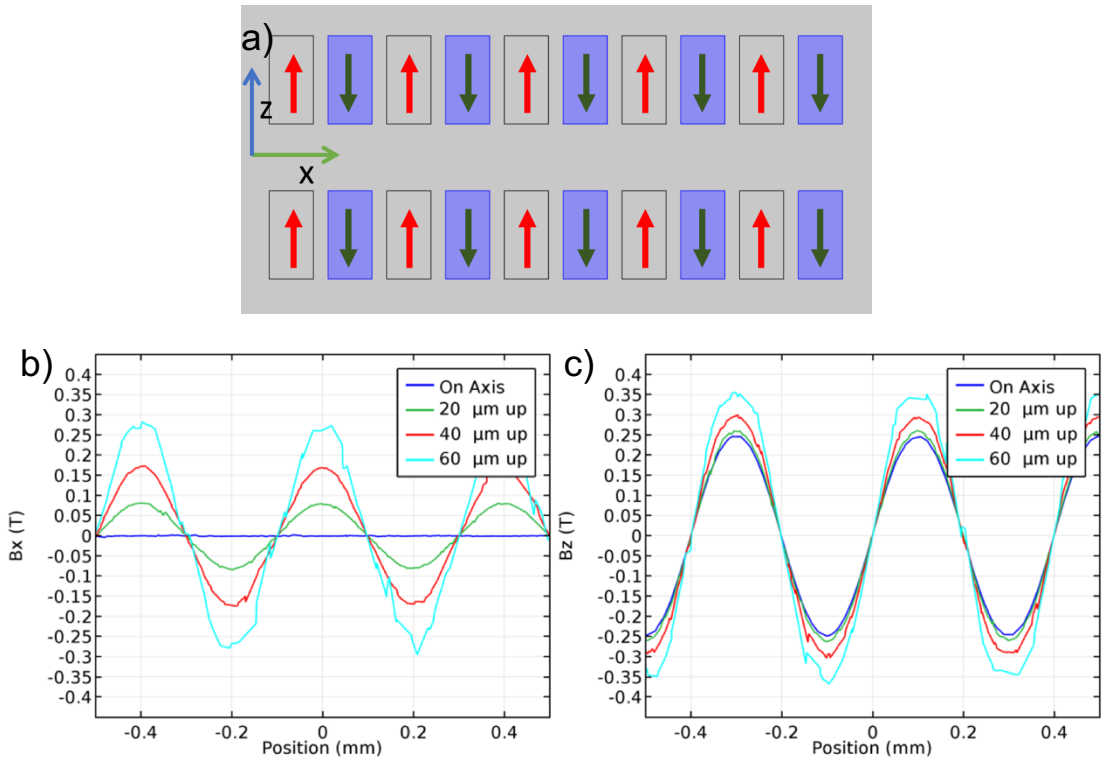

Figure 3.13 a) Schematic of undulator with coordinate axes labeled and corresponding b) x- and c) z-component magnetic flux density profiles

After becoming more familiar with undulators and how the magnetic fields present affect the path of travelling electron, it was discovered that utilizing a decreased width end magnet (the last magnets in the array) would allow for the electron path to remain near and oscillate around, the center axis. The effect of this end magnet width change can be seen in Figure 3.14 where the size of the end magnet in green is adjusted such that the initial peak in magnetic field is the same amplitude as every other peak, rather than approximately half the undulator amplitude, as in the case of a normal sized end magnet.

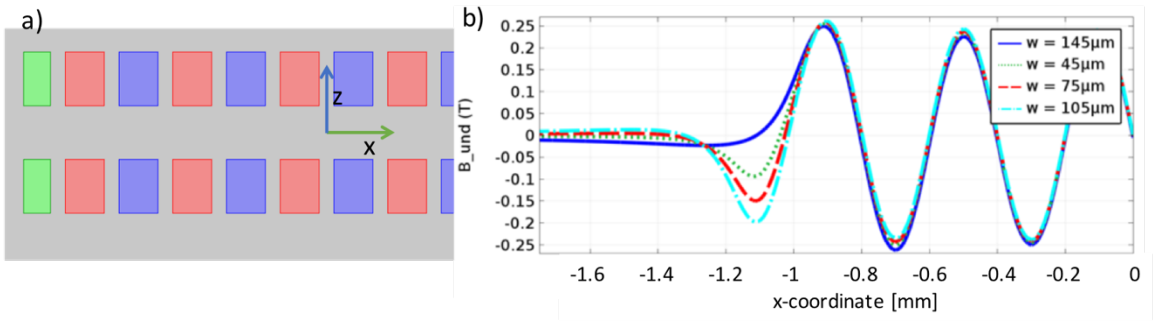

Figure 3.14 a) Schematic of undulator showing adjusted end magnet size and b) corresponding magnetic flux density with different end magnet widths

3.2.3 Halbach Array Simulations

Arrays of magnets where the magnetization rotates in direction through 360˚ have become known as Halbach arrays, whether they are cylindrical in shape as described in section 4.2 or linear as described here in this chapter [39]. Halbach arrays of more than two magnets per period can provide added field strength as the field from multiple magnets is superposed and the total field increases. When the number of magnets per period, M in Figure 3.11, is two, the result is this North/South/North/··· arrangement of magnets rotating through 0˚/180˚/0˚/···, or 90˚/270˚/90˚/···. Any number of magnets can theoretically be used, as long as the magnetizations rotate through a full rotation. However, as was shown in Figure 3.12e, for a linear array as with an undulator, there is little benefit to using more than 4 magnets per period (0˚/90˚/180˚/270˚/0˚ - N/Left/S/Right/N, etc.). Additionally, without using a complex setup of in-plane oriented magnets, three magnets per period would prove a challenge. Therefore, beyond two magnets per period, four magnets per period was the only other focus of this investigation.

Multiple versions of a four magnet per period structure were modeled. Figure 3.15a shows the comparison of these structures for a given magnet thickness of 0.2 mm (200 μm) as a function of period length or periodicity. The regular ideal array is as discussed in previous sections but with a fill factor of one, and the regular structure is with a lower fill factor. The Halbach ideal is the four magnet per period with fill factor of one and the Halbach structure is similarly the flux density the Halbach array would produce upon being laser machined due to the lower fill factor. Figure 3.15b shows the field profile as a cross-section. The color scale indicates vertical magnetizations and flux densities (negative down, positive up), and the grayscale indicates horizontal magnetizations (negative left, positive right) in the magnets between the vertical magnetizations. Similarly, Figure 3.15c shows the hybrid Halbach structure that utilizes in-plane magnetized magnets similar to that in the Halbach structure of Figure 3.15b except that the vertical pieces are actually magnetic irons (or soft ferromagnetic), and as such guide magnetic field to be vertical in those regions. Since the research here was investigating the fabrication of arrays with periodicity between 200 μm and 500 μm, the M = 2 and M = 4 were the only structures attempted, and the M = 4 was more used to test the fabrication capability using in-plane magnets between out-of-plane magnets. The design and fabrication of the physical arrays is described in the next sections. Note how the regular structure provides a higher field for periodicities below approximately 600 μm. This is partially due to the low fill factor where four magnets must fit in a period length and have a fixed amount of material lost between individual magnets.

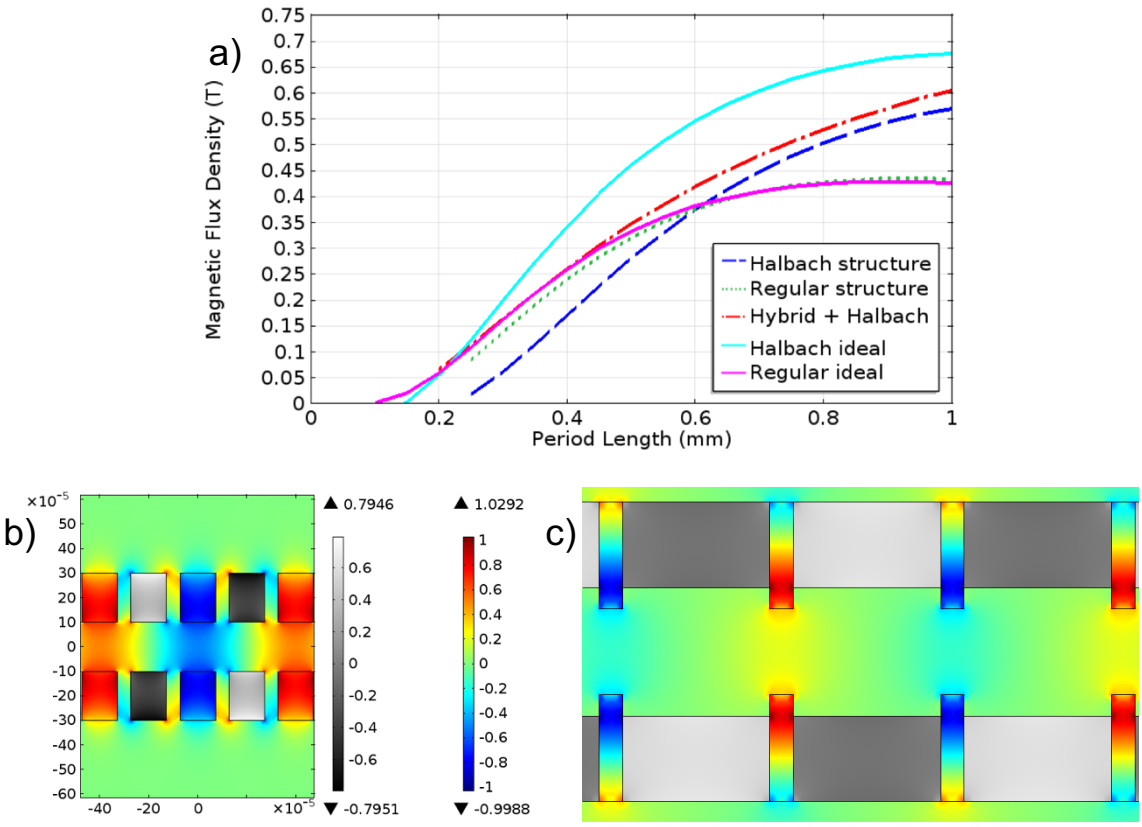

Figure 3.15 a) Chart comparing different undulator architectures and schematics of Halbach arrays of b) purely PM and c) a hybrid structure

3.3 Laser-Fabricated Sinusoidal Magnetic Field PM Array

3.3.1 Magnet Array Design

Once two-dimensional modeling had completed, and realizing that a sinusoidal array also requires a given consistent periodicity within the array, a structure that maintained the periodicity needed to be designed. Additionally, as the magnets used in this fabrication process start as 5 mm x 10 mm x 300 μm substrates from the manufacturer (Pacific Pac Technologies, see Appendix A), any array longer than 10 mm in size would need to be assembled in a manner that also maintains the same periodicity. The

proposed design is shown in Figure 3.16. The design of an alternating array of interdigitated combs provides the consistency in periodicity as desired along with the ability to assemble these combs into an array of any length, as desired. Note how the N-S-N-S-N pattern is maintained across comb boundaries. An array assembled in this manner also allows for many individual micromachined magnets, 2 mm x 150 μm x 300 μm, to be manipulated in relatively large numbers (20 at a time, in this case). Figure 3.17 shows how the same magnet combs can be assembled to provide for increased length arrays by offsetting the insertion of each subsequent comb until the desired length is achieved. Each additional comb piece added provides additional opportunities to break the brittle magnets, and care must be taken to prevent such a case, especially since they are assembled after already being magnetized.

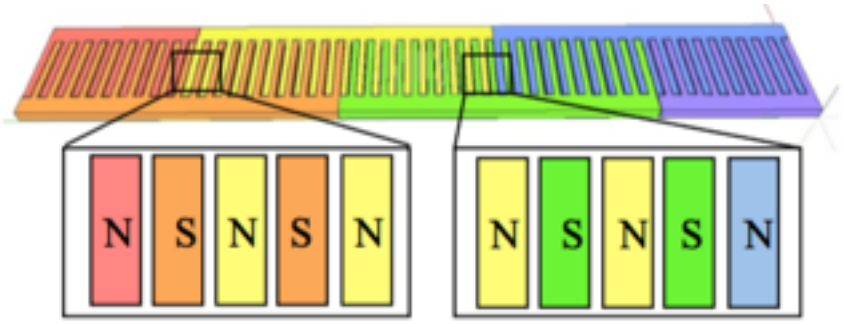

Figure 3.16 Schematic of assembled magnet array that maintains periodicity and an alternating field pattern

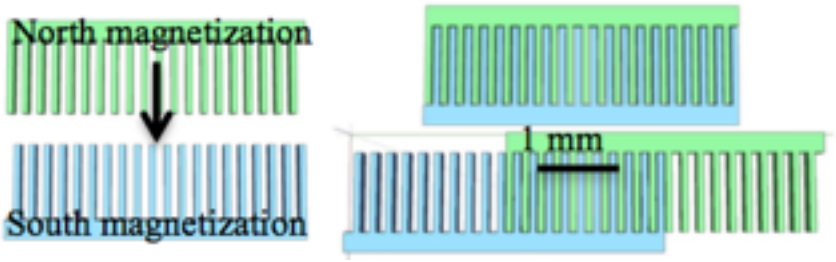

Figure 3.17 Schematic of assembly methods: two combs are laser machined and separated from each other, then can be assembled (top right) as a single array, or (bottom right) as an extended array by offsetting each comb

There are some difficulties associated with creating a PM array in this manner. Primarily, these magnetic materials are very brittle, and with so many long pieces they can break easily. Additionally, these magnets, when placed in this N-S-N-S-N pattern, desire to be as close as possible to their nearest neighbors. This was discovered to be its preferred low magnetic energy state. Precautions must therefore be made to prevent the magnets from shifting horizontally too much from the center between each of its nearest neighbors. The effects of this can be seen in Figure 3.18 where the array is neatly fabricated, but gaps between every other comb finger are easily visible. As part of the overall fabrication process of these combs, they were coated in a uniform 5-10 μm layer of parylene. In addition to providing for more uniformly separated interdigitated fingers, the parylene provides for a low friction surface that aided in assembly as the laser-machined edge of the magnets would not grind one on another. It also provided additional mechanical stability to prevent breakage of comb fingers.

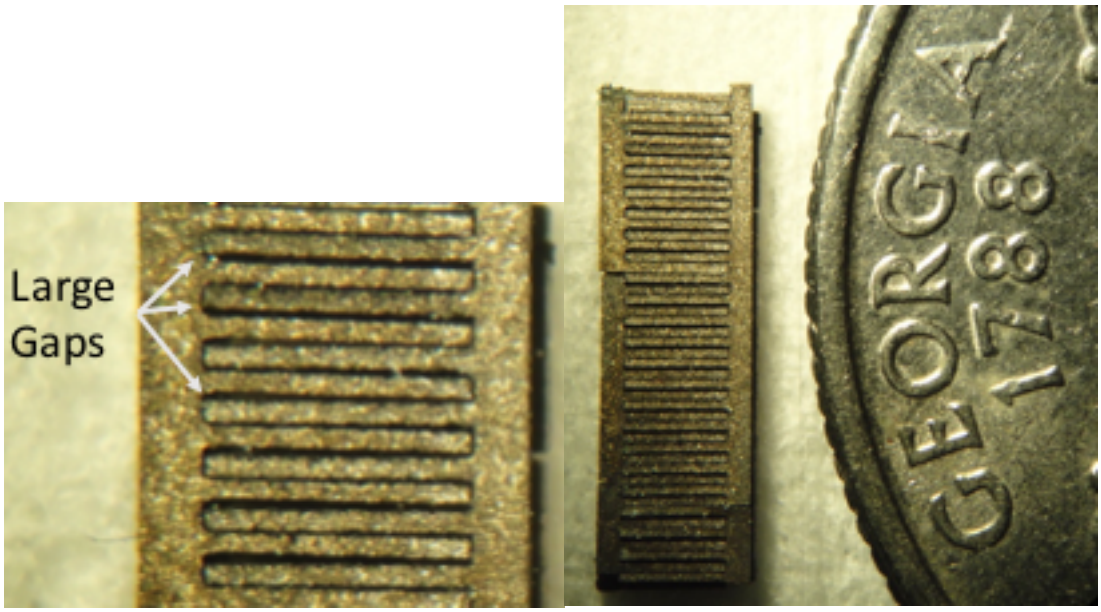

Figure 3.18 Photograph of a magnet array next to a United States Quarter showing uneven gaps between comb fingers

One problem with this assembly and the laser machining of magnets, as was represented by the fill factor from Figure 3.12b and eq. 1.10, is the amount of material that is lost between each magnet in the array; this material can be physical material lost, or magnetically inactive (demagnetized) material, as described in Chapter 2. A model was therefore constructed using COMSOL Multiphysics that plots the resulting ratio of the amplitude of the sinusoidal magnetic field of an array with material lost to that of a nominal-field, perfect magnet array (no material lost). Figure 3.19 shows the schematic of this model and the results follow the same pattern as Figure 3.12b. It can be seen that even with a 40% loss in material, only 20% of the maximum field was lost. For a 400 μm period, 40% material lost would be 160 linear μm of material per period, an 80 μm beam width for the laser (two laser cuts per period) or a smaller beam width of 60 μm with

10 μm HAZ on either side of the cut, for example. As was shown in sections 2.2 and 2.3, this is a reasonable correlation to what appears to be happening with laser machined magnets.

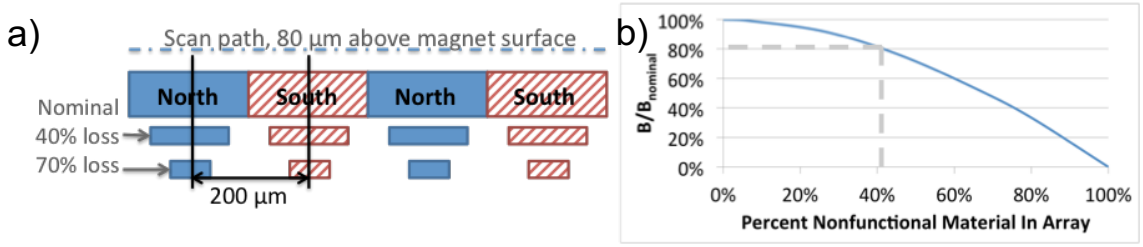

Figure 3.19 a) Schematic of material lost model showing magnet poles, scan path, and material lost and b) the corresponding normalized magnetic flux density as a function of material lost

An additional effect that became apparent through three-dimensional modeling of the arrays and undulators is the magnetic field produced by the bar of the combs. Again this is an effect of magnetic field superposition, but Figure 3.20 shows how the z-component magnetic flux density varies along a line from the north magnetized bar toward the south magnetized bar in the array that passes through a point that has zero z-component on-axis, namely between two oppositely poled comb fingers. In the chart, the slope of z-component magnetic flux density is dependent on the separation distance between the comb bars. A larger separation leads to a smaller change in flux density across the array and a smaller slope. If this slope were detrimental to the functioning of the alternating field device, the comb bars could technically be removed or demagnetized, again using the laser. Now that a design has been created and modeled, and the resulting magnetic flux densities and pattern are sufficient, the physical arrays can be laser machined.

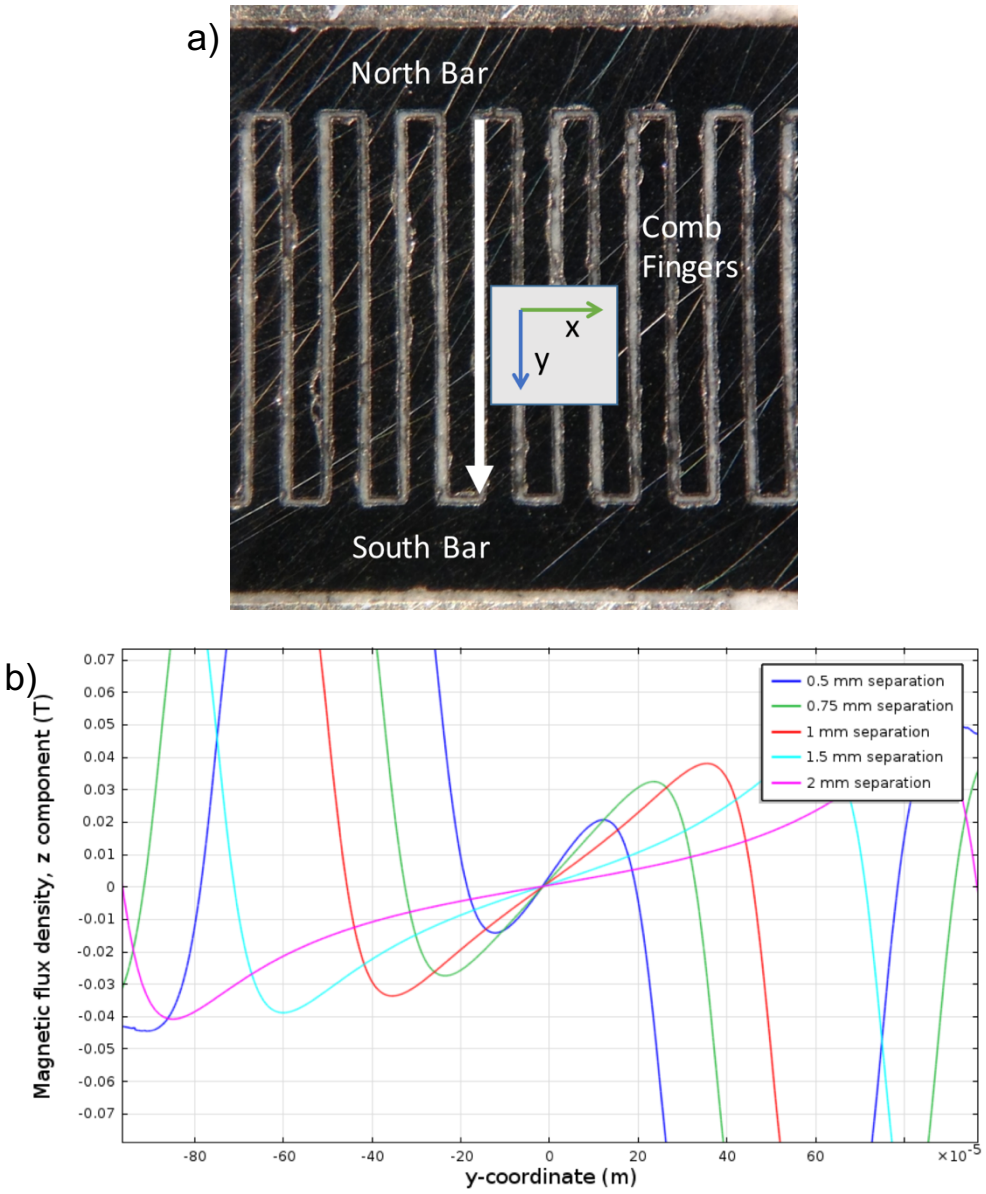

Figure 3.20 a) Photograph with an arrow representing the path traveled for the b) chart that shows the change in z-component magnetic flux density as a function of distance along that arrow and separation between comb bars

3.3.2 Magnet Array Fabrication, Assembly, and Characterization

To create a PM array, a series of SmCo magnets were laser machined using the Nd:YLF laser. Comb periods of 230 μm, 250 μm, 300 μm, and 400 μm with individual magnet widths of between 60 μm and 160 μm were fabricated. Figure 3.21a and b shows two examples of single magnet combs with periodicities of 230 μm and 250 μm. Figure 3.21c shows three polished magnet arrays with periodicities of 300 μm, 250 μm, and 230 μm.

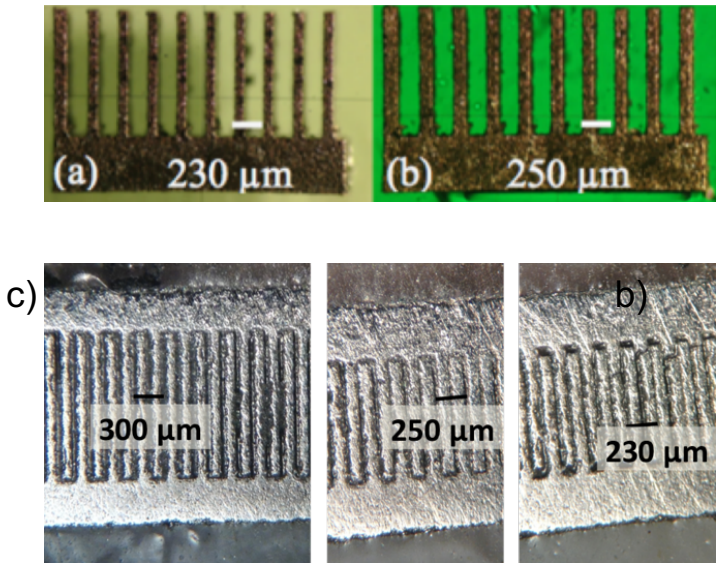

Figure 3.21 Photographs of a) & b) laser machined and c) laser machined and polished magnet arrays of various widths

In order to assess if the comb design matched its intended results, a set of magnet arrays was made from stainless steel of a similar thickness. The assertion here is that by machining a similar aluminum frame, and stainless steel magnets (cheaper, but still slightly magnetic), whether or not machining the SmCo magnet arrays would work would be able to be ascertained. The stainless steel was machined to the same dimensions intended for the SmCo arrays. The magnet array was then adhered to an aluminum

frame by a high vacuum epoxy called TorrSeal (https://www.lesker.com). This epoxy allows for the assembled magnet arrays to be used in high vacuum electron beam lines, which was necessary for use at the collaborator testing facilities, as described in section 3.4. In order to hold the array in place, an aluminum frame was machined using an end mill to have a slot 200 μm deep for the magnets to rest in, with a smaller slot through to the back to insert the epoxy, and four through holes for screws that would be used in the final undulator assembly, described in section 3.2, which is essentially two stacked magnet arrays. The dimensions of these stainless steel arrays were then measured. Figure 3.22 shows the periodicity of multiple arrays as a function of measurement position. This measures the distance between the same point in the previous period, called a running period. The positions of measurement are labeled in Figure 3.22d. Figure 3.22a and b show the widths of the stainless steel comb fingers and the gaps between fingers. The dashed lines represent breaks where a new comb begins. The effect of this separation in combs (the slight distance between magnet bars) was also modeled with a slight but random separation, as shown in Figure 3.23. As can be seen, the model helps identify some slight variations in the overall magnetic field pattern. In Figure 3.22d, the finger widths are measured as points 2 to 3, 4 to 5, and so on; the gaps are measured as 1 to 2, 3 to 4, and so on; and the running periods are measured as points 1 to 5, 2 to 6, and so on. Figure 3.22c shows the running period for the same arrays. This set of measurements essentially shows that 1) the aluminum frames fit well to the 50 period undulator, 2) Torrseal epoxy keeps magnets sufficiently in place and is stable enough to hold the SmCo pieces during polishing, 3) this polishing method yields low surface roughness, and 4) the design was sufficient to allow the assembly SmCo magnet arrays.

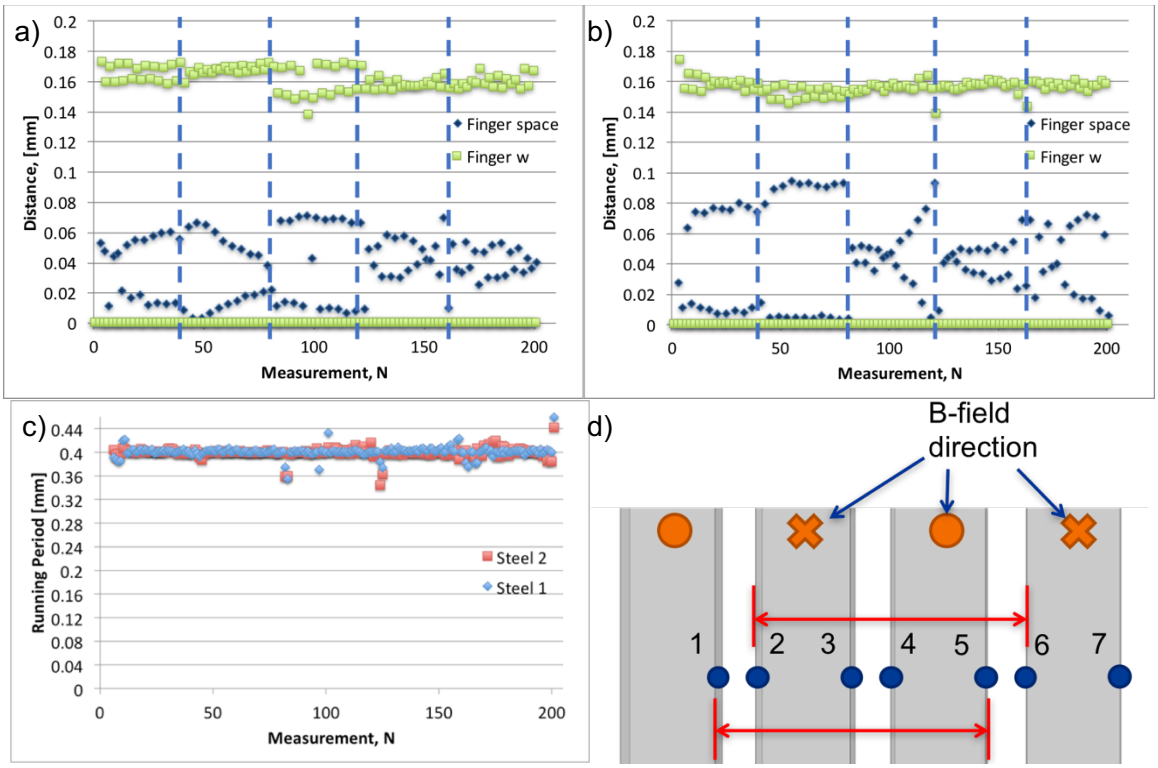

Figure 3.22 Charts indicating the a), b) widths of the comb finger widths and gaps (space) and c) the running period as a function of measurement position for two stainless steel arrays. d) Schematic showing fingers with measurement positions

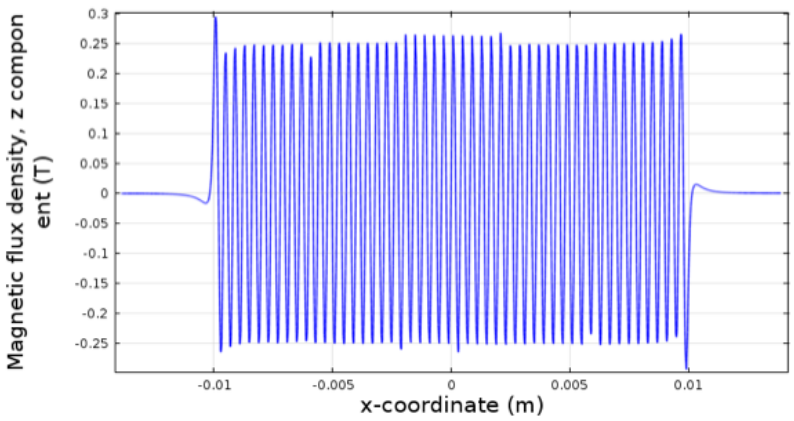

Figure 3.23 Magnetic field of a model simulating the offset of entire combs within the array

Figure 3.24 shows a fully assembled and polished 50-period SmCo array with a nominal periodicity of 400 μm. This device is what was designed to work for the situation described in this dissertation research in section 3.4, but other frames, epoxies, and assembly methods could potentially work as well. The active area of this device, containing the oscillating magnetic field pattern, is 2 mm wide by 20 mm long (the magnet bars on the outside are an additional 500 μm wide).

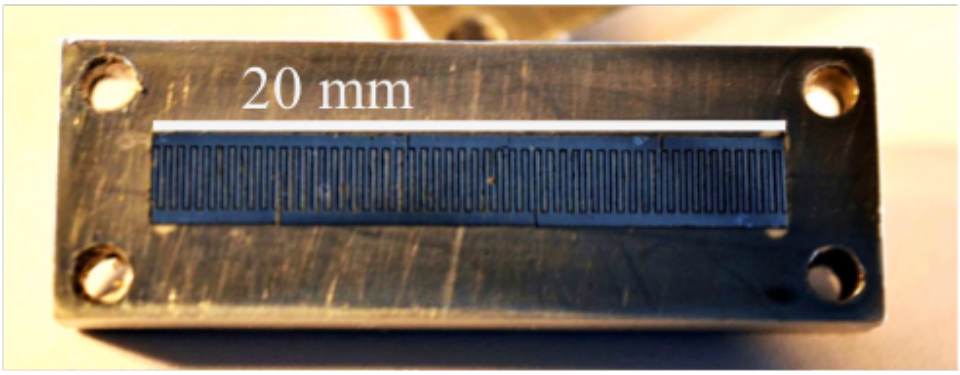

Figure 3.24 Photograph of an assembled and polished magnet array with 50 magnetic period of 400 μm

After the magnet combs are laser machined, cleaned in the citric acid solution, and dipped in an ultrasonic bath, they are coated in a uniform layer of parylene. The magnet combs are then magnetized in a superconducting magnet with a magnetic flux density of at least 7 Tesla, some with a north magnetization, some with a south magnetization. The magnet combs were then assembled, as described in section 3.2.1, with an offset between combs and alternating magnetization. This offset can be seen in Figure 3.24 as the breaks along the comb bars just outside the active area of the comb fingers. The three combs on the top of Figure 3.24 are north magnetized, and the lower ones are

south magnetized. Note also that either end is terminated with a half-length comb that completes the array.

During the assembly, care must be taken to not break the comb fingers; at these widths, the brittle nature of SmCo is more apparent. Due to the oppositely-poled magnetizations of each comb, the combs are highly attracted to one another (as this is a low magnetic energy state: a north pole immediately adjacent to a south pole) and they must not be allowed to snap into place, as that would increase breaking risk as well. Once the magnet array is assembled, the entire array is place into the aluminum frame, adhered with the epoxy, cured, and polished.

A good method for insertion of the epoxy is to place the magnet array and frame face down on top of a non-stick surface such as non-stick aluminum foil and drip the epoxy into the frame slot from the back side. The assembly and epoxy are then placed into a press to hold the magnet array and frame in place while the epoxy cures for up to 24 hours. Additionally, placing in a vacuum chamber while being pressed could aid in this curing process. Upon curing, the assembly is removed from the press and the aluminum foil. Ideally, epoxy will be on top and bottom of the array assembly, indicating it has seeped/percolated into all crevices between the comb fingers. The magnet array assembly is polished in the same manner as that described in section 2.4.1. Part of the aluminum frame design included cutting the length to be equal to the width of the glass slides used in the rock polishing tool to facilitate this polishing process. Once the array is fully polished, it will have all epoxy removed from the top and bottom surfaces, and both the aluminum and SmCo surfaces will be reflective, as can be seen in Figure 3.24. It should be noted here that polishing does not appear to adversely affect the laser

machined SmCo magnets and they appear to maintain their shine indefinitely, as the SmCo does not appear to oxidize.

Figure 3.25 shows a photograph of magnetic viewing paper placed over the magnet arrays from Figure 3.24 above. Dark sections indicate the presence of magnetic field and light sections indicate a field transition from north to south, or south to north (both directions being through the plane of the viewing paper). The meander pattern between the comb fingers is clearly visible here and indicates qualitatively that there is an oscillating field pattern.

Figure 3.25 Photograph of viewing paper placed over two of the polished 400–μm–period magnet array assemblies

In addition to physical measurements of this array, and this qualitative view of the magnetic field with the viewing paper, a magnetic image was taken using a scanning Hall effect sensor. The Scanning Hall Probe System is a system designed by the Interdisciplinary Microsystems Group at University of Florida. It scans a very small (1 μm

or 10 μm on a side) Hall effect sensor above the surface of a magnet to measure the magnetic field at every position above the magnet, essentially giving a magnetic image with a resolution approximately the size of the sensor itself. Due to the limitations of the Hall effect sensor and its assembly in the system, a minimum scan height of at least 50 μm from the surface of the magnets must be maintained. Therefore, most of the magnetic measurements taken and shown here in this section are a safe 80-100 μm above the magnet.

Figure 3.26a shows a portion of the magnetic field distribution over the 400–μm–period magnet array. There are several things to note from this magnetic image. First, the periodicity of the array is indeed 400 μm, and maintained across the width of the array as well. Second, the amplitude of the sinusoidal field is 0.05 T at this scan height of approximately 150 μm, or 0.1 T peak to peak. Third, perhaps less desirable, is the linear offset along Y; this linear offset is created by the bars that maintain the comb periodicity, as mentioned in section 3.2.1. These bars create a nonuniformity along Y, but at the same time provide a strong holding force for a second array placed directly above it, as will be shown in the next section. Nonetheless, if desired, the magnetic field in those bars, or the bars entirely, could be removed post-assembly as mentioned previously. Figure 3.26b shows the difference between the magnetic fields in a COMSOL model and scan line measurements of the magnet array. These show a good deal of agreement and confirm the 400–μm–periodicity of the array. Figure 3.27 shows another representation of this same line scan data, but compares the amplitudes of the COMSOL model and fabricated arrays to that of equation 1.10. These again show good agreement as the measurement distance increases. The greater average amplitude for

the fabricated devices is likely due to the uncertainty in the height measurement on the Scanning Hall Probe System.

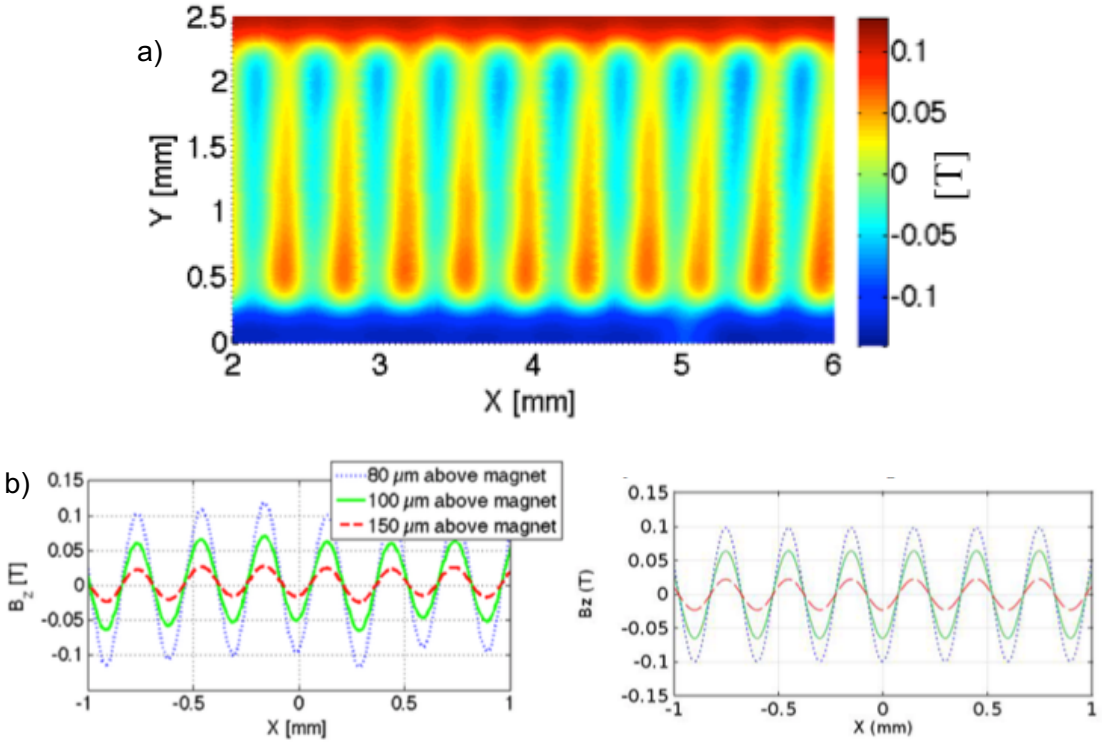

Figure 3.26 Scanning Hall Probe System a) magnetic image of a section of a magnet array and b) sinusoidal line scans over a similar 400-μm-period magnet array compared to a COMSOL model at three heights

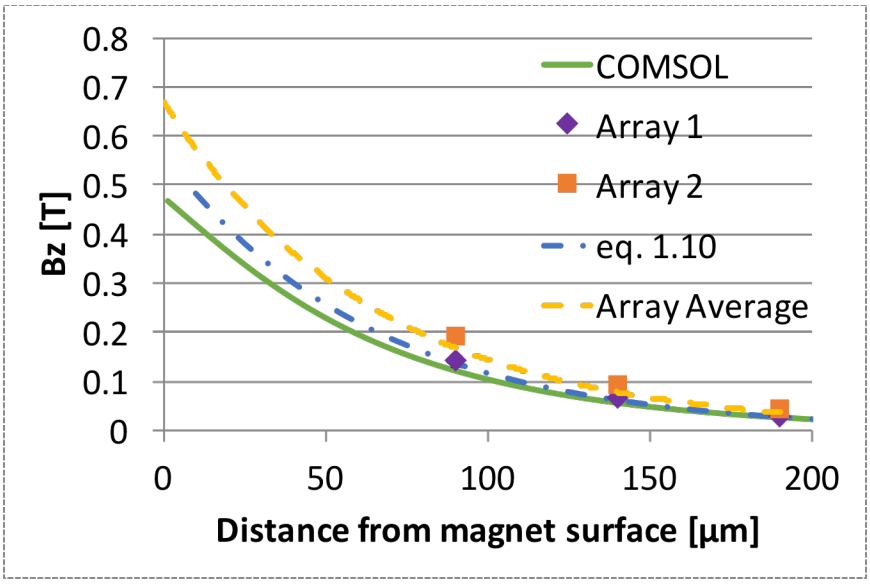

Figure 3.27 Comparison of magnetic flux density generated by COMSOL model, analytical equation 1.10, and measurements of the fabricated magnet arrays

Figure 3.28a shows a comparison of the measurements of four arrays of different periodicities: 230 µm, 250 µm, 300 µm and 400 µm. These confirm that multiple periodicities are readily attainable. The amplitudes of the magnetic flux density correlate with equation 1.10 as shown in Figure 3.12d where the flux density increases with periodicity for a given magnet thickness and gap or measurement height. The field for an undulator on axis is again shown in Figure 3.28b for comparison. The field of a single magnet array is half what this chart shows, and agrees quite well with the amplitudes of the sinusoids in Figure 3.28a.

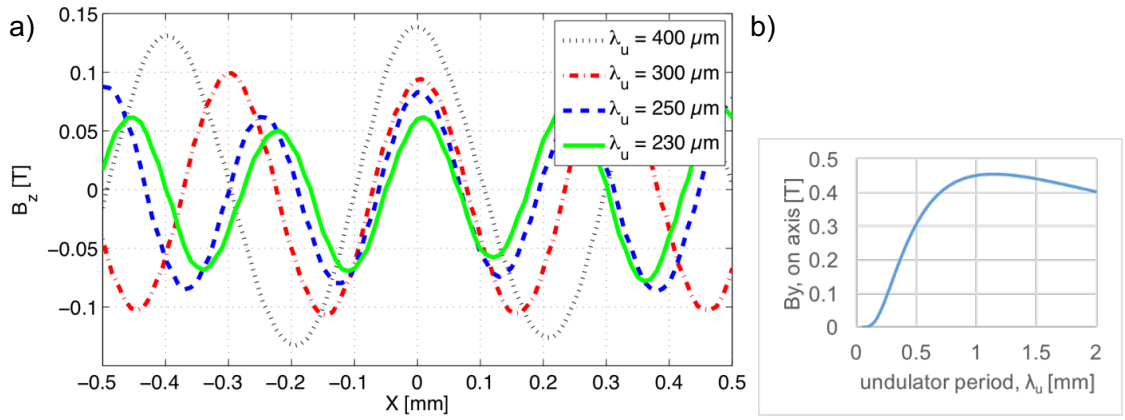

Figure 3.28 Chart showing a) comparison of differing period magnet arrays and b) a repeated chart from Figure 3.12d

As mentioned above, a set of magnet arrays where one magnet array rests directly above the other, relies entirely on the concept of magnetic field superposition. Since the fields of two magnets directly add, it can be shown that two identical magnet arrays will also produce double the magnetic field exactly halfway between them, even in the case of a sinusoidal array such as these. One significant use of a stack of magnet arrays is a magnetic undulator, as was discussed in section 3.1, and the results follow in section 3.4. An additional use of alternating field magnet arrays, namely energy harvesting, will be discussed in section 4.1.

3.4 Free Electron Magnetic Undulators

Using a set of magnet arrays, with matching field directions, an undulator was assembled. When one magnet array is placed directly above the other in close proximity, the magnet arrays vertically snap together; this is mainly due to the large bar magnets at the edge of the magnet combs used to form each array. Additionally, the matching magnetic field pattern of each period within the arrays, along with the bar magnets,

causes the arrays to horizontally snap into place and align with one another period to period. The gap between the undulators is maintained by laser machined shim stock to 50-400 μm gaps, depending on the setup. The magnet array aluminum frames and the gap shim stock have screw holes that allow for attaching the undulator assembly to an adapter or holding frame. A photograph of the assembled microundulator can be seen next to a United States quarter for comparison in Figure 3.29, including the circular holding adapter, 2 rectangular magnet arrays, the copper shim stock, and brass screws. The entire assembled first generation microundulator is 1 cm tall and 1 cm wide by 3 cm long. Additional undulators were fabricated with thinner aluminum frames that make the microundulator assembly 2.5 mm tall. The photograph also shows the relative size of the gap/slit where the electron must enter; the experiments in the following sections used a gap height of 200 μm or 400 μm, the image shows a 400 μm tall gap. With a complete undulator, testing was able to proceed with collaborators at University of California – Los Angeles, University of Michigan – Ann Arbor, and Stanford Linear Accelerator Center.

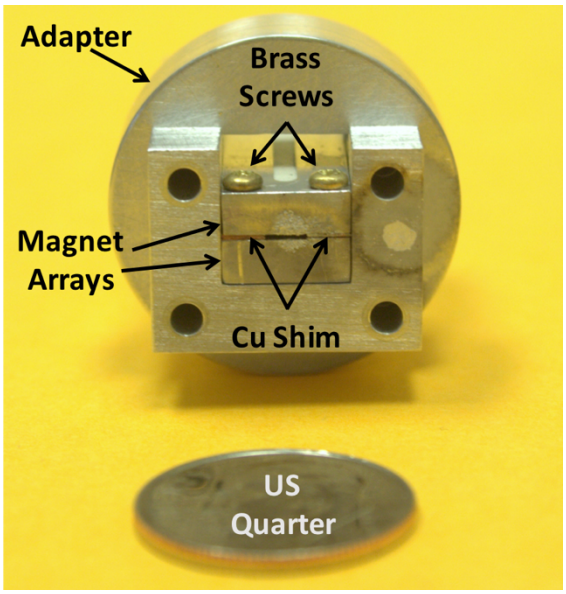

Figure 3.29 Picture of assembled undulator

3.4.1 Measurement and Testing at University of California – Los Angeles

The first collaborator for this testing was the UCLA Particle Beam Physics Laboratory. The facility includes a relatively low electron energy (up to 10 MeV) linear accelerator. The UCLA team also specializes in measuring the undulator field of relatively short length undulators using the pulsed-wire technique [77] [78]. A measurement of the magnetic field inside the undulator cavity would indicate the degree of alignment between the top and bottom magnet arrays and it could confirm that superposition is obeyed within the undulator. Until this point, measuring the magnetic field within a space 200-400 μm tall has been a challenge and the pulsed-wire technique offered an opportunity to make this measurement. Indeed, pulsed wire measurement has been compared to Hall sensor measurement on existing undulators and found comparable for measuring the field and subsequent field integrals below [79] [80], while also allowing field measurement for difficult to reach places, i.e. a microundulator, and adapted to field

pattern measurements for wigglers and undulators tens of meters long [81]. Pulsed-wire measurement has been adapted for use in undulators and wigglers [77] [78] [79] [82], on- and off-axis solenoid fields [83] [78], for quadrupole and sextupole focusing effects within undulators [81] and quadrupole alignment [84].

The pulsed-wire technique involves measuring the effect of the Lorentz force acting on a current-carrying wire. The wire, passing through the magnetic field of interest, is clamped at one end and held at the other by a given mass that maintains tension on the wire; a schematic is shown in Figure 3.30a. A current is then passed through the wire, either a pulse or a step function [77]. The Lorentz force from this current moving through the alternating magnetic field of the undulator deflects the wire so as to create a physical deflection wave in the wire that propagates in both directions from the undulator. Figure 3.30b shows the undulator installed in the pulsed-wire measurement apparatus. The pink spot below the undulator is the laser illuminating the 50 μm diameter wire. In the case of a current pulse, the deflection of the wire, due to a magnetic field $B(z)$, also called the first field integral in the pulsed-wire literature, is:

$$y(t) = \frac{Idt}{2cP}\int_0^{ct} B(z)dz, \tag{3.9}$$

where I is the current in the wire, dt is the time length of the pulse, t is the measurement time, c is the wave velocity on the wire $\sqrt{T/P}$, and T and P are the wire tension and linear density, respectively [77] [85]. This first field integral is directly proportional to the angular deflection of an electron beam passing through the magnetic field [77]. The time length of the pulse should be shorter than the time required for the launched wave to traverse one period of a sinusoidal device, or other significant magnetic feature [82]. For

the case of the 400 μm magnetic period microundulator with a 50–μm–diameter wire and a 50 g mass holding tension, a short pulse time would be less than 10 μs. Similarly, in the case of a step function in current the resulting wire deflection is:

$$y(t) = \frac{I}{2c^2 P} \int_0^{ct} \int_0^{z_1} B(z) dz\, dz_1, \tag{3.10}$$

and is referred to as the second field integral in the literature. The time length of the pulse should be longer than the time required for a launched wave to travel from one end of the magnetic field of interest to the other [82]. In the case of the microundulator, this pulse length would be approximately 250-500 μs depending on the mass used to maintain tension. This second field integral is directly proportional to the electron displacement or trajectory within the magnetic field [77] [82].

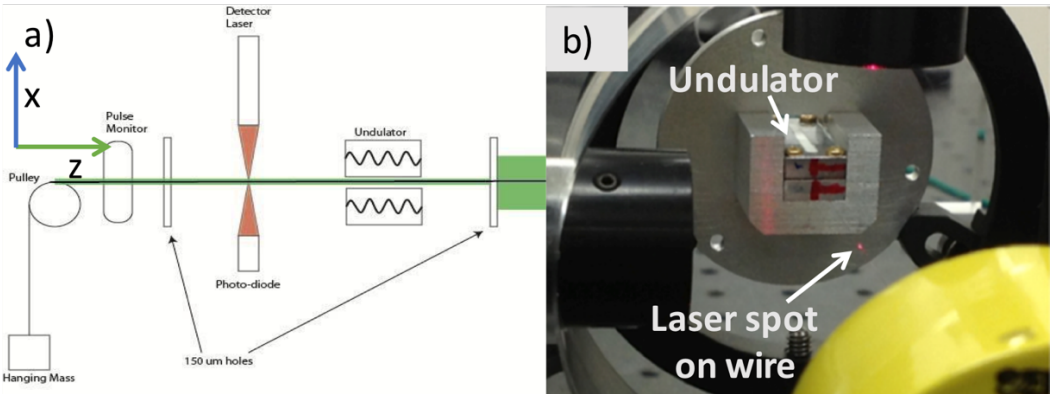

Figure 3.30 a) Schematic of UCLA pulsed-wire setup and b) photograph of the undulator installed in the pulsed-wire setup; the laser used for measurement is illuminating the 50 μm diameter wire

The displacement of the current-generated deflection wave is what is measured by laser micrometers, in both transverse directions (x and y in Figure 3.30a) if necessary. The longer pulse version is similar to a series of pulses in immediate succession, continuing

to integrate the effects of the magnetic field along the wire as the pulse propagates. Therefore, the magnetic field can be calculated from the field integrals by differentiation and the field measured by a Hall sensor can be integrated to obtain the field integrals of the pulsed-wire test for comparison [79] [86].

In order to simulate the effects of a given magnetic field profile on a passing electron bunch, SPECTRA software (http://radiant.harima.riken.go.jp/spectra/) was used. SPECTRA is specifically designed to simulate the EM radiation output based on input electron bunch and magnetic field properties. Using the magnetic field output from a COMSOL Multiphysics model with slight random misalignments, as shown in Figure 3.31a, the electron velocity and travel path were simulated, shown in Figure 3.31b and c, respectively. Note how the electron path/trajectory is moved significantly across the axis. The software can compensate for the position of the electrons within the magnetic field allowing for it to be on axis in the middle of the undulator magnetic field. However, if the electron bunch entered the array in the middle of the entrance, the electrons would start on axis and move significantly away from the axis in a similar manner. This is demonstrated in Figure 3.32. SPECTRA was again used to simulate the electron movement within a magnetic field similar to that of the microundulator by using the scanning hall probe magnetic field data, similar to Figure 3.26b. Note how the trajectory offset from center is present in Figure 3.32c.

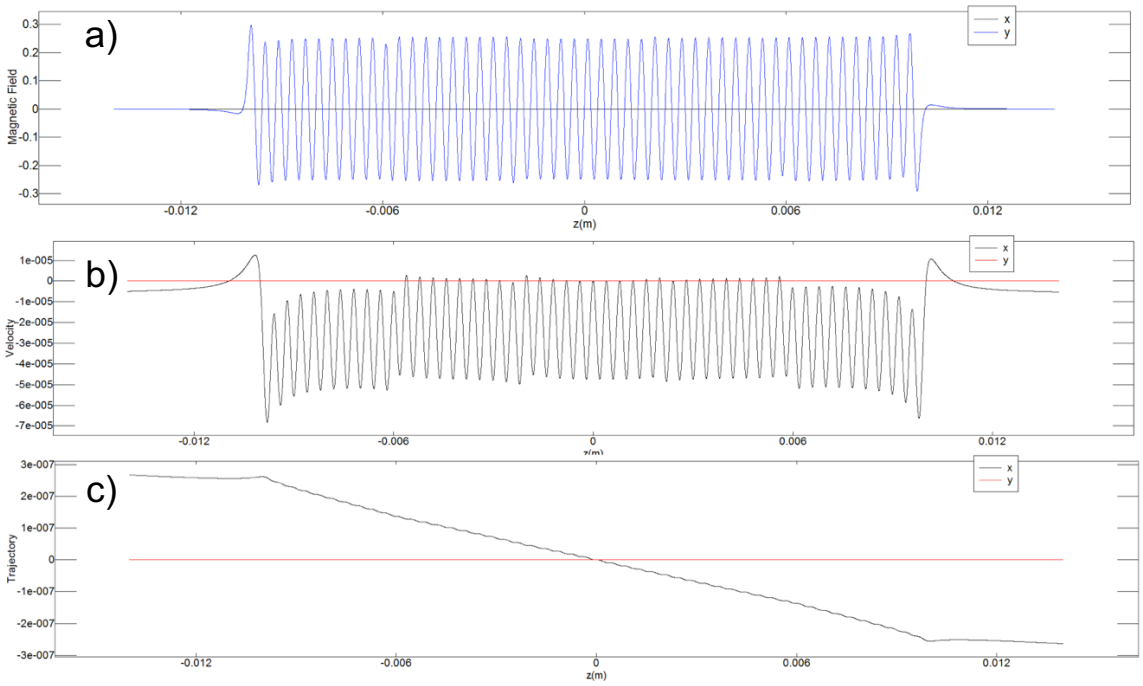

Figure 3.31 Spectra software output using the modeled magnetic field of the microundulator obtained from COMSOL Multiphysics, showing the a) magnetic field used, b) electron velocity, and c) electron trajectory within the magnetic field

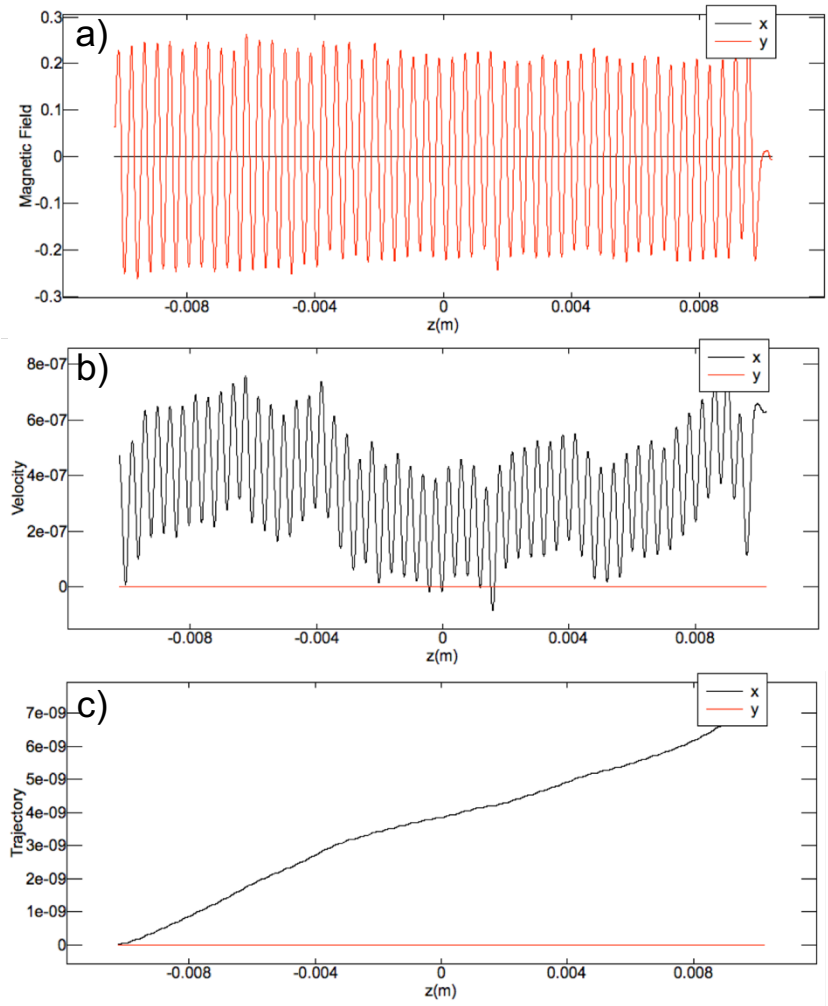

Figure 3.32 Spectra software output using the measured magnetic field of the microundulator obtained from the scanning hall probe, showing the a) magnetic field used, b) electron velocity, and c) electron trajectory within the magnetic field

These simulations are similar to a pulsed-wire measurement performed on a 38 period wiggler at the SOLEIL synchrotron facility in France, as shown in Figure 3.33 [82]. This wiggler, named WSV50 (it has 50 mm periods and fits within the vacuum chamber), has a similar magnetic profile to that of the microundulator, namely an antisymmetric

magnetic field. Again, note the offset in the electron trajectory from beginning to end of the wiggler. The author attributes the offset between the pulsed-wire measurement and the Hall sensor measurement to the sag in the wire, reported similarly elsewhere [81] [82] [84].

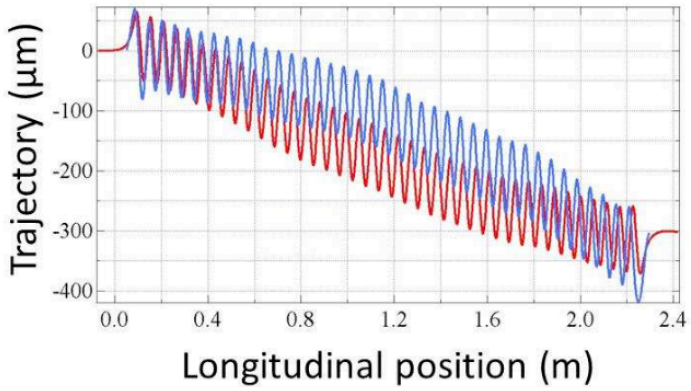

Figure 3.33 Pulsed-wire measurement of WSV50 wiggler at SOLEIL in France; blue is the pulsed-wire measurement, red is the Hall sensor measurement

A measurement of wire displacement was successfully taken on the pulsed-wire apparatus, as shown in Figure 3.34, and indeed resembles that of the simulation and previous measurements for similar magnetic field structures. However, this test confirmed that the individual oscillations expected remained difficult to see. Lastly, an additional measurement utilizing a very low tension mass of 13 grams on a 25 μm diameter wire, and a 250 mA current pulse up to 300 μs in length, as shown in Figure 3.35, shows many individual oscillations. However, the entire complement of oscillations is still not entirely visible. Although the characterization measurement was not complete, the measurement resembles the simulations shown in Figure 3.31 and Figure 3.32 and measurements similar to that shown in Figure 3.33. This likely indicates there is an

undulating magnetic field between the magnet arrays. The next step was to insert the undulator into the UCLA linear accelerator for testing.

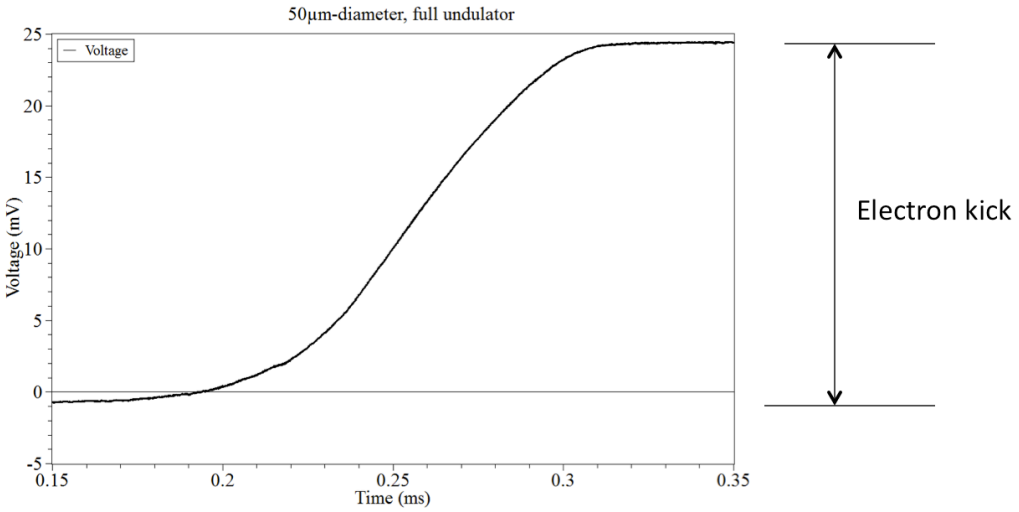

Figure 3.34 Pulsed-wire measurement showing wire displacement on a 50–µm–diameter wire; no undulations are present

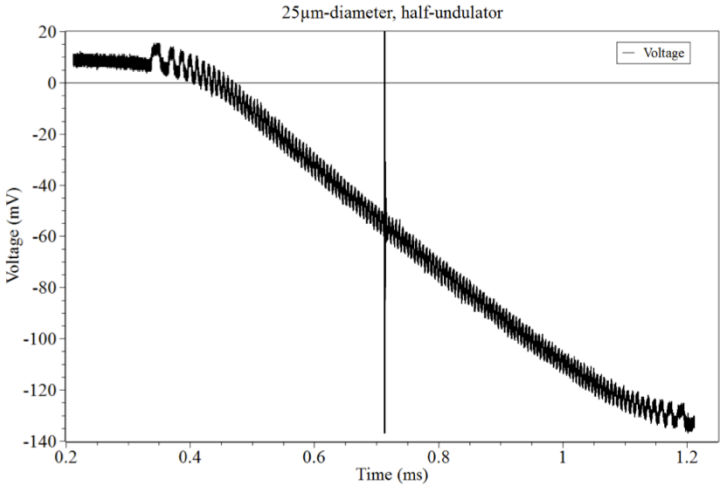

Figure 3.35 Pulsed-wire measurement taken with a 25 µm diameter wire and lower mass value; undulations present but not entirely distinguishable

Placing the 400-μm-period undulator in the 10 MeV PEGASUS electron beam line would ideally generate green light at approximately 520-530 nm, or visible green light. Figure 3.36 shows initial testing demonstrating that 78% of the total initial charge passes through the undulator to the YAG (yttrium aluminum garnet) screen for measurement. This means that the wings of the electron bunch are clipping the outer edges of the undulator structure. As can be seen in the output radiation shown in Figure 3.37, there is some preferential polarization of the output light. The slightly higher number of horizontally polarized photons should indicate that synchrotron radiation is being generated by the undulator, although the data is not conclusive enough for a definitive answer. Undulator radiation from a simple set of stacked magnet arrays, as present in the microundulator, should generate more horizontally polarized light as the electrons should mostly be oscillating in the horizontal plane. The other possibility of this light generation is that it is transition radiation from bouncing off the undulator structure itself or passing through a glass window; this would likely account for some of the radiation, but not the larger horizontal polarization component.

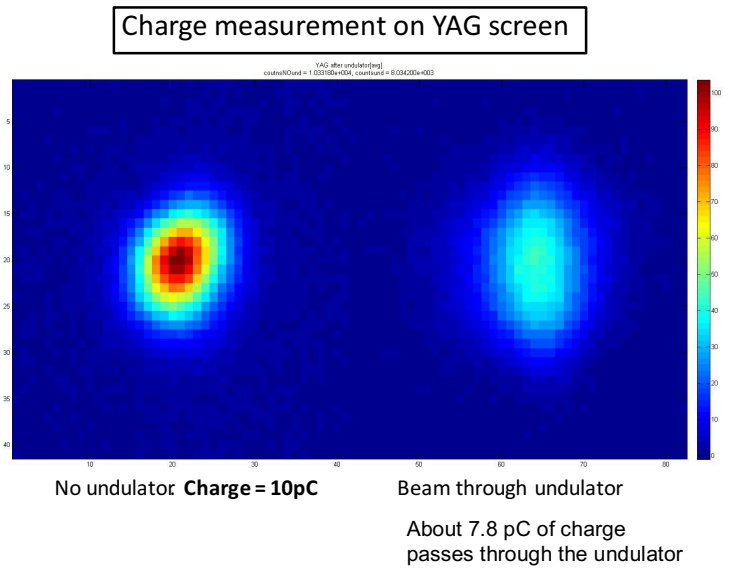

Figure 3.36 Charge measurement on YAG screen (left) without and (right) with the undulator installed

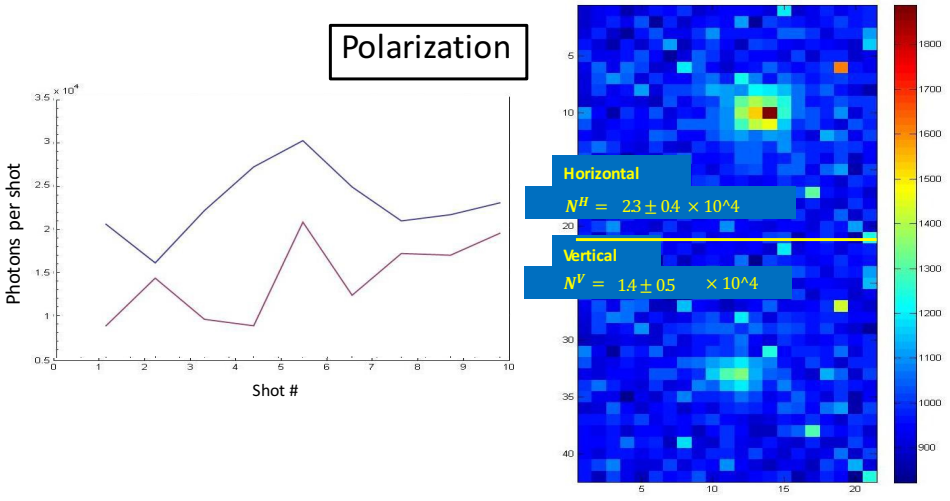

Figure 3.37 (left) Chart showing number of photons received at a camera as a function of shot number with two representative images of the photons measured by the camera with (right-top) horizontal and (right-bottom) vertical polarization

The results of testing and measurement at UCLA indicate that passing an electron bunch through the microundulator will likely continue to be a challenge, and that even characterizing the undulator is a challenge due to the necessary diameters of the wires used in pulsed-wire measurement. The experiment at UCLA was a partial success. The fields within the undulator were confirmed to be similar to that of a full-scale undulator, and the output light polarization indicates some undulator radiation, but the evidence is not clear enough to warrant complete success.

3.4.2 Testing at University of Michigan – Ann Arbor

Collaboration efforts also took us to the University of Michigan at Ann Arbor to work with the Center for Ultrafast Optical Systems. Their HERCULES Laser System is a 300 TW peak power laser (9 J in 30 fs) that operates as a laser-plasma accelerator. A laser-plasma accelerator is a linear accelerator, but instead of traditional electron bunch acceleration and focusing techniques (i.e. high voltages and special magnets), the laser interacts with a gas jet, freeing electrons from the gas that continue to react with the laser [87]. The electrons are then accelerated by the laser created wake in the plasma to a quasi-monoenergetic electron bunch, along with some synchrotron radiation. A conceptual drawing can be seen in Figure 3.38.

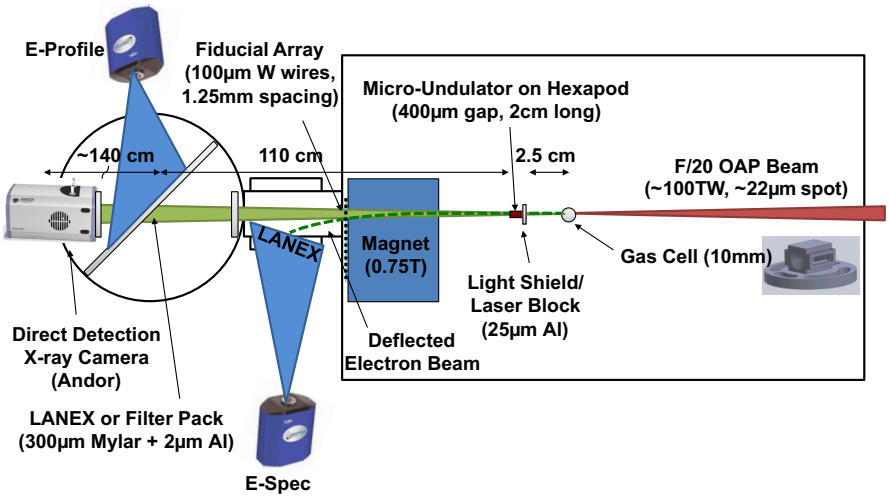

Figure 3.38 Schematic describing components of laser-plasma accelerator and characterization instruments

Figure 3.39a shows the assembled undulator in the holder for the accelerator next to a quarter. Note the size of the undulator gap and the size of the laser blasted sections. As can be seen in Figure 3.39b, and similar to the schematic of the setup, the undulator is sitting behind a light shield that has holes in it. This light shield is intended to block the synchrotron radiation output expected from the accelerated plasma and the laser, which appear as the multiple holes to the right of the undulator. Figure 3.39c shows the undulator in the beam line next to the gas jet. A photograph with a schematic overlay of the undulator within the UM system can be seen in Figure 3.40.

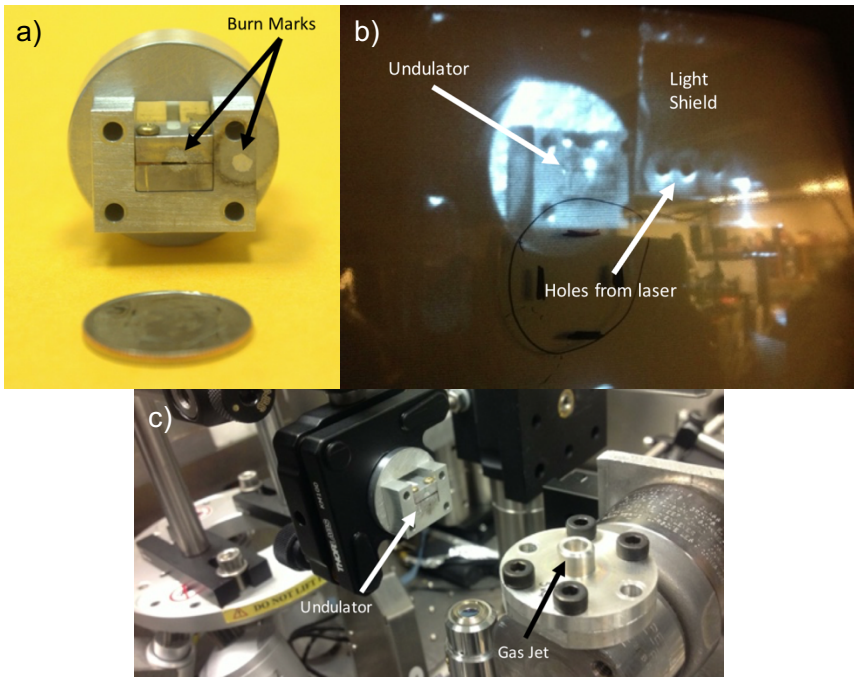

Figure 3.39 Photographs of the undulator a) assembled on a table, b) on a monitor - installed behind a light shield, and c) installed next to the gas jet

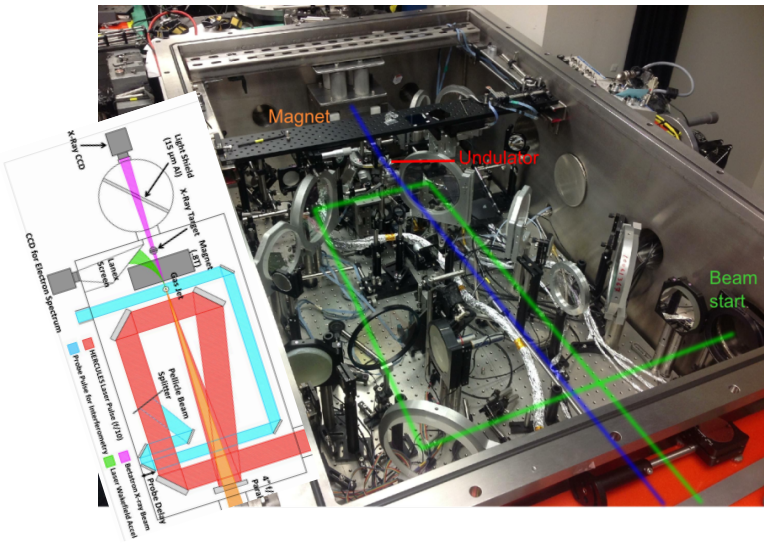

Figure 3.40 Photograph of undulator installed in UM beam line with inset schematic of light and electron paths.

As shown in Figure 3.39a, the burnt sections appear much larger than the gap size; however, the center electron bunch focus is indeed smaller than the gap, and should be at the entrance and exit to the undulator as well. In addition to this obvious problem of the laser and light impinging on the undulator, the placement of the electron bunch and its divergence is not exact, due to the nature of a laser-excited-plasma electron source. This is evident in the output radiation as seen in Figure 3.41. The expected radiation output from this system would be 0.3 nm x-rays, or approximately 4 keV in Figure 3.41. The images show how the Bremsstrahlung radiation is not much different from what should be the microundulator radiation. The takeaway from this experiment is that the electron bunch is either too inaccurate shot to shot or again physically too large (whether at the opening or in the middle of the undulator), possibly due to the wings of the Gaussian electron bunch profile, being at the wrong displacement from the undulator axis, or a combination thereof. The UM team currently has new gas jet targets in development to help with some of these concerns, but the size of the electron beam is going to be a continued problem for microundulators.

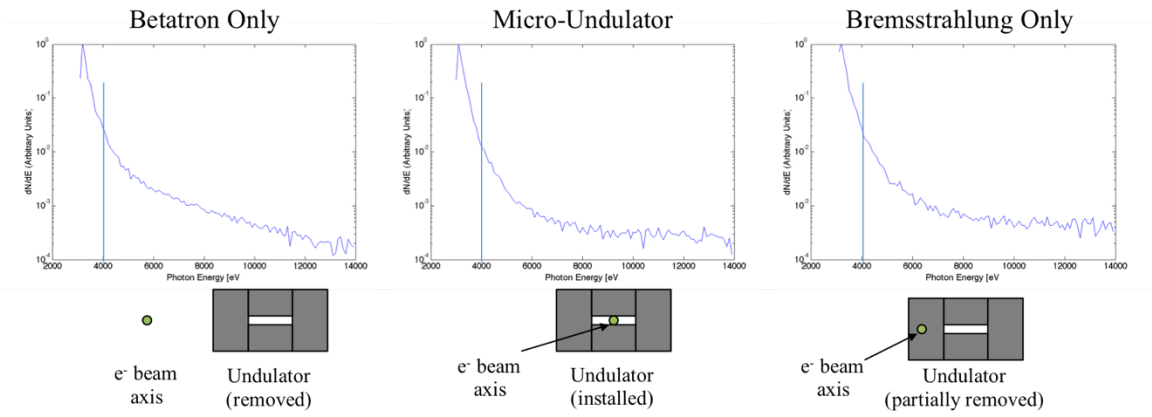

Figure 3.41 Charts showing the energy spectrum of output synchrotron radiation for (left) no device, (middle) undulator, and (right) Bremsstrahlung radiation; blue line indicates predicted undulator radiation energy

As a follow-up to this testing at UM, the undulator was scanned a second time (it had been scanned prior to testing) using the scanning Hall probe system. There was a concern that, with the electron beams and laser impinging on the array, some or all of the magnetic field would be lost. The scan height used in the two scans is different and there are different linear offsets in each scan. The scan height was difficult to maintain uniform with the way the system was set up at the time. The linear offsets are most likely associated with the scan height being slightly different over the full length of the undulator, if the sample was slightly at an angle for example. In the case of this undulator, it could be order tens of microns in thickness difference since the entire size of the device is 1 cm x 3 cm x 4 mm (the second generation had a thickness of 1.2 mm instead of 4 mm, as in the first generation). Figure 3.42 shows the before and after scans from the scanning Hall probe. While a direct comparison cannot be made, the undulator maintains a significant amount of magnetic field as the larger of the two, in red,

is the scan from after the testing at UM. This confirms that the undulator is capable of maintaining its magnetic properties despite being bombarded by electrons, x-rays, and intense laser light. Photographs, shown in Figure 3.43, show the physical damage created by the testing at UM.

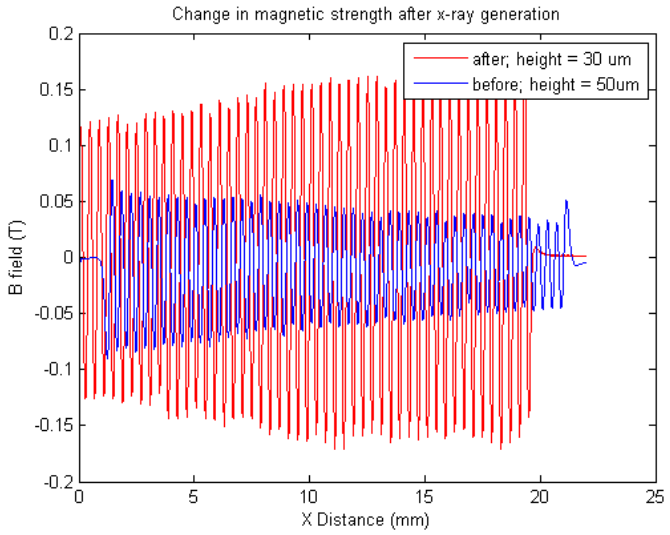

Figure 3.42 Comparison scans of a 1st generation undulator before and after being exposed to a 200–500 MeV electron beam

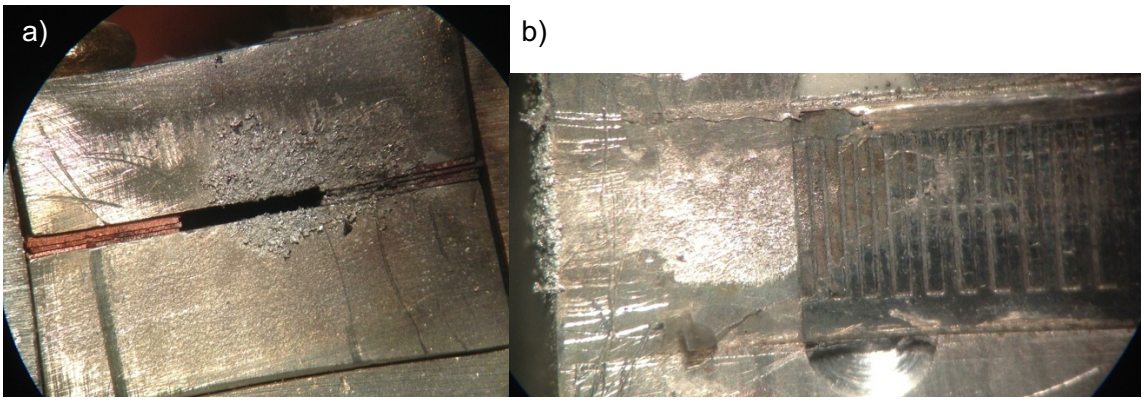

Figure 3.43 Photographs of the combined effects of electron, laser, and x-ray bombardment viewed from a) the electron entrance and b) above a magnet array

3.4.3 Testing at SLAC National Accelerator Laboratory

The SLAC National Accelerator Laboratory was the next experimental collaborator for the DARPA AXiS program; SLAC was initially desired for its ability to create a precise, accurate electron bunch position with a small bunch spot size. SLAC has a number of facilities that produce high-energy electron beams, positron beams, and X-Rays for use in various experiments. In particular, the Facility for Advanced Accelerator Experimental Tests (FACET) suited the requirements of the testing of the microundulator. As can be seen in Figure 3.44, the linear accelerator at SLAC is a 2-mile-long electron track that is capable of accelerating an electron bunch to 20 GeV. Obviously, this is vastly different from the 10 MeV to 400 MeV electron beams used previously.

https://upload.wikimedia.org/wikipedia/commons/thumb/8/8a/Stanford-linear-accelerator-usgs-ortho-kaminski-5900.jpg/1920px-Stanford-linear-accelerator-usgs-ortho-kaminski-5900.jpg

Figure 3.44 Aerial photograph of SLAC National Accelerator Laboratory

Indeed, this was an excessive beam energy for this experiment as the AXiS program was intended to decrease the size of the overall accelerator and X-Ray source, but a number of characteristics made this test a desirable one. Primarily, the electron bunch spot size, divergence, and displacement accuracy would ideally put the electron bunch directly through the 400-μm-period undulator with almost no challenge. Additionally, being the highest-energy linear accelerator in the world, coupling the smallest undulator in the world with it provided a unique opportunity. In fact, the output of the 400-μm-period undulator was expected to be a very high optical energy of 10 MeV (a wavelength 0.1 pm) in the range of gamma emission processes. This experiment would give access to a controlled, focused emission of gamma radiation at 10 MeV.

There were several challenges that arose prior to and during the experiments at SLAC. The first problem encountered came with the approval for the experiment; the proposal was written by collaborators at Los Alamos National Labs (LANL). The original proposal involved utilizing a radioactive thorium sample as part of the detection mechanism that should have shown some decay as a result of the focused gamma bombardment. Due to the mission of SLAC, that portion of the proposal was rejected on grounds that the

research could be used in connection with the nuclear arsenal of the United States Department of Defense. The rest of the experiment was expected to be sufficient, even without the Thorium and so progress toward this experiment continued. The next problem that arose came after arriving at the facility, while experiment staff were being trained and the equipment scanned for contamination and radioactivity. Radiation safety officers are normally quite skilled in dealing with irregular circumstances. However, they discovered that the main measurement device (a gas Cherenkov detector) that LANL brought with them had enough alpha radioactive decay that they were not comfortable having the equipment installed in their facility, despite the fact the beam line happens to be regularly activated every time the beam is activated. With that setback, testing moved forward, knowing testing would be highly limited due to the absence of this instrument.

The undulator was placed within the Kraken Chamber, as can be seen in the IP Area section in the bottom half of Figure 3.45, a layout of devices on the beam line. The instrumentation that was not prohibited was installed at the end of the beam line directly in front of the beam dump. The testing procedure included some basic steps to gather different types of background/undesirable data. First, no undulator was inserted for the background testing. Second, a dummy undulator with the magnets swapped out for stainless steel, but otherwise identical features, was installed. Third, the 1st generation 400–μm–period undulator was installed. Then, had all of that been successful, the 2nd generation undulator with 400–μm–period followed by a 200–μm–period undulator would have been tested.

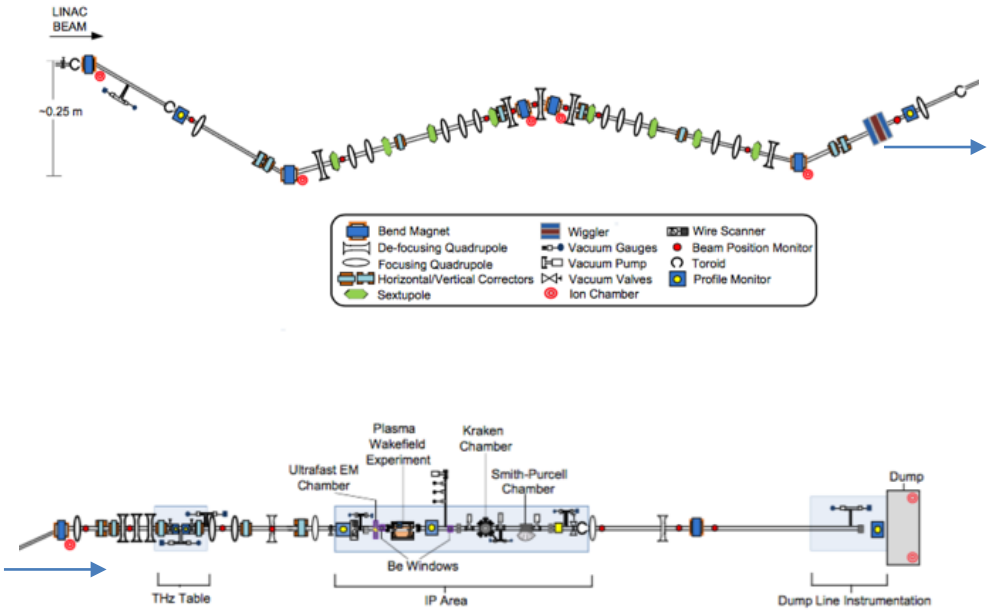

Figure 3.45 Layout map of SLAC insertion devices and chambers along beam line

The undulator assembly can be seen in Figure 3.46; Figure 3.46a is a photograph of two arrays that form an undulator, and Figure 3.46b shows an IR image of the installed set of undulators. The helium-neon (HeNe) laser, used in the setup is used to align the undulators, can be seen as a red dot on the front of one of the undulators. This laser follows the exact path of the electron beam, so having the laser light pass through the undulator should mean the undulator is aligned to the electron beam. It is an impressive feat of engineering that the SLAC FACET beam can pass an electron bunch travelling at 20 GeV speeds at the same consistent, precise location 2 miles down the beam line.

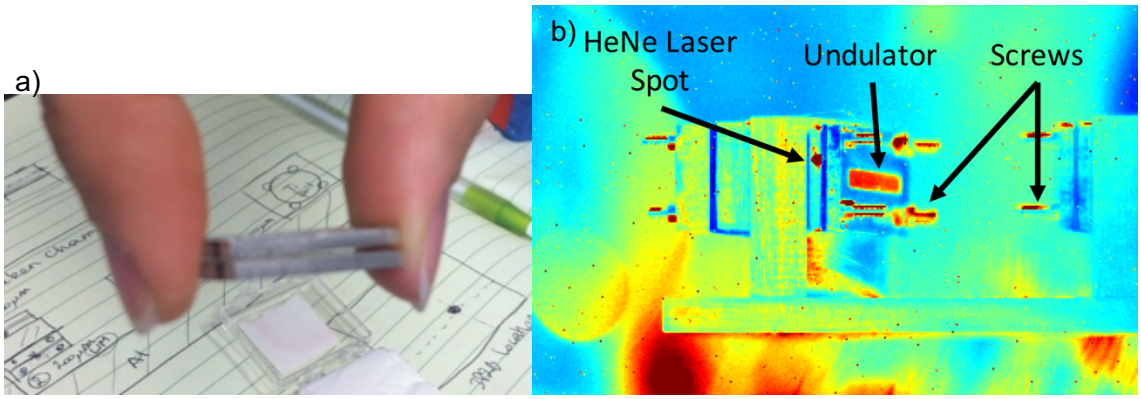

Figure 3.46 a) Photograph of two magnet arrays stacked as in an undulator, and an IR camera image showing three undulators attached to a frame by screws

The mounting frame for the undulators held a phosphor screen, a dummy undulator with a 400 μm gap, a 1st generation undulator with a 400 μm gap, and two 2nd generation undulators having a 400 μm and 200 μm gap. This allowed for the greatest amount of testing with the lowest amount of human interaction once the undulators and tools were installed. This design was required due to the fact the entire beam line tunnel is closed off due to radioactivity while the hardware is active and because the Kraken and similar chambers require multiple hours to achieve the necessary vacuum for testing.

In order to adequately align each of the undulators to the electron beam path without damaging the items inserted into the beam path, a HeNe alignment laser is used, as shown previously. The alignment procedure is as follows. First, the undulator is moved into position using the IR camera image shown in Figure 3.46b. Next, the undulator is tilted, rotated, and translated until the laser light shines through the undulator with the brightest and most uniform beam spot, as shown in Figure 3.47. Figure 3.47a is the IR camera image with no undulator inserted into the beam path (which is beforehand

aligned to the electron beam path), whereas Figure 3.47b and Figure 3.47c show the effect of having a 400– and 200–μm–gap undulator installed, respectively. Note how the beam is partially clipped in both cases. However, as is partially demonstrated in the LANEX images in the next figure, when the undulators were slightly shifted/rotated with the electron beam active, additional Bremsstrahlung radiation would appear, indicating the undulators were fairly well aligned.

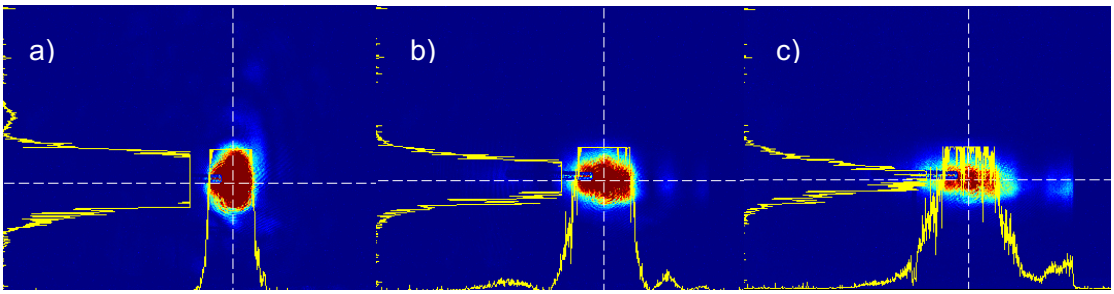

Figure 3.47 Images from alignment camera shows the HeNe laser with a) no undulator inserted, b) the 400–μm–gap undulator inserted, and c) the 200–μm–gap undulator inserted.

The resulting images and experimental data are shown in the next figures. Figure 3.48 shows the time-based signals measured by the Compton Diode instrument for the different undulator cases. A Compton diode is essentially a pair of electrodes separated by an insulator whereby a current is measured as a result of being bombarded by gamma energy photons [88]. The difference in Figure 3.48a from the no undulator (green) case to the centered dummy undulator (black) case was the first sign that the electron bunch was not cleanly passing through the undulator, as the change in signal was close to 500x, indicating a good deal of Bremsstrahlung radiation. The differences continued to rise as the dummy undulator was translated from center position. The

similarity in Figure 3.48b between the two signals also shows that there is no difference when adding the magnets to the undulator, indicating again that Bremsstrahlung radiation was likely dominant in the recorded signal. Figure 3.49 shows four LANEX gamma images showing the gamma output from the electron bunch when a) no undulator is installed, b) the dummy undulator is installed, c) the 400–μm–gap undulator is installed, and d) the 400–μm–gap undulator is installed with a translation of 100 μm. Some observations can be noted from these images. First, the electrons travelling through the system generate some gamma radiation on their own (likely transition radiation for passing through glass, shown in a). Second, the path of the deflected electron bunch is evident in the streak below the central peak (this is due to the bending magnet radiation caused by the beam dump deflection magnet). Third, having any of the undulators in effectively doubles the amount of radiation received, in b) and c), again likely Bremsstrahlung. And fourth, a slight offset again shows a significant increase in radiation received, as in d). Table 3.1 lists the amount of gamma photons that were expected if undulator radiation were achieved.

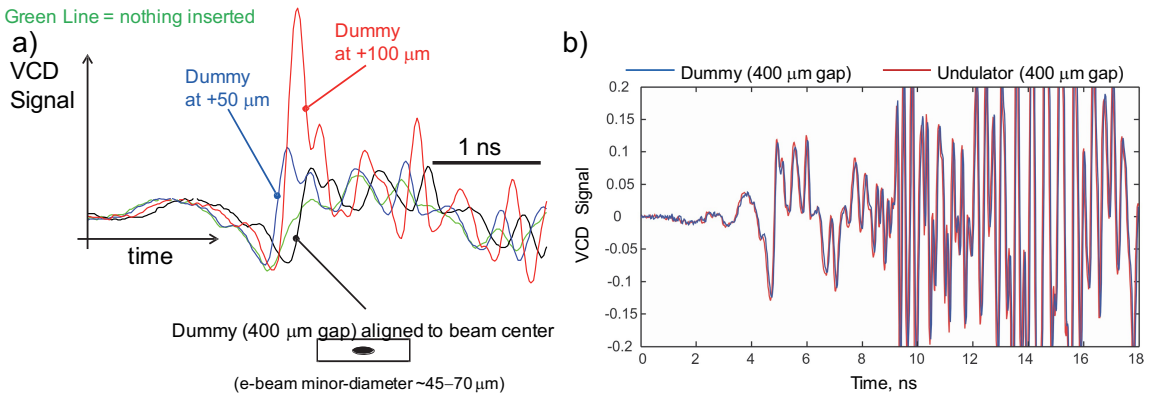

Figure 3.48 Compton diode results from SLAC testing; a) shows the initial time steps with the differences between translated undulators, and b) shows the near identical signal output by the dummy and functional undulator of the same 400–μm–gap.

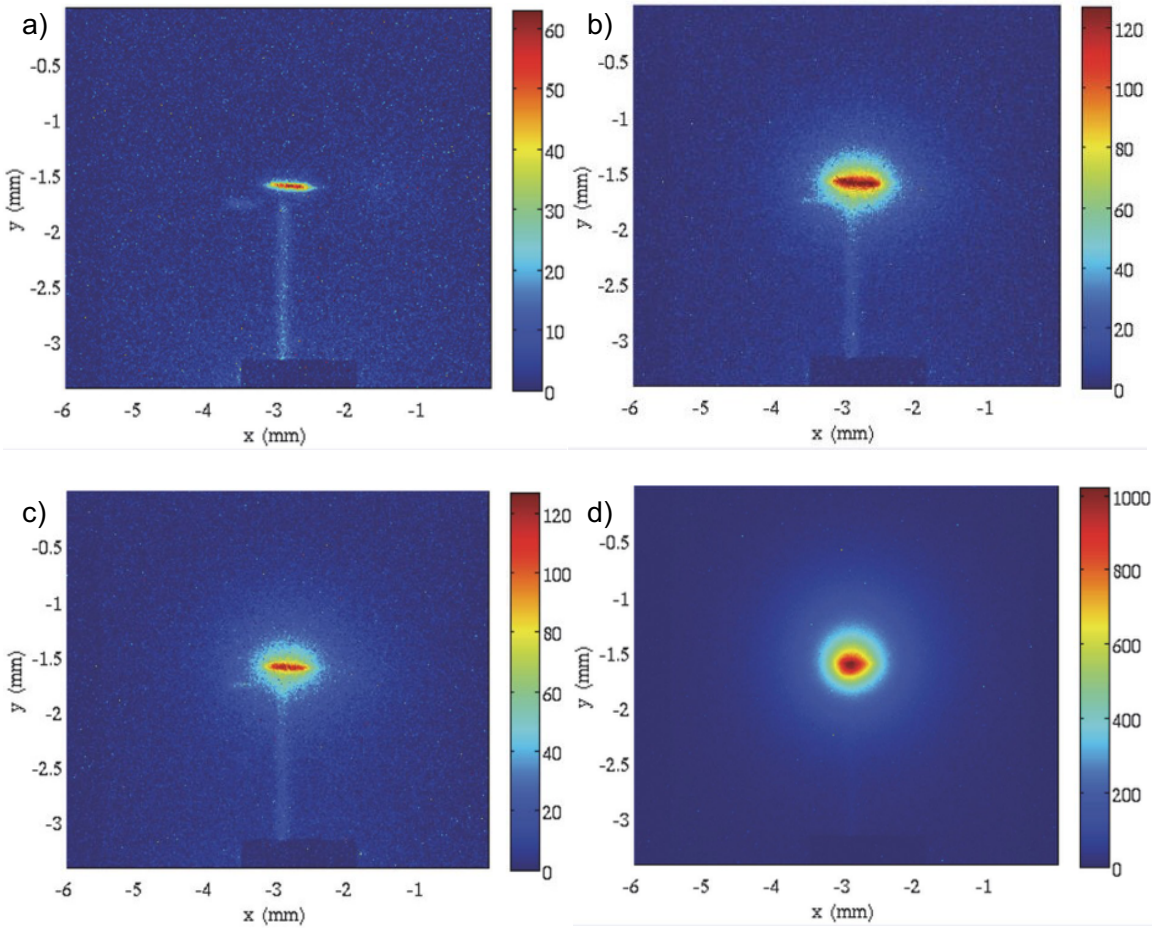

Figure 3.49 LANEX images showing output EM radiation for a) no undulator, b) a dummy undulator, c) a 400–μm–gap undulator, and d) a 400–μm–gap undulator with an offset of 100 μm.

Table 3.1 List of 10 MeV gamma photons per bunch and peak magnetic flux density, based on undulator gap size

Gap	**Peak Undulator Field**	**10 MeV γ's / bunch**
200 mm	0.25 T	$2´10^6$
400 mm	0.063 T	$5´10^5$

When the experiment was finished and LANL had a chance to look more thoroughly at the data collected, along with observations while performing the experiments while at SLAC, the consensus is that the electron beam is still not sufficiently small to pass cleanly through the undulators. The bunch charge (number of electrons in a given bunch, at 3 nC for SLAC) and wings of the electron bunch are the most obvious probable causes. The results suggest that the electron bunch wings are still clipping the undulator due to the significant amount of Bremsstrahlung radiation coming into the collectors. If a significant amount of undulator radiation was being generated during this experiment, it was masked by the sheer intensity of the Bremsstrahlung or possibly the limited measurement hardware.

In all, the experimental testing of undulators proved to be more of a challenge than expected but produced some promising results that open future pathways to having smaller sources of synchrotron radiation. These undulators could be an essential part of that plan.

CHAPTER 4 ADDITIONAL ARBITRARY MAGNETIC FIELD DISTRIBUTIONS

Additional complex magnetic field profiles and applications have also been investigated. COMSOL Multiphysics was used substantially for these investigations for the purpose of design and assembly adjustment as was described for the magnet array. Section 4.1 describes how a magnet array can be used as a low frequency energy harvester. Section 4.2 describes cylindrical Halbach arrays for creating a relatively high constant magnetic field over a volume. Section 4.3 describes a device used to create a small volume with no magnetic field surrounded by magnetic field gradients. Finally, section 4.4 describes an array of alternating pole rings that provide an alternating field similar to that of Chapter 3 and section 4.1.

4.1 Human Excitation Frequency Energy Harvesting

Another significant application for magnet arrays is motors and generators. Generally, permanent-magnet-based motors and generators are rotary devices with the alternating-pole magnets being placed along the circumference of the rotor or stator, with the magnetic field vector pointing radially from or parallel to the motor axis, depending on the architecture [89]. Examples include wind generators, hydroelectric generators, pumps, drills, etc. Motors and generators of varying architectures additionally exist on the submillimeter scale, although generators are generally called energy harvesters at this scale, both with [17] [18] [59] [90] and without magnets (often piezoelectric, electrostatic, or additional types) [91]. Most energy harvesters are based on vibrations from human-scale ten hertz to tens and hundreds of kilohertz, and the harvesting of stray electromagnetic fields. The purpose of this experiment is to utilize the high spatial

frequency magnet array discussed previously to increase human scale oscillation frequencies by 100x.

Magnetic energy harvesters operate using Faraday's law of induction

$$\nabla \times \vec{E} = -\frac{d\vec{B}}{dt} \quad \rightarrow \quad \oint \vec{E} \cdot d\vec{l} = -\frac{d}{dt}\int_S \vec{B} \cdot \hat{n}\, dA, \tag{4.1}$$

where $\vec{E}$ is the electric field, $\vec{B}$ is the magnetic field, S is the coil area surface, and $\vec{l}$ is the path the coil follows. Faraday's law for induced voltage in a coil is then expressed as

$$\mathcal{E} = -N\frac{d\phi}{dt} = -N\frac{\Delta(BA)}{\Delta t}, \qquad \phi = \vec{B} \cdot \vec{S}, \tag{4.2}$$

where $\mathcal{E}$ is the induced electromotive force in volts, N is the number of coil turns, and ϕ is the flux through the coil area surface. In order to increase the voltage induced, either the number of coils or the change in magnetic field must increase or the time required to change the field must decrease. In order to be used with conventional electronics, such as in diode rectification, a voltage of at least 300 mV must be obtained.

One problem associated with utilizing magnetic energy harvesters is that they tend to be low voltage devices, often utilizing a single, relatively large magnet as a seismic mass on the end of a cantilever. This is partly due to the lack of availability of magnets at this scale. On the submillimeter scale, only a small number of turns of a coil are feasible, due to the fabrication processes available. These microcoils are usually fabricated on a single surface, e.g. electroplated copper around a silicon cantilever that holds the magnet. The frequency of magnet oscillation is mostly dictated by the dimensions of the cantilever the magnet sits on and the mass of the magnet. An additional challenge with

energy harvesters is generating appreciable power from frequencies at which most human-based excitations take place: sub 10 Hz. This is due to the slow rate at which the flux changes.

The magnets used in these energy harvesters could benefit from a reduction in size for several reasons. By taking advantage of the higher spatial frequencies of the magnet array described earlier in this chapter [72], while maintaining a high stroke length, the total flux change that occurs happens over a shorter time than the actual excitation, a type of frequency up-conversion [18]. Assuming the change in flux remains close to the single large magnet case, this enables a higher time rate of change of flux, thereby increasing the voltage induced. Additionally, utilizing alternating pole magnets, the flux change is increased as the magnetic field changes from positive B_0 to negative B_0 instead of from positive B_0 to zero, effectively doubling the change in flux.

To compensate for the change in magnetic field profile, a complementary coil must be fabricated. Figure 4.1 shows a photograph of an example coil electroplated on glass. Additional coils could be fabricated complementary to this one on the same surface along with two more on the bottom side of the glass, with good alignment, to further increase the induced voltage. For further increase in coil number, a complicated multilayer microfabrication process would be needed, but with substantially increased complexity.

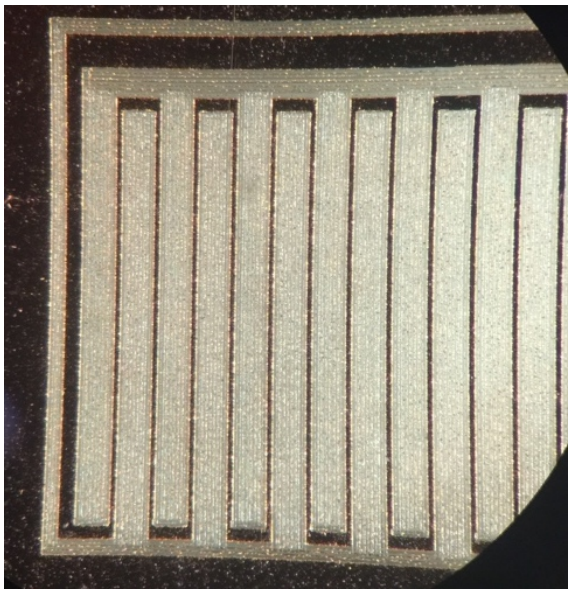

Figure 4.1 Photograph of microfabricated coil winding for magnet array

Looking at the magnet array first as a single magnet, with a coil that matches, followed by how the magnet array increases the induced voltage lends perspective. The magnet array active area is 2 mm wide and 20 mm long and the magnetic flux density amplitude at 100 μm from the surface is approximately 0.1 T. For a length-wise excitation frequency of 5 Hz and a stroke of twice the array length of 40 mm, Δt is 100 ms (a half period) and $\mathcal{E}$ is 0.04 mV:

$$\mathcal{E} = -N\frac{\Delta(BA)}{\Delta t} = -1 \cdot \frac{0.1\ T \cdot (0.002\ m \cdot 0.02\ m)}{0.1\ s} = 0.04\ mV, \tag{4.3}$$

For the magnet array, with the coil in Figure 4.1, the coil area is fifty times (for fifty periods) the single pole area of 2 mm by 200 μm. The associated magnetic flux density amplitude is 0.2 T due to the alternating poles. The oscillation frequency is increased 100x to the equivalent of 500 Hz due to the short travel distance between magnet poles

at the physical oscillation frequency of 5 Hz. Therefore, Δt is 1 ms, and the resulting induced voltage is 4 mV:

$$\mathcal{E} = -N\frac{\Delta(BA)}{\Delta t} = -1 \cdot \frac{0.2\ T \cdot (50 \cdot 0.002\ m \cdot 0.0002\ m)}{0.001\ s} = 4\ mV, \tag{4.4}$$

Some factors that increase this voltage induced are decreasing the distance between the magnet and the coil ($B = 0.25\ T$ at 50 μm from the magnet surface instead of $0.1\ T$ at 100 μm), adding more coils (limited here by magnet thickness), adding a second magnet array as in the undulator case (increasing harvester complexity and limiting coils), and increasing the frequency (limited by human motion but could be higher). For example, if two coils were used that complement each other, at 50 μm height, and 10 Hz operating frequency,

$$\mathcal{E} = -2 \cdot \frac{0.5\ T \cdot (50 \cdot 0.002\ m \cdot 0.0002\ m)}{0.0005\ s} = 40\ mV, \tag{4.5}$$

a very attainable parameter set. Additionally, increasing to 100 Hz could achieve up to 400 mV.

As can be seen in Figure 4.2, the voltage induced is significantly less than the 300 mV necessary for diode rectification, as shown above for low frequencies, but is a large voltage for a single turn of wire at a human excitation frequency from an electromagnetic energy harvester so small [91]. This is partly due to the fact that a 15-μm-thick plastic layer was used to separate the magnet array and the coil.

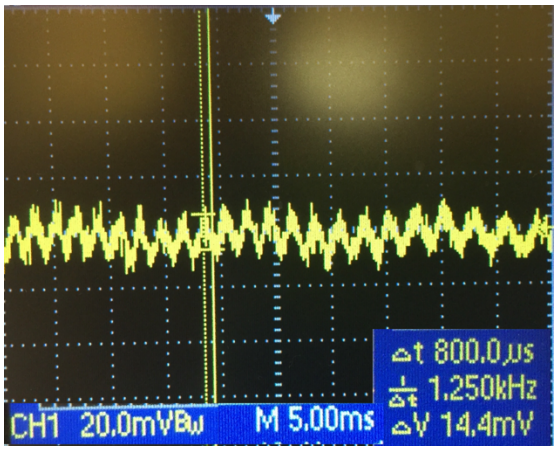

Figure 4.2 Screenshot of induced voltage on magnet array coil

4.2 Constant High Field Over Large Volume

4.2.1 Halbach Cylinder

A similar analog to the magnet array, which is a two-magnet-per-period linear Halbach array, is the Halbach cylinder [27] [28] [92]. Similar to the ability of a linear array to have field only present on the active side (for more than two magnets per period), as shown in Figure 4.3, a Halbach cylinder only has magnetic field on one side as well [93]. The side (inside or outside) of the Halbach cylinder with field is determined by the arrangement of the individual magnets, again relying on superposition. On one side the field is amplified and, in the case where the field is inside the cylinder, the field is uniform across much of the volume within the cylinder; while on the opposite side, the fields cancel. Similar to a linear array, a Halbach cylinder rotates through magnetization directions as it goes through one period. In this case, a period is the full circle. So for k=1, one full magnetization direction rotation takes place as the circumference of the circle is traversed, as shown in Figure 4.4. If physical magnets were placed in this k=1 scenario, the magnetization of each magnet would be point radially outward. This case is not

particularly relevant as no field would be created and this arrangement of magnets would be very difficult to assemble. For the more relevant cases of k=2, k=3, and k=4, two, three, and four full magnetization direction rotations take place as the circumference is traversed, respectively. These arrangements form a strong single direction field (a dipole), a quadrupole, or a sextupole, respectively, which could each be useful along an electron beam line as described in Chapter 3 and shown along the beam line schematic for SLAC in Figure 3.45 [27]. For the sake of simplicity, the k=2 case was studied here and will be referred to as the Halbach cylinder.

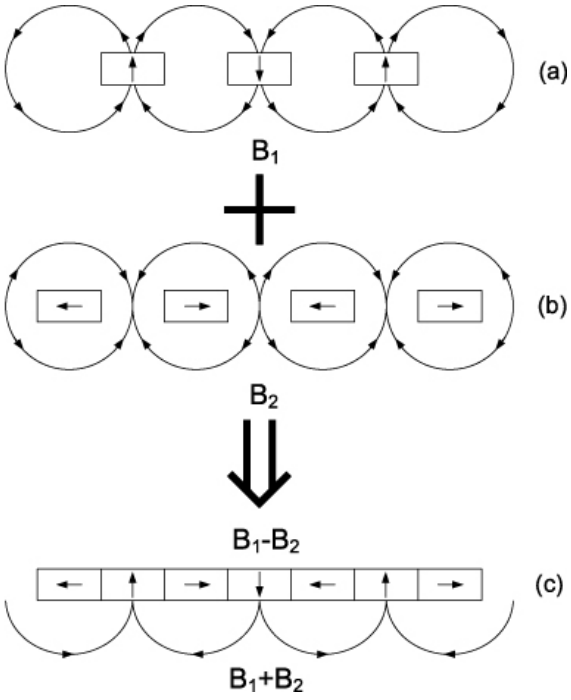

Figure 4.3 Schematic representation of a Halbach array showing superposition of magnet fields

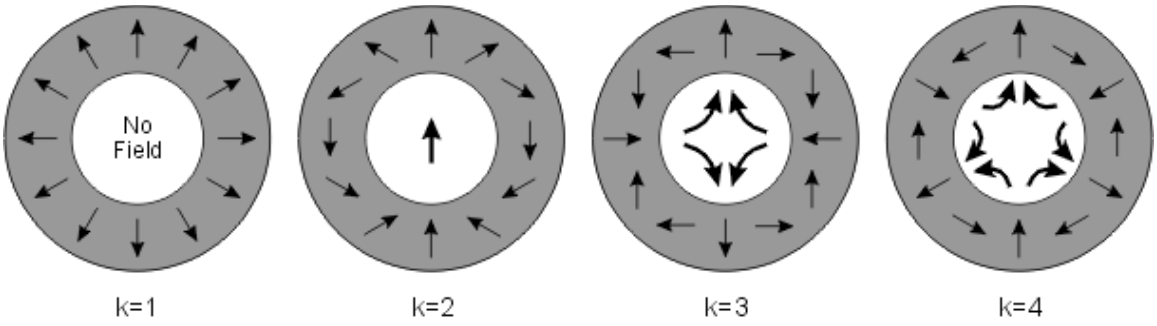

https://en.wikipedia.org/wiki/Halbach_array

Figure 4.4 Schematic representation of Halbach cylinders of one to four magnetization direction rotations per period

COMSOL models were again utilized to determine the ratio of sizes necessary for the Halbach cylinder, specifically magnet thickness, outer diameter, and inner diameter. Figure 4.5a shows a schematic of an 8 discrete magnet Halbach cylinder and Figure 4.5b shows the magnetic flux density along the axis of a Halbach cylinder with outer diameter of 8 mm and inner diameter of 2 mm as a function of magnet thickness and the position along the axis that passes through the center of the Halbach cylinder. Note how for a 1 mm thick Halbach cylinder the magnetic flux density exceeds 0.5 T. As described in section 1.1, as the magnet thickness decreases, the inner and outer diameter should be decreased by the same scale in order to maintain magnetic flux density levels. So, for a 300 μm thick Halbach cylinder with a desired central flux density of 0.5 T, the inner and outer diameter should be 600 μm and 2.5 mm, respectively.

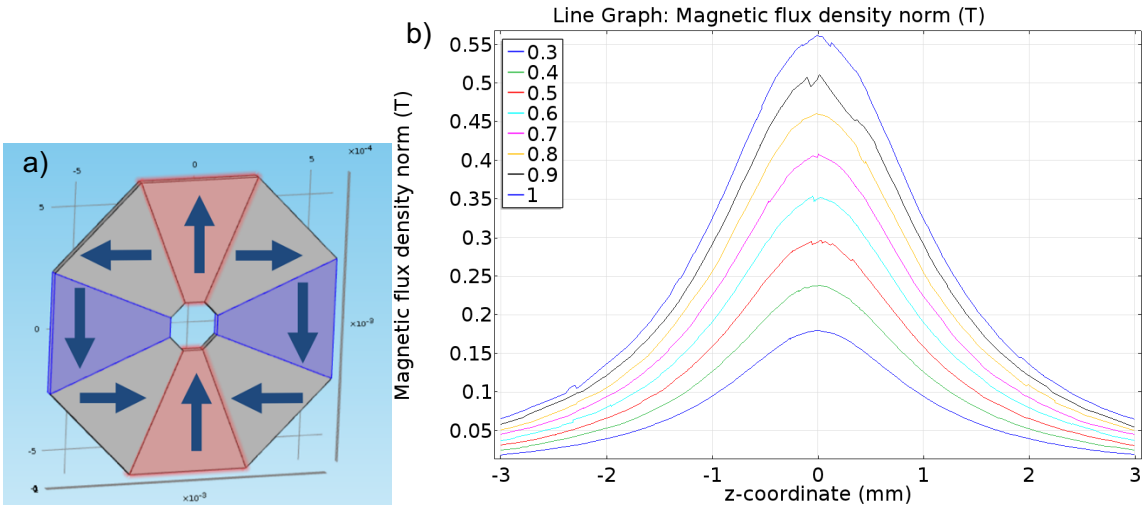

Figure 4.5 a) Schematic showing k=2 Halbach cylinder with 8 discrete magnets and b) corresponding chart showing magnetic flux density as a function of position along the Halbach array axis and magnet thickness (legend)

The Halbach cylinder was fabricated by first cutting the magnets of both 300 μm and 1 mm thickness and marking their preferential magnetization direction. The Si substrate was also laser etched to a depth of approximately 200 μm in the octagonal shape that makes up the outer edge of the Halbach cylinder. The magnets were then installed (after magnetization) individually and adhered to the Si. Due to the arrangement of magnets most in this assembly do not prefer this positioning and require an adhesive to maintain their position. Care should be taken in assembly, as uneven spacing between the magnets will result in a substantial loss in field compared to the model. Figure 4.6 shows a fully fabricated Halbach cylinder with an 8 mm outer diameter and 2 mm inner diameter. The preferential magnetization directions are marked by a line laser etched on the magnet surface and the magnetization directions are marked as green (magnetic south) to red (magnetic north) along those lines. A hole was additionally machined in the

silicon substrate and a Hall sensor was used to measure the magnetic fields within this Halbach cylinder, as shown in the top of Figure 4.7. The black Hall effect sensor is disappearing into the center of the Halbach cylinder in the set of images and individual measurements were taken at 100 μm increments along its axis. The results are shown in the bottom of Figure 4.7 and show good agreement with the COMSOL model and approximately 75% of the simulated field given the unavoidable spacing between magnets.

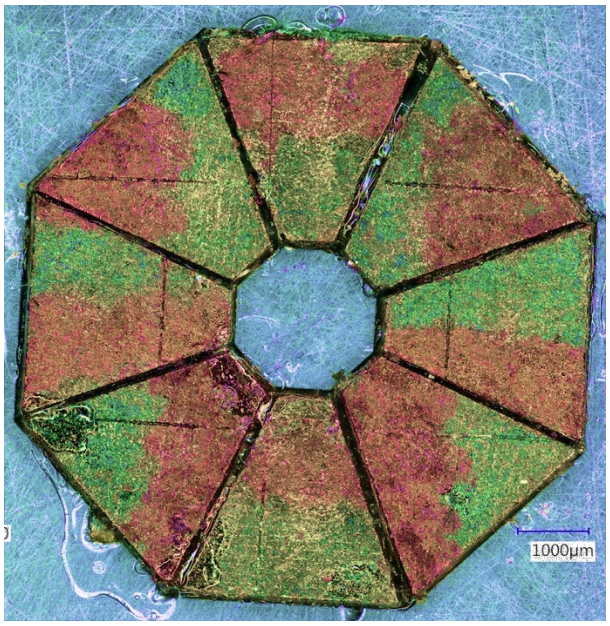

Figure 4.6 Photograph of 2 mm inner diameter Halbach cylinder with 8 discrete magnets; color saturation added to highlight colors indicating magnetization direction

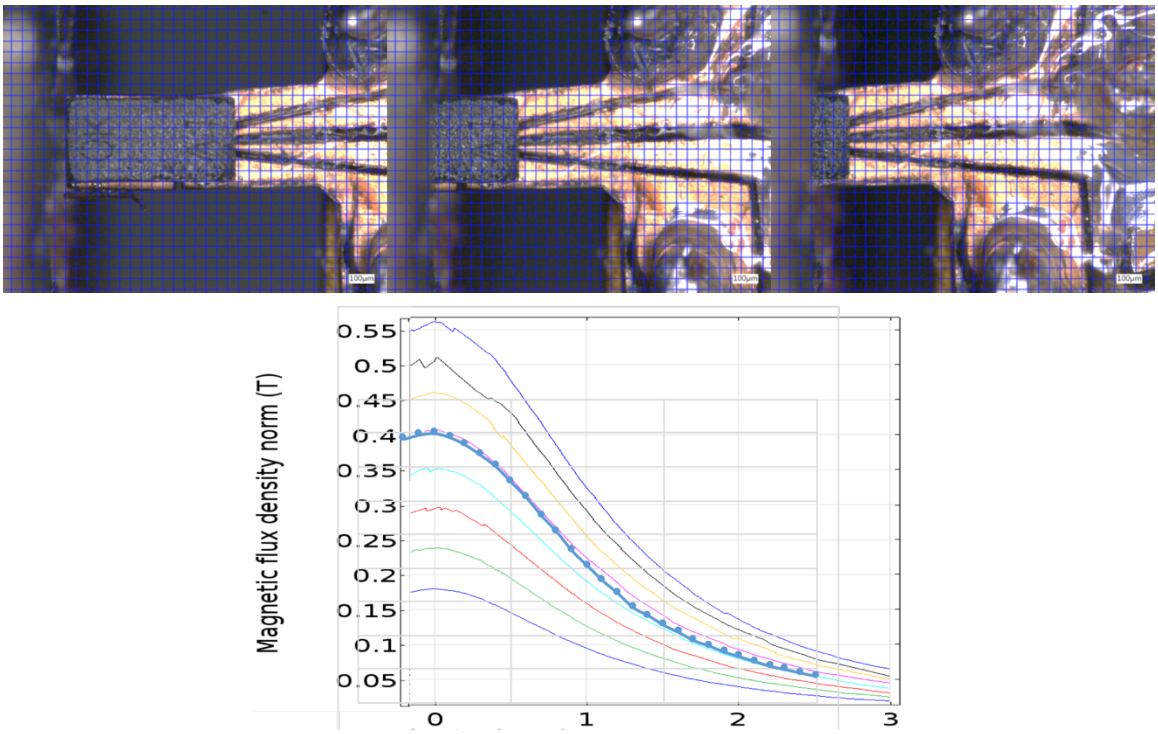

Figure 4.7 (top) Photographs of incremental movements of the Hall effect sensor on copper pads (the grid indicates 100 μm increments) and the measured magnetic flux density at 100 μm increments

4.2.2 Halbach Pseudo-Sphere

While the Halbach cylinder provides a relatively high magnetic flux density along the axis, its more complex counterpart could provide even higher fields, the Halbach sphere. A Halbach sphere is a Halbach cylinder revolved around the magnetic axis, as in Figure 4.8b. For the k=2 cylinder in Figure 4.4, the magnetic axis follows the magnetizations pointing down from the top through the center axis, as in Figure 4.8a. This further amplifies the flux density available in the Halbach core. In the case of laser fabricated micromagnets, taking manufacturing constraints into account, a pseudo-sphere was designed and modeled. The pseudo-sphere involves fabricating two Halbach cylinders,

slicing one in half and placing both halves opposite one another to form an X, as in Figure 4.8c, the resulting magnetic flux densities for this arrangement are shown in Figure 4.9. Note how, for 1 mm thick magnets, the flux density available reaches upwards of 0.9 T. Additionally, one of the added halves could be left off to make the central volume more easily accessible. The results of this modification are shown in Figure 4.10.

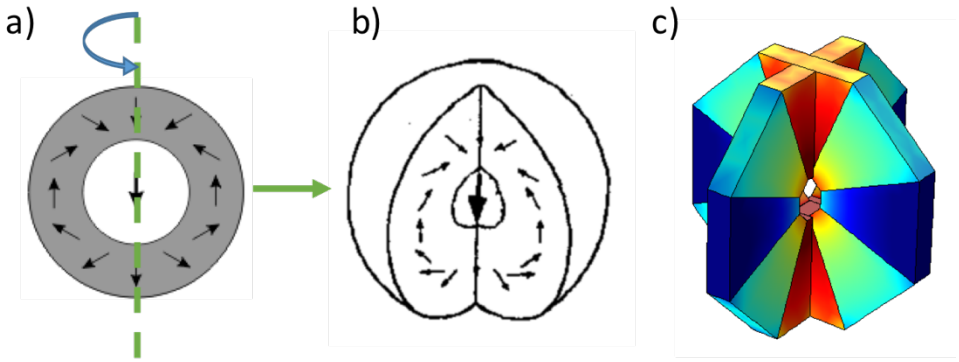

Figure 4.8 Schematic representations of a) the Halbach cylinder revolved around its magnetic axis to form b) the Halbach sphere and c) the Halbach pseudo-sphere that takes fabrication constraints into account

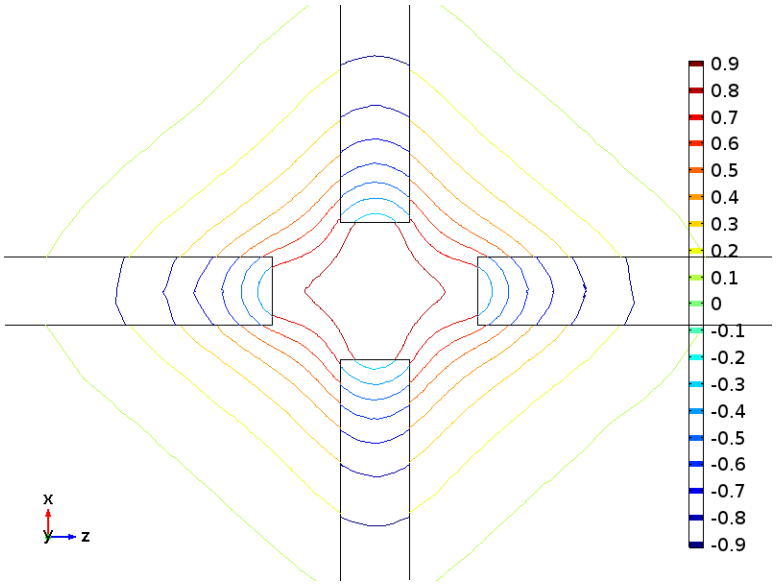

Figure 4.9 Contour plot showing lines of equal flux density within the Halbach pseudo-sphere

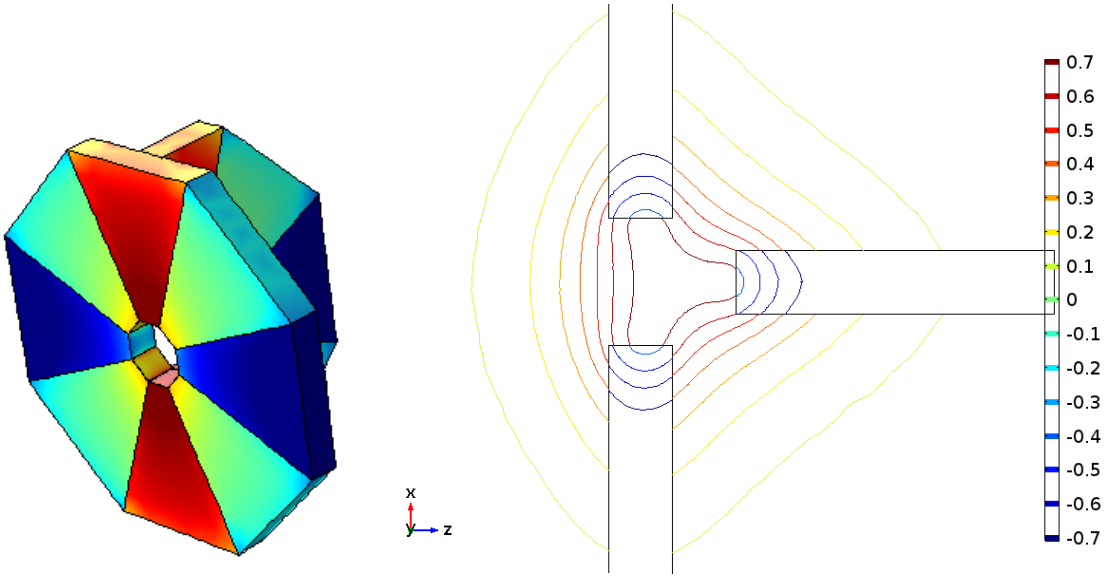

Figure 4.10 Contour plot showing lines of equal flux density within the Halbach pseudo-sphere missing half of the magnets of one cylinder

The Halbach cylinder and sphere provide a relatively high field over most of their inner volume (a cylinder of 1.5 mm diameter and greater than 0.5 mm height or a sphere of diameter 1.5 mm, respectively) and their fabrication complexity is relatively low, providing a strong, powerless alternative to creating relatively strong magnetic fields within a localized volume.

4.3 Undulating Cylinder

An alternative method for creating an undulating magnetic field, similar to that of the magnet array of Chapter 3, involves the stacking of many in-plane magnetized ring magnets, similar to that shown in Figure 4.11a. The magnetic flux density across the center cross section of an in-plane magnetization ring magnet is shown in Figure 4.11b. Alternating the magnetization of adjacent magnets can give an alternating field structure with a periodicity equal to twice the thickness of the magnet. Figure 4.11c shows the magnetic field along the axis of this undulating cylinder. Note how the magnetic flux density peak magnitude for this undulating cylinder is above 0.125 T for a hole 400 μm in diameter. Recall from Chapter 3 that the peak magnetic flux density along the undulator axis was 0.23 T for a 200 μm gap and 0.05 T for a 400 μm gap.

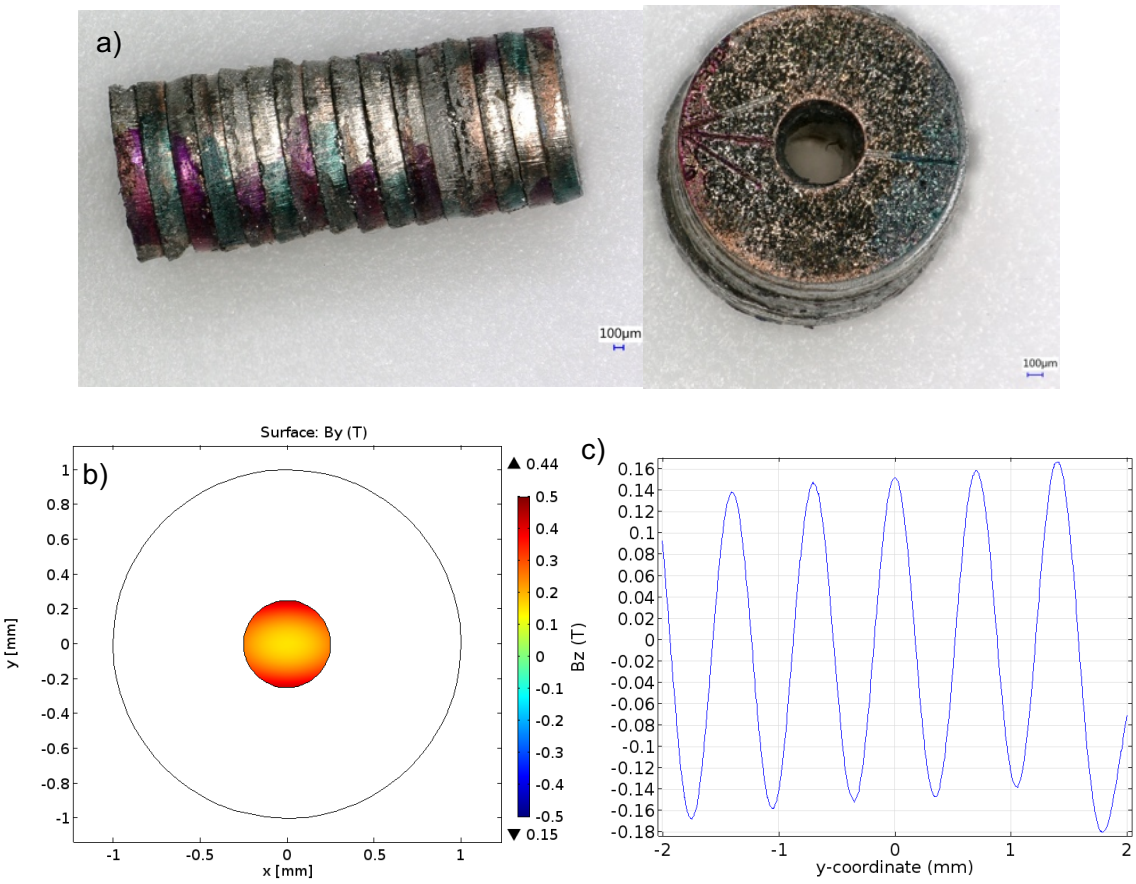

Figure 4.11 Photograph of undulating cylinder prototype and modeled resulting magnetic flux density along the axis

One additional feature of using these in-plane magnetized ring magnets is the ability to rotate individual magnets by less than 180 degrees per magnet from the previous ring magnet to create a helical field profile along the axis of the undulating cylinder. The resulting central axis field profile is shown in Figure 4.12.

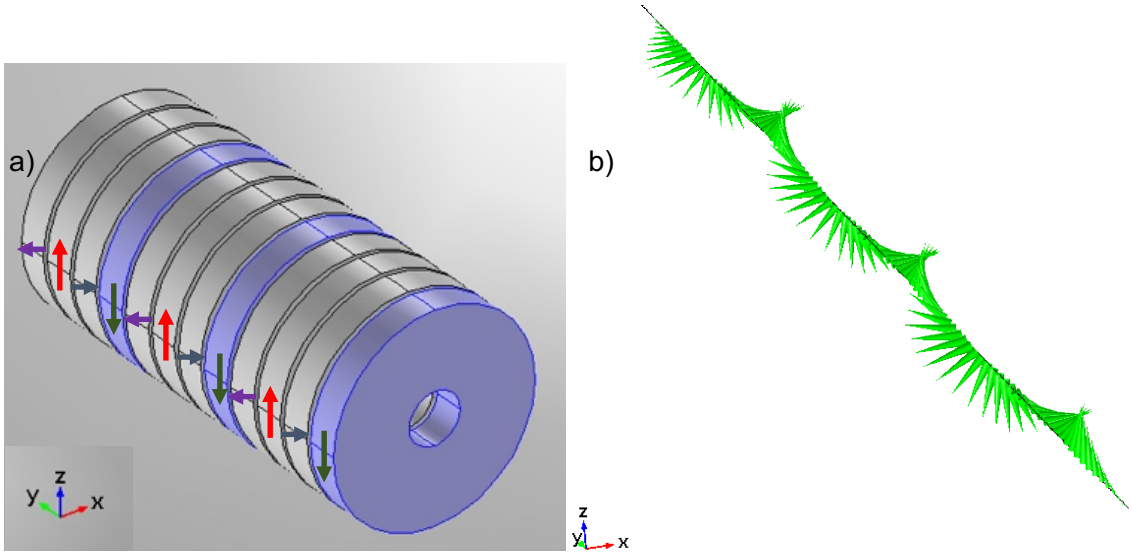

Figure 4.12 a) Schematic of model with highlighted magnetization directions in the plane of the ring and b) field directions along the center axis of a partially rotated ring magnet set

4.4 Arbitrary Magnetic Field Profiles

Magnetic field patterns available from laser-machined micromagnets are only limited by the applications that can utilize the fields they produce. Indeed, several companies exist that design magnetic field patterns to fit the needs of customers on the millimeter and centimeter scale. Simple adaptations would need to take place, but the process and design should be fairly similar for the submillimeter scale. Some additional fields that have not been fully fabricated are a micro-quadrupole, a two-dimensional array of holes in a magnet substrate, and a point of zero magnetic field surrounded by strong field gradients.

4.4.1 Four-Piece Magnetic Quadrupole

An additional insertion device, similar to the undulators and wigglers and as mentioned in section 4.2.1 with the Halbach cylinder, a micro-quadrupole can also be fabricated. In the micro-quadrupole with four magnet pieces, each of four magnets has a magnetization direction rotated 90˚ from its neighbors, as shown by the arrows in Figure 4.13. The colored cones in the 400 μm^2 area between the four pieces show the magnetic flux density direction, with the color designating the strength of the magnetic flux density, at each point. Such a field has the ability to focus a bunch of electrons traveling through it [94].

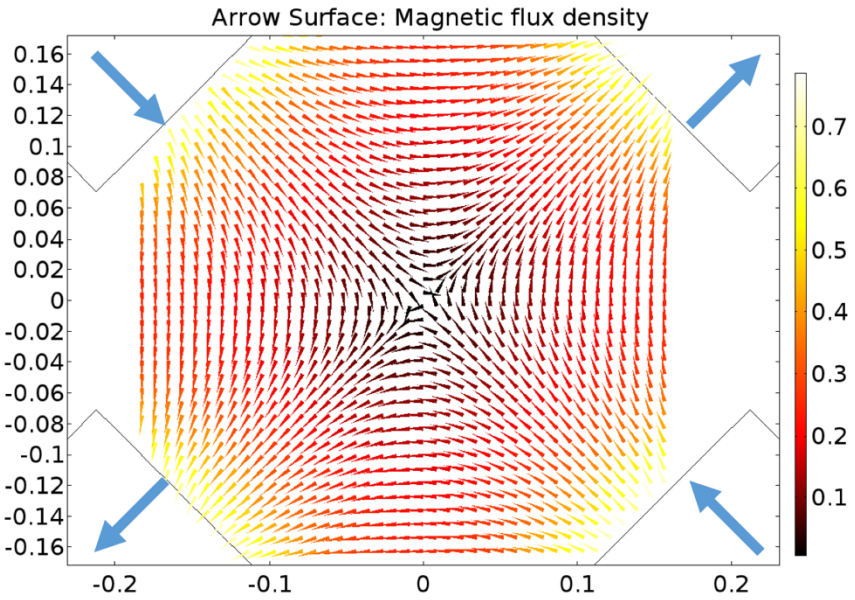

Figure 4.13 Magnetic field directions produced by micro-quadrupole

4.4.2 Two-Dimensional Sinusoidal Field

As mentioned in section 4.1, motors and generators utilize an oscillating magnetic field in conjunction with electrical coils that sense the changing field as the magnets move

with respect to the coils. Applying that same concept to a two-dimensional pattern results in something similar to the field pattern shown in Figure 4.14a. The 5 mm x 10 mm magnet in this scenario has had an array of square holes removed by laser machining. The field in this situation is still sinusoidal, as shown in Figure 4.14b. However, since it relies on a lack of material where it was removed by the laser, the sinusoid is offset based on the ratio of magnet to air.

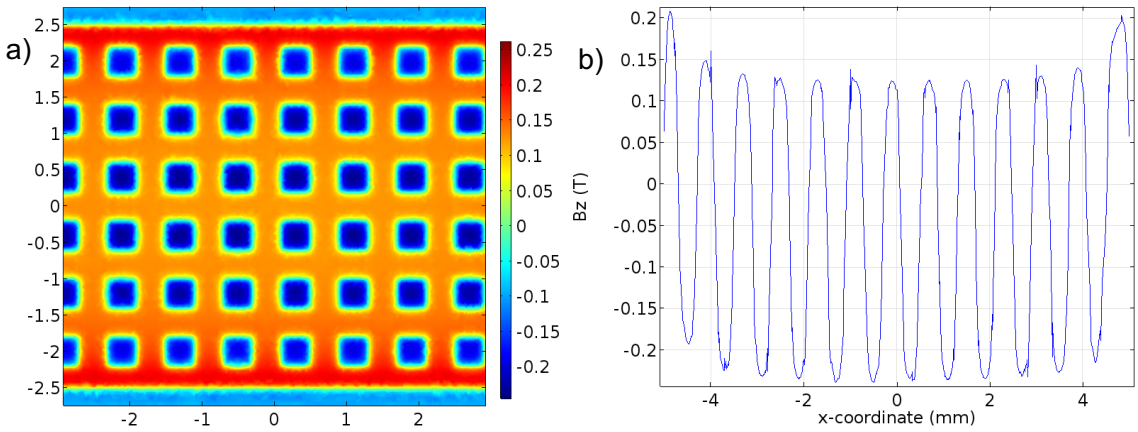

Figure 4.14 Magnetic flux density a) map and b) line scan 50 μm above the magnet substrate surface with 400 μm square holes cut out of the substrate

CHAPTER 5 CONCLUSIONS AND FUTURE WORK

5.1 Conclusions

It has been demonstrated in this dissertation that submillimeter scale magnets can be modeled, laser machined, and assembled to fabricate magnetic field distributions of arbitrary design on the submillimeter scale, as indicated in Figure 5.1. The damaging effects of the laser machining of magnets were modeled and investigated for both NdFeB and SmCo magnetic materials. Applications of multiple field distributions were presented in the previous chapters, and more are presented here for consideration in future research initiatives.

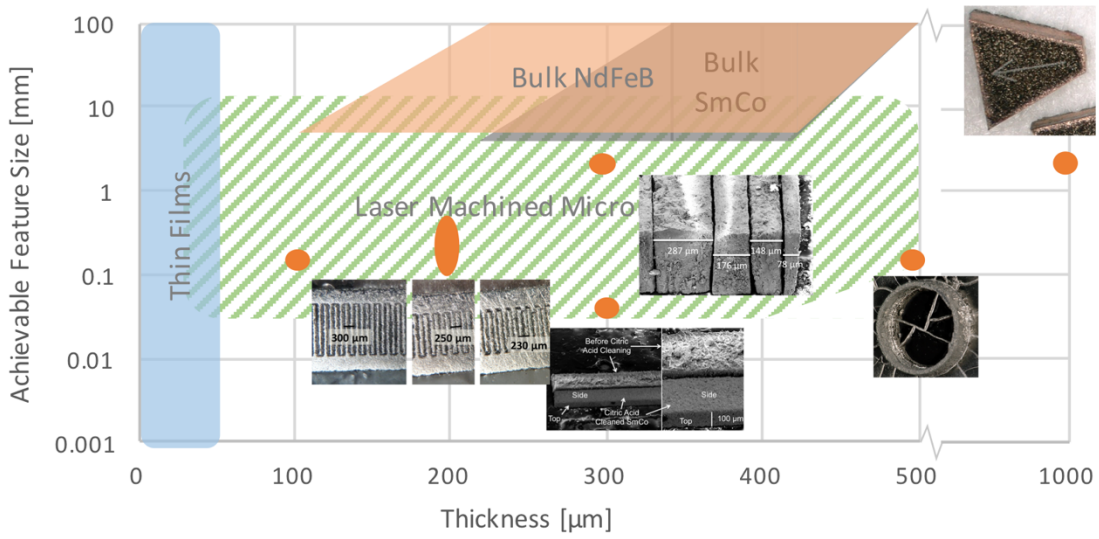

Figure 5.1 Thickness/feature size tradeoffs for different magnet fabrication technologies that also highlights some of the devices fabricated during the course of this dissertation

5.2 Low-Field, Small-Scale MRI

With the relatively large volume magnetic fields of the Halbach cylinder, or half of a Halbach pseudo-sphere, and a correspondingly small microfabricated radio frequency (RF) coil, the essential pieces of a permanent-magnet-based, low-field nuclear magnetic resonance (NMR) system are present. Microcoils have previously been investigated for magnetic resonance imaging (MRI) of skin and other biological objects using millimeter and centimeter scale RF coils [95] [96]. With the addition of high field gradients, such as those associated with the magnet array with some adjustments, a full, portable, microMRI could be fabricated. NMR and MRI operate by placing specific elements within a constant/known magnet field. Known elements with magnetic spins that enable use in magnetic resonance are shown in Figure 5.2 as an adjusted periodic table of elements. While the most common is ^{1}H for research and the only cleared/available medically, many others are in regular use in research: ^{17}O, ^{19}F, ^{23}Na, and ^{31}P are the most commonly used with the human body [97].

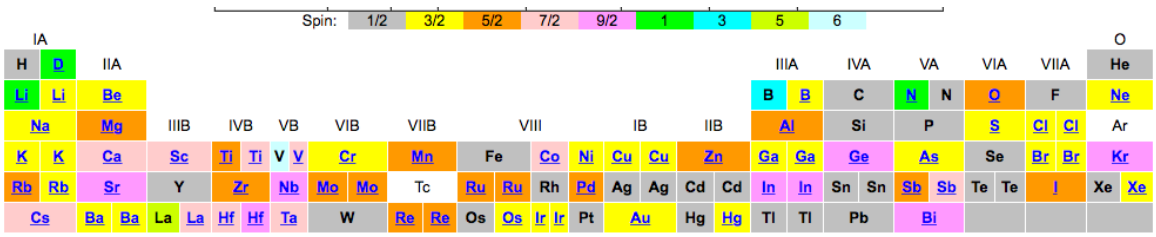

Figure 5.2 Periodic table of elements in magnetic resonance

Magnetic resonance begins by aligning the element half spins with a relatively large, constant magnetic field. The RF coils then tilt the aligned magnetic moments of the half spins off axis using EM radiation at the precession frequency of the desired elements, and the moments begin to precess around the main field axis. As the moments continue

to precess after the RF is turned off, until fully relaxed, they emit radiation at a frequency related to the magnetic field and gyromagnetic ratio of the atomic element the moments are associated with. In NMR, a spectrum is generated that can determine the contents of the sample [96], similar to EDS as shown in section 2.5. An example is shown in Figure 5.3.

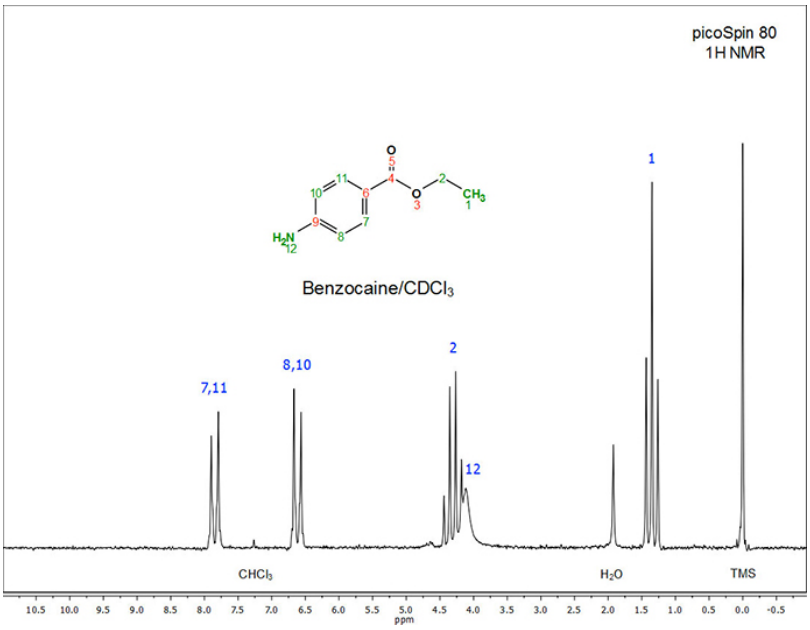

https://www.thermofisher.com/content/dam/LifeTech/Thermo-Scientific/CAD/Marketing-Images/Molecular-Images/picoSpin-pharmaceuticals-Benzocaine-052MCDCl3-690x532.jpg

Figure 5.3 NMR spectrum of benzocaine

As such, a Halbach cylinder with a sample within the main magnetic volume and a corresponding RF microcoil could enable at least portable NMR.

5.3 Breaking Time Reverse Symmetry Using Magneto-Optical Thin Films

An additional use of the undulator from Chapter 3 applies the field within the undulator as an optical switch. Magneto-optical thin films exhibit properties that can break time-reversal symmetry and block (when a magnetic field is aligned to the film – x-direction)

or allow (when a magnetic field is perpendicular to the film – z-direction) the flow of optical energy [98]. Figure 5.4 demonstrates how the magnetic fields vary in the direction of electron travel, $\vec{B}_x$, and for the normal undulator field, $\vec{B}_z$, as in Chapter 3. Figure 5.4a & b are the normal magnetic fields produced by the undulator as designed in Chapter 3. However, Figure 5.4c & d show how the field changes dramatically when one magnet array is offset from the other by a single half-period. In this situation, the magnetic poles are opposing one another, as in Figure 5.5b. Note how the field changes from primarily perpendicular to the film, in z , to primarily along the film, in x, on the axis and relatively so for up to at least 20 μm off axis in either $\pm z$.

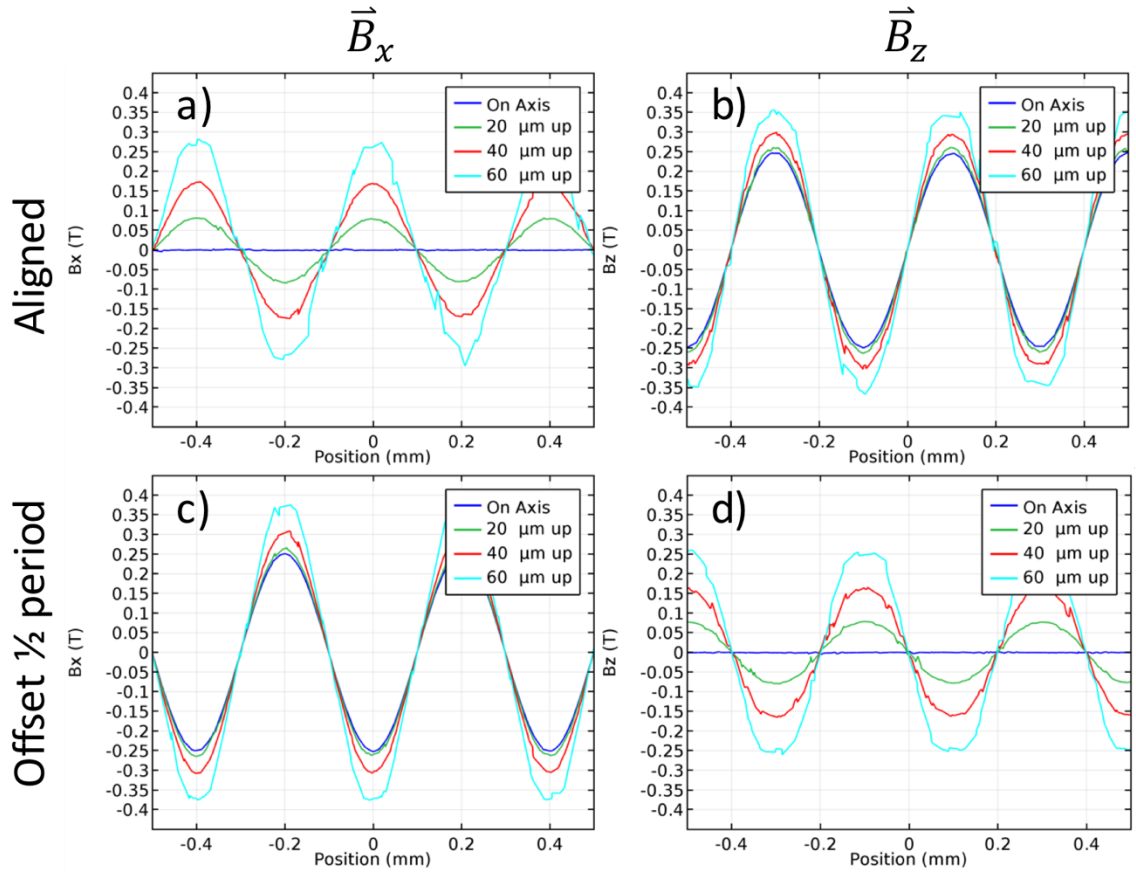

Figure 5.4 Charts showing magnetic flux density along and off the axis between a set of magnet arrays for a) & c) in plane magnetic flux density and b) & d) out-of-plane magnetic flux density for the case where the magnet arrays are a) & b) aligned vs. c) & d) offset by a half period

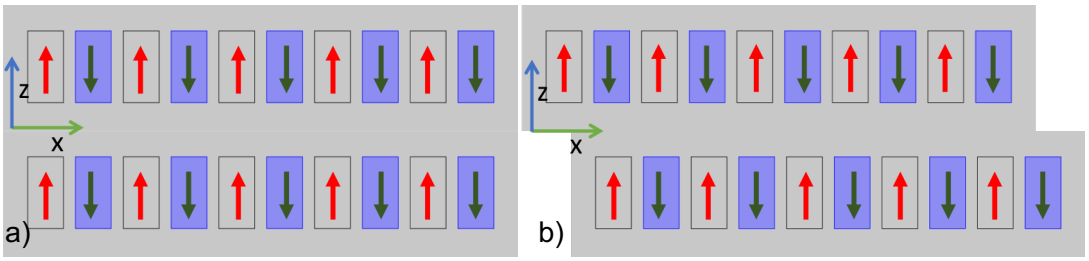

Figure 5.5 Schematic representation of the (left) aligned magnet arrays, and (right) with the lower array offset by a half period such that the magnetizations of individual magnets oppose those of the upper array

5.4 Magnetic Microfluidic Desalination or Ion Manipulation

An interesting application for micromagnets is for use in microfluidic systems. Some applications could involve the movement of particles, such as the iron oxide nanoparticles of section 4.4.1 or the deflection of ions similar to that which is done for the electron within the undulator. Indeed, ions utilize the same force as that of electrons, repeated here,

$$\vec{F} = q\left(\vec{E} + \vec{v} \times \vec{B}\right), \tag{3.1}$$

but the effect of the force is minimized due to the much larger size of the ions and reduced velocity. Large scale demonstrations of this concept are in use as, for example, salt water flow meters [99]. When salt water passes through a magnetic field while travelling down a pipe, the chlorine and sodium ions separate and migrate to opposite sides of the pipe. When that pipe is set up with electrodes, a voltage can then be measured that is an indication of the flow velocity within the pipe, as shown in Figure 5.6, as long as the ion concentration remains fairly uniform. The magnets are at the top and bottom of the figure applying the magnetic field that follows the vertical lines and the

electrodes are on the left and right. The red and blue particles in the image are the chlorine and sodium ions, respectively, as they flow from background to foreground in the left image, or from top-right to bottom-left in the rotated image to the right.

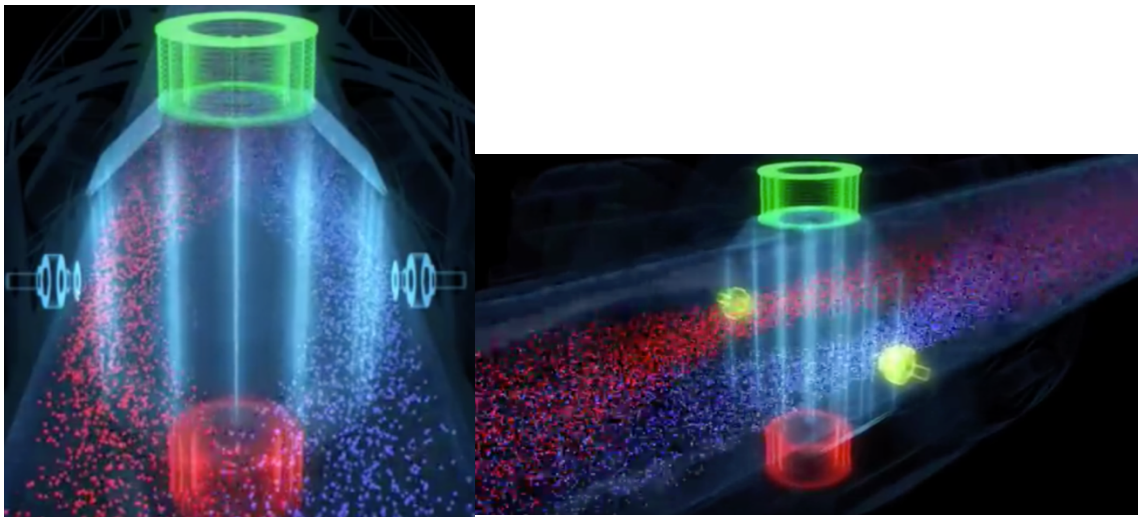

http://www.endress.com/en/Field-instruments-overview/Flow-measurement-product-overview

Figure 5.6 Illustrative representation of a magnetic flow sensor showing the separation of the chlorine and sodium ions in the salt water as red and blue streams

As can be imagined the ions can be manipulated within the fluid. An obvious example with salt water is desalination. Imagining the above figure with a separation into three pipes while under the influence of the magnetic field should yield two pipes with a high concentration of ions that would result in brine when recombined, instead of normal salt water, and the middle pipe would have a reduced concentration of ions or possibly an adequate desalination for drinking.

The same principle could be used to appropriately mix ions in microfluidic channels over short distances where traditional microfluidic channels would have little to no mixing due to a very low Reynolds number. Extending this concept to vacuum processing, electrons

and plasmas could additionally be manipulated to have new and interesting flow/travel patterns that enhance a process flow.

Pacific Pac Technologies

	Micromachining Capability Specification in mm	*http://www.ppactech.com/mcs.htm*
Material Type	NdFeB magnet	SmCo magnet
Slender rod	0.30x30.00mm	0.70x10.00mm
Thin-wall-tube	OD0.90(+/-0.03)-ID0.65(+/-0.05)x4.50mm	OD1.50(+/-0.03)-ID0.60(+/-0.05)x5.00mm
Ring	OD3.00(+/-0.03)-ID0.20(+/-0.03)x0.4(+/-0.005)mm	OD3.00(+/-0.03)- ID0.20(+/-0.03)x0.4(+/-0.005)mm
Tube	ID0.40(+/-0.05)x10.00mm	ID0.40(+/-0.05)x6.00mm
Rectangle	10.00(+/-0.03)x5.00(+/-0.03)x0.10(+/-0.005)mm	10.00(+/-0.03)x5.00(+/-0.03)x0.30(+/-0.005)mm
Disc	D0.50(+/-0.03)x0.20(+/-0.005)mm	D3.00(+/-0.03)x0.25(+/-0.015)mm
Material Type	Ferrite magnet	Alnico magnet
Slender rod	0.70x10.00mm	0.70x10.00mm
Thin-wall-tube	OD1.50(+/-0.03)-ID0.60(+/-0.05)x3.00mm	OD1.50(+/-0.03)-ID0.80(+/-.05)x3.00mm
Ring	OD3.00(+/-0.03)-ID0.20(+/-0.03)x0.4(+/-0.005)mm	OD3.00(+/-0.03)- ID0.20(+/-0.03)x0.4(+/-0.005)mm
Tube	ID0.60(+/-0.05)x6.00mm	ID1.00(+/-0.05)x6.00mm
Rectangle	10.00(+/-0.03)x5.00(+/-0.03)x0.30(+/-0.005)mm	10.00(+/-0.03)x5.00(+/-0.03)x0.10(+/-0.005)mm
Disc	D2.25(+/-0.03)x0.80(+/-0.005)mm D1.00(+/-0.03)x0.50(+/-0.005)mm	OD3.00(+/-0.03)x0.4(+/-0.005)mm
Material Type	Ceramic	Gemstone/Crystal
Slender rod	0.20(+/-0.01)x10.00mm	0.20(+/-0.01)*10.00mm
Thin-wall-tube	OD0.90(+/-0.03)-ID0.65(+/-0.05)x4.50mm	OD0.90(+/-0.03)-ID0.65(+/-0.05)*4.50mm
Ring	OD3.00(+/-0.03)-ID0.20(+/-0.03)x0.4(+/-0.005)mm	OD3.00(+/-0.03)- ID0.20(+/-0.03)*0.4(+/-0.005)mm
Tube	ID0.60(+/-0.05)x5.00mm	ID0.60(+/-0.05)*5.00mm
Rectangle	10.00(+/-0.03)x5.00(+/-0.03)x0.10(+/-0.005)mm	10.00(+/-0.03)*5.00(+/-0.03)*0.10(+/-0.005)mm
Disc	D0.20(+/-0.03)x0.10(+/-0.005)mm	D0.20(+/-0.03)*0.10(+/-0.005)mm
Note:	1. We specialize in odd-shaped machining and precision assemblies.	
	2 . Please check with our sales person for details and special features.	
	3 . Chamfer and break-sharp-edge can be achieved per customer request	
e-mail:	ppac@sbcglobal.net	Tel: 714-252-9411, Fax: 714-252-9414

K&J Magnetics

https://www.kjmagnetics.com/custom.asp

Request Pricing for Custom Neodymium Magnets

Size Limitations:

- 2" max in the magnetized direction
- 4" max diameter for discs and cylinders
- 3" max diameter for rings
- 4" max length and width for blocks
- 1/32" minimum on thickness on any magnet
- 1/16" minimum diameter on outer diameter
- 1/16" minimum diameter on any hole

In other words, your magnet shape should fit within the boundaries of a 4" x 4" x 2" box, with the magnetization direction in the 2" direction.

Also note that neodymium magnets are made from a hard, brittle material. Many shapes that would be easy to manufacture in a steel or aluminum part are not necessarily feasible in a neodymium magnet. Complex shapes or shapes with thin cross sections might not be possible.

Correlated Magnetics Technologies

Results from emails

-Widths as small as 2mm. Suggest no smaller than 3/8".

-Thicknesses thicker than 1mm; even at those thicknesses cost is increased due to waste from grinding the material and from breakage in the process.

-Tolerance is +/- 0.25mm.

-Any grade and any permanent magnetic material. Large range of coatings available.

-No minimum pole size for most applications, poles can be overwritten to create extremely small regions.

-Note that the transition gap between regions can get larger than the regions if the regions get extremely small. There will always be a transition gap even if two magnets are glued together.

polymagnet.com

Quotation - Pacific PAC Technologies, Inc.

30306 Esperanza Tel: 949-459-8811

Rancho Santa Margarita, CA 92688 Fax: 949-459-8816

Attn:		Date:	October 9, 2015
To:		Ref:	
		Inq.#:	
		FOB:	
Tel:		Terms:	
Email:			

Item	Description	Quantity Each	Unit Price
	Part Numbers: SM30-TBDs Unit: Inch SmCo 30/25 Rectangular Magnets Br=10.7-11.2 kGauss, Hc>=8.8 kOe, Hci>=25.0 kOe, (BH) max=28.0-31.0 MGOe +/-0.004 for un-specified dimensions Supplied oriented parallel to (M) dimension and un–magnetized		
1	L0.400xW0.200xT0.012(M)+/-.002	40	$9.25
2	L0.400(M)xW0.200xT0.012+/-.002	15	$9.25
3	L0.400(M)xW0.200xT0.040,	25	$10.50
4	L0.400xW0.400xT0.040(M)	10	$11.84
	Estimated Shipping		$84
Total ***			$973.65

David Dai, Sr. Application Engineer

Laser programming for Nd:YLF laser

Programming language is built by Resonetics, Inc. using Turbo C++. The software utilizes the Oregon Micro Systems (OMS) PC39 family of commands to run the hardware controllers.

This program machines a 10-period comb of 400 μm periodicity on the Nd:YLF laser

```
; BP_COMB5
; CONVERTED FROM C:\Users\brock\Desktop\BP_comb.DXF
; Using RESONETICS DXF CONVERTER Ver. 2.1
; Date:  10/20/2011
; Time:  10:16:36
; Standard Cutting Mode
;------------------------------------------------------------
AA      LP0,0,0,0       ;Stage initial position
;------------------------------------------------------------
OL3     ;Beam Stop Open
OL5     ;Process Air
OL0     ;Laser Enable
PW100           ;Laser Pulse Width  (usec)
PP1000          ;Laser Pulse Period (usec)
;------------------------------------------------------------

%1=2.54         ;slew velocity mm/s
%2=0.03         ;velocity mm/s
%3=10           ;number of comb prongs
%4=4            ;number of cuts for each line
%5=0.5      ;frame width
%6=0.15                 ;x cut length
%7=0.75                 ;y cut length
%8=%6*2*%3 ;overall comb length
%9=%7+%5*2;overall comb width
%10=%7+%5  ;prong y start cutting

GET "HOW MANY TIMES TO CUT BACK AND FORTH (3=6+1)?",%4

VL%1,%1                         ; Set slew velocity
AC127,127               ; Set slew acceleration
MA0,%10                         ; Move to
```

```
; ---- Start contour 1 -----
ls%3                    ; comb prong loop
ls%4                    ; cut +x prong
VL%2,%2                         ; Set cutting velocity
AC127,127               ; Set cutting acceleration
PN100                   ; Piercing
CutREL %6,0             ; Cut relative to current position: (x,y)
CutREL -%6,0
le
CutREL %6,0
ls%4                    ; cut -y prong
VL%2,%2                         ; Set cutting velocity
AC127,127               ; Set cutting acceleration
PN100                   ; Piercing
CutREL 0,-%7
CutREL 0,%7
le
CutREL 0,-%7
ls%4                    ; cut +x prong
VL%2,%2                         ; Set cutting velocity
AC127,127               ; Set cutting acceleration
PN100                   ; Piercing
CutREL %6,0
CutREL -%6,0
le
CutREL %6,0
ls%4                    ; cut +y prong
VL%2,%2                         ; Set cutting velocity
AC127,127               ; Set cutting acceleration
PN100                   ; Piercing
CutREL 0,%7
CutREL 0,-%7
le
CutREL 0,%7
le

; ---- Start contour 2 -----
ls%4                    ; cut +y to comb edge
VL%2,%2                         ; Set cutting velocity
AC127,127               ; Set cutting acceleration
PN100                   ; Piercing
CutREL 0,%5
CutREL 0,-%5
le
CutREL 0,%5
ls%4                    ; cut -x to comb edge
VL%2,%2                         ; Set cutting velocity
```

```
AC127,127               ; Set cutting acceleration
PN100                   ; Piercing
CutREL -%8,0
CutREL %8,0
le
CutREL -%8,0
ls%4                    ; cut -y to comb edge
VL%2,%2                         ; Set cutting velocity
AC127,127               ; Set cutting acceleration
PN100                   ; Piercing
CutREL 0,-%9
CutREL 0,%9
le
CutREL 0,-%9
ls%4                    ; cut -x to comb edge
VL%2,%2                         ; Set cutting velocity
AC127,127               ; Set cutting acceleration
PN100                   ; Piercing
CutREL %8,0
CutREL -%8,0
le
CutREL %8,0
ls%4                    ; cut +y to last cut to prev line
VL%2,%2                         ; Set cutting velocity
AC127,127               ; Set cutting acceleration
PN100                   ; Piercing
CutREL 0,%5
CutREL 0,-%5
le
CutREL 0,%5

VL2.54,2.54             ; Set slew velocity
AC127,127               ; Set slew acceleration
MA0,0 ; Move back to Stage initial position
;-------------------------------------------------------------
OH3    ;Beam Stop Close
OH5    ;Process Air
OH0    ;Laser Enable
;-------------------------------------------------------------
; End of file
```

Laser programming for Green IPG laser

Programming is done through the IPG Photonics built Chroma.net laser programming software.

This program machines SmCo rectangles 2 mm x 500 µm and 300 µm thick on the green laser

1	Call [Global]GLPMacroHeader
2	Stage Counters(X Axis,Y Axis,Z Axis,Theta Axis)=Zero
3	Laser Set Field(GLP, Current Setpoint = 50.0 %)
4	Laser Set Field(GLP, Repetition Rate = 100000 Hz)
5	Delay 1500 mSec
6	Laser Set Field(GLP, Start Laser)
7	Call [Global]GLPGalvoProf3
8	Delay 4000 mSec
9	Check Laser State GLP = Running
10	Comment: **********Macro writing begins here**********
11	Set Variable LineLengthX = 500
12	Set Variable LineLengthY = 2000
13	Set Variable LineLengthXHalf = LineLengthX ÷ 2
14	Set Variable LineLengthYHalf = LineLengthY ÷ 2
15	Set Variable LineLengthXHalfNeg = LineLengthX ÷ -2
16	Set Variable LineLengthYHalfNeg = LineLengthY ÷ -2
17	Set Variable LinePasses = 250
18	Comment: Variables above here
19	Galvo Jump(0.0 µm, 0.0 µm)
20	Start Loop: Passes=LinePasses
21	Move-From Origin:X Axis=0.0, Y Axis=LineLengthYHalf
22	Call GLPsub_GalvoLineXWide(LineLengthX)
23	Galvo Jump(0.0 µm, 0.0 µm)

```
23  Galvo Jump(0.0 µm, 0.0 µm)
24  Galvo Wait Flag(1)
25  Galvo Execute
26  Galvo Wait For Galvo(1, 600.0 Sec)
27  Move-From Origin:X Axis=LineLengthXHalf, Y Axis=0.0
28  Call GLPsub_GalvoLineYWide(LineLengthY)
29  Galvo Jump(0.0 µm, 0.0 µm)
30  Galvo Wait Flag(1)
31  Galvo Execute
32  Galvo Wait For Galvo(1, 600.0 Sec)
33  Move-From Origin:X Axis=0.0, Y Axis=LineLengthYHalfNeg
34  Call GLPsub_GalvoLineXWide(LineLengthX)
35  Galvo Jump(0.0 µm, 0.0 µm)
36  Galvo Wait Flag(1)
37  Galvo Execute
38  Galvo Wait For Galvo(1, 600.0 Sec)
39  Move-From Origin:X Axis=LineLengthXHalfNeg, Y Axis=0.0
40  Call GLPsub_GalvoLineYWide(LineLengthY)
41  Galvo Jump(0.0 µm, 0.0 µm)
42  Galvo Wait Flag(1)
43  Galvo Execute
44  Galvo Wait For Galvo(1, 600.0 Sec)
45  Move-Incremental:Z Axis=1.00
46  End Loop
47  Move-From Origin:Z Axis=0.00
48  Galvo Jump(0.0 µm, 0.0 µm)
49  Comment:  This section runs the galvo script above
50  Galvo Jump(0.0 µm, 0.0 µm)
51  Galvo Wait Flag(1)
52  Galvo Execute
53  Galvo Wait For Galvo(1, 600.0 Sec)
54  Comment:  Until here
55  Comment:  **********Macro writing ends here**********
56  Move-From Origin:X Axis=0.0, Y Axis=0.0
57  Stage Counters(X Axis,Y Axis,Theta Axis,Z Axis)=Restore to Default
58  Call [Global]GLPMacroFooter
    (Click to Add New Line)
```

APPENDIX C Magnetic Material Properties

Material Grade	Sm2Co17 30/25	Nd2Fe14B N48	Nd2Fe14B N52
Hci [kA/m]	2000	965	1000
Hci [kOe]	25	12.1	12.3
Br [T]	1.1	1.4	1.45
BHmax [kJ/m3]	240	374	406
BHmax [MGO]	30	47	51
Curie Temp [˚C]	800	300-400	300-400
Tmax [˚C]	300	100	100
Reversible Temperature Coefficient of Remanence [%/˚C]	-0.03	-0.12	-0.12
Reversible Temperature Coefficient of Coercivity [%/˚C]	-0.2	-0.75	-0.75
Coefficient of Thermal Expansion (Parallel to Magnetization) [10^-6/˚C]	8	7.5	7.5
Coefficient of Thermal Expansion (Perpendicular to Magnetization) [10^-6/˚C]	11	-0.1	-0.1
Thermal Conductivity [W/(m•K)]	11.6	8.9	8.9
Specific Heat Capacity [J/(kg•K)]	375	460	460
Compressive Strength [N/mm2]	700	950	950
Flexural Strength [N/mm2]	125	250	250
Tensile Strength [N/mm2]	35	75	75
Tensile Strength [kg/mm2]	3.6	8	8
Resistivity μΩ•cm	86	150	150
Density [g/cm^3]	8.3	7.5	7.5
Vickers Hardness [D.P.N]	575	570	570
Young's Modulus [10^11 N/m2]	1.2	1.6	1.6
Poisson's Ratio	0.27	0.24	0.24
Rigidity [N/m2]	150	0.64	0.64

Magnetic Material Phase Diagrams

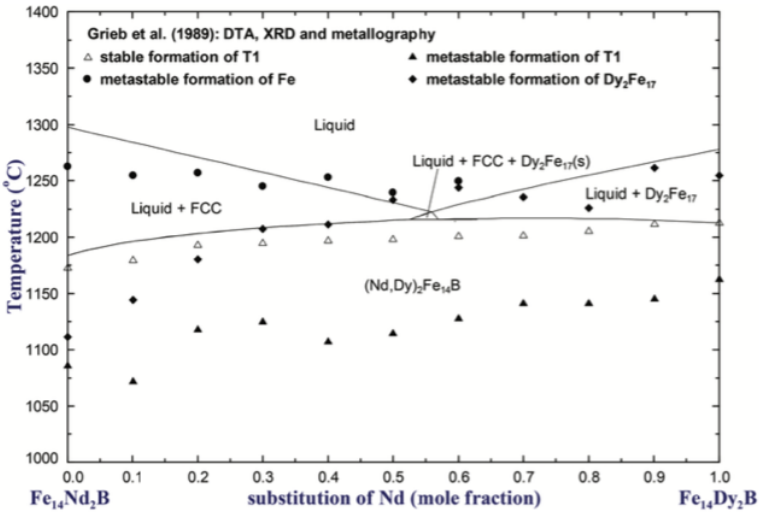

http://pubs.rsc.org/en/content/articlehtml/2015/GC/C4GC02232G [100]

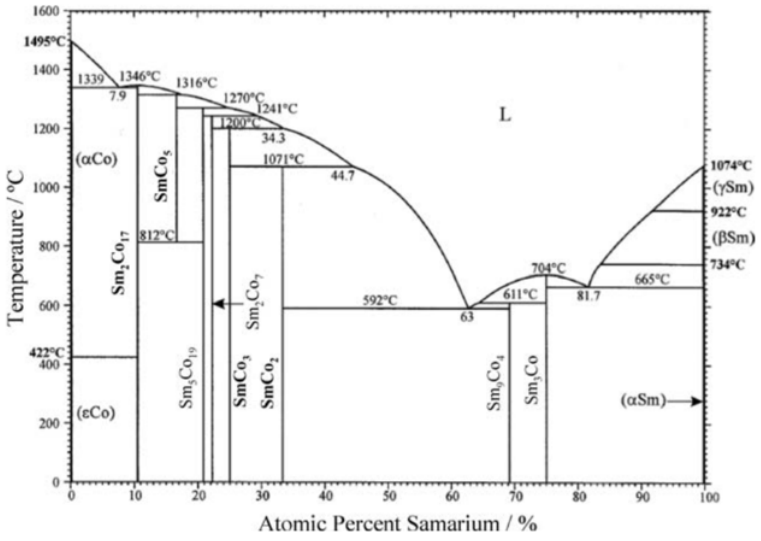

[101]

APPENDIX D Magnet Images

Rectangles, combs, Iris images

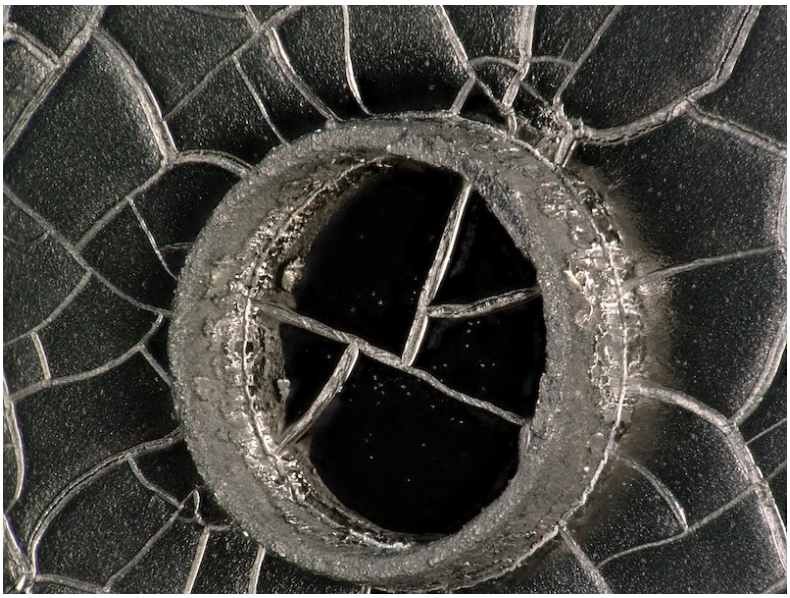

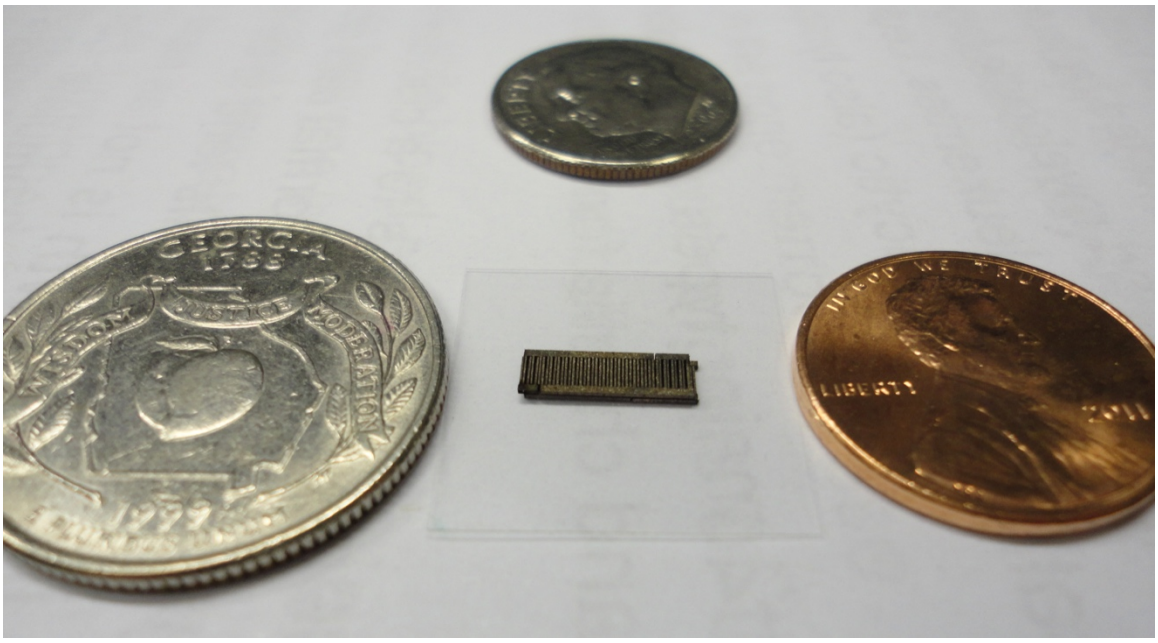
GEORGIA
1788
WISDOM
JUSTICE
MODERATION
LIBERTY

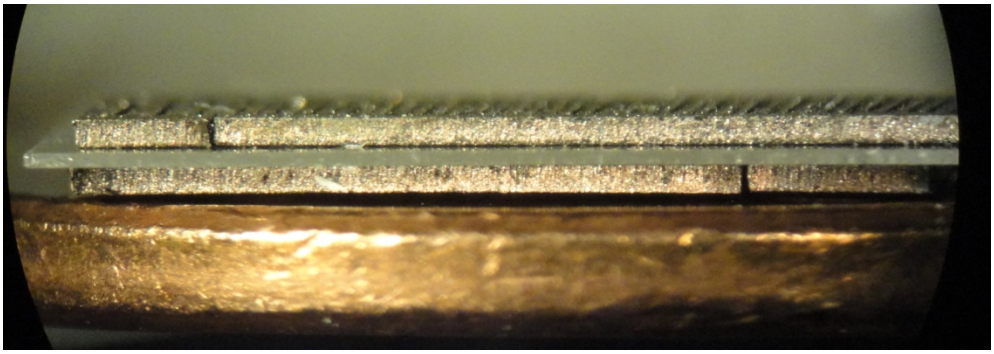

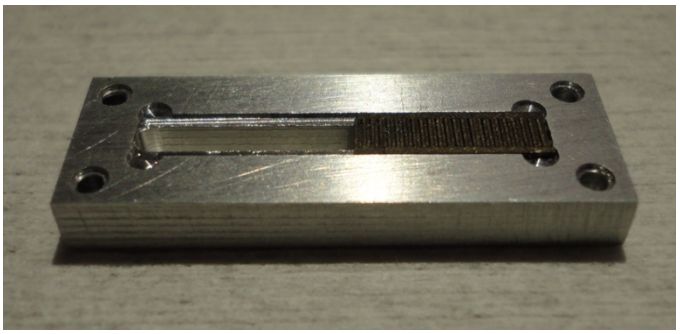

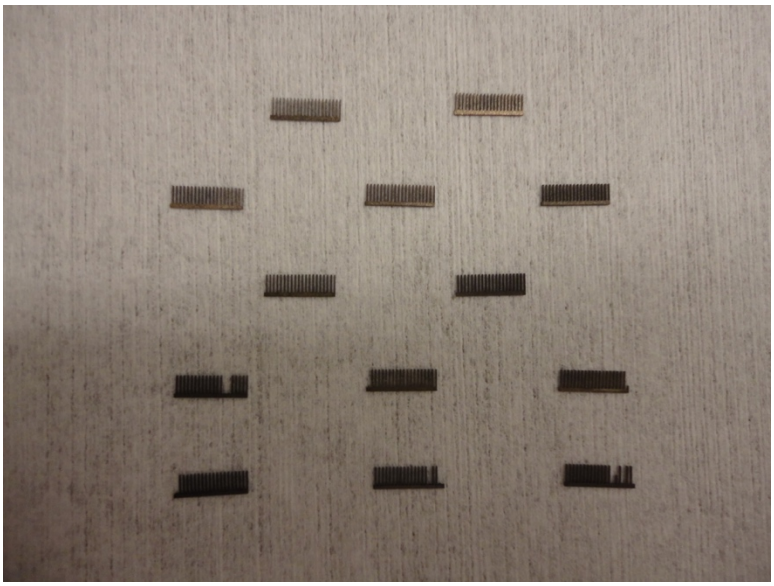

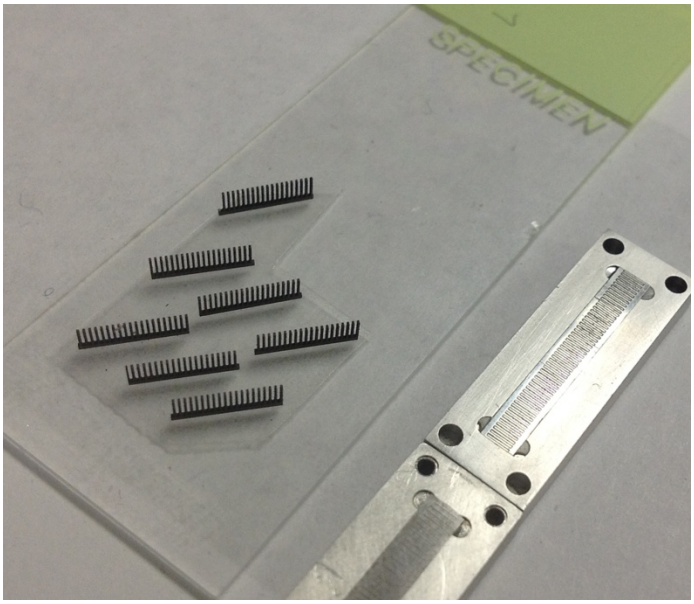
SPECIMEN

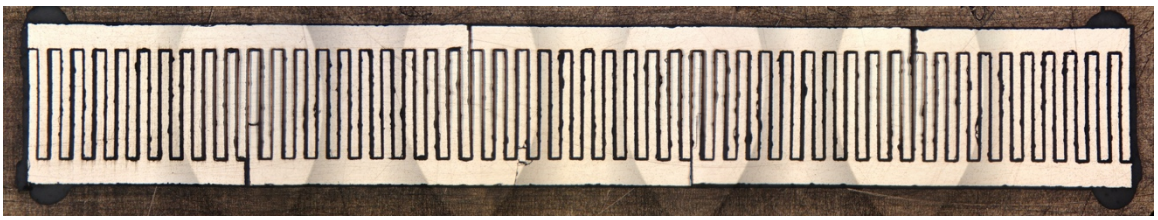

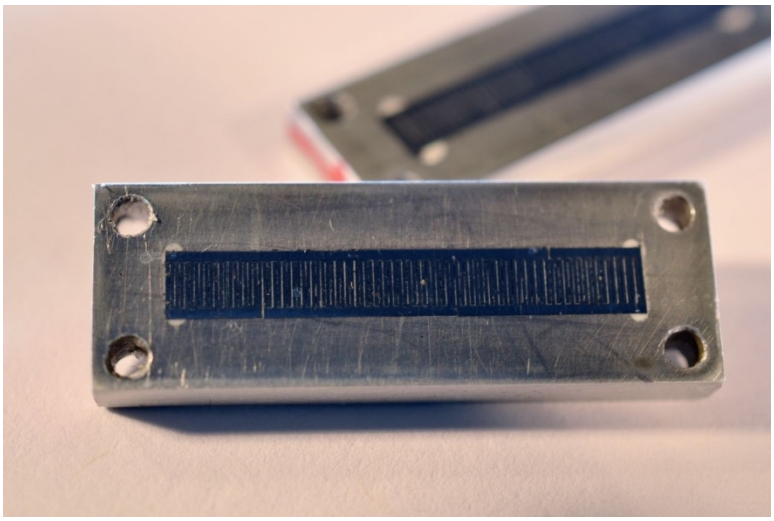

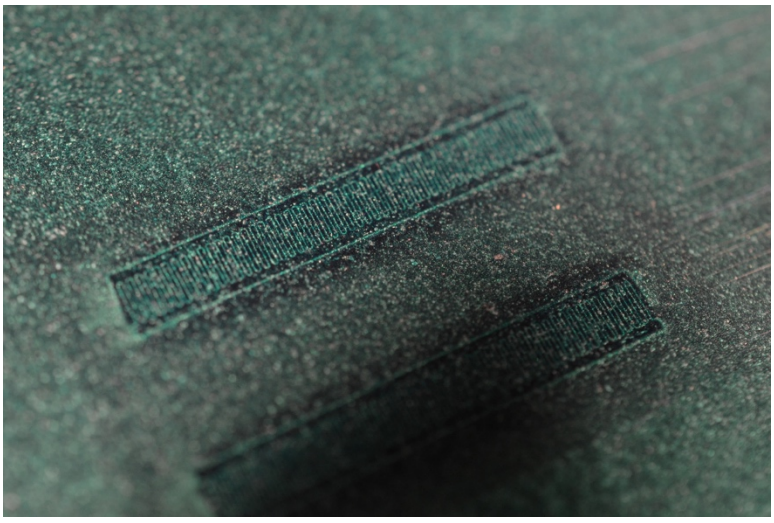

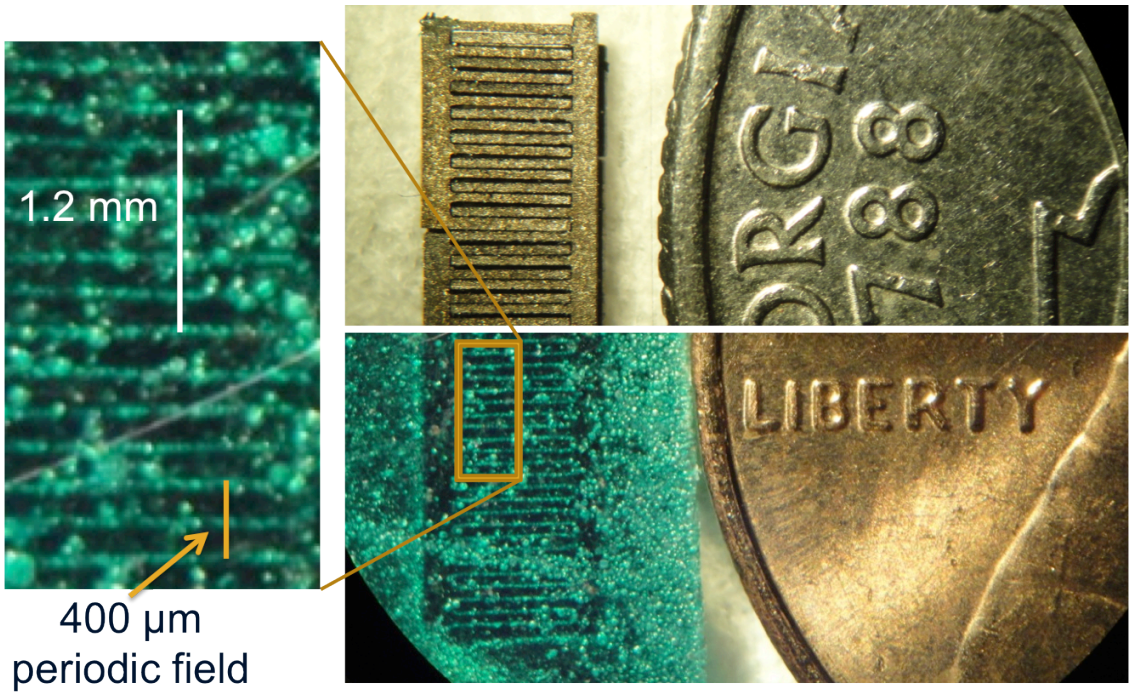
1.2 mm
400 µm
periodic field
LIBERTY

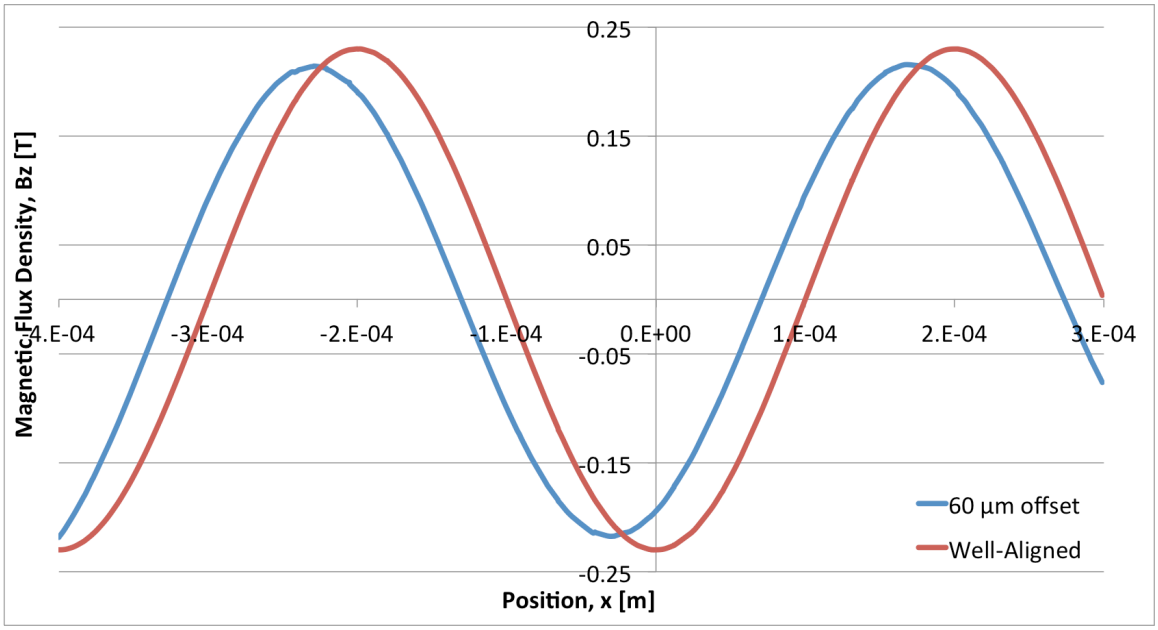
0.25
0.15
0.05
-0.05
-0.15
-0.25
-4.E-04
-3.E-04
-2.E-04
-1.E-04
0.E+00
1.E-04
2.E-04
3.E-04
Magnetic Flux Density, Bz [T]
Position, x [m]
60 µm offset
Well-Aligned

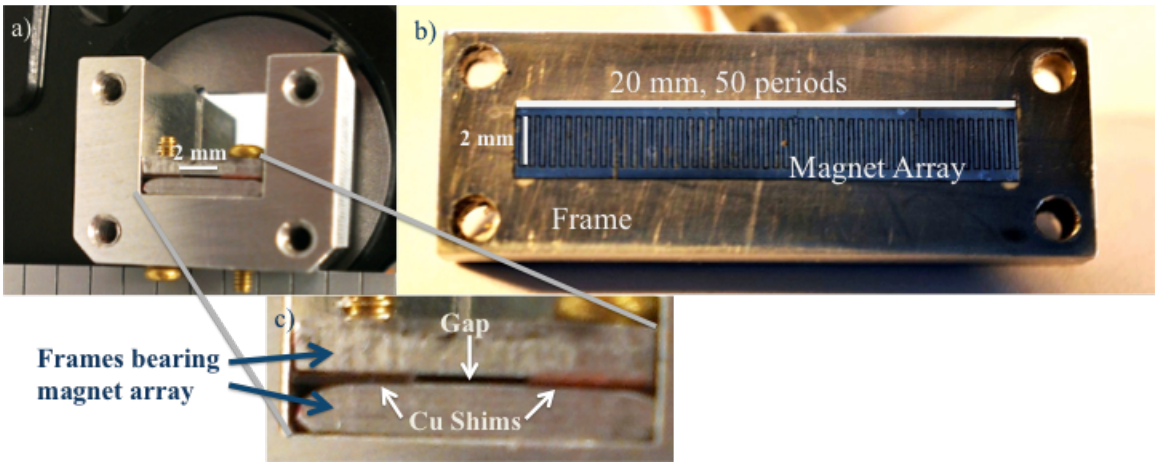
a)
2 mm
b)
20 mm, 50 periods
2 mm
Magnet Array
Frame
c)
Gap
Frames bearing
magnet array
Cu Shims

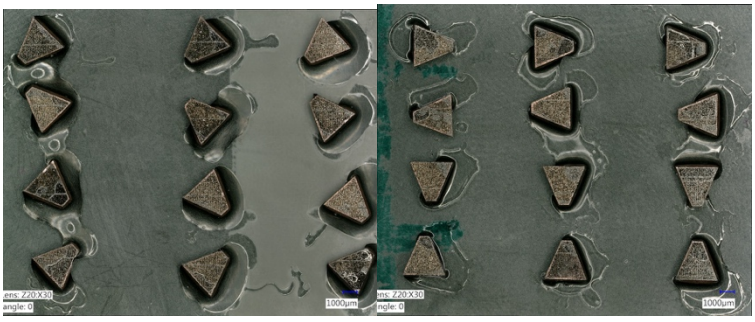

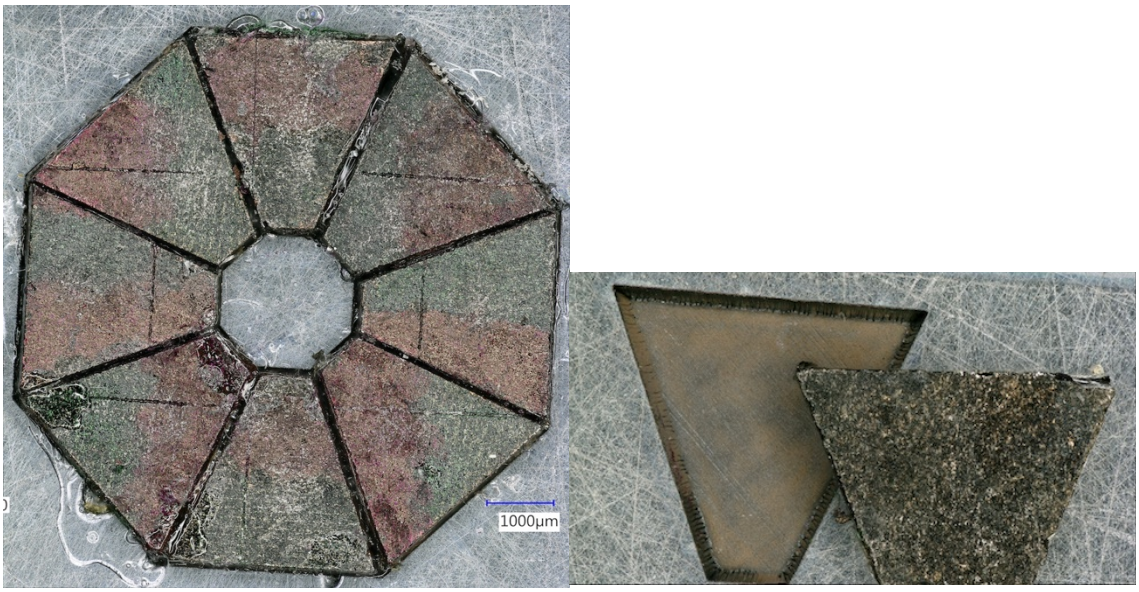
1000µm

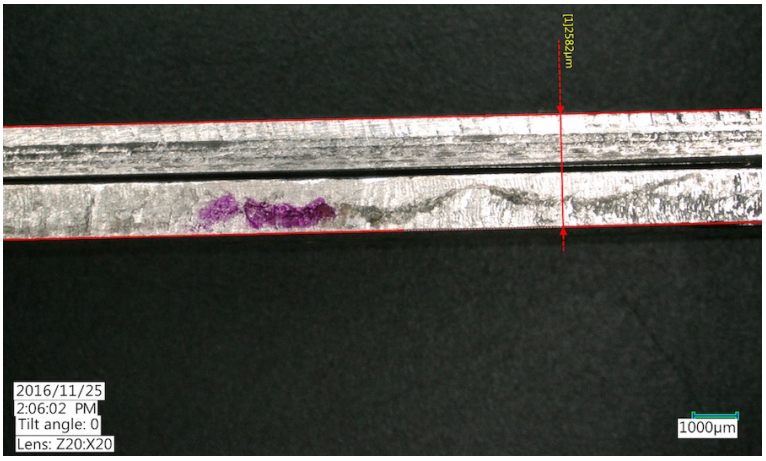
1125821μm
2016/11/25
2:06:02 PM
Tilt angle: 0
Lens: Z20:X20
1000μm


100μm


Lens: Z20:X50
Tilt angle: 0
8:43:06 AM
2016/10/17
100μm

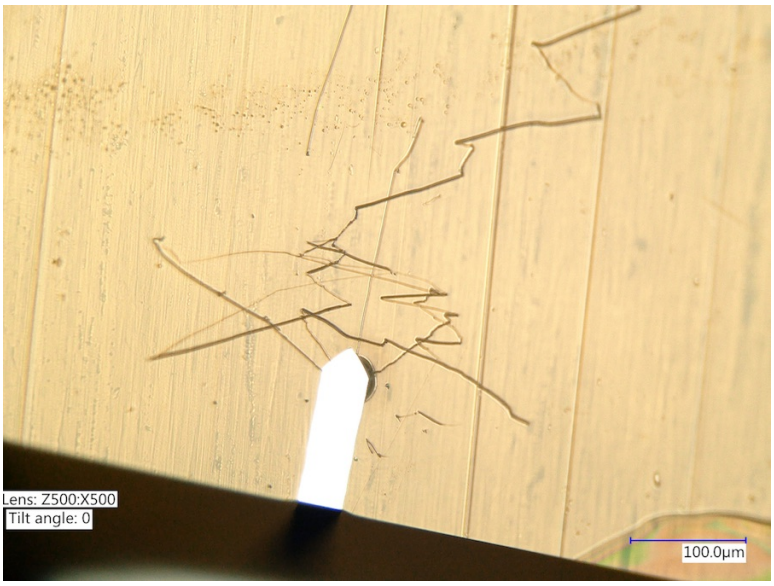
Lens: Z500:X500
Tilt angle: 0
100.0µm

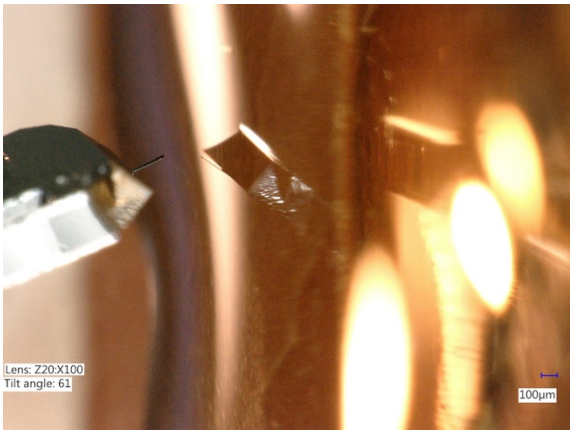
Lens: Z20:X100
Tilt angle: 61
100µm

APPENDIX E Magnetic Force Microscopy Images

NdFeB Green Laser Comparison

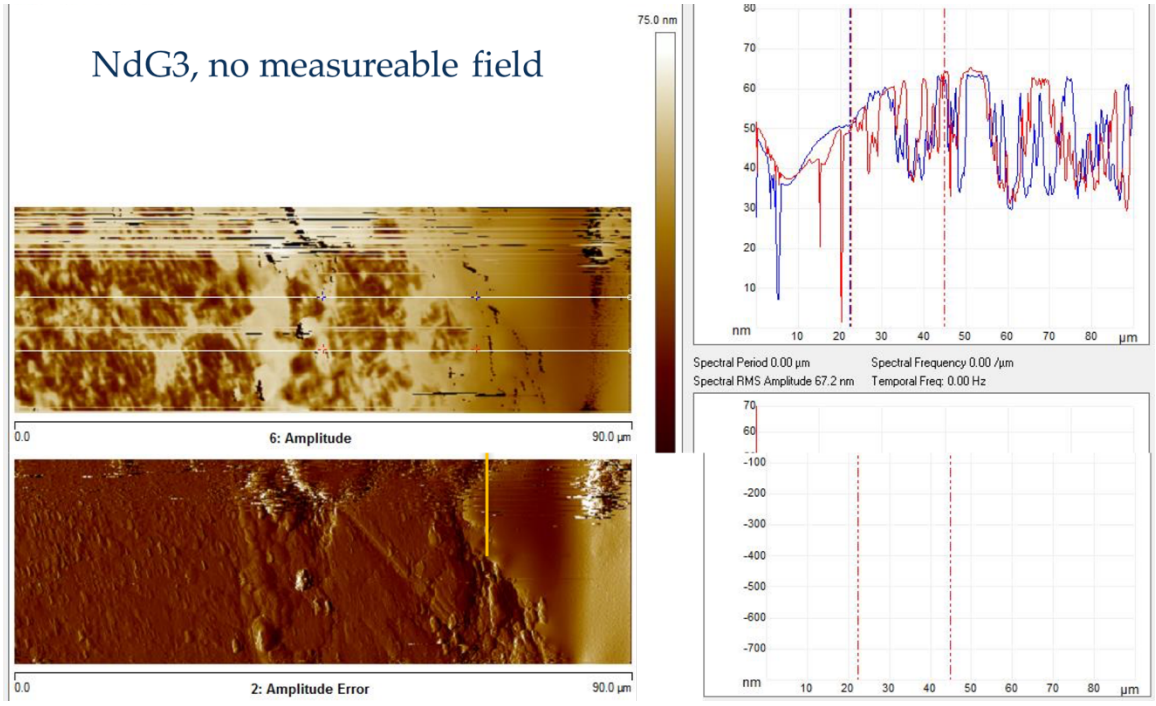

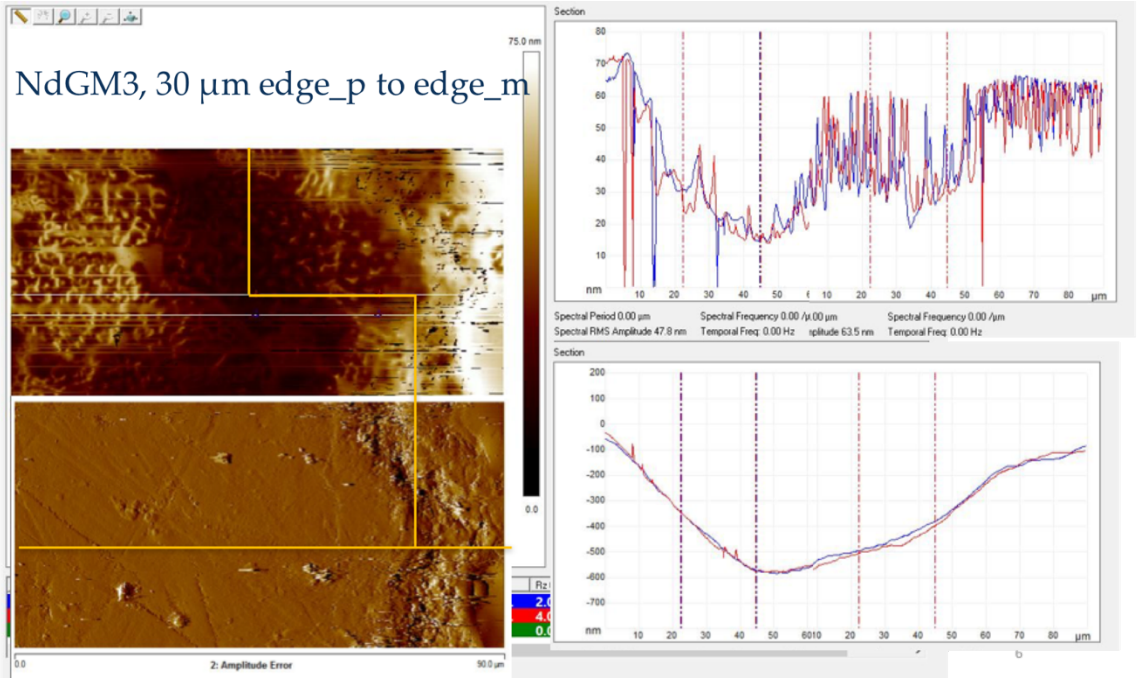

NdFeB Excimer Laser Comparison

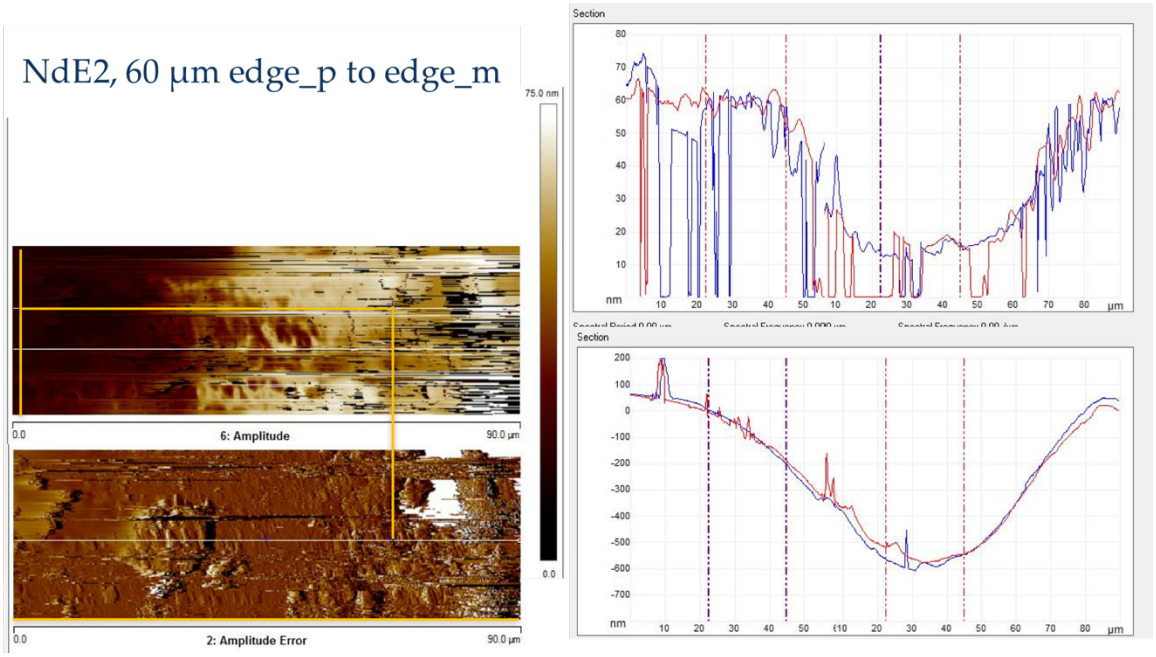

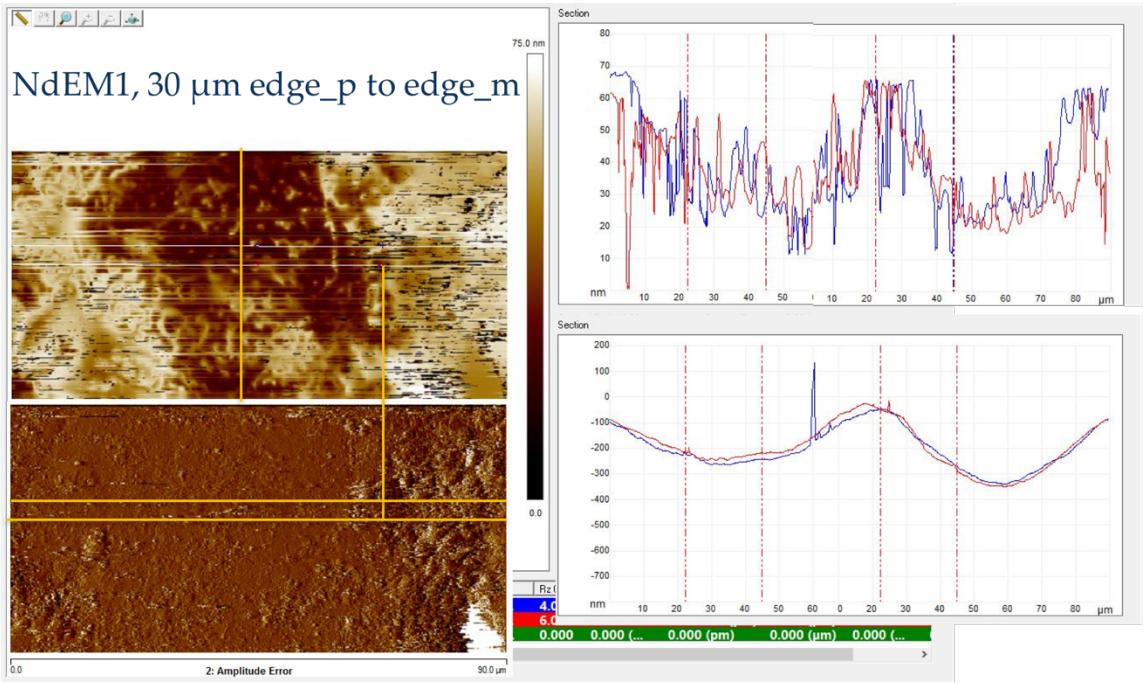

NdFeB QCW Laser Comparison

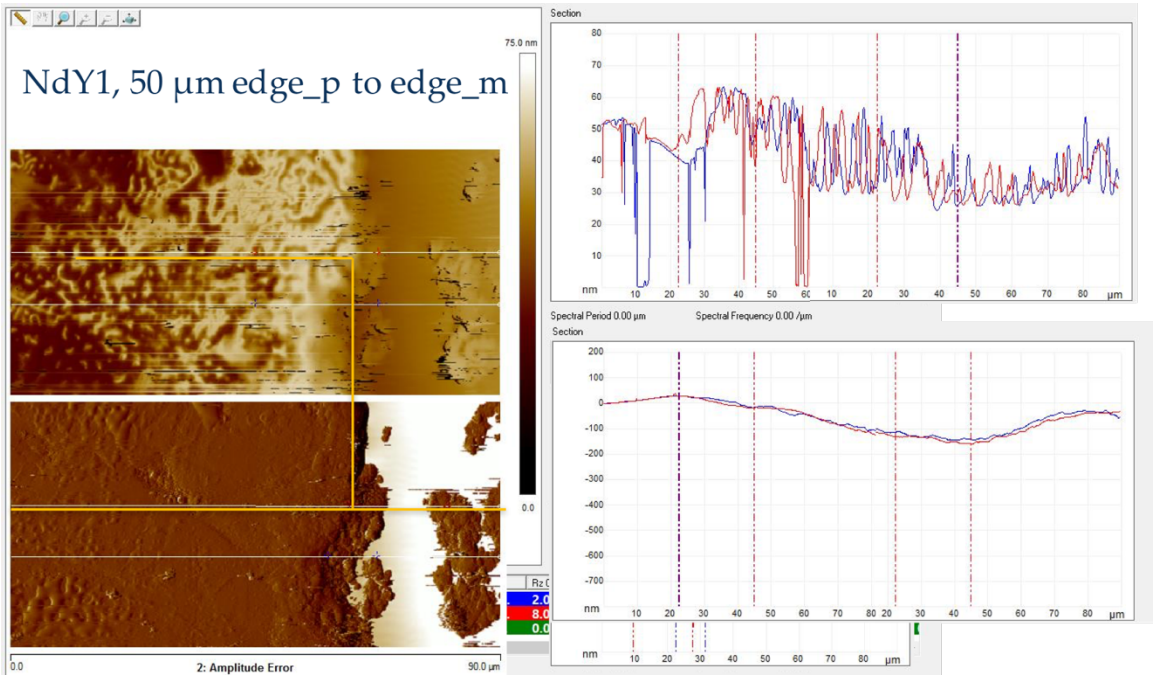

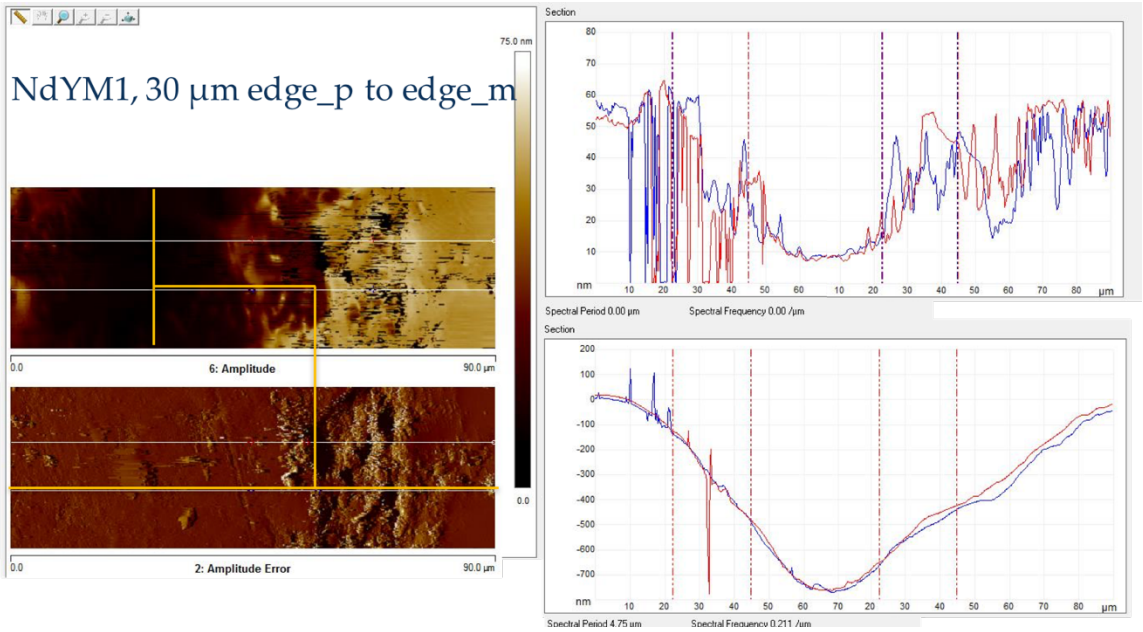

SmCo Green Laser Comparison

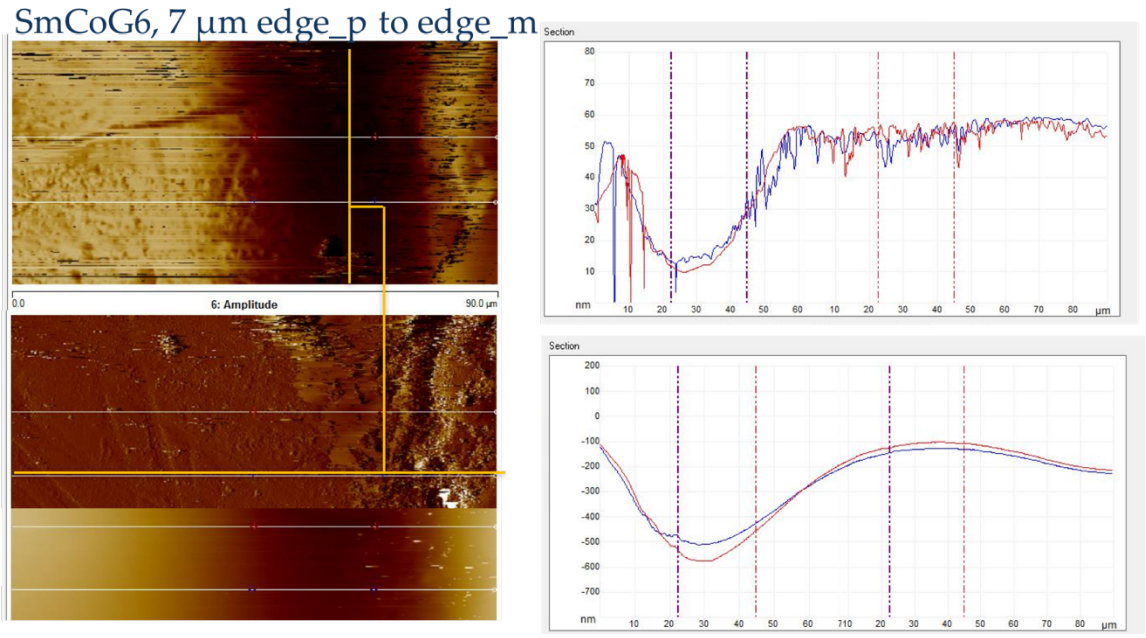

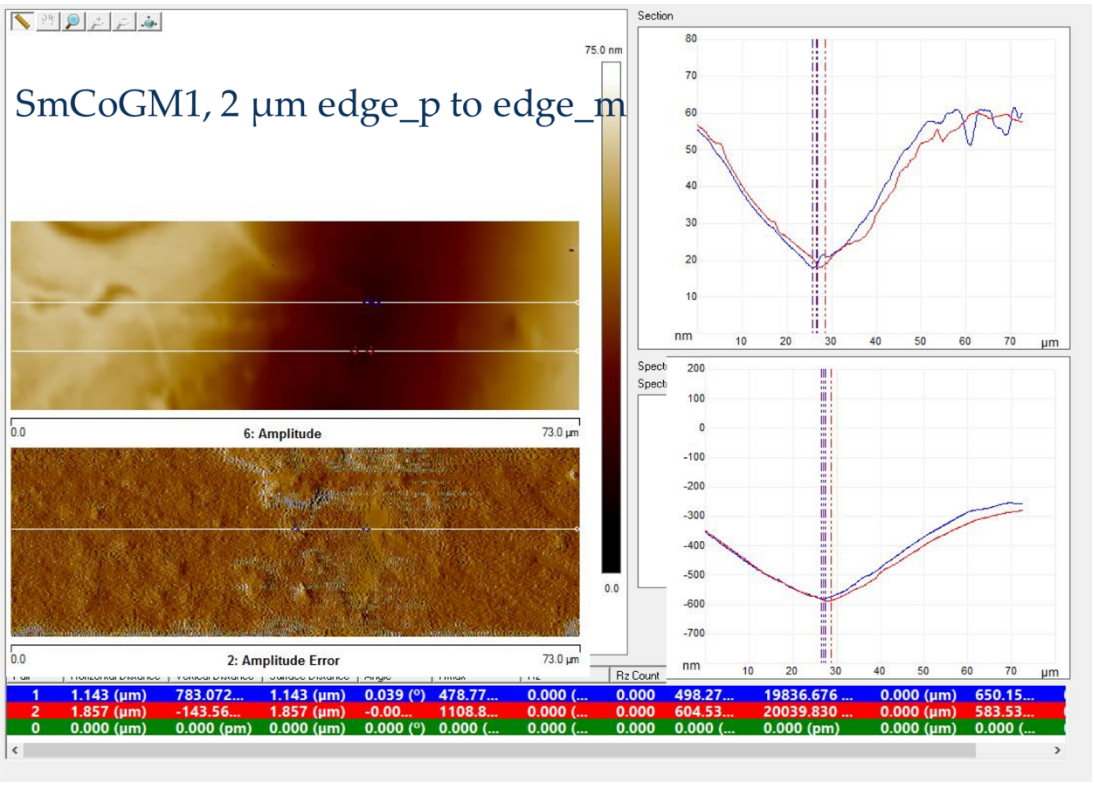

SmCo Excimer Laser Comparison

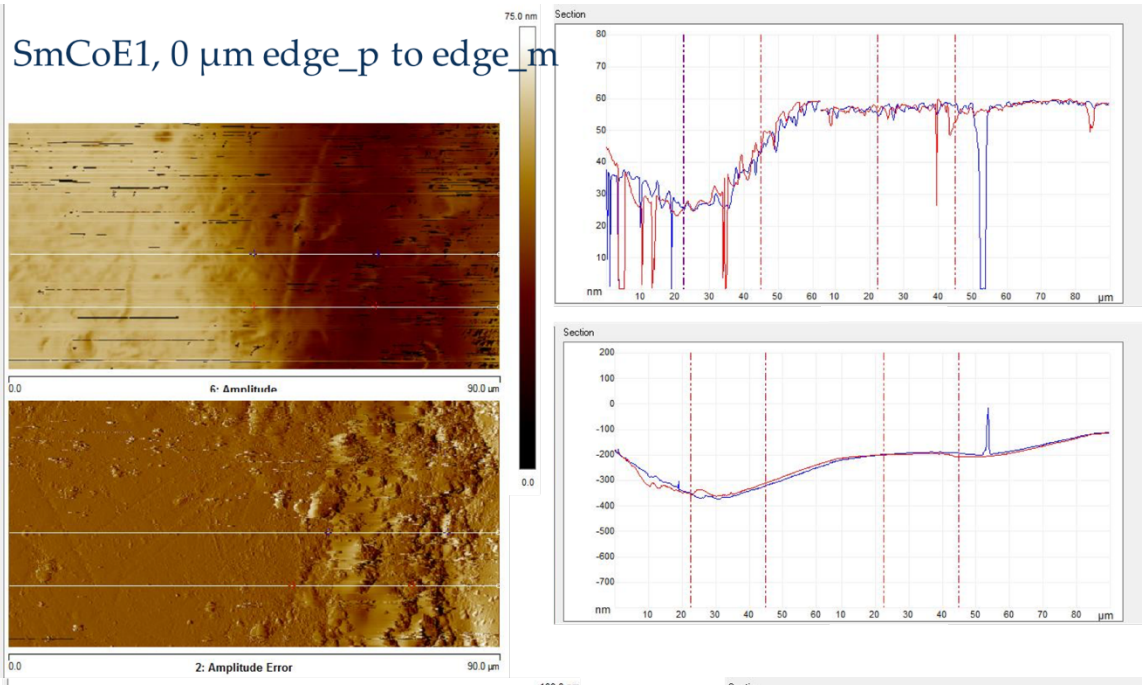

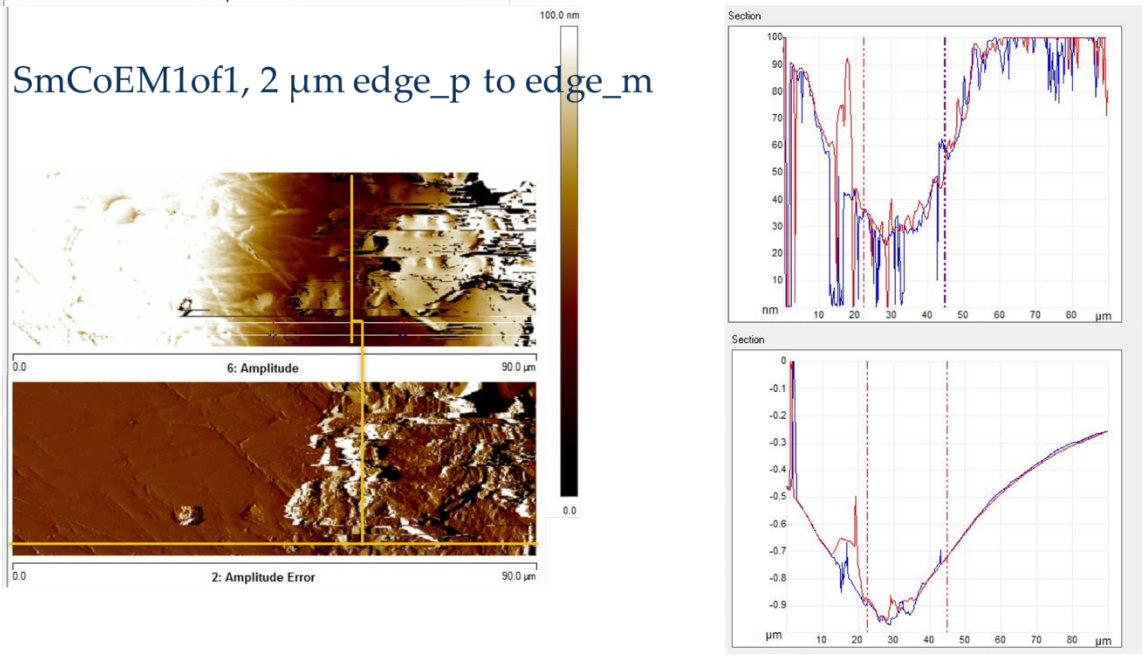

SmCo QCW Laser Comparison

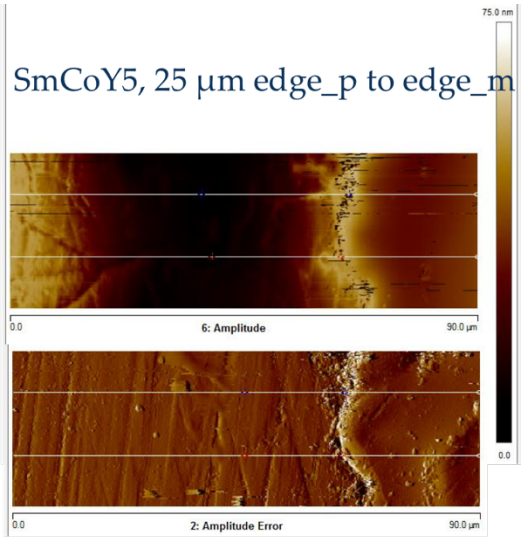

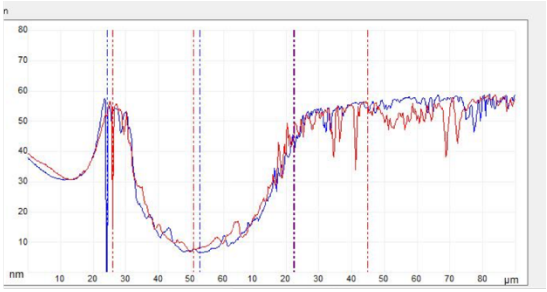

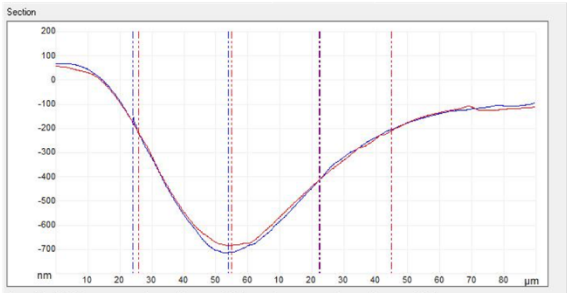

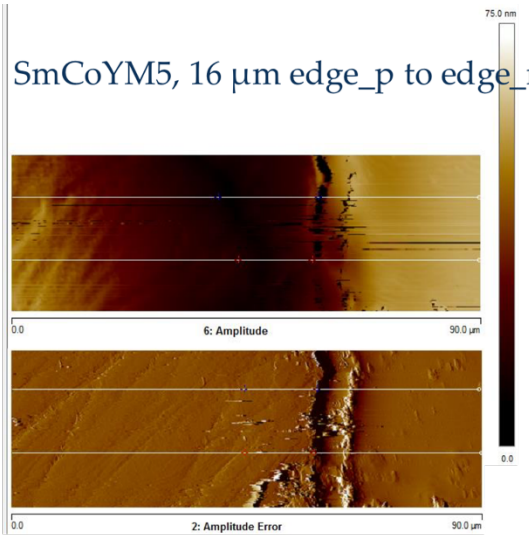

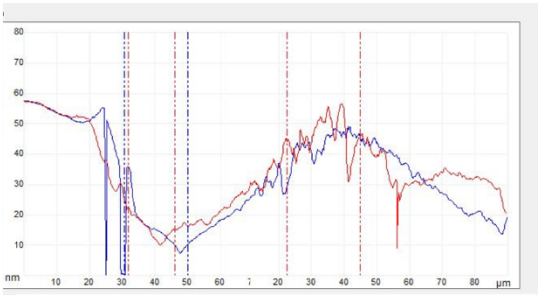

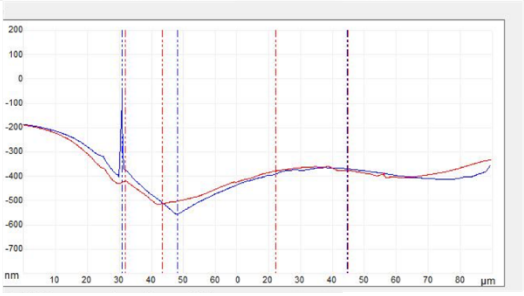

BIBLIOGRAPHY

[1] O. Cugat, G. Reyne, J. Delamare and H. Rostaing, "Novel magnetic micro-actuators and systems (MAGMAS) using permanent magnets," *Sensors and Actuators A,* vol. 129, no. 2006, pp. 265-269, 2006.

[2] D. Arnold and N. Wang, "Permanent Magnets for MEMS," *Journal of Microelectromechanical Systems,* vol. 18, no. 6, pp. 1255-66, December 2009.

[3] J. Camacho and V. Sosa, "Alternative method to calculate the magnetic field of permanent magnets with azimuthal symmetry," *Revista Mexicana de Física E,* vol. 59, no. 2013, pp. 8-17, January 2013.

[4] N. Dempsey, N. Kornilov and O. Cugat, "Thick hard magnetic films for MAGMAS: some key issues," in *Proceedings of HPMA'04 High Performance Magnets and Applications - MAGMAS*, Annecy, France, 2004.

[5] J. Livingston, "The History of Permanent Magnet Materials," *The Journal of the Minerals, Metals, and Materials Society,* vol. 42, no. 2, pp. 30-34, February 1990.

[6] E. Andrade, "The Early History of the Permanent Magnet," *Endeavour,* vol. 17, no. 65, p. 9, January 1958.

[7] O. Cugat, J. Delamare and G. Reyne, "Magnetic Micro-Actuators and Systems (MAGMAS)," *IEEE Transactions on Magnetics,* vol. 39, no. 5, pp. 3607-3612, Nov 2003.

[8] B. A. Peterson, O. D. Oniku, W. C. Patterson, D. Le Roy, A. Garraud, F. Herrault, N. M. Dempsey, D. P. Arnold and M. G. Allen, "Technology Development for Short-period Magnetic Undulators," *Physics Procedia,* vol. 52, no. 2014, pp. 36-45, 2014.

[9] S. Kohara, K. Suzuya, Y. Kashihara, N. Matsumoto, N. Umesaki and I. Sakai, "A Horizontal Two-Axis Diffractometer for High-Energy X-ray Diffraction Using Synchrotron Ratiation on Bending Magnet Beamline BL04B2 at SPring-8," *Nuclear Instruments and Methods in Physics Research A,* Vols. 467-468, no. 2001, pp. 1030-1033, 2001.

[10] J. Gieras and M. Wing, Permanent Magnet Motor Technology, 2nd Edition ed., New York: Marcel Dekker Inc., 2002.

[11] B. Chalmers, W. Wu and E. Spooner, "An Axial-Flux Permanent-Magnet Generator For A Gearless Wind Energy System," *IEEE Transactions on Energy Conversion,* vol. 14, no. 2, Jun 1999.

[12] P. Lauterbur, "Image Formation by Induced Local Interactions: Examples of Employing Nuclear Magnetic Resonance," *Nature,* vol. 242, no. 5394, pp. 190-191, March 1973.

[13] W. Alderman, "Magnetic door latch". Patent US 2586900 A, 26 February 1952.

[14] W. Mathauser, "Magnetic self-aligning quick-disconnect for a telephone or other communications equipment". Patent US 3808577 A, 30 April 1974.

[15] R. Matick, Computer Storage Systems and Technology, New York: John Wiley & Sons, 1977.

[16] L. David, "Valve with magnetic actuator". Patent US 3368791 A, 13 February 1968.

[17] D. Arnold, *Magnetic Machines for Microengine Power Generation,* Atlanta: Georgia Institute of Technology, 2004.

[18] S. Cheng and D. P. Arnold, "A Study of Multi-Pole Magnetic Generator for Low-Frequency Vibrational Energy Harvesting," *Journal of Micromechanics and Microengineering,* vol. 20, no. 025015, p. 10pp, 2010.

[19] C. Dieppedale, B. Desloges, H. Rostaing, J. Delamare, O. Cugat and J. Meunier-Carus, "Ultra-fast levitating magnetic bi-stable microactuator with integrated permanent magnets," in *Proceedings of IEEE Sensors 2004*, Vienna, Austria, 2004.

[20] W. Trimmer, "Microrobots and Micromechanical Systems," *Sensors and Actuators,* vol. 19, pp. 267-87, 1989.

[21] L. Lagorce and M. Allen, "Micromachined Polymer Magnets," in *Micro Electro Mechanical Systems, 1996, MEMS '96, Proceedings*, San Diego, 1996.

[22] A. Garraud, O. Oniku, W. Patterson, E. Shorman, D. Le Roy, N. Dempsey and D. Arnold, "Microscale Magnetic Patterning of Hard Magnetic Films Using Microfabricated Magnetizing Masks," in *MEMS 2014*, San Francisco, 2014.

[23] O. D. Oniku and D. P. Arnold, "Microfabrication of High Performance Thick Co80Pt20 Permanent Magnets for Microsystems Applications," *ECS Transactions,* vol. 50, no. 10, pp. 167-174, 2013.

[24] O. D. Oniku, R. Regojo, Z. A. Kaufman, W. C. Patterson and D. P. Arnold, "Batch patterning of sub-millimeter features in hard magnetic films using pulsed magnetic fields and soft magnetizing heads," *IEEE Transactions on Magnetics,* vol. In Press, 2013.

[25] K. Narasimhan, M. Wells and D. Ratnam, "Rare earth–cobalt magnets with low reversible temperature coefficient," *Journal of Applied Physics 49, 2072 (1978),* vol. 49, no. 3, pp. 2072-74, March 1978.

[26] L. Bates, "Domain Wall Pinning," *Contemporary Physics,* vol. 15, no. 6, pp. 562-564, 1974.

[27] K. Halbach, "Strong Rare Earth Cobalt Quadrupoles," in *Particle Accelerator Conference*, San Francisco, CA, 1979.

[28] K. Halbach, "Physical and Optical Properties of Rare Eath Cobalt Magnets," *Nuclear Instruments and Methods: II Beam Guidance Systems,* vol. 187, pp. 109-117, 1981.

[29] Y. Kaneko, "Highest Performance of Nd–Fe–B Magnet Over 55 MGOe," *IEEE Transactions on Magnetics,* vol. 36, no. 5, pp. 3275-78, September 2000.

[30] J. Ormerod and S. Constantinides, "Bonded permanent magnets: Current status and future opportunities," *Journal of Applied Physics,* vol. 81, no. 8, pp. 4816-20, 15 April 1997.

[31] C. Yang, X. Zhao, G. Ding, C. Zhang and B. Cai, "An Axial Flux Electromagnetic Micromotor," *Journal of Micromechanics and Microengineering,* vol. 11, no. 2001, pp. 113-117, 2001.

[32] T. Clarence, "Method for making micromagnets". US Patent US3460248 A, 12 August 1968.

[33] E. Callaghan and S. Maslen, *The Magnetic Field of a Finite Solenoid,* Cleveland, OH: NASA Lewis Research Center, 1960, p. 26.

[34] J. Miller, M. Bird, S. Bole, A. Bonito-Oliva, Y. Eyssa, W. Kenney, T. Painter, H.-J. Schneider-Muntau, L. Summers, S. Van Sciver, S. Welton, R. Wood, J. Williams, E. Bobrov, Y. Iwasa, M. Leupold, V. Stejskal and R. Weggel, "An Overview of the 45-THybrid Magnet System for the New National High Magnetic Field Laboratory," *IEEE Transactions on Magnetics,* vol. 30, no. 4, pp. 1563-71, July 1994.

[35] J. Harrison, A. Joshi, J. Lake and R. Candler, "Surface-micromachined magnetic undulator with period length between 10 μm and 1 mm for

advanced light sources," *Phys. Rev. ST Accel. Beams,* vol. 15, no. 7, p. 070703, 2012.

[36] Y. Li, J. Kim, M. Kim, A. Armutlulu and M. Allen, "Thick Multilayered Micromachined Permanent Magnets With Preserved Magnetic Properties," *Journal of Microelectromechanical Systems,* vol. 25, no. 3, pp. 498-507, June 2016.

[37] M. Nakano, S. Sato, H. Fukunaga and F. Yamashita, "A Method of Preparing Anisotropic Nd-Fe-B Film Magnets by Pulsed Laser Deposition," *Journal of Applied Physics,* vol. 99, no. 08N301, p. 3, April 2006.

[38] J. Clarke, The Science and Technology of Undulators and Wigglers, Oxford University Press, 2004.

[39] K. Halbach, "Permanent Magnet Undulators," *Journal de Physique, Colloque C1,* vol. 44, no. 2, pp. 211-216, February 1983.

[40] D. Vokoun, M. Beleggia, L. Heller and P. Sitner, "Magnetostatic Interactions and Forces Between Cylindrical Permanent Magnets," *Journal of Magnetism and Magnetic Materials,* vol. 321, no. 2009, p. 3758–63, 2009.

[41] A. Beaulieu, "Transversely Excited Atmospheric Pressure CO2 Lasers," *Applied Physics Letters 16, 504 (1970);,* vol. 16, no. 12, pp. 504-505, June 1970.

[42] R. D. Schaeffer, Fundamentals of Laser Micromachining, 1st Edition ed., Boca Raton, FL: CRC Press, 2012, p. 260.

[43] M. S. Brown and C. B. Arnold, "Fundamentals of Laser-Material Interaction and Application to Multiscale Surface Modification," in *Laser Precision Microfabrication*, vol. 135, K. Sugioka, M. Meunier and A. Piqué, Eds., Springer, 2010.

[44] C. Schaffer, A. Brodeur and E. Mazur, "Laser-induced breakdown and damage in bulk transparent materials induced by tightly focused femtosecond laser pulses," *Measurement Science and Technology,* vol. 12, no. 11, pp. 1784-94, October 2001.

[45] D. Bäuerle, Laser processing and chemistry, 4. Edition, Ed., New York: Springer, 2011.

[46] J.-C. Weeber, J. Krenn, A. Dereux, B. Lamprecht, Y. Lacroute and J. Goudonnet, "Near-field observation of surface plasmon polariton propagation

on thin metal stripes," *Physical Review B,* vol. 64, no. 4, p. 045411, July 2001.

[47] B. Christensen, K. Vestentoft and P. Balling, "Short-Pulse Ablation Rates and the Two-Temperature Model," *Applied Surface Science,* vol. 253, pp. 6347-52, January 2007.

[48] D. Bäuerle, Laser Processing and Chemistry, Berlin: Springer, 2000.

[49] A. Hamad, "Effects of Different Laser Pulse Regimes (Nanosecond, Picosecond and Femtosecond) on the Ablation of Materials for Production of Nanoparticles in Liquid Solution," in *High Energy and Short Pulse Lasers*, R. Viskup, Ed., Online - Open Access, InTech, 2016, p. 424 pp.

[50] X. Mao, A. Ciocan and R. Russo, "Preferential Vaporization during Laser Ablation Inductively Coupled Plasma Atomic Emission Spectroscopy," *Applied Spectroscopy,* vol. 52, no. 7, pp. 913-18, 1998.

[51] N. Bulgakova and A. Bulgakov, "Pulsed laser ablation of solids: transition from normal vaporization to phase explosion," *Applied Physics A,* vol. 73, pp. 199-208, 2001.

[52] R. Stolan, D. Ashkenasi, A. Rosenfeld and E. Campbell, "Coulomb explosion in ultrashort pulsed laser ablation of Al2O3," *Physical Review B,* vol. 62, no. 19, pp. 168-73, November 2000.

[53] "IPG Photonics Micromachining Services," [Online]. Available: http://www.ipgphotonics.com/appGroup/view/61/Application_Center%2FMicromachining_Services. [Accessed 3 October 2016].

[54] "Resonetics Lightspeed Application Development Lab," [Online]. Available: http://resonetics.com/lightspeed-adl/. [Accessed 3 October 2016].

[55] F. Herrault, C.-H. Ji, S. Rajaraman, R. Shafer and M. Allen, "Electrodeposited Metal Structures in High Aspect Ratio Cavities Using Vapor Deposited Polymer Molds and Laser Micromachining," in *Transducers 2007: The 14th International Conference on Solid-State Sensors, Actuators and Microsystems*, Lyon, France, 2007.

[56] S. Davis, M. Prausnitz and M. Allen, "Fabrication and Characterization of Laser Micromachined Hollow Microneedles," in *Transducers 2003: 12th International Conference on Solid-State Sensors, Actuators and Microsystems*, 2003.

[57] Y. Choi, S.-O. Choi, R. Shafer and M. Allen, "Highly Inclined Electrodeposited Metal Lines Using an Excimer Laser Patterning Technique," in *Transducers*

2005: 13th International Conference on Solid-State Sensors, Actuators, and Microsystems, 2005.

[58] Y.-K. Yoon, R. Powers, Y. Choi, C. Courcimault and M. Allen, "Micromachined polymeric microvasculatures: A three-dimensional microfluidic system using inclined SU-8 structures and laser machining," in *226th American Chemical Society National Meeting, September 2003*, 2003.

[59] F. Herrault, *Microfabricated air-turbine and heat-engine-driven permanent-magnet generators,* Toulouse: Université de Toulouse, 2009.

[60] B. A. Peterson, F. Herrault, O. D. Oniku, Z. A. Kaufman, D. P. Arnold and M. G. Allen, "Assessment of Laser-Induced Damage in Laser-Micromachined Rare-Earth Permanent Magnets," *IEEE Transactions on Magnetics,* vol. 48, no. 11, pp. 3606-3609, 2012.

[61] "Laser Heating of a Silicon Wafer with Ablation," COMSOL Multiplhysics, [Online]. Available: https://www.comsol.com/model/laser-heating-of-a-silicon-wafer-with-ablation-28241. [Accessed 2015].

[62] C. Pinciuc and M. Matthews, *Finite Element Modeling of Laser Materials Processing,* COMSOL Multiphysics, 2014.

[63] J.-P. Kruth, P. Mercelis, J. Van Vaerenbergh, L. Froyen and M. Rombouts, "Binding mechanisms in selective laser sintering and selective laser melting," *Rapid Prototyping Journal,* vol. 11, no. 1, pp. 26-36, 2005.

[64] "How Neodymium Magnets are Made," K&J Magnetics Inc., [Online]. Available: https://www.kjmagnetics.com/blog.asp?p=how-neodymium-magnets-are-made. [Accessed 2016].

[65] R. Lee, E. Brewer and N. Schaffel, "Processing of neodymium-iron-boron melt-spun ribbons to fully dense magnets," *IEEE Transactions on Magnetics,* Vols. MAG-21, no. 5, pp. 1958-63, September 1985.

[66] K. Uestuener, M. Katter and W. Rodewald, "Dependence of the Mean Grain Size and Coercivity of Sintered Nd-Fe-B Magnets on the Initial Powder Particle Size," *IEEE Transactions on Magnetics,* vol. 42, no. 10, pp. 2897-99, October 2006.

[67] P. Whitey, H. Kennett, P. Bowen and I. Harris, "The Magnetic and Mechanical Properties of NdFeB Type Permanent Magnets and the Effect of Quenching," *IEEE Transactions on Magnetics,* vol. 26, no. 5, pp. 2619-21, September 1990.

[68] F. Ferri, M. Pereira-da-Silva and E. Marega, "Chapter 3: Magnetic Force Microscopy: Basic Principles and Applications," in *Atomic Force Microscopy - Imaging, Measuring and Manipulating Surfaces at the Atomic Scale*, V. Bellitto, Ed., Rijeka, InTech, 2012, p. 18.

[69] M. Koblischka and U. Hartmann, "Recent advances in magnetic force microscopy," *Ultramicroscopy,* vol. 97, pp. 103-112, 2003.

[70] D. Goll and H. Kronmüller, "High-performance permanent magnets," *Naturwissenschaften,* vol. 87, pp. 423-438, 2000.

[71] Y. Li, H. Evans, I. Harris and I. Jones, "The Oxidation of NdFeB Magnets," *Oxidation of Metals,* vol. 59, no. 1, pp. 167-182, February 2003.

[72] B. A. Peterson, W. C. Patterson, F. Herrault, D. P. Arnold and M. G. Allen, "Laser-micromachined permanent magnet arrays with spatially alternating magnetic field distribution," in *PowerMEMS*, Atlanta, 2012.

[73] D. Attwood, Soft X-Rays and Extreme Ultraviolet Radiation: Principles and Applications, Cambridge University Press, 1999.

[74] G. Brown, K. Halback, J. Harris and H. Winick, "Wiggler and Undulator Magnets - A Review," *Nuclear Instruments and Methods,* vol. 208, pp. 65-77, 1983.

[75] D. Attwood, *Synchrotron Radiation for Materials Science Applications,* Berkeley, CA: University of California - Berkeley, 2007.

[76] H. Kitamura, "Polarization of Undulator Radiation," *Japanese Journal of Applied Physics,* vol. 19, no. 4, pp. L185-L188, April 1980.

[77] R. Warren, "Limitations On The Use Of The Pulsed-Wire Field Measuring Technique," *Nuclear Instruments and Methods in Physics Research,* vol. 1988, no. A272, pp. 257-263, 1988.

[78] D. Arbalaez, A. Madur, T. Wilks, A. Bartlett, S. Prestemon and R. Schlueter, *Analysis of Pulsed Wire Magnetic Field Measurements for Undulators,* Lawrence Berkeley National Lab, 2010.

[79] M. Gehlot, G. Mishra, G. Sharma and J. Hussain, "An overview of the undulator field measurement studies at insertion device lab, DAVV," *Journal of Physics: Conference Series,* vol. 365, p. 4 pp, 2012.

[80] P. Bousine, S. Tolmachev and A. Varfolomeev, "Detailed analysis of pulsed-wire technique accuracy," *Nuclear Instruments and Methods in Physics Research A,* vol. 393, pp. 414-418, 1997.

[81] N. Osmanov, S. Tolmachev and A. Varfolomeev, "Further development of the pulsed wire technique for magnetic field and focusing strength measurements in long undulators," *Nuclear Instruments and Methods in Physics Research A,* vol. 407, pp. 443-447, 1998.

[82] M. Valléau, C. Benabderahmane, M. Couprie, O. Marcouillé, F. Marteau and J. Vétéran, "Measurements of SOLEIL Insertion Devices Using Pulsed Wire Method," in *Proceedings of IPAC2011*, San Sebastián, Spain, 2011.

[83] J. Melton, M. Burns and D. Honaberger, "Pulsed Taut-Wire Measurement of the Magnetic Alignment of the ITS Induction Cells," in *Particle Acclerator Conference*, Washington, D.C., 1993.

[84] C. Fortgang, L. Dauelsberg, C. Geisik, D. Liska and R. Shafer, "Pulsed Taut-Wire Alignment of Multiple Permanent Magnet Quadrupoles," in *Proceedings of the Linear Accelerator Conference 1990*, Albuquerque, NM, USA, 1990.

[85] V. Kumar and G. Mishra, "Analysis of pulsed wire method for field integral measurements in undulators," *PRAMANA — Journal of Physics,* vol. 74, no. 5, pp. 743-53, May 2010.

[86] D. Preston and R. Warren, "Wiggler field measurements and corrections using the pulsed wire technique," *Nuclear Instruments and Methods in Physics Research A,* vol. 318, pp. 794-97, 1992.

[87] V. Malka, J. Faure, Y. Gauduel, E. Lefebvre, A. Rousse and K. Phuoc, "Principles and applications of compact laser–plasma accelerators," *Nature Physics,* vol. 4, pp. 447-453, June 2008.

[88] H.-D. Gräf, J. Herrmann, M. Hüning, U. Laier, P. Mohr, M. Platz, A. Richter, B. Schweizer, S. Watzlawik and H. Weise, "Compton diodes as diagnostic tools in accelerator operation," *Nuclear Instruments and Methods in Physics Research A,* vol. 512, no. 3, pp. 453-58, June 2003.

[89] C. Underhill, Magnets: A Practical Treatise on Electromagnetic Devices, Their Circuits, and the Specific Forms and Characteristics of Electromagnets and Permanent Magnets Employed, First Edition ed., New York: McGraw-Hill Book Company, Inc., 1924, p. 468.

[90] V. Challa and D. Arnold, "MEMS Electrodynamic Vibrational Energy Harvesters Using Multi-pole Magnetic Architectures," in *PowerMEMS 2012*, Atlanta, GA.

[91] S. Beeby, M. Tudor and N. White, "Energy harvesting vibration sources for microsystems applications," *Measurement Science and Technology,* vol. 17, pp. R175-R195, 2006.

[92] F. Bloch, O. Cugat, G. Meunier and J. Toussaint, "Innovating Approaches to the Generation of Intense Magnetic Fields : Design and Optimization of a 4 Tesla Permanent Magnet Flux Source," *IEEE Transactions on Magnetics,* vol. 34, no. 5, pp. 2465-68, September 1998.

[93] D. Zhu, S. Beeby, J. Tudor and N. Harris, "Vibration energy harvesting using the Halbach array," *Smart Materials and Structures,* vol. 21, no. 10, p. 11 pp, June 2012.

[94] J. Harrison, Y. Hwang, O. Paydar, J. Wu, E. Threlkeld, J. Rosenzweig, P. Musumeci and R. Candler, "High-gradient microelectromechanical system quadrupole electromagnets for particle beam focusing and steering," *Physical Review Special Topics - Accelerators and Beams,* vol. 18, no. 2, p. 023501, 17 02 2015.

[95] J. Barral, N. Bangerter, B. Hu and D. Nishimura, "In Vivo High-Resolution Magnetic Resonance Skin Imaging at 1.5 T and 3 T," *Magnetic Resonance in Medicine,* vol. 63, no. 3, pp. 790-796, March 2010.

[96] P. Van Bentum, J. Janssen and A. Kentgens, "Towards nuclear magnetic resonance μ-spectroscopy and μ-imaging," *The Analyst,* vol. 129, pp. 793-803, August 2004.

[97] "Standard Periodic Table with NMR bibliography for quadrupole nuclei with half-integer spins," 8 February 2013. [Online]. Available: http://www.pascal-man.com/periodic-table/periodictable.html. [Accessed 2016].

[98] L. Bi, J. Hu, P. Jiang, H. Kim, D. Kim, M. Onbasli, G. Dionne and C. Ross, "Magneto-Optical Thin Films for On-Chip Monolithic Integration of Non-Reciprocal Photonic Devices," *Materials,* vol. 2013, no. 6, pp. 5094-5117, November 2013.

[99] R. De Luca, "Lorentz force on sodium and chlorine ions in a salt water solution flow under a transverse magnetic field," *European Journal of Physics,* vol. 30, pp. 459-466, 2009.

[100] M.-A. Van Ende, I.-H. Jung, Y.-H. Kim and T.-S. Kim, "Thermodynamic optimization of the Dy–Nd–Fe–B system and application in the recovery and

recycling of rare earth metals from NdFeB magnet," *Green Chemistry,* vol. 17, pp. 2246-62, 2015.

[101] M. Tokushige, H. Hongo, T. Nishikiori and Y. Ito, "Formation of Sm-Co Intermetallic Compound Nanoparticles Based on Plasma-Induced Cathodic Discharge Electrolysis in Chloride Melt," *Journal of The Electrochemical Society,* vol. 159, no. 1, pp. E5-E10, 2012.

[102] W. Liu, S. Suzuki, D. Li and K. Machida, "Magnetic Properties of Fe-Pt Thick-Film Magnets prepared by RF Sputtering," *Journal of Magnetism and Magnetic Materials,* vol. 302, no. 2006, pp. 201-205, September 2005.

[103] K. Benyounis, A. Olabi and M. Hashmi, "Effect of Laser Welding Parameters on the Heat Input and Weld-bead Profile," *Journal of Materials Processing Technology,* Vols. 164-165, no. 2005, pp. 978-85, 2005.

[104] J. Ion, Laser Processing of Engineering Materials: Principles, Procedure and Industrial Applications, Boston: Elsevier/Butterworth-Heinemann, 2005.

[105] "Specialized Course on Magnets," in *CERN Accelerator School*, Bruges, Belgium, 2009.

[106] R. Grechishkin, S. Chigirinsky, M. Gusev, O. Cugat and N. Dempsey, Magnetic Nanostructures in Modern Technology, B. Azzerboni, G. Asti, L. Pareti and M. Ghidini, Eds., Dordrecht: Springer-Kluwer Academic, 2007, p. 195.

[107] N. M. Dempsey, A. Walther, F. May, D. Givord, K. Khlopkov and O. Gutfleisch, "High performance hard magnetic NdFeB thick films for integration into micro-electro-mechanical systems," *Applied Physics Letter,* vol. 90, p. 092509, 2007.

[108] T. Hezel, B. Krevet, H. O. Moser, J. A. Rossmanith, R. Rossmanith and T. Schneider, "A superconductive undulator with a period length of 3.8 mm," *J. Synchrotron Radiat,* vol. 5, pp. 448-450, 1998.

[109] T. Lawrence, R. Ten Haken and A. Giaccia, "Principles of Radiation Oncology," in *Cancer: Principles and Practices of Oncology*, 8th ed., V. J. DeVita, T. Lawrence and S. Rosenberg, Eds., Philadelphia, Lippincott Williams and Wilkins, 2008.

[110] G. Was, Fundamentals of Radiation Materials Science: Metals and Alloys, Springer, 2007.

[111] R. Tatchyn, A. Toor, J. Hunter, R. Hornady, D. Whelan, G. Westenskow, P. Sonka, T. Cremer and E. Källne, "Generation of Soft X-Ray/VUV Photons

with a Hybrid/Bias Micropole Undulator on the LLNL Linac," *Journal of X-Ray Science and Technology,* vol. 1, no. 1, pp. 79-98, 1989.

[112] Arnold Magnetic Technologies, *Sintered Neodymium-Iron-Boron Magnets - N48,* Rochester, NY: Arnold Magnetic Technologies Corporation, 2015.

[113] H. Kirchmayr, "Permanent magnets and hard magnetic materials," *Journal of Physics, D: Applied Physics,* vol. 29, no. 1996, pp. 2763-78, 1996.

[114] R. Stamps, S. Breitkreutz, J. Åkerman, A. Chumak, Y. Otani, G. Bauer, J. Thiele, M. Bowen, S. Majetich, M. Kläui, I. Prejbeanu, B. Dieny, N. Dempsey and B. Hillebrands, "The 2014 Magnetism Roadmap," *Journal of Physics D: Applied Physics,* vol. 47, no. 33, p. 333001, July 2014.

[115] Y. Li, J. Kim, M. Kim, A. Armutlulu and M. Allen, "Thick Multilayered Micromachined Permanent Magnets With Preserved Magnetic Properties," *Journal of Microelectromechanical Systems,* vol. 25, no. 3, p. 10, June 2016.

VITA

Brock Peterson was born in 1986 in Seattle, Washington. Brock received his B.S. degree in Electrical Engineering from Brigham Young University, Provo, in August 2010. At BYU, he was involved in research studying sodium-based MRI, designing RF resonant coils. He received his M.S. degree in Electrical and Computer Engineering from Georgia Institute of Technology, Atlanta, in 2013. He received his Ph.D. degree in Electrical and Systems Engineering from University of Pennsylvania in 2016.

He was a Micron/IMMERSE Scholar during the summers of 2009 and 2010 at BYU. He was awarded an honorable mention as part of the NSF GRFP application process in 2012 while at GT, and later became a SMART Scholarship awardee for the duration of his education at Penn, 2014-2016.

Brock began his research with the MicroSensors and MicroActuators group in May 2011 and moved with Dr. Mark Allen from Georgia Tech to Penn at the end of 2013. The focus of his research has been on laser machined micromagnets and the applications of spatially arbitrary magnetic field patterns and specifically highly spatially oscillating, strong magnetic field patterns. He has accepted a civilian engineer position at Picatinny Arsenal as part of the Army Research and Development Engineering Center.

His research interests include lasers and optics, magnets, micromagnets, high energy particle physics, and electromagnetics in general.